Development of 3D-Printed Cartilage Constructs and Their Non-Invasive Assessment by Synchrotron-Based Inline-Phase Contrast Imaging Computed Tomography

A Thesis Submitted to the
College of Graduate Studies and Research
In Partial Fulfillment of the Requirements
For the Degree of Doctor of Philosophy
In the Division of Biomedical Engineering
University of Saskatchewan
Saskatoon, SK., Canada

By

ADEOLA DEBORAH OLUBAMIJI

Permission to Use

In presenting this thesis in partial fulfillment of the requirements for a Postgraduate degree from the University of Saskatchewan, I agree that the Libraries of this University may make it freely available for inspection. I further agree that permission for copying of this thesis in any manner, in whole or in part, for scholarly purposes may be granted by the professor or professors who supervised my thesis work or, in their absence, by the Head of the Department or the Dean of the College in which my thesis work was done. It is understood that any copying or publication or use of this thesis or parts thereof for financial gain shall not be allowed without my written permission. It is also understood that due recognition shall be given to me and to the University of Saskatchewan in any scholarly use which may be made of any material in my thesis. Requests for permission to copy or to make other use of material in this thesis in whole or part should be addressed to:

Head of the Division of Biomedical Engineering
57 Campus Drive, University of Saskatchewan
Saskatoon, Saskatchewan S7N 5A9
Canada

Abstract

One goal of cartilage tissue engineering (CTE) is to create constructs for regeneration of hyaline cartilage. Three-dimensional (3D)-printed cartilage constructs fabricated from polycaprolactone (PCL) and chondrocyte-impregnated alginate mimic the biphasic nature of articular cartilage and offers great promise for CTE applications. However, ensuring that these constructs provide biologically conducive environment and mechanical support for cellular activities and articular cartilage regeneration is still a challenge. That said, the regulatory pathway for medical device development requires validation of implants such as these through *in vitro* bench test and *in vivo* preclinical examination prior to their premarket approval. Furthermore, mechano-transduction and secretion of cartilage-specific ECM are influenced by mechanical stimuli directed at chondrocytes. Thus, ensuring that these cartilage constructs have mechanical properties similar to that of human articular cartilage is crucial to their success. Non-invasive imaging techniques are required for effective evaluation of progression of these cartilage constructs. However, current non-invasive techniques cannot decipher components of the cartilage constructs, nor their time-dependent structural changes, because they contain hydrophobic and hydrophilic biomaterials with different X-ray refractive indices.

The aims of this thesis were to develop 3D-printed cartilage constructs that biologically and mechanically mimic human articular cartilage and to investigate synchrotron radiation inline phase contrast computed tomography (SR-inline-PCI-CT) as a non-invasive imaging technique to characterize components of these constructs and associated time-dependent structural changes. The first objective was to determine *in vitro* biological functionality of the cartilage constructs over a 42-day period with regards to cell viability and secretion of extracellular matrix by traditional invasive assays. In parallel, performance of SR-inline-PCI-CT for non-invasive visualization of components and associated structural changes within the constructs *in vitro* over a 42-day was examined. To achieve this objective, three sample-to-detector distances (SDDs): 0.25 m, 1 m and 3 m were investigated. Then, the optimal SDD with better phase contrast and edge enhancement fringes for characterization of the multiple refractive indices within the constructs was utilized to visualize their structural changes over a 42-day culture period. Like the first objective, the second objective was to examine *in vivo* biological functionality of the cartilage constructs by traditional invasive assays and utilize SR-inline-PCI-CT to non-invasively visualize components of the hybrid cartilage constructs over a 21-day period post-implantation in mice. The

third objective was to modulate mechanical properties of PCL framework of the 3D-printed PCL-based cartilage constructs to mimic mechanical properties of human articular cartilage. To achieve this, effect of modulation of PCL's molecular weight (M_W) and scaffold's pore geometric configurations: strand size (SZ), strand spacing (SS), and strand orientation (SO), on mechanical properties of 3D-printed PCL scaffolds were studied. Then, regression models showing the effect of SZ, SS, and SO on porosity, tensile moduli and compressive moduli of scaffold were developed. Compressive and tensile properties of these scaffolds were compared with those of human articular cartilage. Then, "modulated PCL scaffolds" with mechanical and biomimetic properties that better mimic human articular cartilage was identified and recommended for fabrication of PCL-based cartilage constructs.

This thesis demonstrated effective *in vitro* and *in vivo* biological performance of the 3D-printed hybrid cartilage constructs studied and presented a significant advancement in CTE applications. To be precise, cell viability was at a minimum of 77 % and secretion of sulfated GAGs and Col2 increased progressively within cartilage constructs over a 42-day *in vitro*. Similarly, cell viability was consistently above 70 %, and secretion of sulfated GAGs and Col2 increased post-implantation of constructs in mice over a 21-day period. Furthermore, SR-inline-PCI-CT demonstrated phase contrast and edge-enhancement fringes effective for visualization of the different components and subtle variations within the biphasic cartilage constructs, and thus, offers great potential for their non-invasive and three-dimensional visualization. Lastly, this thesis presented a significant advancement towards development of PCL constructs with mechanical behavior that mimic that of human articular cartilage. The statistical regression models developed showed the effect of SZ, SS, and SO on porosity, tensile moduli and compressive moduli of scaffolds and recommended sets of parameters for fabrication of "modulated PCL scaffolds" with mechanical properties that better mimic mechanical behavior of human articular cartilage. These "modulated PCL scaffolds" could serve as a better framework and could guide more effective secretion of cartilage-specific ECM within PCL-based constructs for CTE applications.

Acknowledgements

I would like to express my utmost gratitude to God Almighty and my supervisors, Dr. Daniel Chen and Dr. Brian Eames, for their advice, encouragement and support. I would also like to thank my Advisory Committee members: Dr. Bill Kulyk, Dr. Dean Chapman, Dr. Ning Zhu, and Dr. Assem Hedayat for their valuable comments and suggestions. In addition, I appreciate Dr. Tuanjie Chang, Dr. Zohreh Izadifar, Dr. David Cooper, Dr. Ali Honaramooz, Dr. Chijioke Nwankwo and Dr. Kingsley Iroba for their guidance during image acquisition, biological experiments, animal surgery and statistical analysis. The scientific and moral guidance from Dr. Ikechuckwuka Oguocha and Dr. Akindele Odeshi are also greatly appreciated. My thanks also go to Doug Bitner, Louis Roth, Rob Peace, Ken Jodrey and Ning Cao at the College of Engineering for the technical support I received during scaffold fabrication and mechanical testing.

I acknowledge the financial supports granted to me by the University of Saskatchewan (via Saskatchewan Innovation and Opportunity Scholarship and Bone Imaging Research Fellowship), College of Engineering (via Engineering Graduate Research Fellowship), Division of Biomedical Engineering (via the Devolved Graduate Research Scholarship), CIHR-THRUST training program (via CIHR-THRUST Fellowship) and Saskatchewan Health Research Foundation (SHRF) (via Tissue Engineering Research Group (TERG) grant to my supervisors). In addition, I would like to acknowledge Canadian Light Source (CLS) (Biomedical Imaging & Therapy Beamline), where all synchrotron imaging experiments were pursued. Specifically, I would like to thank Dr. George Belev and other scientists from the CLS for their dedicated technical support. Also, I would like to thank my colleagues from the Biofabrication Laboratory and Dr. Eames's Laboratory for their encouragements and assistance.

I would like to thank my family: Mr. & Mrs. Olubamiji and my brothers Dayo Olubamiji, Kolawole Olubamiji & Foluso Olubamiji. In addition, my gratitude goes to my uncles: Mr. Akinsola Oluwole, Mr. Clement Oluwole, Dr. Soji Oluwole and Dr. Francis Oluwole for their support, encouragements and prayers. Finally, I would like to thank Dr. & Mrs. Ayo & Lara Akerele, Mr. & Mrs. Ayodeji & Bolanle Adeoni, Dr. Reginald Adiele, Mr. Olayide Olorunleke, Dr. & Mrs. Steve & Jania Jimbo, Miss Abidemi Olomola, Miss Oluwatomisin Iwajomo, Dr. & Mrs. Olaniyi & Olusola Olaloku, Dr. Olubunmi Adewoyin, Mr. Cesare Ibba, Mrs Ijeoma Nwamuo, Mr. Alaba Nafiu and Mr. Carl Magnus for their support, mentorship, encouragements and prayers.

Dedication

This PhD dissertation is dedicated to my dad (Taiwo Isaac Olubamiji), my late sister (Omoleye Dorcas Olubamiji who lost her battle to cancer on December 16th, 2013), my late mentor (Ayodeji Olatunbosun who passed away on February 27th, 2012 right before defending his PhD dissertation) and my unborn children. My daily strength came from memories and thoughts of you, and my someday is a reality because of you.

Table of Contents

List of Figures

List of Tables

List of Equations

Table of Abbreviation

Abbrevation	Explanation
AM	Additive manufacturing
ANOVA	Analysis of variance
BBD	Box–Behnken design
BMIT-ID	Biomedical Imaging and Therapy-Insertion Device
BTE	Bone tissue engineering
$CaCl_2$	Calcium chloride dehydrate
CFI	Canadian Foundation for Innovation
CLS	Canadian Light Source
Col2	Collagen type II
CT	Computed tomography
CTE	Cartilage tissue engineering
DAPI	6-diamidino-2-phenylindole
DDP	Drop on demand printing
DEI	Diffraction-enhanced imaging
DFI	Dark-field imaging
DMOADs	Dietary supplements and disease modifying osteoarthritic drugs
DPCI	Differential phase contrast imaging
ECM	Extracellular matrix
EthD-1	Ethidium homodimer
FDM	Fused deposition modelling
GAGs	Glycosaminoglycans
GNPs	Gold nanoparticles
HEPES	4-(2-hydroxyethyl)-1-piperazineethanesulfonic acid
Inline-PCI-CT	Inline phase contrast imaging computed tomography
ITS+	Insulin-transferrin-selenium plus
KES	K-edge subtraction
LDM	Low-temperature deposition manufacturing
MIR	Multiple image radiography

MMPs	Matrix-metalloproteinases
MRI	Magnetic resonance imaging
MVA	Medium viscosity alginate
M_W	Molecular weight
NESI	Near-edge spectral imaging
NSERC	Natural Sciences and Engineering Council of Canada
OA	Osteoarthritis
PAD-BA	Phase-attenuation duality Born algorithm
PBST	Phosphate buffer saline Tween-20
PCL	Polycaprolactone
PGA	Polyglycolide
PED	Precision extruding deposition
PET	Poly (ethylene terephthalate)
PITRE	Phase-sensitive X-ray Image processing and Tomography Reconstruction
PLGA	Poly (d, l-lactic-co-glycolic acid)
PLLA	Poly (L-lactide)
PMA	Premarket approval
RC	Rocking curve
SDD	Sample-to-detector propagation distance
SEI	Secondary electron image
SEM	Scanning electron microscopy
SFF	Solid freeforming
SHRF	Saskatchewan Health Research Fund
SLS	Selective laser sintering
SKM	Stemline1 Keratinocyte Medium II calcium free
SO	Strand orientation
SR	Synchrotron radiation
SR-μCT	Synchrotron radiation micro-computed tomography
SS	Strand spacing
SZ	Strand size

USAXS	Ultra-small-angle X-ray scattering
WED	Western Economic Diversification
Z	Atomic number
3D	Three dimensional
2D	Two-dimensional
µCT	Micro-computed tomography

Chapter 1: Introduction

1.1. Articular Cartilage and the Pathogenesis of Osteoarthritis

Articular, hyaline cartilage is a smooth and avascular tissue found in the extremities of bones at the diarthrodial joints. It provides a lubricated gliding surface, allows easy transmission of loads and articulation, and enables easy movement at the diarthrodial joints under physiologic conditions [1-2]. Although hyaline cartilage is avascular in nature, its composition and organization is quite complex. Human articular cartilage has a thickness of approx. 2 - 4 mm, compressive modulus of approx. 1.16 ± 0.20 MPa – 7.75 ± 1.45 MPa [3] and tensile moduli of approx. 10.1 MPa - 24 MPa [4-5] depending on its location in the body. Furthermore, the articular cartilage is considered a biphasic structure in nature. The solid phase makes up 20 % – 35 % by volume, is permeable, and its building block is the extracellular matrix (ECM). The ECM is rich in collagen, proteoglycans, minerals and other components in minute quantities. On the other hand, the fluid phase is composed of water containing dissolved ions and makes up about 65 % – 80 % by volume of the articular cartilage [6-8]. The relationship between the components of both phases provides hyaline cartilage with its compressive resilience through the negative electrostatic repulsion forces. To be precise, its fluid phase supports mechanical loading by transmitting or redistributing the load through the pores of the solid phase matrix and application of pressure gradient across articular cartilage, thereby reducing the amount of stress exerted on the solid phase of the articular cartilage during high interstitial fluid pressurization with mechanical load [9-12]. It also has a sparse population of cartilage cells (chondrocytes) which represents approx. 5 % by volume of the articular cartilage [2, 10, 13]. Chondrocytes synthesize all components of the articular cartilage, and therefore play a major functional role in how the articular cartilage is generated and functions [14-15]. The articular cartilage is also considered to be viscoelastic in nature and as such, its stress-strain behavior is dependent on the strain rate. This viscoelasticity results from both flow-independent mechanisms, which are associated with the intermolecular friction within collagen-proteoglycan matrix, and flow-dependent mechanisms, which are associated with interstitial fluid flow and its frictional drag [9, 16-17].

Osteoarthritis (OA), a degenerative joint disease, is the most prevalent type of arthritis and has been reported as one of the leading cause of disability in the world. OA currently affects approximately 4.4 million Canadians and has a huge indirect economic burden on social systems and health care systems as it causes loss of work hours and early retirements [2, 18-19]. It is widely

considered as being prevalent in seniors and the elderly, as its probability of occurring increases with age. In fact, 80 % of seniors age 65 or older have radiographic indication of OA. However, OA has been reported in people as young as 15 years old. Further, OA is more prevalent in females than males with an average female to male ratio of 1.5 [2, 18, 20]. The pathogenesis of OA causes changes in cartilage metabolism. This is often accompanied by joint swelling, joint pain, bone remodeling and erosion of articular cartilage covering opposing surfaces of bones, thereby leading to joint stiffness and in some cases reduced mobility. These dramatic changes are associated with physiological fluctuations of degradation and synthesis of ECM by chondrocytes [21-22]. Therefore, investigation of OA transits between biochemistry and biomechanics [23]. Biochemically, the activity of chondrocytes changes and production of proteolytic enzymes (soluble mediators) such as matrix metalloproteinase 13 (MMP13) and cytokines becomes high [24 - 26]. This consequently leads to softening, ulceration and fibrillation that degrade the articular cartilage. This may also cause sclerosis of the subchondral bone and results in the growth of osteophytes at the joint margins. Biomechanically, obesity, genetics, joint injury and muscle weakness could have mechanical implications and cause hyaline cartilage to start showing symptoms of OA. These symptoms may include wear and tear, bone morphological changes and changes in the cartilage ECM [23]. Despite the severity of OA, absence of blood supply to facilitate cartilage self-repair coupled with the resulting morphological changes of neighboring tissues (subchondral bones and synovium) make management of OA challenging. Thus, the mechanism of OA and its proper management can be described as ambiguous [19, 22, 24].

Different nonsurgical approaches have been studied for treating or alleviating the pain associated with OA-affected joint. The use of dietary supplements and disease modifying osteoarthritic drugs (DMOADs) such as matrix-metalloproteinases (MMPs) inhibitors, cytokine inhibitors, bisphosphonates and glucosamine are some of the non-surgical pharmacological methods studied for treating OA [24, 27-29]. However, no significant improvement or detectable radiographic progression in cartilage regrowth has been associated with the use of these DMOADs [23]. Other non-surgical non-pharmacological treatments such as physiotherapy, weight reduction, and use of analgesics or corticoid have also been recommended. These approaches were reported to be suitable as initial treatment of OA but with no potential to regenerate the damaged articular cartilage [30-31]. Surgical OA treatment approaches that are being investigated include arthroplasty, arthroscopic debridement or lavage, osteochondral autograft or allograft

transplantation, autologous chondrocyte implantation and marrow-stimulation techniques such as abrasion or microfracture [32-36]. Despite the advancement of these surgical approaches for OA treatment, they are plagued with disadvantages. For example, arthroscopic debridement or lavage has been speculated to have no significant effect on OA or provided only short-term solution while arthroplasty has a 10 % - 30 % patient dissatisfaction or no improvement post-implantation and a lifespan of 15-20 years under considerable loading, less stress and proper care [37-40]. Ultimately, regeneration of hyaline cartilage by either non-surgical or surgical treatments is still deemed elusive, and there is the need for a continuous effort to find a more reliable treatment for OA [34].

1.2. Cartilage Tissue Engineering

Cartilage tissue engineering (CTE) uses a combination of biomaterials, bioactive molecules and living cells to engineer a 3D environment (constructs / scaffolds) suitable for regeneration of the articular cartilage. To develop functional constructs for CTE applications, these constructs must mimic the natural characteristics of the articular cartilage [41-45]. Specifically, it is highly recommended that the constructs mimic the biological functions of native articular cartilage by containing chondrocytes (or cells that can differentiate into chondrocytes) and provide a biphasic microenvironment that enables cell proliferation and differentiation. In addition, these constructs should mimic the 3D architecture, mechanical characteristics and 100 % pore interconnectivity of the articular cartilage to enable provision of the appropriate mechanotransductive environment and exchange of nutrients and wastes [41, 46-48, 134]. Selection of biomaterials with the appropriate biocompatibility and biodegradability profile is one of the most significant steps in tissue engineering (TE), as the inherent properties of fabricated scaffolds could depend on it. Based on their biocompatibility, mechanical behavior, degradation profile and so on, a wide range of biomaterials has been used for fabrication of scaffolds for CTE applications. Naturally occurring highly hydrated polymer networks called hydrogels (e.g. collagen [51], fibroin [56], chitosan [57], hyaluronic acid [58] and alginate [59]) have shown great potential for CTE, especially, in terms of promoting chondrogenesis, mimicking the biphasic, biological and natural cellular milieu of articular cartilage. Conversely, these natural biomaterials exhibit poor mechanical properties, relatively quick degradation (especially when not crosslinked), vary from one batch to another and could be expensive [60-61, 134]. Thus, examination of cheap and easily sourced synthetic polyester-based resorbable biomaterials with better mechanical properties, such as polyglycolide (PGA) [62], poly (L-lactide) (PLLA) [63], poly (d, l-lactic-co-

glycolic acid) (PLGA) [64] and PCL [65], have been studied for CTE applications. However, the high rigidity of their scaffolds and their less favorability for cellular activities when compared with the naturally occurring hydrogels, make their exploration for CTE applications challenging [63]. As such, composite of these biomaterials has been investigated and reported to enable reduction of rigidity of these scaffolds. Interestingly, composite such as PLLA and PCL investigated for CTE showed that addition of PCL enabled reduction of rigidity, thereby causing increased viscoelasticity and flexibility of these scaffolds [63]. In addition, PCL has good bioresorbability, a slower degradation rate (ranging from months to years), low cost, excellent viscoelastic properties, and non-immunogenicity [66]. As such, the use of PCL framework for tissue engineering applications is becoming very popular.

After the biomaterial of choice is selected for TE applications, modulation of the structural integrity or mechanical properties of the scaffolds fabricated from these biomaterials is often the next important stage of TE prior to fabrication. Various conventional fabrication techniques such as injection molding, porogen leaching, foaming or textile meshes have been widely investigated for fabrication of complex scaffolds for TE applications [130-132]. Moreover, scaffolds fabricated using these conventional techniques have uncontrollable porosity, lack 100 % pore-interconnectivity, are mostly non-reproducible and may involve the use of cytotoxic solvents [42, 45, 52, 54, 130-132]. Advanced additive manufacturing (AM) or solid freeforming (SFF) technologies circumvent the challenges of conventional fabrication techniques. They enable fabrication of scaffolds with hierarchical pore geometries and ensure tailoring different mechanical behavior and mass transport properties for various applications. First, AM utilizes computer-aided-design (CAD) data to create customized architectures and design complex structures. These customized architectures are then fabricated in a controlled layer-by-layer manner specified by a user. Because of the ability to control the structural characteristic of scaffolds fabricated, these techniques guarantee controlled porosity, 100 % pore interconnectivity, minimal material waste and scaffold reproducibility in a manner not achievable by conventional fabrication techniques [134]. SFF techniques for fabrication processes are divided into three groups: laser-based techniques (e.g. selective laser sintering (SLS) [85, 87, 90, 133]), drop-based techniques (e.g. ink-jet printing [135]) and nozzle-based techniques (e.g. extrusion-based techniques such as precision extruding deposition (PED), fused deposition modelling (FDM) and drop on demand printing (DDP) [49-52]). Extrusion-based SFF techniques include processes with material melting (e.g.

FDM [44] and 3D fiber deposition [55]) and processes without material melting (e.g. low-temperature deposition manufacturing (LDM) [128]). Despite the potentials for all these AM techniques for TE applications, finding a technique for fabrication of hybrid scaffolds from multiple materials, e.g. polymer melts and water-filled hydrogel with cell inclusions and other biological inclusions, is still very difficult.

The introduction of the 3D-Bioplotter™ pioneered at the Freiburg Materials Research Center [129] made possible fabrication of a remarkably wide range of biomaterials with large temperature ranges. Just like other SFF techniques, bioplotting enables reproducibility, the ability to achieve 100 % pore-interconnectivity and relatively easy control of fabrication parameters [46-48]. But unlike other extrusion-based 3D-printing systems, the 3D-Bioplotter™ enables fabrication of hybrid constructs by side-by-side printing of polymer melts and water-filled hydrogel with cells and other biological inclusions thereby making it easy to control the mechanical characteristics of the constructs, cell distribution within the constructs and mimicking the biphasic nature of the articular cartilage [41, 46-47, 53, 55]. Since these biphasic 3D-printed PCL-based cell-laden constructs are currently receiving a lot of attention for CTE applications, *in vitro* and *in vivo* examinations of the biological functions of these cartilage constructs is crucial to their success [46 - 48, 67]. In fact, the regulatory pathway for medical device development requires their validation through *in vitro* bench test and *in vivo* preclinical examination in animal models for such implant prior to premarket approval (PMA) [68-69]. Therefore, one of the knowledge gaps identified is the "*investigation of the biological functionality of these 3D-printed PCL/alginate/cells cartilage constructs through an in vitro bench test and an in vivo examination in animal models*".

1.3. Mechanical Properties of 3D-Printed Cartilage Constructs for CTE applications

Because of the previously highlighted characteristics of PCL and alginate hydrogel, this thesis focuses on exploration of the potentials of 3D-printed PCL/alginate/cells constructs for CTE applications. Mechanically, the PCL component of the hybrid construct is a dense framework that provides structural support and mechanical properties to the 3D-printed PCL/alginate/cells cartilage constructs [52]. Conversely, the alginate hydrogel component provides microporous environment that helps transmission or redistribution of mechanical loads through pores of the PCL structure. The mechanical interactions and the 3D structural integrity between the solid and

the liquid components of the hybrid cartilage constructs are similar to those experienced in native articular cartilage [9-12]. Moreover, tensile and compressive moduli of human articular cartilage of femoral condyles vary greatly compared to that of previously investigated PCL-based scaffolds (different sizes and fabricated using different fabrication techniques) (See Table 1.1). Having said that, biosynthesis activities of cells in articular cartilage or in CTE constructs are sensitive to mechanical stimuli [70-72]. In fact, dynamic compression as low as 0.5 MPa – 1.0 MPa at physiological frequencies of 0.01 Hz – 1.0 Hz has been reported to stimulate secretion of extracellular matrix (ECM) in native articular cartilage [71-72]. This means that using constructs with mechanical properties much higher than that of the native articular cartilage will cause stress-shielding of mechano-transduction and hinder transmission of mechanical stimuli directed at cells within these constructs and, consequently affect secretion of cartilage-specific ECM. In a like manner, utilizing constructs with mechanical properties lower than those of articular cartilage may result in overloading and excessive stressing of the cells within the constructs, and consequently negatively influencing secretion of ECM or resulting in cell mortality. Therefore, mechanical properties of these PCL-based cartilage constructs are very crucial and should be similar to those of the articular cartilage to enable the cells in these constructs reach their full potentials for regeneration of hyaline cartilage. Despite this fact, most PCL-based constructs investigated for CTE applications are developed to biologically mimic properteis of native articular cartilage, and very little to no attention is paid to estimation of mechanical properties of these constructs and ensuring that they are comparable with human articular cartilage [46-47, 67]. As such, another unsolved challenge associated with these 3D-printed PCL/alginate/cells cartilage constructs is finding a strategy to systematically tailor their mechanical properties to better mimic mechanical properties of human articular cartilage.

Several investigators have studied the effect of molecular weight (M_W) on biomaterials' and scaffolds' mechanical parameters such as elastic modulus, yield stress, fracture toughness and impact strength [73-75]. For example, mechanical properties of scaffolds increased with an increase in M_W of PCL blended with poly (ethylene terephthalate) (PET) [76]. However, no research investigating the effect of molecular weight of PCL on mechanical properties of scaffolds for CTE applications has been conducted. Besides, the influence of pore geometry and porosity on the mechanical properties of tissue constructs/scaffolds has also been well studied [42, 44, 52, 55, 77-78]. In fact, a direct relationship is reported to exist between porosity and mechanical properties

of scaffolds. To be specific, a scaffold's porosity is directly associated with its pore geometry parameters such as strand size (SZ), strand spacing (SS) and strand orientation (SO) [42, 45, 52, 55]. Accordingly, understanding these relationships may enable better design of porous structures for different TE applications [42, 44, 49, 55]. Unfortunately, studies that investigated optimization of PCL scaffolds structure mostly focused on bone TE applications or used conventional fabrication techniques for their scaffold fabrication [49-52]. Therefore, the second knowledge gap identified in this thesis is that "*modulation of molecular weight of PCL and pore geometric configurations (i.e. SS, SO and SZ) of scaffolds may influence the mechanical behavior of 3D-printed PCL scaffolds and enable obtaining PCL-based constructs with mechanical properties like that of human articular cartilage*".

Table 1. 1: Compressive and tensile moduli of human articular cartilage and PCL scaffolds reported in literature

	Compressive moduli (MPa)	**Tensile moduli (MPa)**
Articular cartilage (human femoral head)	1.16 ± 0.20 – 7.75 ± 1.45 [3]; 4.3 ± 1.4 – 13.0 ± 4.2 [77]; 3.2 ± 1.6 [79]; 2.22 ± 0.65 – 3.10 ± 0.84 [81]; 1 – 19.5 [82]; 0.079 ± 0.039 – 2.10 ± 2.69 [83]; 0.679 ± 0.162 – 1.816 ± 0.868 [84]	54.6 ± 37.6 [79]; 0.76 ± 0.13 [80]; 10.1 [4]; 24 [5]
PCL scaffolds fabricated by SLS, Injection molding, electrospinning, PED, FDM, DDP	215.4 ± 6.6 [50]; 52 ± 2 – 67 ± 4 [85]; 14.9 ± 0.6 [87]; 59 [88]; 150 – 200 [89]; 44.0 ± 3.2 [92]; 41.9 [93]	105 ± 15 [50]; 53 ± 36 [86]; 277.06 ± 27.66 [90]; 2.9 - 5.2 [91]; 35.5 ± 5.8 [87]

1.4. SR-Inline-PCI-CT for Non-Invasive Assessment of 3D-printed Hybrid Cartilage Constructs

Owing to the difference in the X-ray attenuation coefficients and densities of the hydrophobic PCL, hydrophilic alginate hydrogel, cells and time-dependent structural changes within the biphasic 3D-printed cartilage constructs that may be associated with either biodegradation of formation of ECM, their non-invasive characterization and monitoring is challenging, particularly during *in situ* tissue repair [94 - 97]. An effective, non-invasive, 3D imaging technique suitable for CTE should have the capacity to (1) track the progression of newly

forming tissues, (2) monitor degradation profiles of all components of the constructs, and (3) delineate host-construct integration in a continued manner in the same animal or human without destroying or posing a risk to the animal or the tissues of interest [95, 98-99]. Traditional invasive assays complemented by two-dimensional (2D) imaging techniques provide standard assessments of cell viability and secretion of ECM in tissue-engineered constructs [47, 97, 100-101]. However, these traditional assays provide 2D representation, are invasive, and require excising the samples such that samples can only be assayed at one time-point. Therefore, they are unsuitable for *in vivo* and longitudinal assessment of functionality of the 3D-printed hybrid constructs investigated in this thesis in animal models [47, 97, 100-101]. 3D optical imaging techniques, such as confocal microscopy, optical coherence tomography, and Raman spectroscopy have been studied as alternatives to 2D imaging techniques for TE applications [102-105]. Unfortunately, these techniques have shorter penetration depth and often require the use of contrast agents to enhance their sensitivity to visualize cartilage [95, 97, 106]. Furthermore, positron emission tomography and single-photon emission computed tomography possesses high penetration depth and have been praised for successfully tracking cells *in vivo* [107-108]. However, these techniques require the use of radioactive agents that might have a negative effect on cell performance. In addition, these techniques often experience poor temporal and spatial resolution that consequently limits visualization of microstructural details, which is critical for tracking time-dependent progression of biomaterial degradation and tissue growth [107-108]. Furthermore, positron emission tomography, single-photon emission computed tomography [107-108, 116], and radiography (such as micro-CT and CT) can assess structural details of tissue constructs. Unfortunately, poor contrast from low density and high water content materials, such as cartilage and hydrogels, is a major drawback when considering these techniques for CTE applications [109-110]. Magnetic resonance imaging (MRI) is an established preclinical and clinical technique, well known for its ability to delineate soft tissue contrast. Therefore, MRI is often used for visualizing cartilage damage, tissue remodeling, soft tissue constructs, and was even used recently with contrast agents to track cells within constructs [99, 111-115]. However, MRI has poor spatial resolution, provides poor imaging contrast of hydrophobic materials and tissues, and sometimes needs contrast agents to boost sensitivity. Thus, its use for effective non-invasive characterization of partly hydrophobic and partly hydrophilic PCL/alginate/cells cartilage constructs studied in this thesis is not feasible [113, 125]. In summary, non-invasive characterization and monitoring of hydrophobic PCL,

hydrophilic alginate hydrogel, and living cells within hybrid cartilage constructs is challenging, particularly *in vivo.*

Since the discovery of synchrotron light, different non-invasive 3D imaging techniques that are invaluable for biomedical applications and material sciences have emerged. Novel synchrotron-radiation inline phase contrast imaging computed tomography (SR-inline-PCI-CT) uses variations in phase shifts of X-rays passing through samples to visualize materials with different refractive indices, electron densities, and atomic numbers, without requiring exogenous contrast agents [117-119]. At diagnostic X-ray energies, the SR-inline-PCI-CT technique produces its image signal from refraction generated from the real part of the refractive index of a sample. These refraction signals are up to 1000 times greater than the absorption signal generated from the imaginary part of the material refractive index and are used as source of image signal for conventional X-ray absorption imaging techniques [117-120]. Although researchers are currently exploring six or more PCI techniques, SR-inline-PCI-CT has the simplest experimental setup, uses no optical element (e.g., gratings or diffracting crystals) and was the first phase-contrast technique to be pioneered [117-119]. Due to the high lateral (spatial) coherence of synchrotron X-rays, SR-inline-PCI-CT translates variations in densities and refractive indices of different materials into edge enhancement at their interfaces in the images [121]. Thus, SR-inline-PCI-CT offers a robust capability to characterize hard and soft tissues, tissue constructs fabricated from single or multiple biomaterials and their associated gradually growing neo-tissue with multiple weak X-ray absorption and low refractive indices [96-99, 122-125]. That said, the capability of SR-inline-PCI-CT for characterization of fine details in soft tissues was previously assumed to be subordinate to that of diffraction-enhanced imaging [98, 122, 125]. Thus, whether SR-inline-PCI-CT can be optimized for non-invasive characterization of the components of the engineered PCL/alginate/cells or for soft tissue engineering in general becomes another critical research question. A few studies have explored sample-to-detector propagation distance (SDD) as a key parameter for optimization of SR-inline-PCI for imaging of samples with varying densities and refractive indices. This is because varying SDD changes the spatial coherence of the incident X-rays which affects the edge enhancement fringes and the details at interfaces of materials within samples, and consequently affects image quality provided by SR-inline-PCI-CT [98, 118-119, 121, 123-126]. Meanwhile, the refractive indices and thickness of the sample, pixel size of the detector, and the imaging energy used for acquiring SR-inline-PCI images also determine the optimum

SDD, and affects the phase contrast provided by the technique [127]. As such, one size does not fit all with regards to the SDD that will provide the appropriate edge enhancement fringes and phase contrast for characterization of different sample types. Summarily, another knowledge gap identified is that "*modulation of SDD may enhance spatial coherence and phase contrast, and hence capability of SR-inline-PCI-CT for characterization of the different refractive indices present within the hybrid PCL/alginate/cells constructs and their time-dependent structural changes*".

1.5. Research Aims and Objectives

The aim of this thesis is to develop 3D-printed cartilage constructs that biologically and mechanically mimic human articular cartilage and to investigate SR-inline-PCI-CT as a non-invasive imaging technique to characterize these cartilage constructs and their time-dependent secretion of ECM. The hypotheses are (1) the environment provided by 3D-printed cartilage constructs can support cell viability and progressive secretion of cartilage-specific ECM over time *in vitro* and *in vivo*; (2) advanced SR-inline-PCI-CT is effective for non-invasive assessment of the multiple refractive indices present within the 3D-printed PCL/alginate/cells constructs and their associated time-dependent changes; and (3) modulation of molecular weight and pore geometric parameters (i.e. SS, SO and SZ) of the 3D-printed PCL scaffolds enables tailoring mechanical behavior of these scaffolds/frameworks to mechanically mimic native articular cartilage. To test these hypotheses, the specific objectives of this thesis are set as follows.

The first objective was to determine *in vitro* biological functionality of the cartilage constructs and investigate SR-inline-PCI-CT for non-invasive visualization of the components and associated structural changes within the cartilage constructs *in vitro* over a 42-day period. To do this, PCL/alginate/cells cartilage constructs were fabricated and their *in vitro* biological performance were examined by quantifying changes in cell viability and secretion of sulfated GAGs and Col2 over a 42-day period. In addition, three sample-to-detector distances (SDDs) (0.25, 1 and 3 m) were investigated for characterization of individual components of the hybrid cartilage constructs by comparing phase contrast, edge enhancement fringes and consequent image quality. Then, optimal SDD identified was utilized to delineate time-dependent structural changes within the PCL/alginate/cells constructs over a 42-day period *in vitro*.

The second objective was to examine performance of SR-inline-PCI-CT to visualize non-invasively the 3D-printed hybrid cartilage constructs implanted subcutaneously in mice over a 21-

day period. In parallel, traditional invasive assays interrogated the *in vivo* functionality of the implanted hybrid cartilage constructs with regards to cell viability and secretion of sulfated GAGs and Col2 at 7, 14 and 21 days post-implantation in nude mice.

The third objective was to modulate mechanical properties of the PCL framework of the 3D-printed PCL-based cartilage constructs to mimic the mechanical properties of the human articular cartilage. To do this, the effect of modulation of the PCL's M_W and scaffold's pore geometric configurations (i.e. SZ, SS, and SO) on mechanical properties of 3D-printed PCL scaffolds was investigated. PCL scaffolds were fabricated using PCL with different molecular weight (10, 000 g/mol, 45, 000 g/mol and 80, 000 g/mol) and subjected to mechanical tests to determine the optimal molecular weight for fabrication of PCL-based cartilage constructs. After identifying PCL with the molecular weight most feasible for fabrication of PCL scaffolds, it was used to fabricate scaffolds with various pore geometric configurations: SZ, SS, and SO. Then, statistical regression models showing the effect of SZ, SS, and SO on porosity, tensile moduli and compressive moduli of scaffolds were developed. From the statistical regression models, the pore geometric configurations for fabrication of "modulated PCL scaffolds" with mechanical properties that better mimic mechanical behavior of human articular cartilage was obtained and recommended as a framework for subsequent studies focused on fabrication of PCL-based constructs for CTE applications.

1.6. Organization of the Dissertation

This dissertation consists of 6 chapters. It includes the introduction chapter, four chapters adopted from four manuscripts and a chapter summarizing conclusions drawn from research and recommendations for future studies.

Chapter 2 presents a literature review that discusses recent developments in synchrotron-based biomedical imaging techniques and their potentials for bone and cartilage tissue engineering applications. The first section describes the technical features, the advantages and the limitations of these techniques. The second section focuses on applications of these synchrotron-based techniques to bone and cartilage tissue engineering applications. Lastly, cues for identification of an effective synchrotron-based imaging technique for specific and different tissue engineering applications are discussed alongside recommendations for future research.

The first section of **Chapter 3** describes *in vitro* biological functionality of 3D-printed PCL/alginate/cells cartilage constructs with respect to cell viability and secretion of cartilage-

specific ECM over a 42-day period by traditional invasive assays. The second section examines the potential of the novel non-invasive SR-inline-PCI-CT for visualization of the individual components of the biphasic 3D-printed cartilage constructs and their associated subtle time-dependent structural changes. To be precise, the study investigates the effect of modulation of SDD on phase contrast, and consequently image quality offered by SR-inline-PCI-CT for characterization of the multiple densities and refractive indices found within the biphasic cartilage constructs. Then, the study utilizes the optimized settings of SR-inline-PCI-CT for visualization of the interfaces of the associated fine structural changes within the cartilage constructs *in vitro* over a 42-day period.

Chapter 4 presents the *in vivo* examination of the biological functionality of 3D-printed PCL/alginate/cells constructs with respect to cell viability and secretion of cartilage-specific ECM over a 21-day period post-implantation in nude mice. In addition, the study utilizes the optimized SR-inline-PCI-CT established in chapter 3 for non-invasive visualization and characterization of the biphasic components of these constructs and their associated structural changes in nude mice over a 21-day period.

Chapter 5 examines the effect of molecular weight and pore geometric configurations: SS, SO and SZ, on compressive and tensile moduli of PCL scaffolds. Statistical regression models showing the effect of pore geometric configurations on porosity and mechanical properties of scaffolds were developed. From the statistical regression models, the pore geometric configurations for fabrication of "modulated PCL scaffolds" with mechanical properties that better mimic mechanical behavior of human articular cartilage was identified and recommended as a framework for subsequent studies focused on fabrication of PCL-based constructs for CTE applications.

Chapter 6 presents the conclusions drawn from this research work, followed by suggestions and recommendations for possible future studies.

1.7. Contributions of the Primary Investigator

All manuscripts included in this thesis are co-authored and contributions of all authors are greatly appreciated and acknowledged. However, it is the mutual understanding of all these authors that Adeola Deborah Olubamiji, as the first author, is the primary investigator of the research work.

1.8. References

1. Sophia Fox AJ, Bedi A, Rodeo SA. (2009). "The basic science of articular cartilage: structure, composition, and function." *Sports Health.* 1 (6), 461-8.

2. Thomas A, and Schmitz N. (2011). "Pathogenesis and pathology of osteoarthritis." *Rheumatology* 414, 1741-59.

3. Chen SS, Falcovitz YH, Schneiderman R, Maroudas A, Sah RL. (2001). "Depth-dependent compressive properties of normal aged human femoral head articular cartilage: relationship to fixed charge density." *Osteoarthritis Cartilage.* 9 (6), 561-569.

4. Akizuki S, Mow VC, Müller F, Pita JC, Howell DS, Manicourt DH. (1986). "Tensile properties of human knee joint cartilage: I. Influence of ionic conditions, weight bearing, and fibrillation on the tensile modulus." *J Orthop Res.* 4 (4), 379-92.

5. Temple MM, Bae WC, Chen MQ, Lotz M, Amiel D, Coutts RD, Sah RL. (2007). "Age- and site-associated biomechanical weakening of human articular cartilage of the femoral condyle." *Osteoarthritis Cartilage*. 15 (9), 1042-52.

6. Ateshian GA, Warden WH, Kim JJ, Grelsamer RP, Mow VC. (1997). "Finite deformation biphasic material properties of bovine articular cartilage from confined compression experiments." *J Biomech.* 30 (11-12), 1157-64.

7. Mow VC, Guo XE. (2002). "Mechano-electrochemical properties of articular cartilage: their inhomogeneities and anisotropies." *Annu Rev Biomed Eng* 4, 175-209.

8. Mow VC, Ateshian GA, Ratcliffe A. (1992). “Anatomic form and biomechanical properties of articular cartilage of the knee joint”. In: Finerman GAM, Noyes FR. (Eds.) *Biology and Biomechanics of the Traumatized Synovial Joint: The Knee as a Model.* 2nd ed. (pp 55-81) Rosemont, IL: American Academy of Orthopaedic Surgeons

9. Flik KR, Verma N, Cole BJ, Bach BR. (2007). "Articular Cartilage: Structure, Biology and Function." In Williams R. (eds) *Cartilage Repair Strategies*. (pp 1-12). New Jersey: *Humana Press Inc.*

10. Buckwalter JA, Mankin HJ. (1998). "Articular cartilage, part 1: tissue design and chondrocyte-matrix interaction." *Instr Course Lect.* 47, 477-86.

11. Mankin HJ, Mow VC, Buckwalter JA, Iannotti JP. (1994). "Orthopaedic Basic Science." In Simon SR (Eds) *Form and function of articular cartilage*. (pp 1-44)Rosemont, IL: American Academy of Orthopaedic Surgeons.

12. Maroudas A. (1979). "Physiochemical properties of articular cartilage." In Freeman MAR (Ed). *Adult Articular Cartilage* (pp 215-290). Kent: Cambridge University Press.

13. Buckwalter JA, Mankin HJ. (1997). "Articular cartilage, part 1: tissue design and chondrocyte-matrix interaction." *J Bone Joint Surg Am.* 79, 600-611.

14. Erggelet C, Mandelbaum BR, Mrosek EH, Scopp JM. (2008). In Volkert G. (Eds) *Principles of Cartilage Repair*. (pp 3-72). Wurzburg Germany: Steinkopff. 3-72.

15. Bhosale AM, Richardson JB. (2008). "Articular cartilage: structure, injuries and review of management." *Br Med Bull.* 87, 77-95.

16. Hayes WC, Bodine AJ. (1978). "Flow-independent viscoelastic properties of articular cartilage matrix." *J Biomech*. 11 (8-9), 407-419.

17. Woo SL-Y, Mow VC, Lai WM. "Biomechanical properties of articular cartilage. (1986). " In Chen S, Skalak R. (Eds) *Handbook of Bioengineering.* Vol. 4 (pp 1-4.44). New York: McGraw-Hill Book Co.

18. Bombardier C, Hawker G, Mosher D. (2011, Fall) "The Impact of Arthritis in Canada: Today and Over 30 Years." *Athritis Alliance of Canada*. 1-52. Retrieved from http://www.ergoresearch.com/wpcontent/uploads/2012/04/Impact%20on%20arthrisis%20in%20Canada_Today%20and%20over%20the%20next%2030%20years.pdf.

19. Woolf AD, Pfleger B. (2003). "Burden of major musculoskeletal conditions." *Bull World Health Organ* 81 (9) 646–656.

20. Lawrence RC, Helmick CG, Arnett FC, Deyo RA, Felson DT, Giannini EH, Heyse SP, Hirsch R, Hochberg MC, Hunder GG, Liang MH, Pillemer SR, Steen VD, Wolfe F. (1998). "Estimates

of the prevalence of arthritis and selected musculoskeletal disorders in the United States." *Arthritis Rheum.* 41 (5), 778-99.

21. Torzilli PA, Grigiene R, Borrelli J, Helfet DL. (1999). Effect of impact load on articular cartilage: cell metabolism and viability, and matrix water content. *J Biomech Eng*. 121 (5), 433-44.

22. Lawrence JS, Bremner JM, and Bier F. (1996). "Osteoarthrosis. Prevalence in the population and relationship between symptoms and x-ray changes." *Ann Rheum Dis.* 25 (1), 1–24.

23. Felson DT, Lawrence RC, Dieppe PA, Hirsch R, Helmick CG, Jordan JM, Kington RS, Lane NE, Nevitt MC, Zhang Y, Sowers M, McAlindon T, Spector TD, Poole AR, Yanovski SZ, Ateshian G, Sharma L, Buckwalter JA, Brandt KD, Fries JF. (2000). "Osteoarthritis: new insights. Part 1: the disease and its risk factors." *Ann Intern Med*. 133 (8), 635-46.

24. Qvist P, Bay-Jensen AC, Christiansen C, Dam EB, Pastoureau P, Karsdal MA. (2008). "The disease modifying osteoarthritis drug (DMOAD): Is it in the horizon?" *Pharmacol Res* 58 (1), 1-7.

25. Pelletier JP, Lajeunesse D, Reboul P, Mineau F, Fernandes JC, Sabouret P, Martel-Pelletier J. (2001). "Diacerein reduces the excess synthesis of bone remodeling factors by human osteoblast cells from osteoarthritic subchondral bone." *J Rheumatol.* 28 (4), 814-24.

26. Gierman LM, van El B, van der Ham F, Koudijs A, Stoop R, Verheijen JH, Kloppenburg M, van Osch GJ, Stojanovic-Susulic V, Huizinga TW, Zuurmond AM. (2013). “Profiling the secretion of soluble mediators by end stage osteoarthritis synovial tissue explants reveals a reduced responsiveness to an inflammatory trigger.” *PLoS One*. 8 (5), e62634.

27. Krzeski P, Buckland-Wright C, Bálint G, Cline GA, Stoner K, Lyon R, Beary J, Aronstein WS, Spector TD. (2007). "Development of musculoskeletal toxicity without clear benefit after administration of PG-116800, a matrix metalloproteinase inhibitor, to patients with knee osteoarthritis: a randomized, 12-month, double-blind, placebo-controlled study." *Arthritis Res Ther.* 9 (5), R109.

28. Spector TD, Conaghan PG, Buckland-Wright JC, Garnero P, Cline GA, Beary JF, Valent DJ, Meyer JM. (2005). "Effect of risedronate on joint structure and symptoms of knee osteoarthritis: results of the BRISK randomized, controlled trial." *Arthritis Res Ther* 7 (3), R625-33.

29. Magnano MD, Chakravarty EF, Broudy C, Chung L, Kelman A, Hillygus J, Genovese MC. (2007). "A pilot study of tumor necrosis factor inhibition in erosive/inflammatory osteoarthritis of the hands." *J Rheumatol*. 34 (6), 1323-7.

30. Zhang W, Moskowitz RW, Nuki G, Abramson S, Altman RD, Arden N, Bierma-Zeinstra S, Brandt KD, Croft P, Doherty M, Dougados M, Hochberg M, Hunter DJ, Kwoh K, Lohmander LS, Tugwell P. (2008). "OARSI recommendations for the management of hip and knee osteoarthritis, Part II: OARSI evidence-based, expert consensus guidelines." *Osteoarthritis Cartilage* 16 (2), 137-62.

31. Zhang W, Moskowitz RW, Nuki G, Abramson S, Altman RD, Arden N, Bierma-Zeinstra S, Brandt KD, Croft P, Doherty M, Dougados M, Hochberg M, Hunter DJ, Kwoh K, Lohmander LS, Tugwell P. (2007). "OARSI recommendations for the management of hip and knee osteoarthritis—part I: critical appraisal of existing treatment guidelines and systematic review of current research evidence." *Osteoarthritis Cartilage*. 15 (9), 981-1000.

32. Welch T, Mandelbaum B, Tom M. (2016). "Autologous Chondrocyte Implantation: Past, Present, and Future." *Sports Med Arthrosc* 24 (2), 85-91.

33. Levine DW, Roaf PL, Duguay SJ. (2009). "Characterized chondrocyte implantation results in better structural repair when treating symptomatic cartilage defects of the knee in a randomized controlled trial versus microfracture." *Am J Sports Med.* 37 (3), e3.

34. Yen YM, Cascio B, O'Brien L, Stalzer S, Millett PJ, Steadman JR. (2008). "Treatment of osteoarthritis of the knee with microfracture and rehabilitation." *Med Sci Sports Exerc*. 40 (2), 200-205.

35. Hangody L, Füles P. (2003). "Autologous osteochondral mosaicplasty for the treatment of full-thickness defects of weight-bearing joints: ten years of experimental and clinical experience”." *J Bone Joint Surg Am*. 85 (2), 25 -32.

36. Chang RW, Falconer J, Stulberg SD, Arnold WJ, Manheim LM, Dyer AR. (1993). "A randomized, controlled trial of arthroscopic surgery versus closed-needle joint lavage for patients with osteoarthritis of the knee." *Arthritis Rheum.* 36 (3), 289-96.

37. Greengard S. (2012). "What is Knee Replacement Revision Surgery?" *Healthline*. Retrieved July 20, 2016 from http://www.healthline.com/health/total-knee-replacement-surgery/revision.

38. Rönn K, Reischl N, Gautier E, Jacobi M. (2011). "Current surgical treatment of knee osteoarthritis." *Arthritis.* 2011, 454873 (pp 9).

39. Nilsdotter AK, Toksvig-Larsen S, Roos EM. (2009). "Knee arthroplasty: are patients' expectations fulfilled? A prospective study of pain and function in 102 patients with 5-year follow-up". *Acta Orthopaedica.* 80 (1), 55-61.

40. Nilsdotter AK, Petersson IF, Roos EM, Lohmander LS. (2003). "Predictors of patient-relevant outcome after total hip replacement for osteoarthritis—a prospective study." *Ann Rheum Dis.* 62, 923-930.

41. Woodfield TB, Moroni L, Malda J. (2009). "Combinatorial approaches to controlling cell behaviour and tissue formation in 3D via rapid-prototyping and smart scaffold design." *Comb Chem High Throughput Screen.* 12 (6), 562-579.

42. Moroni L, de Wijn JR, van Blitterswijk CA. (2006). "3D fiber-deposited scaffolds for tissue engineering: influence of pores geometry and architecture on dynamic mechanical properties." *Biomaterials* 27 (7), 974-985.

43. Malda J, Woodfield TB, van der Vloodt F, Wilson C, Martens DE, Tramper J, van Blitterswijk CA, Riesle J. (2005). "The effect of PEGT/PBT scaffold architecture on the composition of tissue engineered cartilage." *Biomaterials* 26 (1), 63-72.

44. Woodfield TB, Malda J, deWijn J, Péters F, Riesle J, van Blitterswijk CA. (2004). "Design of porous scaffolds for cartilage tissue engineering using a three-dimensional fiber-deposition technique." *Biomaterials* 25 (18), 4149-61.

45. Lin AS, Barrows TH, Cartmell SH, Guldberg RE. (2003). "Microarchitectural and mechanical characterization of oriented porous polymer scaffolds." *Biomaterials* 24 (3), 481-489.

46. Izadifar Z, Chang T, Kulyk W, Chen D XB, Eames BF. (2016). "Analyzing biological performance of 3D-printed, cell-impregnated hybrid constructs for cartilage tissue engineering." *Tissue Engineering, Part C: Methods.* 22 (3), 173-188.

47. Kundu J, Shim JH, Jang J, Kim SW, Cho DW. (2015). "An additive manufacturing-based PCL-alginate-chondrocyte bioprinted scaffold for cartilage tissue engineering." *J Tissue Eng Regen Med.* 9(11), 1286-97.

48. Schuurman W, Khristov V, Pot MW, van Weeren PR, Dhert WJ, Malda J. (2011). "Bioprinting of hybrid tissue constructs with tailorable mechanical properties." *Biofabrication* 3 (2) 021001-021008.

49. Minton J, Janney C, Akbarzadeh R, Focke C, Subramanian A, Smith T, McKinney J, Liu J, Schmitz J, James PF, Yousefi AM. (2014). "Solvent-free polymer/bioceramic scaffolds for bone tissue engineering: fabrication, analysis, and cell growth." *J Biomater Sci Polym Ed.* 25 (16), 1856-1874.

50. Lu L, Zhang Q, Wootton DM, Chiou R, Li D, Lu B, Lelkes PI, Zhou J. (2014). "Mechanical study of polycaprolactone-hydroxyapatite porous scaffolds created by porogen-based solid freeform fabrication method." *J Appl Biomater Funct Mater*. 12 (3), 145-154.

51. Lu L, Zhang Q, Wootton D, Lelkes P I, Zhou, J. (2010). "A novel sucrose porogen-based solid freeform fabrication system for bone scaffold manufacturing." *Rapid Prototyping Journal* 16 (5), 365-376.

52. Lebourg M, Sabater Serra R, Más Estellés J, Hernández Sánchez F, Gómez Ribelles JL, Suay Antón J. (2008). "Biodegradable polycaprolactone scaffold with controlled porosity obtained by modified particle-leaching technique." *J Mater Sci Mater Med.* 19 (5), 2047-53.

53. Cigan AD, Roach BL, Nims RJ, Tan AR, Albro MB, Stoker AM, Cook JL, Vunjak-Novakovic G, Hung CT, Ateshian GA. (2016). “High seeding density of human chondrocytes in agarose

produces tissue-engineered cartilage approaching native mechanical and biochemical properties". *J Biomech*. 49 (9), 1909-17.

54. Correlo VM, Boesel LF, Pinho E, Costa-Pinto AR, Alves da Silva ML, Bhattacharya M, Mano JF, Neves NM, Reis RL. (2009). "Melt-based compression-molded scaffolds from chitosan-polyester blends and composites: Morphology and mechanical properties." *J Biomed Mater Res A* 91 (2), 489-504.

55. Zein I, Hutmacher DW, Tan KC, Teoh SH. (2002). "Fused deposition modeling of novel scaffold architectures for tissue engineering applications." *Biomaterials* 23 (4),: 1169-85.

56. Talukdar S, Nguyen QT, Chen AC, Sah RL, Kundu SC. (2011). "Effect of initial cell seeding density on 3D-engineered silk fibroin scaffolds for articular cartilage tissue engineering." *Biomaterials.* 32 (34), 8927-37.

57. Bhardwaj N, Nguyen QT, Chen AC, Kaplan DL, Sah RL, Kundu SC. (2011). "Potential of 3-D tissue constructs engineered from bovine chondrocytes/silk fibroin-chitosan for *in vitro* cartilage tissue engineering." *Biomaterials* 32 (25), 5773-81.

58. Correia CR, Moreira-Teixeira LS, Moroni L, Reis RL, van Blitterswijk CA, Karperien M, Mano JF. (2011). "Chitosan scaffolds containing hyaluronic acid for cartilage tissue engineering." *Tissue Eng Part C Methods*. 17 (7), 717-30.

59. You F, Wu X, Zhu N, Lei M, Eames B, and Chen XB. (2016). "3D Printing of Porous Cell-laden Hydrogel Constructs for Potential Applications in Cartilage Tissue Engineering," *ACS Biomaterials Science & Engineering* 2 (7), 1200-1210

60. Sell SA, Francis MP, Garg K, McClure MJ, Simpson DG, Bowlin GL. (2008). "Cross-linking methods of electrospun fibrinogen scaffolds for tissue engineering applications." *Biomed Mater.* 3 (4), 045001.

61. Zeugolis DI, Khew ST, Yew ES, Ekaputra AK, Tong YW, Yung LY, Hutmacher DW, Sheppard C, Raghunath M. (2008). "Electro-spinning of pure collagen nano-fibres - just an expensive way to make gelatin?" *Biomaterials*. 29 (15), 2293-305.

62. Kuo YC, Leou SN. (2006). "Effects of Composition, Solvent, and Salt Particles on the Physicochemical Properties of Polyglycolide/Poly(lactide-co-glycolide) Scaffolds." *Biotechnol Prog*. 22 (6), 1664-70.

63. Zhao J, Yuan X, Cui Y, Ge Q, Yao K. (2004). "Preparation and characterization of poly(L - lactide)/ poly(ϵ-caprolactone) fibrous scaffolds for cartilage tissue engineering." *Journal of Applied Polymer Science*, 91 (3), 1676-168.

64. Yoo HS, Lee EA, Yoon JJ, Park TG. (2005). "Hyaluronic acid modified biodegradable scaffolds for cartilage tissue engineering." Biomaterials. 26 (14), 1925-33.

65. Bean AC, Tuan RS. (2015). "Fiber diameter and seeding density influence chondrogenic differentiation of mesenchymal stem cells seeded on electrospun poly (ε-caprolactone) scaffolds." *Biomed Mater* 10 (1), 015018.

66. Woodruff MA, Hutmacher DW. (2010). "The return of a forgotten polymer—Polycaprolactone in the 21st century." *Progress in Polymer Science* 35 (10), 1217-1256.

67. Pati F, Jang J, Ha DH, Won Kim S, Rhie JW, Shim JH, Kim DH, Cho DW. (2014). "Printing three-dimensional tissue analogues with decellularized extracellular matrix bioink." *Nat Commun*. 2 (5), 3935.

68. Drues M. "Are You Sure You Know The Best Regulatory Pathway For Your New Medical Device?" (2015, March 18). Retrieved 04 July, 2016 from <http://www.meddeviceonline.com/doc/are-you-sure-you-know-the-best-regulatory-pathway-for-your-new-medical-device-0001>.

69. United States Code. "Food and Dugs: Drugs and Devices (Part A) - Premarket Approval (PMA)." (2010). Retrieved on 04 July 2016 from <https://www.gpo.gov/fdsys/pkg/USCODE-2010-title21/html/USCODE-2010-title21-chap9-subchapV-partA-sec360e.htm>.

70. Hendrikson W J, Rouwkema J, van Blitterswijkac C A and L Moroni L. (2015). Influence of PCL molecular weight on mesenchymal stromal cell differentiation. *RSC Adv.* 5 (67), 54510.

71. Sah RL, Kim YJ, Doong JY, Grodzinsky AJ, Plaas AH, Sandy JD. (1989). "Biosynthetic response of cartilage explants to dynamic compression." *J Orthop Res*. 7 (5), 619-636.

72. Wong M, Siegrist M, Cao X. (1999). "Cyclic compression of articular cartilage explants is associated with progressive consolidation and altered expression pattern of extracellular matrix proteins." *Matrix Biol.* 18 (4), 391-399.

73. Nunes RW, Martin JR, Johnson J.F. (1982). "Influence of molecular weight and molecular weight distribution on mechanical properties of polymer." *Polymer Engineering & Science* 22 (4), 205-228.

74. Walsh DJ and Termonia Y. (1988). "Mechanical Properties of Low Molecular Weight Polymers as a Function of Temperature." *Polymer Communications* 29, 90-92.

75. Tuba F, Oláh L, Nagy P. (2014). "Towards the understanding of the molecular weight dependence of essential work of fracture in semicrystalline polymers: A study on polycaprolactone." *EXPRESS Polymer Letters* 8 (11), 869-879.

76. Lim K.Y., Kim B.C., and Yoon K.J. (2002). "The Effect of Molecular Weight of Polycaprolactone on the Ester Interchange Reactions during Melt Blending with Poly(ethylene terephthalate)." *Polymer Journal* 34 (5), 313-319.

77. Shepherd DE, Seedhom BB. "The 'instantaneous' compressive modulus of human articular cartilage in joints of the lower limb." *Rheumatology* (Oxford). 38.2 124-32.

78. Kovacik J. (1999). "Correlation between Young's modulus and porosity in porous materials." *Journal of Material Science Letters* 18, 1007-1010.

79. Magnussen RA, Guilak F, Vail TP. (2005). "Cartilage degeneration in post-collapse cases of osteonecrosis of the human femoral head: altered mechanical properties in tension, compression, and shea." *J Orthop Res.* 23 (3), 576-583.

80. Wong BL, Sah RL. (2010). "Mechanical asymmetry during articulation of tibial and femoral cartilages: local and overall compressive and shear deformation and properties." *J Biomech* 43 (9), 1689-95.

81. Démarteau O, Pillet L, Inaebnit A, Borens O, Quinn TM. (2006). "Biomechanical characterization and *in vitro* mechanical injury of elderly human femoral head cartilage: comparison to adult bovine humeral head cartilage." *Osteoarthritis Cartilage.* 14 (6), 589-96.

82. Barker MK, Seedhom BB. (2001). "The relationship of the compressive modulus of articular cartilage with its deformation response to cyclic loading: does cartilage optimize its modulus so as to minimize the strains arising in it due to the prevalent loading regime?" *Rheumatology (Oxford).* 40 (3), 274-84.

83. Schinagl RM, Gurskis D, Chen AC, Sah RL. (1997). "Depth-dependent confined compression modulus of full-thickness bovine articular cartilage." *J Orthop Res.* 15 (4), 499-506.

84. Athanasiou KA, Agarwal A, Dzida FJ. (1994). "Comparative study of the intrinsic mechanical properties of the human acetabular and femoral head cartilage." *J Orthop Res.* 12 (3), 340-349.

85. Williams JM, Adewunmi A, Schek RM, Flanagan CL, Krebsbach PH, Feinberg SE, Hollister SJ, Das S. (2005). "Bone tissue engineering using polycaprolactone scaffolds fabricated via selective laser sintering." *Biomaterials*. 26 (23), 4817-27.

86. Baker SR, Banerjee S, Bonin K, Guthold M. (2016). "Determining the mechanical properties of electrospun poly-ε-caprolactone (PCL) nanofibers using AFM and a novel fiber anchoring technique." *Mater Sci Eng C Mater Biol Appl.* 59, 203-12.

87. Eshraghi S, Das S. (2010). "Mechanical and microstructural properties of polycaprolactone scaffolds with one-dimensional, two-dimensional, and three-dimensional orthogonally oriented porous architectures produced by selective laser sintering." *Acta Biomater*. 6 (7), 2467-76.

88. Shor L, Güçeri S, Chang R, Gordon J, Kang Q, Hartsock L, An Y, Sun W. (2009). "Precision extruding deposition (PED) fabrication of polycaprolactone (PCL) scaffolds for bone tissue engineering." *Biofabrication.* 1 (1), 015003 (pp 10).

89. Wang F, Shor L, Darling A, Khalil, S. (2004). "Precision extruding deposition and characterization of cellular poly-epsilon-caprolactone tissue scaffold." *Rapid Prototyping Journal* 10 (1), 42-49.

90. Doyle H, Lohfeld S, McHugh P. (2014). "Predicting the elastic properties of selective laser sintered PCL/β-TCP bone scaffold materials using computational modelling." *Ann Biomed Eng*. 42 (3), 661-77.

91. Croisier F, Duwez AS, Jérôme C, Léonard AF, van der Werf KO, Dijkstra PJ, Bennink ML. (2012). "Mechanical testing of electrospun PCL fibers." *Acta Biomater* 8 (1), 218-24.

92. Mondrinos MJ, Dembzynski R, Lu L, Byrapogu VK, Wootton DM, Lelkes PI, Zhou J. (2006). "Porogen-based solid freeform fabrication of polycaprolactone-calcium phosphate scaffolds for tissue engineering." *Biomaterial*s 27 (25), 4399-408.

93. Hutmacher DW, Schantz T, Zein I, Ng KW, Teoh SH, Tan KC. (2001). "Mechanical properties and cell cultural response of polycaprolactone scaffolds designed and fabricated via fused deposition modeling." *J Biomed Mater Res.* 55 (2), 203-16.

94. Zehbe R, Schmitt VH, Kirkpatrick CJ, Brochhausen C. (2015). "High resolution X-ray tomography – three-dimensional characterisation of cell-scaffold constructs for cartilage tissue-engineering." *Materials Science and Technology* 31 (2), 167-173.

95. Zehbe R., Haibel A., Riesemeier H, Gross U, Kirkpatrick CJ, Schubert H, Brochhausen C. (2011). "Going beyond histology. Synchrotron micro-computed tomography as a methodology for biological tissue characterization: from tissue morphology to individual cells." J R Soc Interface 7 (42), 49-59.

96. Zhu N., A. Rajaram A., Olubamiji A., D.J. Schreyer D.J.,Wysokinski T.W. ,Belev G., Chen X.B. (2015). "Optimization of in-line phase contrast imaging setup for *in vivo* visualization of hydrogel scaffolds in nerve tissue engineering applications." *4th TERMIS 2015 World Congress*. Boston.

97. Appel AA, Larson JC, Garson AB 3rd, Guan H, Zhong Z, Nguyen BN, Fisher JP, Anastasio MA, Brey EM. (2014). "X-ray phase contrast imaging of calcified tissue and biomaterial structure in bioreactor engineered tissues." *Biotechnol Bioeng* 112 (3), 612-620.

98. Zhu N, Chapman D, Cooper D, Schreyer DJ, Chen X. (2011). "X-ray diffraction enhanced imaging as a novel method to visualize low-density scaffolds in soft tissue engineering." *Tissue Eng Part C Methods*. 17 (11), 1071-1080.

99. Izadifar Z, Honaramooz A, Wiebe S, Belev G, Chen X, Chapman D. (2016). “Data of low-dose phase-based X-ray imaging for *in situ* soft tissue engineering assessments.” *Biomaterials*. 6, 644-651.

100. Huebsch ND, Mooney DJ. (2007). "Fluorescent resonance energy transfer: a tool for probing molecular cell–biomaterial interactions in three dimensions." *Biomaterials* 28 (15), 2424-2437.

101. Boskey A., Pleshko Camacho N. (2007). "FTIR imaging of native and tissue-engineered bone and cartilage." *Biomaterials* 28 (15), 2465-2478.

102. Huzaira M, Rius F, Rajadhyaksha M., Anderson RR., Gonzalez S. (2001). "Topographic variations in normal skin, as viewed by *in vivo* reflectance confocal microscopy." *J Invest Dermato*. 116, 846-852.

103. Muller M, Zumbusch A. (2007). "Coherent anti-Stokes Raman scattering microscopy." *Chemphyschem* 8, 2156-217.

104. Ahearne M, Bagnaninchi PO, Yang Y, El Haj A. (2008). "Online monitoring of collagen fibrealignmentintissue-engineeredtendonbyPSOCT." *J Tissue Eng Regen Med* 2, 521-52.

105. Hofmann MC, Whited BM, Criswell T, Rylander MN, Rylander CG, Soker S, Wang G, Xu Y. (2012). "A fiber-optic-based imaging system for nondestructive assessment of cell-seeded tissue-engineered scaffolds." *Tissue Eng Part C Methods*. 18 (9), 677-687.

106. Heinrich L, Freyria AM, Melin M, Tourneur Y, Maksoud R, Bernengo JC, Hartmann DJ. (2007) . “Confocal laser scanning microscopy using dialkylcarbocyanine dyes for cell tracing in hard and soft biomaterials.” *J Biomed Mater Res B Appl Biomater* 81 (1), 153-61.

107. Mertsching H., Walles T., Hofmann M., Schanz J., and Knapp W.H. (2005). “Engineering of a vascularized scaffold for artificial tissue and organ generation.” Biomaterials 26 (33), 6610-7.

108. Zhou J., Lin H., Fang T., Li X., Dai W., Uemura T., and Dong J. (2010) . “The repair of large segmental bone defects in the rabbit with vascularized tissue engineered bone.” *Biomaterial*s. 31 (6), 1171-9.

109. Cartmell S, Huynh K, Lin A, Nagaraja S, Guldberg R. (2004). "Quantitative microcomputed tomography analysis of mineralization within threedimensional scaffolds *in vitro*." . *J Biomed Mater Res A* 69 (1), 97-104.

110. van Lenthe GH, Hagenmüller H, Bohner M, Hollister SJ, Meinel L, Müller R. (2007). "Nondestructive micro-computed tomography for biological imaging and quantification of scaffold-bone interaction *in vivo." Biomaterials* 28 (15), 2479-90.

111. Nitzsche H, Metz H, Lochmann A, Bernstein A, Hause G, Groth T, Mäder K. (2009) . "Characterization of scaffolds for tissue engineering by benchtop-magnetic resonance imaging." Tissue Eng Part C Methods. 15 (3), 513-21.

112. Potter K, Butler JJ, Horton WE, Spencer RG. (2000). "Response of engineered cartilage tissue to biochemical agents as studied by proton magnetic resonance microscopy." *Arthritis Rheum* 43 (7), 580-90.

113. Prang P, Müller R, Eljaouhari A, Heckmann K, Kunz W, Weber T, Faber C, Vroemen M, Bogdahn U, Weidner N. (2006). "The promotion of oriented axonal regrowth in the injured spinal cord by alginate-based anisotropic capillary hydrogels." *Biomaterials* 27 (19), 3560-9.

114. Poirier-Quinot M, Frasca G, Wilhelm C, Luciani N, Ginefri JC, Darrasse L, Letourneur D, Le Visage C, Gazeau F. (2010). "High-resolution 1.5-Tesla magnetic resonance imaging for tissue-engineered constructs: a noninvasive tool to assess three-dimensional scaffold architecture and cell seeding." Tissue Eng Part C Methods. 16 (2), 185-200.

115. Guermazi A, Eckstein F, Hayashi D, Roemer FW, Wirth W, Yang T, Niu J, Sharma L, Nevitt MC, Lewis CE, Torner J, Felson DT. (2015). "Baseline radiographic osteoarthritis and semi-quantitatively assessed meniscal damage and extrusion and cartilage damage on MRI is related to quantitatively defined cartilage thickness loss in knee osteoarthritis: the Multicenter Osteoarthritis Study." *Osteoarthritis Cartilage* 23 (12), 2191-2198.

116. Nam YS, Park TG. (1999). "Porous biodegradable polymeric scaffolds prepared by thermally induced phase separation." *J Biomed Mater Res*. 47 (1), 8-17.

117. Gabor D. (1948). A new microscopic principle. *Nature* 161, 777.

118. Wilkins SW, Gureyev TE, Gao D, Pogany A, and Stevenson AW. (1996). "Phase-contrast imaging using polychromatic hard X-rays". *Nature* 384, 335 – 338.

119. Spanne P, Raven C, Snigireva I, Snigirev A. (1999). "In-line holography and phase-contrast microtomography with high energy x-rays." *Phys Med Biol*. 44 (3), 741-749.

120. Davis TJ, Gao D, Gureyev TE, Stevenson AW, and Wilkins AW. (1995). "Phase-contrast imaging of weakly absorbing materials using hard X-rays." *Nature* 373, 595-598.

121. Zhou S, Brahme A. (2008). "Development of phase-contrast X-ray imaging techniques and potential medical applications." *Physica Medica* 24, 129-148.

122. Sun, W., Li, Z.R., Yang, Y.R., Shi, Z.C., Wang, B., Liu. (2011)."Experimental study on phase-contrast imaging with synchrotron hard X-ray for repairing osteonecrosis of the femoral head." *Orthopedics.* 34 (9), e530-e534.

123. Murrie RP, Morgan KS, Maksimenko A, Fouras A, Paganin DM, Hall C, Siu KK, Parsons DW, Donnelley M. (2015). "Live small-animal X-ray lung velocimetry and lung micro-tomography at the Australian Synchrotron Imaging and Medical Beamline." *J Synchrotron Radiat* 22 (4), 1049-1055.

124. Murrie RP, Stevenson AW, Morgan KS, Fouras A, Paganin DM, Siu KK. (2014). "Feasibility study of propagation-based-contrast X-ray lung imaging on the imaging and Medical Beamline at the Australian Synchrotron." *J Synchrotron Radiat.* 21 (2), 430-445.

125. Izadifar Z, Chapman LD, Chen X. (2014). "Computed tomography diffraction enhanced imaging for *in situ* visualization of tissue scaffolds implanted in cartilage." *Tissue Eng Part C Methods* 20 (2), 140-148.

126. Bronnikov AV. (2008). "Phase-contrast CT: Fundamental theorem and fast image reconstruction algorithms." *Optics Express* 3223-3241.

127. Jia QJ., Chen Y., Li G., and Jiang XM. (2012). "Optimization of the in-line X-ray phase-contrast imaging setup considering edge-contrast enhancement and spatial resolution." *2012 Chinese Physical Society and the Institute of High Energy Physics of the Chinese Academy of Sciences and the Institute of Modern Physics of the Chinese Academy of Sciences and IOP Publishing Ltd* 36 (3), 267-274.

128. Liua W, Wanga D, Huanga J, Weib Y, Xionga J, Zhua W, DuanaL, Chena J, Sunc R, Wanga D. (2016). Low-temperature deposition manufacturing: A novel and promising rapid prototyping technology for the fabrication of tissue-engineered scaffold. *Materials Science and Engineering: C.* 70 (2), 976-982.

129. Landers, R., Pfister, A., Hübner, U. et al. (2002). "Fabrication of soft tissue engineering scaffolds by means of rapid prototyping techniques." *Journal of Materials Science.* 37 (15), 3107-3116.

130. Johnson T1, Bahrampourian R, Patel A, Mequanint K. (2010). Fabrication of highly porous tissue-engineering scaffolds using selective spherical porogens. *Biomed Mater Eng*. 20 (2), 107-18.

131. Zhou C1, Ma L, Li W, Yao D. (2011). Fabrication of tissue engineering scaffolds through solid-state foaming of immiscible polymer blends. *Biofabrication.* 3 (4), 045003.

132. Senel-Ayaz HG1, Perets A, Govindaraj M, Brookstein D, Lelkes PI. (2010). Textile-templated electrospun anisotropic scaffolds for tissue engineering and regenerative medicine. *Conf Proc IEEE Eng Med Biol Soc*. 2010, 255-8.

133. Yeong WY1, Sudarmadji N, Yu HY, Chua CK, Leong KF, Venkatraman SS, Boey YC, Tan LP. (2010). Porous polycaprolactone scaffold for cardiac tissue engineering fabricated by selective laser sintering. *Acta Biomater.* 6 (6), 2028-34.

134. Narayan R. (2013). *Rapid Prototyping of Biomaterials: Principles and Applications.* Sawston, Cambridge: Woodhead Publishing.

135. Zhang Y, Tse C, Rouholamin D Smith PJ. (2012). Scaffolds for tissue engineering produced by inkjet printing. *Central European Journal of Engineering* 2 (3), 325-335.

Chapter 2: Review of Potentials of Synchrotron-Based Biomedical Imaging Techniques for Bone and Cartilage Tissue Engineering

This chapter was adopted from the publication of “Olubamiji, A.D., Izadifar, Z., Chen, D.X. Synchrotron imaging techniques for bone and cartilage tissue engineering: potential, current trends, and future directions. Tissue Engineering: Part B Reviews 20:5 (2013):503-22”. According to the Copyright Agreement, "the authors retain the right to include the journal article, in full or in part, in a thesis or dissertation".

2.1. Abstract

Biomedical imaging is crucial to the success of bone / cartilage tissue engineering (TE) by providing detailed 3D information on tissue-engineered scaffolds and associated bone/cartilage growth during the healing process. Synchrotron radiation (SR)-based biomedical imaging is an emerging technique for this purpose that has been drawing considerable recent attention. Due to the unique properties of synchrotron light, SR biomedical imaging can provide information that conventional X-ray imaging is not able to capture. SR biomedical imaging techniques notably differ from conventional imaging in both physics and implementation. Thus, they vary regarding both capability and popularity for biomedical imaging applications. In the earlier decade, synchrotron-based imaging was used in bone / cartilage TE to characterize bone/cartilage scaffolds and tissues as well as the varying degrees of success in reconstruction. However, several key issues should be addressed through research before SR biomedical imaging can be advanced to a non-invasive method for application to live animals and eventually to human patients. This review briefly presents recent developments in this area, focusing on different synchrotron-based biomedical imaging techniques and their advantages and limitations, as well as reported applications to bone and cartilage TE. Key issues and challenges are also identified and discussed along with recommendations for future research.

2.2. Introduction

Three dimensional (3D) biomedical imaging plays a major role in determining the efficiency of tissue-engineered regeneration. It allows examination of microstructural, biochemical, and biological properties of the tissue-engineered scaffolds and its interaction with the host tissues before and after implantation [1]. X-ray absorption imaging (such as μCT and CT)

[2], ultrasound [3] and MRI [1, 4] are among the prevalent 3D imaging methods used for non-invasive characterization of cartilage and bone tissues, scaffolds microarchitecture and tissue growth. Although these techniques are widespread for clinical diagnosis and tissue engineering (TE) related biomedical imaging, certain limitations restrain their capability to completely unravel tissue engineering imaging related problems. Some of these limitations are low spatial resolution, limited penetration depth of optical wavelengths in samples [5], poor contrast of low Z elements [6], artifacts [7-8], reports of uncomfortable anxiety and claustrophobia [9].

There is no doubt that interesting recent advancements have been made in TE in the recent times. Nonetheless, further advancement required to advance TE to its full potential via animal and clinical (human) trials. These animal and clinical trials, which may involve longitudinal (long-term) *in vivo* examinations of the same live *in situ* tissues, will make no tangible contribution to TE without an effective 3D biomedical imaging technique to monitor their success. An effective, non-invasive, 3D biomedical imaging technique to facilitate advancements should have the capacity to (1) track the process of cell growth into newly formed tissues (i.e., cell migration, cell-scaffold adhesion, and differentiation); (2) monitor construct biodegradation kinetics; and (3) examine the host-construct integration in a continued manner in the same animal or human without destroying or posing a risk to the animal or the tissues of interest [10-11]. Since the discovery of synchrotron light, different non-invasive 3D imaging techniques that are invaluable for bio-medical applications and material sciences have emerged. The next section discusses the basic physics of major synchrotron-based biomedical imaging techniques with potential applications to bone and cartilage TE.

2.3. Synchrotron Imaging

Synchrotron light is an electromagnetic radiation produced when charged particles (i.e., electrons) are ejected from an electron gun by an electric field and then sped up in a linear accelerator. The particles are further accelerated to near the speed of light in a booster ring before being transferred to a storage ring. In the storage ring, bend magnets cause the electrons to change direction, and this results in a change in their velocity vector and, consequently, the radiation of synchrotron light. The properties of synchrotron light, to be discussed in detail next, significantly improve contrast sensitivity in X-ray imaging systems [12]. Due to the inherent advantages and potential of synchrotron-based light sources, several 3D biomedical imaging techniques have been developed [13-18]. The successful implementation of these methods in recent years demonstrates

that synchrotron-based biomedical imaging techniques may be translated to TE applications. These methods will further advance TE by enabling non-invasive and longitudinal delineation of construct morphometry, neo-tissue growth, construct degradation kinetics, and host–implant interface dynamics [8, 10, 11, 17].

2.3.1. Phase-contrast Imaging

PCI uses variations in the phase shifts of emerging X-rays to characterize structural properties of samples with similar electron density, low atomic number materials, and soft tissues without the use of exogenous contrast agents [19-21]. At diagnostic X-ray energies, PCI relies on variations in the real part of the refractive index of tissues that are several orders of magnitude more important than the imaginary part used as the source of absorption contrast. In addition, unlike conventional diagnostic X-ray imaging that is dominated by incoherent Compton scattering, most implementations of PCI are based on coherent X-ray scattering for observation of refraction and interference [19-21]. Several PCI techniques have been developed based on obtainable information and differences in implementation. In the next section, we briefly discuss major PCI techniques that are currently or have the potential to be employed in TE.

2.3.1.1. Inline-PCI

Inline-PCI, also called propagation-based imaging or inline holography, had its breakthrough in 1948. Inline-PCI was the first phase-contrast technique pioneered; it requires no optical element (e.g., gratings or diffracting crystals) and has the simplest experimental set-up [23-26]. It explores the phase shifts caused by variations in the refractive index and thickness of materials and captures these variations in measured intensity as edge enhancement between different regions [25]. This edge enhancement is a significant advantage of inline holography and results from the high lateral (spatial) coherence of inline-PCI achievable using a small effective source or large sample-to-detector distance [23-26]. An X-ray source such as a third-generation synchrotron X-ray source, a microfocus X-rays tube, or an ultrafast-laser-based plasma X-ray source is required to obtain high lateral coherence [24, 26, 27]. In addition, the sample-to-detector-distance is selected to fall in the Fresnel zone, a region between the absorption zone and the far field (Fraunhofer zone), as shown in Fig. 2.1 a [28]. The continuous phase variations result in enhanced and defined boundaries [23-27]. To optimize the sensitivity of this method, the sample-detector-distance should be limited to the Fresnel zone and completely avoid the Fraunhofer zone, and the spatial resolution of the detector, X-ray source size, and refractive properties of the samples

should be considered [23-27].

2.3.1.2. X-ray Interferometry

In 1966, Bonse and Hart pioneered the use of three Laue-case (LLL) analyzers in a method referred to as X-ray interferometry [13, 29]. X-ray interferometry is regarded as the most sensitive technique to measure phase shifts. It requires the high spatiotemporal coherence that is achievable by a high brilliance source such as a synchrotron or free-electron laser [29-31]. The set-up of the interferometer (Fig. 2.1 b) employs three perfect diffracting crystals [32]. The splitter crystal divides the incident X-ray beam into two coherent and spatially separated beams. One of the two beams pass through the sample, positioned between the mirror and analyzer, while the second beam acts as an unperturbed reference. The beams are then reflected via Laue-case diffraction at the mirror crystal. The two beams interfere at the entrance of the analyzer crystal, traverse the analyzer crystal, and produce intensity distributions detected by comparing the two beams. These intensity distributions are measured as phase shifts caused by the inhomogeneity in samples [13, 29-32].

2.3.1.3. Diffraction-Enhanced Imaging

Diffraction-enhanced imaging (DEI), also known as analyzer-based imaging, was studied in the mid-1990s by Davis *et al.,* Ingal and Beliaevskaya, and Chapman *et al*. [14, 33-34]. This method utilizes a three-crystal setup that consists of a double crystal monochromator with asymmetric reflecting planes and an analyzer crystal (Fig. 2.1 c) [28]. The double crystal monochromator uses Bragg geometry to select a small energy band monochromatic beam from the incident polychromatic spectrum to traverse the object [12, 14, 33-35]. The beam exiting the object then hits the analyzer crystal, which diffracts the X-rays that align only within its angular acceptance to the detector with a modulation given by the rocking curve (RC). All other photons that fall out of the angular acceptance window of the analyzer are of scatter origin, and their removal causes enhancement of the image contrast [14, 33-34]. To obtain images, the analyzer is tuned at the half-maximum reflectivity of the RC and images are taken on both the high angle (yH) and low angle (yL) sides [38-40]. The intensities measured on the high angle (I_H) and low angle (I_L) sides (Fig. 2.1 c) are employed to calculate the refraction angle image ($\Delta\theta_Z$; Eq. 2.1) and apparent absorption (I_R; Eq. 2.2) image obtained in the sensitivity direction Z, as follows:

$$\Delta\theta_Z = \frac{I_H R(\theta_L) - I_L R(\theta_H)}{I_L \frac{dR}{d\theta}(\theta_H) - I_H \frac{dR}{d\theta}(\theta_L)} \quad (2.1)$$

$$I_R = \frac{I_L \frac{dR}{d\theta}(\theta_H) - I_H \frac{dR}{d\theta}(\theta_L)}{R(\theta_L)\frac{dR}{d\theta}(\theta_H) - R_H \frac{dR}{d\theta}(\theta_L)}, \quad (2.2)$$

where R is the analyzer reflectivity as a function of analyzer rocking angle (θ), $\Delta\theta_Z$ is the refracted X-rays or the refraction angle intensity, and I_R is the apparent absorption intensity [12, 14].

The apparent absorption image is then separated into absorption contrast and extinction contrast. The ability of DEI to separate these two contrasts is an advantage over conventional X-ray imaging methods [12, 14]. The refraction effects of the X-rays and the thickness gradients of the sample greatly affect the refraction angle images. This results in intrinsic edge enhancement at the boundaries within tissues and enables DEI to provide clear and crisp refraction angle images. The absorption image relies on the linear integration of tissue absorption that, in turn, depends on the thickness of the sample [36]. Although DEI exhibits excellent scatter rejection, it is limited by its sensitivity to only the vertical components of the refracted beam; further research is required to extend its sensitivity [12]. DEI also has trouble in characterizing homogeneous fine structures, and the images contain ultra-small-angle X-ray scattering (USAXS) properties that can degrade image contrast [37-39]. Other DEI-based methods are gradually evolving to address these challenges.

Rigon *et al.* [37] proposed an extension of DEI in a technique that employs the intensity measurements obtained from the peak and the two half-slopes of the RC. Unlike classical DEI, this technique also uses the second rather than the first derivative of the RC. This method generates apparent absorption, refraction, and USAXS images [37]. Multiple image radiography (MIR) is an optimized version of (bone) tissues *in situ* with considerable structural detail [40]. This method may encounter limitations in sensitivity regarding the wave field in one direction. This limitation, which is characteristic of all analyzer-based phase-sensitive imaging techniques, may prevent the full delineation of samples with fibers oriented in many orientations, for example, cartilage. However, Li *et al*. suggested solutions that may be applied to this problem [40].

2.3.1.4. Dark-Field Imaging

Dark-field imaging (DFI) relies on monochromaticity and small angular divergence associated with its crystal optics. The Bragg-Bragg-Laue geometry of DFI simultaneously produces dark-field and bright-field images. The Bragg–Bragg geometry of the double crystal monochromator is used to generate a monochromatic beam from the incident beam, asymmetric diffraction of the beam, and reduction of the beam angular divergence [15, 41-43]. The generated beam then hits and traverses the sample to be incident on the Laue-geometry analyzer, which then,

with small-angle scattering, diffracts and splits the modulated beam as shown in Fig. 2.1 d [41]. One of the two refracted beams produce intensities recorded by the area detectors as dark-field images, while the other beam generates bright-field images. This method requires no analyzer tuning and suppresses background illumination. Hence, DFI can be used to obtain high spatial resolution images of weak refraction-based signals exiting soft tissues [15, 41, 42]. DFI is also achievable using grating interferometry [43].

2.3.1.5. Differential PCI using X-ray Gratings

While most PCI techniques require highly brilliant monochromatic sources, such as synchrotron sources, differential PCI (DPCI) works with low brilliance polychromatic X-ray sources [16]. DPCI is also called Talbot-Lau interferometry. DPCI relies on angular filtering of the transmitted X-ray beam by micro-periodic gratings followed by conversion of the angular beam deviations from refraction into intensity patterns recorded by the detector [44-45]. Depending on the brilliance of the X-ray source, DPCI requires two or three transmission gratings. Its intensity is separated into absorption, refraction, USAXS, and sometimes dark-field components. The setup (Fig. 2.1 e) consists of the source grating or beam splitter (G_0), phase grating (G_1), and analyzer absorption (G_2) grating, with their respective periods (p) and distances from the detector [44]. G_0 consists of grids that divide the incident beam into an array of line sub-sources which are individually spatially coherent but mutually incoherent. The X-rays exiting each aperture of G_0 irradiate the sample and experience slight refraction. After the beam transmits the object, G_1 causes intensity modulation and splits the beam into two out-of-phase beams. One of these beams traverses the object and interferes with the other beam that exited G_0, in the region behind G_1 and in the plane of G_2, to produce periodic interference fringes. The linear periodic interference fringe patterns are transformed into intensity modulations that are recorded by the detector [12, 44-45]. Unlike most PCI methods, DPCI enables a large field of view using large pixel-size detectors and requires less mechanical stability, which enables large image sampling [16, 45]. In addition, DPCI is attracting clinical attention because of its capacity to use low brilliance polychromatic X-ray sources to scan soft tissues at a high spatial resolution [16, 47].

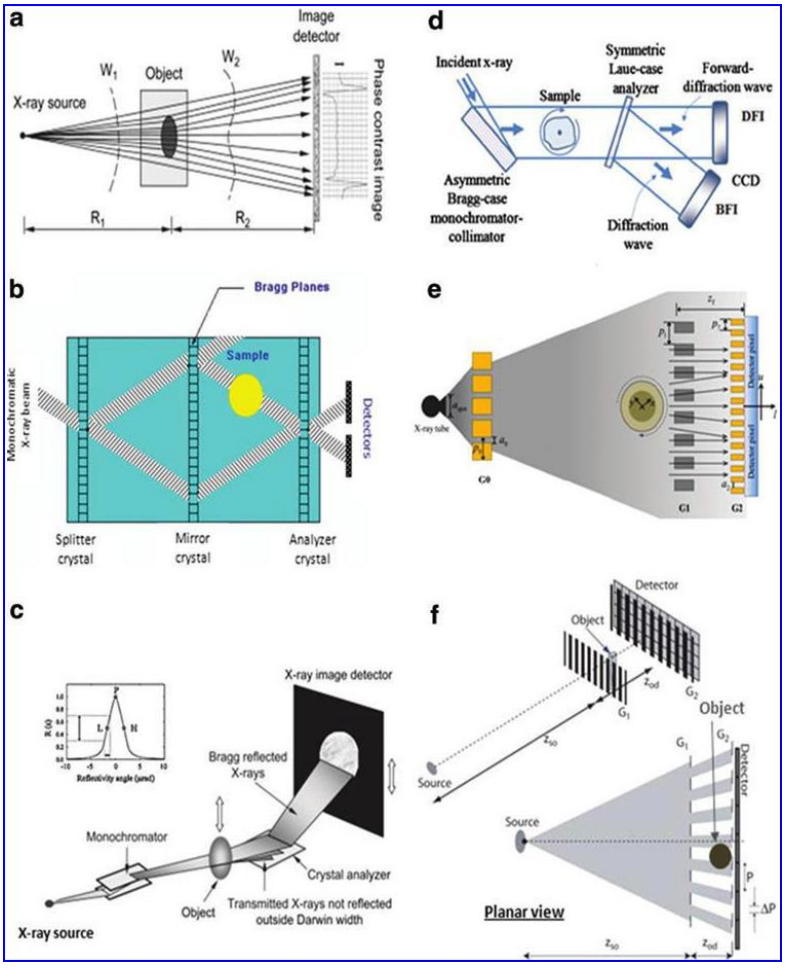

Fig. 2.1: Schematic diagrams illustrating the image acquisition setup of different phase-contrast X-ray imaging techniques: (a) inline PCI [28]; (b) X-ray interferometry; (c) DEI [28]; (d) DFI [41]; (e) differential PCI [44]; and (f) coded-aperture phase contrast imaging [49].

2.3.2. K-Edge Subtraction

Contrast-enhanced K-edge subtraction (KES) imaging, also known as dichromography or dual-energy subtraction imaging, uses biocompatible and higher atomic number contrast agents to increase the sensitivity and contrast of low density tissues [52]. It was pioneered by Jacobson in 1953 and uses either a synchrotron or compact X-ray tube source and a Bragg-case crystal monochromator system [53-55]. It relies on the large jump in attenuation coefficient (e.g., up to a factor of 6 for iodine) that occurs at the K-edge energy of the contrast agent, while the attenuation coefficient of the other components (e.g., surrounding matrix) of the object changes only minimally [55-57]. To implement KES imaging, two mono-energetic X-ray beams with defined energies of just below and above the K-edge of the contrast agent are selected from the incident polychromatic beam as shown in Fig 2.2. The sample is imaged

with the two selected X-ray energies to simultaneously obtain two intensity images, one of which is subtracted from the other to give a difference image. The difference image (Eq. 2.3) is solved to generate the projected densities (images) of the matrix, $\rho_M t_M$ (Eq. 2.4), and the contrast material, $\rho_C t_C$ (Eq. 2.5):

$$\begin{bmatrix} r_L \\ r_H \end{bmatrix} = \begin{bmatrix} -\ln\frac{I_L}{I_0} \\ -\ln\frac{I_H}{I_0} \end{bmatrix} = \begin{bmatrix} \frac{\mu}{\rho_M}(E_L)\rho_M t_M + \frac{\mu}{\rho_c}(E_L)\rho_C t_C \\ \frac{\mu}{\rho_M}(E_H)\rho_M t_M + \frac{\mu}{\rho_c}(E_H)\rho_C t_C \end{bmatrix} \quad (2.3)$$

$$\rho_M t_M = \frac{\frac{\mu}{\rho_c}(E_H)r_L - \frac{\mu}{\rho_c}(E_L)r_H}{\frac{\mu}{\rho_M}(E_L)\frac{\mu}{\rho_c}(E_H) - \frac{\mu}{\rho_c}(E_L)\frac{\mu}{\rho_M}(E_H)} \quad (2.4)$$

$$\rho_C t_C = \frac{\frac{\mu}{\rho_M}(E_H)r_L - \frac{\mu}{\rho_M}(E_L)r_H}{\frac{\mu}{\rho_M}(E_L)\frac{\mu}{\rho_c}(E_H) - \frac{\mu}{\rho_c}(E_L)\frac{\mu}{\rho_M}(E_H)}, \quad (2.5)$$

where I is the photon intensity; subscripts M, C, L, and H indicate the matrix, the contrast material, below K-edge, and above K-edge, respectively; ρ is the density of the material; t is the thickness of the material; I_0 is the number of photons in the incident beam; $\frac{\mu}{\rho}(E)$is the mass attenuation coefficient of the material; and $r = \ln\frac{I}{I_0}$ [12, 52, 54]. The presence of bones, motional image blurring, and cross-over artifacts caused by beam crossing in addition to the technical complexity and rarity of synchrotron sources constitute major obstacles to KES imaging [56]. Thus, new applications are being developed to optimize the method. KES has been combined with CT (KES-CT) for extensive quantification of the spatial distribution of contrast agent in samples [57]. In addition, Zhong *et al.* investigated a lab-based rotating anode X-ray source and single bent Laue monochromator for KES angiography to address the scarcity of synchrotron facilities [55]. The recent development of three-energy KES has also contributed to advancements in KES imaging. In three-energy KES, a third image is simultaneously taken using a harmonic energy far above the K-edge energy of the contrast agent. The third image resolves the bone component, which is an artifact source in the images acquired above and below the K-edge [56, 58]. Similarly, near-edge spectral imaging (NESI), an extended version of KES imaging that enables scanning from an energy just below to an energy just above the K-edge of the contrast material, has been developed. NESI has numerous advantages over KES imaging, including increased photon flux (up to a factor of 5), elimination of motion artifacts, and easy characterization of additional components such as bone [56]. Furthermore, shaping the X-ray spectrum such that the two energies are very close to the K-edge of the contrast material has been reported to optimize the sensitivity of KES [59].

In addition, the use of a bent Laue monochromator has been reported to optimize photon flux, integrated reflectivity, and tolerance to diffraction due to a large solid diffraction angle [56]. Finally, the cytotoxicity of contrast agents and the selection of a contrast material with a suitable absorption energy to prevent photon starvation during biomedical imaging should also be taken into consideration [60].

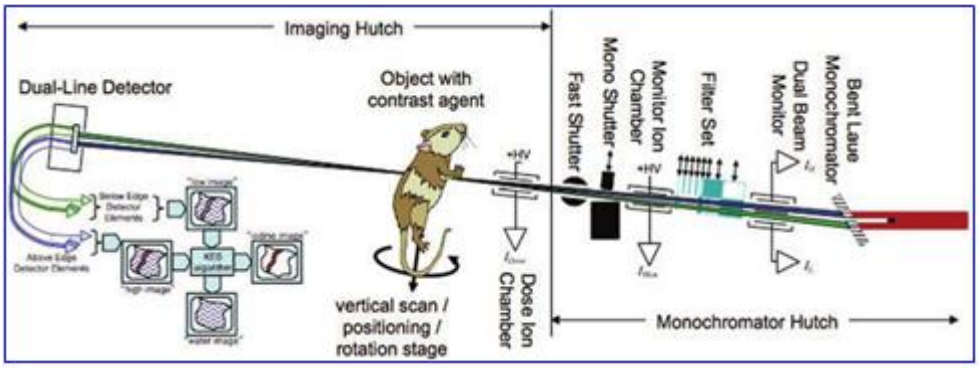

Fig. 2.2: Schematic diagram of KES imaging setup with a single bent Laue monochromator with splitter [12].

2.3.3. Synchrotron Radiation Micro-Computed Tomography (SR-µCT)

SR-µCT is the synchrotron-based version of the µCT systems introduced by Feldkamp *et al.,* 1989 [61]. The high photon flux (typically about 10^8 photons/s), high brilliance of the X-ray source, small angular beam divergence and consequent improved spatial resolution and higher signal-to-noise ratio, and faster acquisition time are benefits of SR-µCT over standard µCT systems. In addition, the ability to tune the synchrotron X-ray energy addresses issues with respect to beam hardening artifacts, reconstruction artifacts, and geometrical artifacts that occur in standard µCT imaging [63-66]. SR-µCT employs a collimated monochromatic beam generated from a double crystal monochromator for generation of absorption contrast. The monochromatic beam illuminates a sample mounted and fixed on a rotatable stage (Fig. 2.3) [69]. The intensity of the transmitted beam is recorded by an electro-optic detector positioned close to the sample to avoid phase contrast [61-66]. An extension of SR-µCT is the use of synchrotron-based phase contrast techniques, as discussed above, in what is known as phase contrast microtomography [64 - 67]. PC-µCT combines the properties of SR-µCT and phase contrast techniques for simultaneous generation of phase contrast alongside the absorption contrast usually produced in SR-µCT. This technique is much more sensitive, especially to soft tissues, and can generate absorption images at greatly reduced absorbed doses; this method is more prevalent in bone and cartilage TE characterization [64-67].

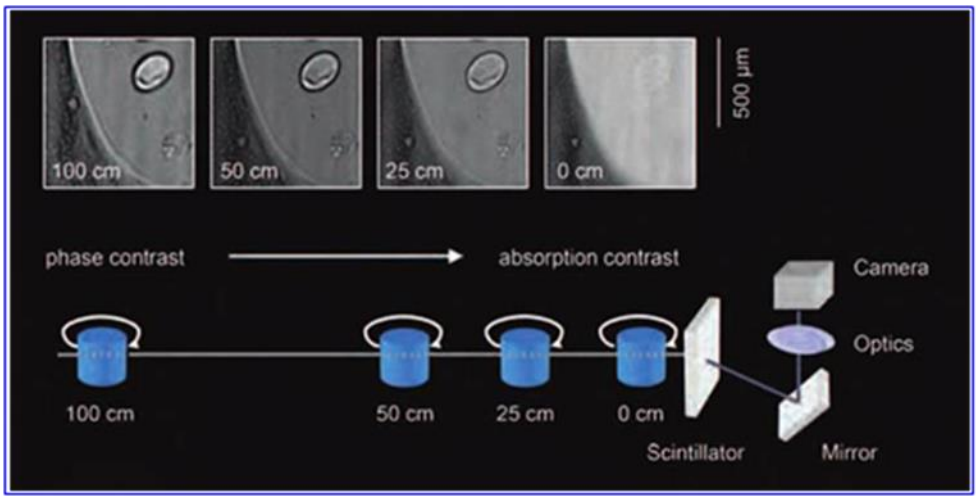

Fig. 2.3: Schematic diagram of part of a synchrotron radiation µCT imaging setup. Inset images illustrate the effect of X-ray propagation distance on inline phase contrast images (transition of absorption-contrast image to phase-contrast image by sample-to-detector distance) [69].

2.4. Applications of Synchrotron Imaging to Bone and Cartilage TE

2.4.1 Potential Applications to Bone TE

Bone tissues have high absorption coefficients, therefore making their imaging easier than for soft tissues. Several conventional non-invasive imaging methods, such as µCT, ultrasound, and MRI are commonly used for bone imaging and bone tissue engineering (BTE) applications [1, 3-4]. BTE requires delineation of surrounding soft tissues, knowledge of the degradation kinetics of the implanted construct, and bone remodeling profiles alongside host bone. Thus, imaging techniques with the capacity to simultaneously visualize both hard and soft materials with high and low absorption coefficients are in high demand. Synchrotron-based imaging methods provide information and possess different advantages above and beyond conventional imaging techniques. A summary of the advantages and disadvantages of synchrotron-based imaging techniques for TE applications is provided in Table 2.1. This information includes architectural properties, degradation kinetics of constructs, regenerated tissue quality as characterized by vascularization, and integration of the constructs with the surrounding host tissue. In the next section, we discuss the status and capabilities of synchrotron-based techniques used in BTE and conditions similar to those encountered in BTE.

2.4.1.1. Synchrotron Radiation Microcomputed Tomography

SR-μCT is an absorption-based imaging technique that can be used for 3D quantitative and qualitative characterization of tissue properties at a spatial resolution even smaller than 1 mm [68]. It exhibits faster scanning time than laboratory μCT [65] and benefits from the advantages of synchrotron source X-rays [66-67]. SR-μCT has a demonstrated capacity to obtain 3D information about trabecular and cortical bone microarchitecture at a spatial resolution less than 10 mm [63, 65]. SR-μCT has also been employed for 3D characterization of scaffold properties, such as pore connectivity, pore size, wall thickness, and anisotropy, as well as functional changes resulting from tissue regeneration [2, 69]. In fact, SR-μCT enables characterization of scaffold micro- and macro-structures in a manner not possible with 2D scanning electron microscope (SEM) analysis [67].

SR-μCT has been employed for bone imaging and scaffold characterization as well as in a few BTE studies. SR-μCT was used by Yue *et al.* [66] to identify scaffold morphology, mineral distribution within scaffold pores, and tissue in-growth in 4-week-old explants of a bioactive glass foam scaffold implanted between the muscle and tibia of a mouse (Fig. 2.4) [66]. In a similar study, SR-μCT was used to successfully identify scaffold architecture and bone ingrowth into cell-loaded hydroxyapatite scaffolds implanted in immunodeficient mice for 8 weeks. The bone ingrowth was estimated in terms of total volume fraction, distribution, and thickness of the newly formed bone tissue in the pores of the implant and the scaffold architecture in terms of porosity and spatial distribution of walls [70]. The same group explored the ability of SR-μCT to examine the progressive resorption of and bone ingrowth into scaffolds implanted in immunodeficient mice for longer repair times of 8, 16, or 24 weeks [71-72].

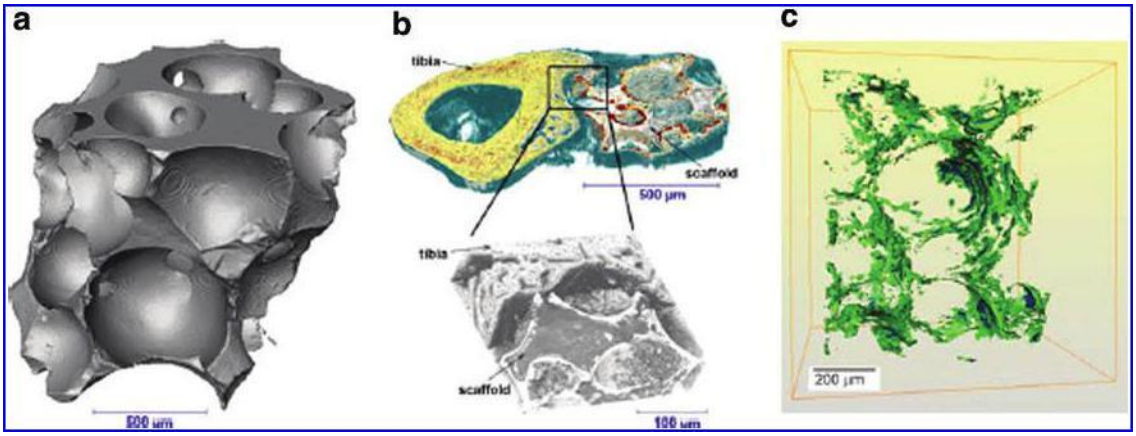

Fig. 2.4: SR-μCT images of a bioactive scaffold: (a) scaffold morphology and pores before implantation; (b) 4 weeks after implantation (ex vivo) between the muscle and tibia of a mouse showing changes in the scaffold and some tissue growing into the pores of the scaffold; and (c) calcium distribution within the scaffold [66].

The use of gold nanoparticles (GNPs) as contrast agents for enhancing X-ray attenuation in the region of interest using SR-μCT has also been investigated. In two recent studies, Astolfo *et al.* used SR-μCT to localize and track GNP-labeled cells [73-74]. In one of these studies, they investigated the increased sensitivity obtained from inclusion of GNPs *ex vivo*, by injecting GNP-labeled gliomal cells into the brain of adult male Wistar rat for 16 days, and *in vitro*, by suspending the labeled cells in 5 % agarose gel [73]. The *in vitro* experiment demonstrated that the enhanced contrast enabled assessment of individual GNP-loaded cells along with the surrounding lacunae. Although the *in vivo* imaging resolution was four times lower and the number of projections was reduced compared with similar *ex vivo* imaging (to address the dose issue), it was still possible to localize the clusters of cells (Fig. 2.5). The latter study showed a reasonable compromise between dose and image resolution, which is the case in most longitudinal *in vivo* studies [74]. Although the application of SR-μCT to track the performance of labeled cells in TE constructs is yet to be investigated, successful results may be extrapolated to BTE for tracking tissue ingrowth into TE constructs [73-74].

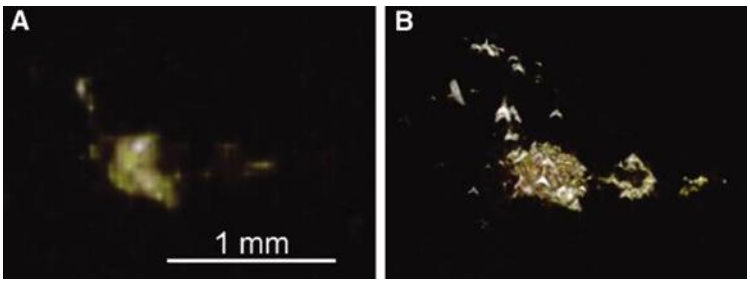

Fig. 2.5: Gold nanoparticle-enhanced 3D rendered SR-μCT images showing the effect of varying spatial resolution: (A) low dose *in vivo* image and (B) high dose ex vivo image 3D, three-dimensional [74].

Several studies have applied SR-μCT with great success to bone tissue imaging and the characterization of the functionality of scaffolds used in BTE [65-75]. However, the majority of these examinations focused on tissue samples or *in vitro* studies. This is mainly due to the high radiation dose coupled with large exposure times to achieve very high resolution. This trade-off should be satisfied when high quality and quantitative imaging is desired. The inclusion of nanoparticles as contrast agents may enhance tissue sensitivity even when spatial resolution is reduced [73-74]. Overall, SR-μCT is a suitable imaging technique for highly detailed (e.g. cellular level) qualitative and quantitative nondestructive characterization of constructs and tissue regrowth. However, due to the limitations associated with this technique, such as small sample size (less than 1 mm^3), high radiation dose, and scanning time, candidate samples may be limited

to excised specimens and small animals (noninvasive *in vivo* imaging) [75].

2.4.1.2. Inline-PCI-CT (and PC-µCT)

Even though applications of SR-µCT have been very successful regarding the characterization of scaffolds, bone, and bone growth kinetics [65 - 75], this technique is unable to clearly identify differences between several low-density tissues [66]. PC-µCT can be used to obtain phase-contrast images alongside ab-sorption contrast images of tissues. On one hand, its phase contrast provides sensitivity to poorly absorbing biological samples with low absorption contrast, such as soft tissues, such that it can differentiate various tissue types. On the other hand, its absorption contrast provides greater detail for tissues with high absorption contrast [8, 65]. Several groups have used PC-µCT or inline-PCI-CT to characterize bone tissues and the functionality of biomaterial scaffolds or constructs used in BTE. In one such study, inline-PC-µCT was used to identify different phases resulting from the organization of the extracellular matrix, from fibrils into net-works, formed within scaffolds seeded with stem cells after 15 days in culture [68]. Weiss *et al.* [75] used PC-µCT to examine the microstructure, bone ingrowth, mineralized and un-mineralized bone tissue network, and tissue-implant inter-face of an injectable bone substitute and macroporous blocks implanted in a rabbit model and reported results consistent with conventional 2D histomorphometric analysis [75]. Similarly, Sun *et al*. [84] successfully applied inline-PCI-CT and DEI to characterize the repair of osteonecrosis in rabbits using nano-hydroxyapatite/collagen and autologous mesenchymal stem cells. Both techniques demonstrated identification of the biomaterial–host interface, bone tissue formation, and substitution of biomaterials with newly grown tissues over a period of 12 weeks [84]. In another study, SR-µCT and PC-µCT were investigated and com- pared regarding imaging bone in-growth coupled with angio- and micro-vasculogenesis. Although scaffold materials and mineralized bone were visible using both imaging techniques, PC-µCT provided information on the scaffold material, bone ingrowth, and vessel network resulting from microvasculogenesis (Fig. 2.6) [76].

During the bone remodeling stage of a tissue-engineered joint, certain details with low or similar densities are challenging to decipher using absorption-based imaging techniques, even at an optimum photon energy [66]. Phase contrast-based imaging is a potential technique for deciphering structural details and microvasculogenesis during tissue regeneration and remodeling. In addition to regeneration progress, inline-PC-µCT can decipher scaffold biodegradation kinetics and other non-bone surrounding tissues [68, 75-76]. Although SR-µCT is currently the most

prevalent technique used for bone imaging and BTE, inline-PC-µCT's experimental simplicity, contrast resolution that is many orders of magnitude higher than the absorption contrast, and ability to decipher the growth of vessel networks resulting from angio- and micro-vasculogenesis, changes in scaffold material, and bone ingrowth may be attractive for BTE applications [65, 68, 75-76].

PC-µCT may be an ideal technique for highly detailed (e.g., cellular level) qualitative and quantitative characterization of engineered constructs, hard and soft tissues re-growth *in vitro*, and tissue samples obtained from small animals. However, extrapolating this method for use in *in vivo* studies requires that certain trade-offs be made regarding image quality and absorbed radiation dose. With appropriate manipulations, inline-PCI-CT may be a better candidate than SR-µCT for the characterization of tissue-engineered repair *in vivo* in large animals [84].

Table 2.1: Advantages and disadvantages of commonly used synchrotron X-ray imaging techniques

	Advantages	**Disadvantages**
SR-µCT	Simple experimental setup, Image pixel size of approximately 0.28 mm [66]; Predominantly used for ex vivo and *in vitro*, imaging of hard tissues, e.g. bone imaging [65 - 76]	Cannot specifically identify tissue types [66]; High absorbed radiation dose due to high spatial resolution imaging
Inline-PCI-CT	Simplest phase-sensitive imaging experimental setup. Edge enhancement for weakly absorbing materials, e.g., soft tissues [23-26].	High energy, lower dose imaging, scatter production at high energy. Practical limitations with extreme propagation distances; infrastructure limitation.
Inline-PC-µCT	Specific identification of tissue types [66]. Simple experimental setup [76]. Image pixel size of approximately 0.7 mm [73]. Excellent for soft and hard tissues imaging *ex vivo* and *in vitro*	High absorbed radiation dose due to high resolution imaging; limitation for *in vivo* imaging. Heavy image data processing; requires data-intensive computing systems
DEI	Acquisition of absorption- and refraction-based contrast sensitive to small density change. Scatter free; enables higher energy, lower dose Imaging. Suitable for soft and hard tissue imaging. Suitable for thick object imaging *in vivo, ex vivo,* and *in vitro* [77-81]	Does not compensate for USAXS; sensitive to only the vertical components of the refracted beam [37-39]. High sensitivity of the setup to motion, e.g. artifact production by object movement or analyze sensitivity to background physical noise. Requires at least two sets of scans; longer imaging time, patient

		discomfort
DPCI	Large field of view (large sample) imaging. Acquisition of differential phase, USAXS, and absorption contrasts [47]. Use of low-brilliance polychromatic X-ray Sources [16, 45]	Limited angular acceptance of the beam; grating apertures are longer in the X-ray propagation direction than in the vertical direction. Sensitive to vibration as aperture dimensions are very small. Field of view is limited by grating's manufacturing Process [47].
CAXPCI	Use divergent, polychromatic, and commercially available X-ray sources and area detectors; easier transfer to clinical application. Unwanted beams are removed before the beam passes through the sample; lower radiation dose imaging [48-50].	Difficulties with increasing the source-to-detector distance beyond 1 m for clinical systems; challenges with providing the major beam requirement of coherency.
KES-CT	Quantitative and qualitative imaging of very low absorbing or refracting objects (i.e. cells). Identification and quantitative separation of different components of the object, e.g. contrast material, bone, and soft tissues [60].	Reliance on contrast materials; exogenous and risk of cytotoxicity. Requires two sets of scans; longer imaging time, patient discomfort
DFI	No background illumination. Detection of differences in microscopic density fluctuations in soft tissues. Suitable for soft tissue imaging [15, 82, 83]	High radiation dose than inline-PCI and absorption imaging [82].

CAXPCI, coded-aperture phase-contrast imaging; DEI, diffraction-enhanced imaging; DFI, dark field imaging; DPCI, differential phase contrast imaging; KES-CT, K-edge subtraction computed tomography; PC-μCT, phase contrast microcomputed tomography; SR-μCT, synchrotron radiation microcomputed tomography; USAXS, ultra-small-angle X-ray scattering.

2.4.1.1. Diffraction-Enhanced Imaging

Excellent scatter rejection and the ability to separate apparent absorption contrast (vs. extinction contrast) and refraction contrast are advantages of DEI over conventional X-ray imaging methods. As such, researchers have used this method for imaging bone [93], the bone-cartilage interface [94] and BTE applications [70]. Cooper *et al.* successfully used DEI to characterize trabecular bone architecture in human cadaveric radii, forearm, and hand within intact tissues [93]. DEI provided information about boundaries between bone tissues with differing refractive indices: inter-individual differences in trabecular texture, cortical pores, and resorption spaces associated with newly forming osteons. They concluded that DEI may be suitable for the detection of early

changes associated with bone loss [93]. Connor *et al.* report increased contrast for imaging interfaces and contrast-to-noise-ratio gain using DEI compared with SR radiography in their study of interface gaps when titanium pins were implanted into bone defects [95-96]. Similarly, DEI and inline-PCI-CT used as complementary techniques enabled the characterization of osteonecrosis repair [84]. In fact, the image details showed the boundary of the bone graft and the trabecular network (Fig. 2.7) [84]. Although DEI is not a currently prominent characterization technique in BTE, refraction images obtained alongside the apparent absorption images from DEI can provide additional information about the functionality of the constructs and the quality of their integration with host tissues [22].

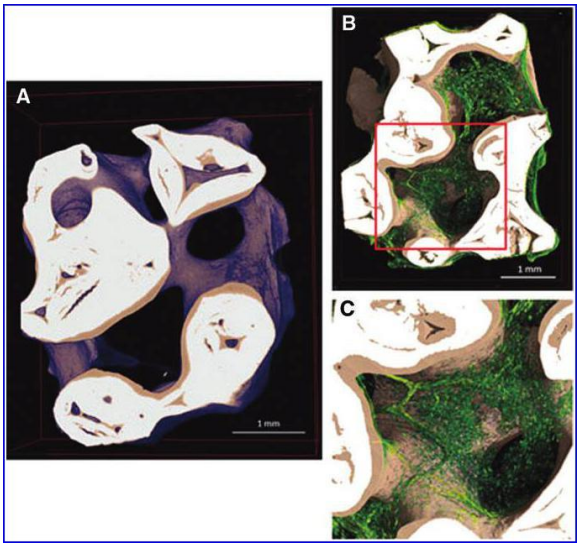

Fig. 2.6: (A) Three-dimensional SR-μCT image showing scaffold material as white and bone ingrowth as brown 24 weeks post-implantation in immu-nodeficient mouse; (B) 3D PC-μCT image showing scaffold material in white, bone ingrowth in brown, and vessel ingrowth in green at 24 weeks post-implantation in immunodeficient mice; and (C) magnified image of identified region in

(B) [79].

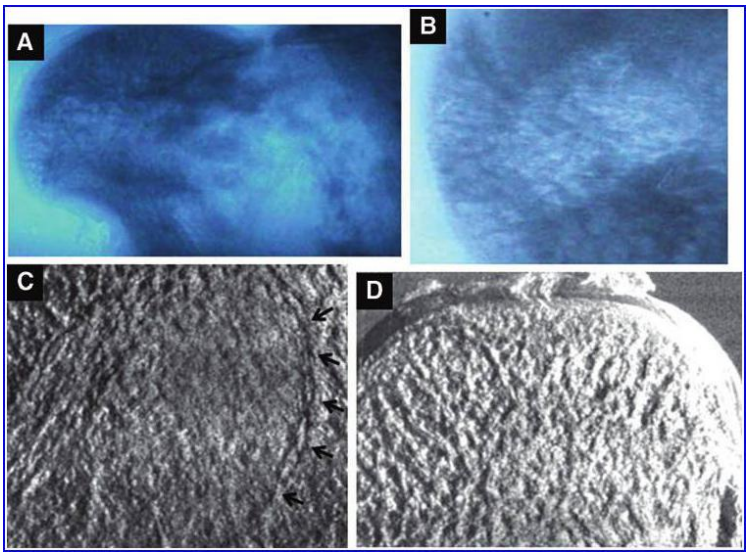

Fig. 2.7: Visualization of tissue engineered osteonecrosis repair using inline-PCI (A, B) and DEI (C, D) as complementary imaging techniques; bone defect re-pair at 8 weeks (A, C) and 12 weeks (B, D) post-operation [84]. Black arrows show the boundary of the bone graft area with sur-rounding tissue.

2.4.1.2. K-Edge Subtraction/K-Edge Subtraction Computed Tomography

Researchers have evaluated KES for applications to mammography, coronary angiography, and cancer cell imaging [53-54, 58-60]. However, the potential of KES (or KES-CT) for TE applications has not been considered. The ability of KES to differentiate between materials with varying attenuation coefficients and isolate these different attenuations makes it attractive for quantitative imaging of bone tissue-engineered scaffolds, possibly new tissue ingrowth, and surrounding bone tissue. Though the method is yet to be investigated for any TE application, including bone, Cooper et al. recently investigated the principle in a rat specimen treated with strontium (Sr) ranelate [60]. They reported that they could trace Sr uptake within the micro-architectural features of vertebrae (Fig. 2.8). Comparison of the Sr map obtained by KES-CT and electron probe microanalysis showed a slightly lower concentration of Sr in the KES-CT (1.36 % to 2 % by mass) data (Fig. 2.8). However, KES-CT is nondestructive and may be preferable regarding preserving the sample and enabling mapping of the bone formed over the dosing period [60]. Although this study was not directed toward BTE, it demonstrates the potential of this method for tracking and enhancing bone growth in BTE using Sr as a contrast agent and North American nutraceutical Sr supplements for osteoporosis [60].

In summary, studies to date show that different SR imaging techniques offer great potential for

BTE applications. They can aid in making advances in current TE studies as well as future extensions of TE studies to longitudinal *in vivo* animal and clinical studies. For live animal imaging, currently available methods should be improved to reveal detailed information about bone ingrowth, scaffold degradation kinetics, and interaction with surrounding tissues at a lower radiation dose. *Ex vivo* BTE imaging would be highly valuable for optimization of scaffold properties and design to better repair bone damage. However, determining the appropriate trade-offs to positively contribute to the advancement of these techniques toward safe and long-term characterization in BTE for *in vivo* studies is crucial.

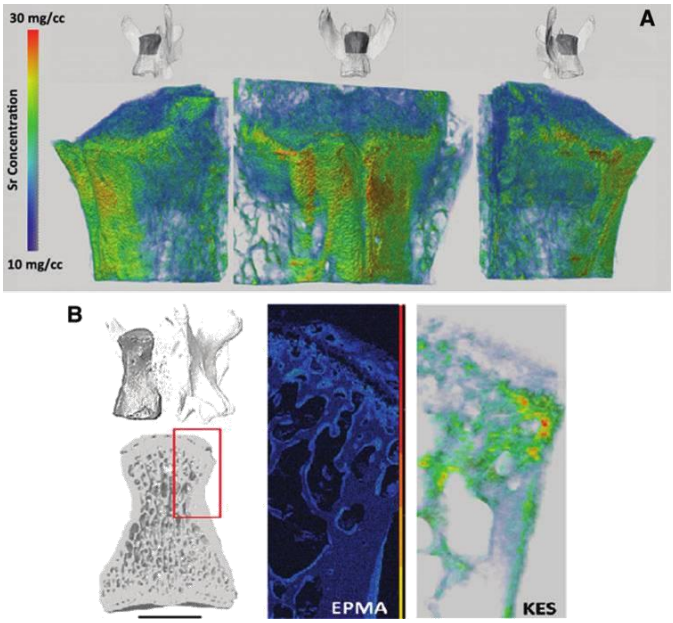

Fig. 2.8: (A) Volumetric 3D KES images showing the uptake of Sr and the trabecular, cortical, and periosteal bone remodeling/growth; (B) magnified image of identified region used for comparison of the distribution of Sr by KES and electron probe microanalysis (EPMA) [60].

2.4.2 Potential Applications to Cartilage TE

The high-water content and low density of cartilage tissue produces negligible X-ray attenuations that limit its visualization using conventional absorption-based X-ray imaging techniques [6, 68]. MRI is commonly used to examine cartilage and to identify damage and loss of tissue without contrast media [6]. Nevertheless, the poor spatial resolution of MRI and inability to resolve specific tissue types when compared with synchrotron-based techniques is the bottleneck of this modality [6, 34]. Synchrotron imaging techniques were initially investigated due to the demand for superior imaging techniques for early and accurate diagnosis of cartilage damage and disease, such as the detection of osteoarthritis (OA) in its early stages. As such, most studies

in the literature have concentrated on synchrotron imaging techniques for the visualization and characterization of healthy and damaged / diseased cartilage tissue as well as the cartilage–bone interface. A review of these studies, in addition to the few studies that investigated techniques for cartilage TE, will inform and provide a better understanding about the potential and limitations of these techniques for cartilage TE applications.

2.4.2.1. Inline-PCI (and PC-µCT)

The simplicity of implementation, provision of outstanding contrast of less dense samples without the use of contrast agents, and edge enhancement are notable advantages of inline-PCI. Inline-PCI is a powerful tool for characterization of the cell-scaffold matrix, new tissue ingrowth, and bone–cartilage interface where the refractive indices vary greatly [6, 25, 28]. The combination of inline-PCI with either CT or µCT has been studied for 3D visualization of articular cartilage [6, 17]. One such study, conducted by Ismail and colleagues, used a bench-top microfocus X-ray source with polychromatic, incoherent X-rays as well as synchrotron coherent X-rays to examine the cartilage–bone interface and different zones of cartilage [6]. They recorded edge enhancement, especially using synchrotron X-rays, which was sufficient to visualize low density cartilage and the cartilage–bone interface with transitional zones from the articulating surface down to subchondral bone [6]. In a similar study, Zehbe *et al.* [85] used PC-µCT for 3D qualitative and quantitative characterization of articular cartilage; the 3D rendered images revealed information which was superior to that obtained from conventional serial histology (Fig. 2.9). Using the 3D images, various tissues under physiological and pathological conditions were differentiated. In addition, tissue structure and cellular level changes, such as spatial cell density and the shape and orientation of the lacunae inside the soft tissues, were quantified without destruction of the tissues [85]. Using high-resolution PCI, Choi *et al.* [89] characterized the microstructural features of healthy cartilage as well as inflammatory and pathological changes in the arthritic joint of mice *in vivo*, also showing results comparable to those of micro-CT or histological analysis.

2.4.2.2. Synchrotron Radiation Microcomputed Tomography

Tissue-engineered scaffolds have also been characterized using SR X-ray imaging techniques [85-87, 97-98]. In studies using SR-µCT, a quantitative description and information about the scaffold microstructure and/or cell clusters in culture or in 3D scaffolds were obtained. Due to the light element constituents of cells (water), contrast agent staining, that is, Au-lysine and silver enhancer, were used to increase the contrast between cells and the surrounding medium in

absorption-based imaging [98]. In a similar manner, using SR-µCT yielded good results regarding the visualization of chondrocytes embedded in a porous gelatin scaffold and physical properties of the scaffold including porosity, surface area, circulation, and pore directionality (width and height of pores) [88]. Although most reported studies concentrate on *in vitro* examinations, the techniques and ideas used may be extrapolated to the visualization of tissue-engineered repair in exercised tissue samples and future *in vivo* applications. Like BTE, SR-µCT is more applicable to high resolution, detailed *ex vivo* investigations of tissue-engineered scaffolds and constructs, which are used to evaluate excised scaffolds or tissue constructs for improving TE strategies.

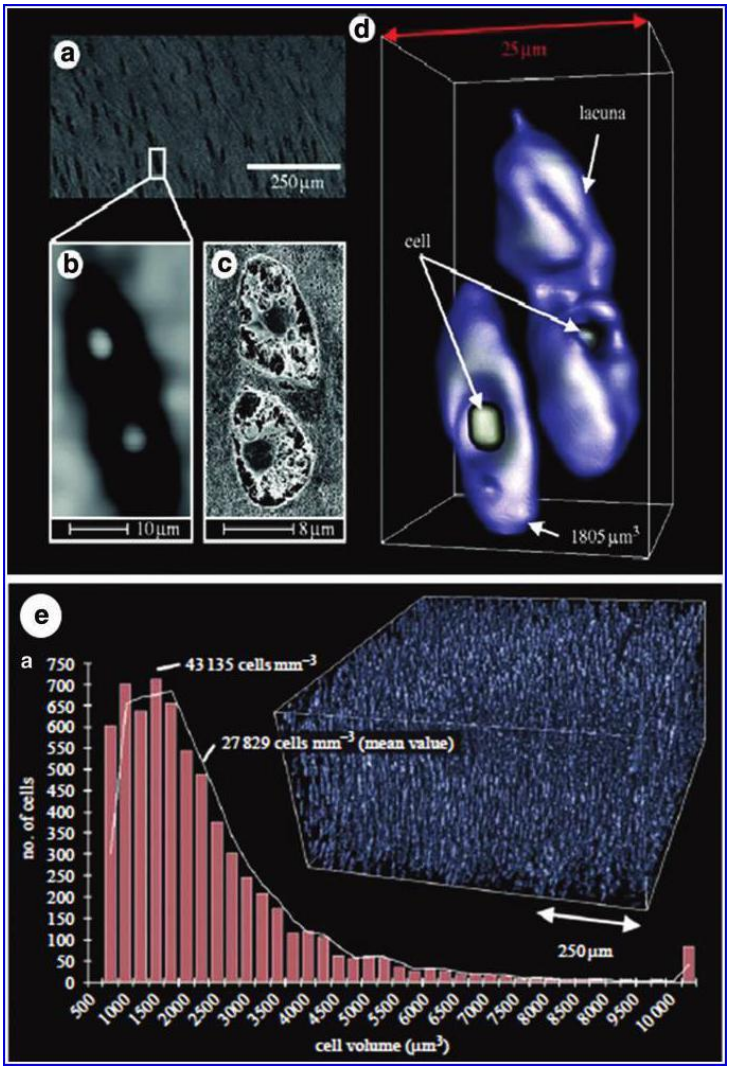

Fig. 2.9: Images showing cellular in-formation from the frontal lacuna in the soft tissue of an articular cartilage (a) original scanning electron micro-scope image from histological tissue; (b) region of interest containing lacuna doublet with chondrocytes in the centers from histological tissue; (c) similar sliced image data from inline-PC-µCT; (d) 3D rendering of (c); and (e) quantitative analysis of cell density from inline-PC-µCT (adapted from Zehbe *et al*. [85]).

2.4.2.3. X-ray Interferometry

X-ray interferometry is commonly used for characterizing variations in micro-calcifications, fat, blood vessels, and soft tissues. It has been reported to be beneficial for the early detection of breast cancer, colon cancer, necrosis, and kidney disease [13, 29]. X-ray interferometry is suitable for deciphering minute variations in densities within less dense soft tissues such as cartilage [77, 108]. While little is known about the application of X- ray interferometry to cartilage TE, this method has great potential for TE applications, especially for the delineation of variations in soft tissues resulting from new tissue growth. However, the heat radiated from the body can de-form the interferometer, as samples are typically placed close to the crystal lamellae [28]. In addition, this method may be unsuitable for resolving objects with sharp soft-hard tissue structural boundaries with a large refractive index difference, such as the bone–cartilage interface or implant-host interface [28]. The good news is that researchers have continued to explore the method and have recently reported some progress [108].

2.4.2.4. Diffraction-Enhanced Imaging

DEI is capable of scatter rejection, is sensitive to density differences in tissues, can be optimized through varying the analyzer angular setting without increasing the radiation dose, and provides multiple types of information such as absorption, refraction, and extinction images [99]. Hence, this method is promising for the 3D characterization of microstructural properties of regions with varying densities, especially in low X-ray absorbing materials such as native and tissue-engineered cartilage. DEI has been used to visualize cartilage tissue with appreciable structural detail in both *ex vivo* [77-79] and *in situ* samples [17, 80-81]. High levels of detail in the cartilage structure, such as the structural organization of collagen fiber bundles within the articular cartilage, have been revealed using a DEI system [98]. Issever *et al.* reported the visualization of cartilage matrix, including changes in hypodensities that were strongly hypothesized to be chondrocyte lacunes [77]. Similarly, Wagner *et al.* used color-coding DEI to explore the internal structure of healthy and pathological joints. In their study, a comparison of DEI with MRI showed that the same level of structural detail may be revealed by MRI but only after a much-prolonged exposure which might not be practical with a patient [79]. Muehleman *et al.* differentiated stages of a cartilage lesion from a normal state to a down-to-bone erosion state in intact canine joints *in situ* using a DEI system [80].

The high spatial resolution combined with the refraction-based mechanism of DEI enabled

visualization of early-stage cartilage degeneration and defects in intact human knee and ankle joints *in situ* [80]. These results were further confirmed by histological and gross analysis.[81] AB-PCI was also used for the characterization of osteoarthritic and normal cartilage matrices both *ex vivo* and *in vivo* [40, 91-92]. In fact, the investigated technique enabled quantitative and qualitative characterization of the zonal pattern in the cartilage matrix, zonal thicknesses, chondrocyte homogeneity and alignment, and matrix fibrillation (Fig. 2.10 B, C) [91]. Coan *et al.* tested this imaging modality on *in vivo* samples and observed a high level of contrast for depicting anatomic structural details and pathological features of an osteoarthritic articular joint [92]. Similarly, Li *et al.* imaged intact human knee and obtained structural details such as cartilage tissue, cruciate ligaments, loose connective tissue, menisci, and chondrocalcinosis (Fig. 2.10 A) [40].

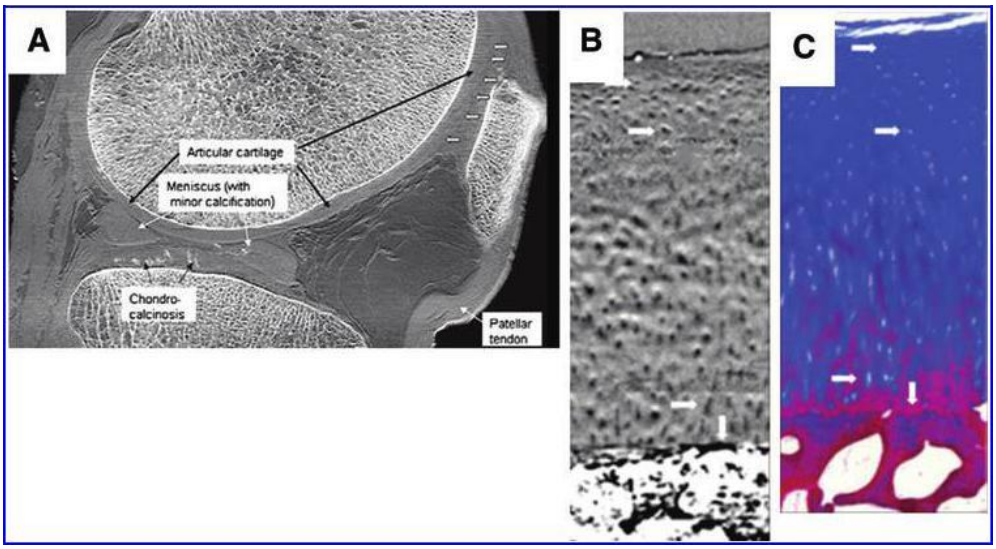

Fig. 2.10: (A) AB imaging of cadaveric human knee joint showing enhanced contrast imaging of soft tissues and bone with structural de-tails *in situ* [40] and (B) AB-CT imaging of cartilage specimen ex vivo, with zonal structural detail comparable to (C) histological analysis [91]. Arrows in B, C are pointing at the same locations in both images to compare visibility of minute details.

Researchers have conducted extensive studies in cartilage imaging and diagnosis of cartilage disease using DEI and ABI. However, very few studies have explored the potential of DEI and ABI for characterization in cartilage TE. DEI-CT has proven to be ideal for visualizing thick TE sections and samples with varying densities and tissue types, such as scaffolds, OA affected cartilage, and newly regenerated tissue. In a recent study, Izadifar *et al.* characterized TE scaffolds implanted in the knee cartilage of a piglet joint using DEI-CT, inline-PCI-CT, and MRI [17]. The results demonstrate the superiority of DEI-CT over inline-PCI-CT and MRI (Fig. 2.11 A-C) for imaging TE scaffolds *in situ*. The results also show that DEI-CT could effectively

delineate the cartilage microstructures and track the scaffolds and different soft tissues surrounding the joint better than the other two methods (Fig. 2.11 D) [17]. In a similar study by Zhu *et al.*, DEI was compared with laboratory-based radiography, SR-radiography, and inline-PCI at the same energy [18]. Their results show that DEI offered better structural and microstructural quantification of soft tissues over the other three methods because of its ability to reject X-ray scatter [18]. DEI and ABI are not only capable of providing information about cartilage, bone, and scaffolds present in the joints, but may also offer supportive information about surrounding tissues such as tendons, ligaments, adipose pads, and skin [17, 40]. DEI image quality may be enhanced without changing the resolution but rather by changing positions on the RC. In addition, DEI produces absorption, extinction, and refraction contrasts that translate into more information than what is obtainable from normal absorption-based imaging. Thus, DEI can facilitate noninvasive *in vivo* studies of 3D tissue-engineered constructs, cartilage ingrowth into the constructs, and surrounding hard and soft tissues in living animal models, and thus demonstrates potential for future clinical studies.

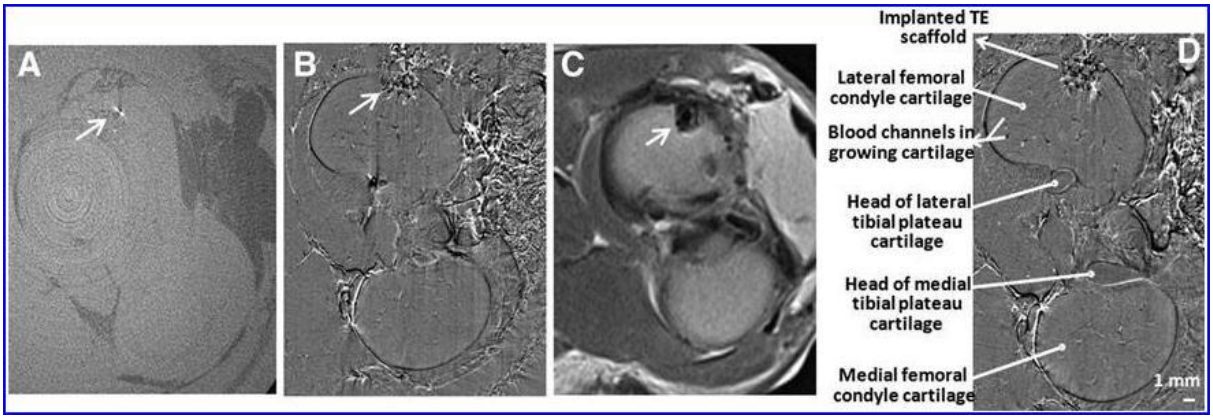

Fig. 2.11: Images of scaffolds implanted in the lateral femoral cartilage of a piglet stifle joint, with arrows showing the position of the scaffolds: (A) inline-phase-contrast CT acquired at 37 mm; (B) DEI-CT acquired at 37 mm; and (C) magnetic resonance imaging acquired at 310 mm. (D) Tissues visible in the DEI images [17].

2.4.2.5. Dark-Feld Imaging

DFI with an asymmetric-cut monochromator with Bragg geometry and a Laue-case analyzer crystal has also been investigated for cartilage visualization. The absence of background illumination caused by non-refracted X-rays, its simplicity when compared with DEI, and its single exposure imaging capability enables DFI to be used to obtain higher refraction-based image contrast and minute details of soft tissues such as cartilages [15, 41-43, 82-83]. Ando *et al.* examined the morphology of articular cartilage at a femoral head and a shoulder in a human cadaver under simulated clinical imaging conditions using DFI and ordinary X-ray absorption

imaging [82]. Their results (Fig. 2.12 a, b) obtained using DFI clearly depict the cartilage region better than an ordinary absorption X-ray image. Interestingly, they concluded that DFI possesses clinical potential for accurate assessment of articular cartilage and associated disorders [82]. Despite little being known about the use of DFI for TE applications, its single exposure imaging principle, clinical potential, and ability to simultaneously image both cartilage and subchondral bone demonstrate promise for TE applications involving many tissue types. Useful imaging specifications and parameters employed in the earlier studies for imaging cartilage and bone tissues and /or engineered constructs are summarized in Table 2.2 for interested readers.

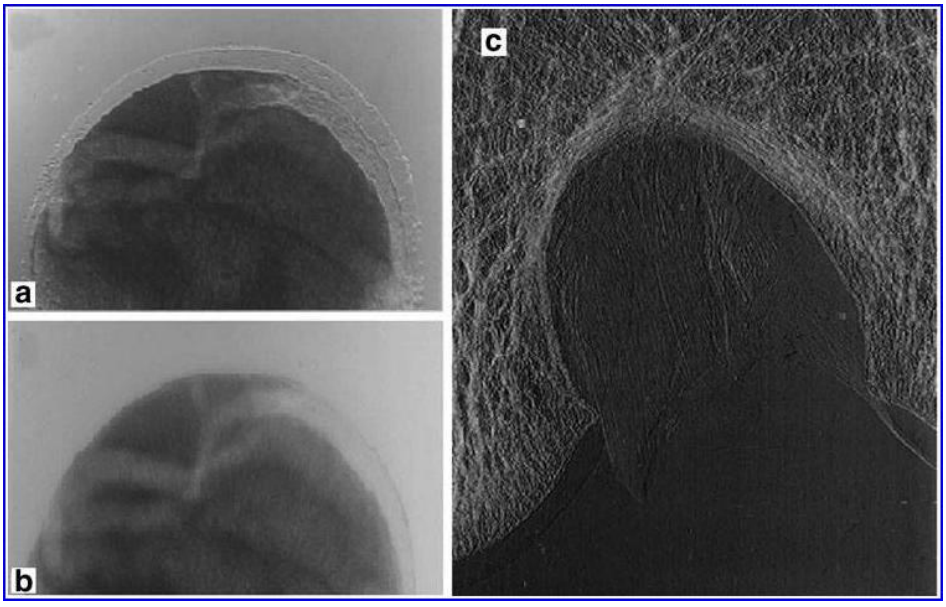

Fig. 2.12: (a) DFI image clearly showing the articular cartilage of a human femur joint immersed in water to mimic clinical conditions; (b) ordinary X-ray absorption image of the same femur joint; and (c) image of the distal end of a human femur immersed in formalin clearly showing the articular cartilage and femoral condyle [82].

2.5. Research Issues and Future Directions

The inherent advantages of a synchrotron light source help overcome numerous intrinsic limitations of conventional imaging systems, such as poor spatial resolution, soft tissue contrast deficiency, X-ray filtration, high absorbed dose, several modality-specific artifacts, and so on [7, 64]. Enhancing the capability of SR-based imaging techniques to effectively visualize scaffolds designed to aid tissue regeneration *ex vivo* and to enable progressive monitoring of the associated growth and construct degradation kinetics in living animals is a necessity. In the next section, we discuss issues and areas that require further development to make SR-based techniques effective for TE applications.

2.5.1. Contrast Media as Sensitivity Enhancer

The use of staining or contrast-enhanced media for enhancement of *in vivo* 3D visualization of tissues and cells architecture has been investigated with CT and MRI for angiography, mammography, and TE applications [101 - 102]. Due to its tunability (i.e., ability to select precise energies above and below the absorption edge of the contrast media of interest), contrast-enhanced KES may offer enhanced sensitivity for visualization and quantification of the complex 3D morphology and microarchitecture of soft and hard tissues. The effectiveness of KES has been evaluated for applications to mammography, coronary angiography, and cancer cell imaging [52, 57, 59]. However, the potential of KES (or KES-CT) for TE applications has not been considered.

Labeling scaffolds or cells with bioinert contrast media with a K-edge energy in the range used in SR-biomedical imaging may improve the sensitivity for tracking cells, new tissue growth, and scaffold degradation kinetics. In some cases, contrast agents may also exert beneficial biochemical effects that may enhance cellular activity. For instance, both Sr- and barium-based materials have been studied as contrast media for KES. Interestingly, they have also been re-ported to influence cellular activity, material dissolution rate, bone remodeling, and provision of non-bridging oxy-gen that may optimize new tissue growth [60, 102-103]. Un-fortunately, Cooper *et al.* noted that the relatively low K-edge of Sr (16.105 keV) may be a limitation, as this energy is lower than for most biomedical imaging methods [60].

The use of GNPs as a contrast media to enhance SR-μCT has also been considered [73-74]. Astolfo *et al*. report that the presence of GNPs facilitates a reduction in spatial resolution while maintaining the ability to localize the area of interest with acceptable image quality [74]. Functionalized GNPs have also been reported to promote cell attachment, which is beneficial to TE applications [103].

2.5.2. Combining Synchrotron Techniques

To optimize the properties of constructs used in bone and cartilage TE, researchers often examine the functionality of their constructs in animal models. Even though longitudinal progressive monitoring of the functionality of the constructs is most desirable, they usually characterize the tis-sue ingrowth and properties of the implanted construct *ex vivo*. One of the prevalent techniques for examining excised samples is 2D SEM analysis [67]. SR techniques have different and interesting properties that may provide 3D cellular-level details in a manner comparable to SEM [67]. For example, inline-PCI has a faster acquisition time, a simpler setup,

and can offer nondestructive details of thin soft tissues [66]. DEI can effectively delineate thick samples with regions containing varying densities, including soft and hard tissues, and provide refraction, absorption, and extinction contrasts [17]. Contrast-enhanced KES-CT or three-energy KES may improve sensitivity and enable characterization of construct degradation kinetics or tissue ingrowth. This may consequently enable effective delineation of the source of the newly growing tissues, that is, if they are from the host tissues or introduced labelled cells. Based on the capabilities of the different methods and the information obtainable, these methods can be combined for quantitative and qualitative examination of excised samples. Complementary use of DEI and inline-PCI-CT has been used to enable characterization of osteonecrosis repair [84]. Although using two SR-based imaging methods may provide more information about construct performance and the quality of integration of constructs with host tissues, this is only advisable for excised samples due to radiation dose and long exposure times posing risks to live animals and humans. However, the use of a source with a high flux and brightness, as discussed next, may serve to significantly reduce these concerns [12].

2.5.3. Toward Laboratory and Clinical Applications of Synchrotron Techniques in TE

Despite synchrotron light's interesting advantages, the scarcity of sources, their unavailability for routine clinical use, high costs, and associated complex instrumentation are challenges for researchers [48]. Researchers have engaged in the development of lab-based microfocus X-ray sources that have excellent sensitivity and increased contrast-to-noise ratio and which are suitable for clinical and biomedical applications [16, 45-49, 105]. Wilkins and colleagues reported one of the earliest implementations of lab-based inline-PCI [24], and successful implementations have since then been re-ported by many others [105-106]. Researchers have also developed DPCI with a conventional X-ray source and imaging detector [45-47, 107]. Furthermore, research regarding CAXPCI has focused primarily on the use of conventional X-ray sources and area detectors for laboratory or clinical PCI [48 - 50]. Though massive efforts have been directed toward the development of clinical PCI, to the best of the authors' knowledge, this progress is still best described as ''moving towards,'' and we look forward to commercialization of such systems [107]. Challenges that have limited the clinical implementation of PCI include beam-hardening artifacts and differential phase clipping [106, 109]. Furthermore, the gantry of clinically used X-ray imaging systems cannot practically be lengthened beyond 1 meter; however,

a longer source-to-detector distance is important for effective phase contrast [49]. The trade-off between image quality, exposure time, and absorbed dose is also a factor to be carefully considered for the clinical use of PCI methods [48].

2.5.4. Influence of Synchrotron Source

Flux and brilliance are the major markers of X-ray beam quality and vary from one synchrotron facility to another. The use of high-energy and high-brilliance sources generates a range of X-rays that comprise a hard and highly penetrating beam which is critical for biomedical imaging [12, 109]. For progression to higher brightness, insertion devices such as a wiggler or undulator with the capability to optimize brilliance (number of photons / second / solid angle bandwidth) by many orders of magnitude when compared with bending magnets may be used [12]. These increments in brightness mostly depend on the electron beam size, angular distribution, or excursion angle and may notably de-crease the exposure time and dose used for experiments [12]. Hence, the use of insertion devices to boost brightness will facilitate the use of synchrotron sources for imaging live animals and possibly humans, optimize image quality, and reduce the exposure time and dose [12, 109].

Table 2.2: Summary of imaging parameters used for synchrotron radiation-based imaging of engineered constructs or bone and cartilage tissues

Technique	**X-ray source / Imaging Energy**	**Sample condition**	**Spatial resolution (µm)**	**Field of view**	**Exposure time**	**Dose rate**	**References**	**Segmentation / 3D rendering**
SR-µCT	Synchrotron / 9–27 keV	Excised: fresh / freeze-dried	1.4–5	2–10 mm	0.7–3 s		[66, 67, 70, 74, 85-88]	Histogram-, Gaussian-, intensity-, threshold-based segmentation
Inline-PCI	Benchtop (X-ray tube) / 7-40 keV	Excised: thin sections	13		1 min		[6]	3Drendering: OsiriX v. 3.0, VGStudio MAX v. 1.2.1,

								AMIRA 5.2, ImageJ
Inline-PCI	Synchrotron /7-40 keV	Excised: fresh / *in vivo*	1.48–37	1.18–4 X 0.89 - 74 mm^2	25 ms–2.5 s	1.6–3 Gy/s	[6, 17, 89]	Histogram-based segmentation; 3D rendering: Avizo
DEI-CT	Synchrotron / 17 - 50 keV	Excised: fresh / fixed	3.6–50	4 mm (vertical) x 74 mm	3.5–7 s	0.8 - 3 Gy (total); 0.01–0.34 mGy/s	[17, 77-79, 81, 90]	Histogram-based segmentation; 3D rendering: Avizo
AB-PCI	Synchrotron / 26-52 keV	Excosed: fixed / *in vivo*	8–47	9 x 9 cm^2	0.5 s-planar imaging; 67 ms/ projection	20 mGy–0.2 Gy (total); 0.3 mGy/s	[91, 92]	

AB-PCI, analyzer-based phase-contrast imaging; 3D, three-dimensional.

2.6. Conclusions

This review reports on technological developments, ad-vantages, applications, and the potential of SR-based X-ray imaging techniques for bone and cartilage TE. SR-based imaging techniques are evolving as robust assessment techniques for TE as well as biomedical applications, in general, and could offer advantages over currently used evaluation techniques. For the high spatial resolution and quantitative imaging required for the characterization of engineered scaffolds and tissue growth *ex vivo* and *in vitro*, this review suggests exploring high-resolution SR-based imaging methods or combining different but complementary SR-based techniques. Using SR-based methods for the characterization of engineered scaffolds and tissue growth *in vivo* requires strategic adaptations or trade-offs; for example, enabling the acquisition of acceptable image quality at reduced radiation dose. In this regard, nanoparticles can be employed as contrast agents, the photon flux and brilliance can be increased, and the employed imaging technique can

be modified, such as is done in AB-PCI compared with standard DEI. Although the use of SR-based imaging techniques is not yet as prevalent in TE as in biomedical imaging, representative examples of biomedical imaging applications of SR-based techniques are promising. The results from these works can be extrapolated to TE and used as a guide for tissue engineers regarding choosing the right technique to suit their specific applications.

2.7. Acknowledgments

This work was supported by grants from the Saskatchewan Health Research Foundation (SHRF) and the Natural Sciences and Engineering Research Council of Canada (NSERC).

2.8. Disclosure Statement

The authors hereby declare that neither competing financial interests nor conflicts of interest exist.

2.9. References

1. Xu H, Othman SF, and Magin RL. (2008). “Monitoring tissue engineering using magnetic resonance imaging”. *J Biosci Bioeng,* 106 (6), 515-527.
2. Cancedda R, Cedola A, Giuliani A, Komlev V, Lagomarsino S, Mastrogiacomo M, Peyrin F, Rustichelli F. (2007). “Bulk and inter-face investigations of scaffolds and tissue-engineered bones by X-ray microtomography and X-ray micro-diffraction”. *Biomaterials,* 28 (15), 2505-2524.
3. Marvel S, Okrasinski S, Bernacki SH, Loboa E and Dayton PA. (2009). Applications of low intensity pulsed ultrasound for functional bone tissue engineering using adult stem cells. *Ultrasonics Symposium (IUS),* 2009 IEEE International, 357.
4. Potter K, Sweet DE, Anderson P, Davis GR, Isogai N, Asamura S, Kusuhara H, Landis WJ. 2006. “Non-destructive studies of tissue-engineered phalanges by magnetic resonance microscopy and X-ray microtomography”. *Bone*, 38 (3), 350-8.
5. Ma L, Gao C, Mao Z, Zhou J, Shen J, Hu X, and Han C. (2003). “Collagen/chitosan porous scaffolds with improved biostability for skin tissue engineering”. *Biomaterials.,* 24(26):4833-41
6. Ismail EC, Kaabar W, Garrity D, Gundogdu O, Bunk O, Pfeiffer F, Farquharson MJ, and Bradley DA. (2010). “X-ray phase contrast imaging of the bone–cartilage interface”. *Appl Radiat Isot* 68 (4-5), 767–771.
7. Kowalski J, Kwan HH, Prionas SD, Allision AC, and Fajardo LF. (1992). “Characterization and applications of the disc angiogenesis system”. *Exp Mol Pathol.,* 56 (1), 1-19.
8. Guldberg RE, Duvall CL, Peister A, Oest ME, Lin ASP, Palmer AW, and Levenston ME. (2008). “3D imaging of tissue integration with porous biomaterials”. *Biomaterials* 29(28):3757-61.
9. Khan, A.N. (2015, December, 30) “Imaging of meniscus abnormalities in the temporomandibular joint: overview”. Retrieved August 02, 2016 from http:// emedicine.medscape.com/article/385129-overview.
10. Zhu N, Chen XB, and Chapman D. (2010). “A brief review of visualization for nerve tissue engineering applications”. *Biomimetrics Biomater Tissue Eng.* 7, 81-99.
11. Hendee WR, Cleary K, Ehman RL, Fullerton GD, Grundfest WS, Haller J, Kelley CA, Meyer AE, Murphy RF, Phillips W, Torchilin VP. (2008). “Bioengineering and imaging re-search opportunities workshop V: summary of findings on imaging and characterizing structure and function in native and engineered tissues”. *Radiology.* 248 (2),342-7.
12. Chapman LD. (2013, January). Health research using synchrotron techniques. Lecture on

synchrotron radiation basics [Power-Point slides]. *Division of Biomedical Engineering University of Saskatchewan, course tools Blackboard*. Retrieved on June 23, 2013 from https://bblearn.usask.ca.

13. Takeda T, Momose A, Wu J, Yu Q, Zeniya T, Lwin TT, Yoneyama A, and Itai Y. (2002). "Vessel imaging by interferometric phase-contrast x-ray technique". *Circulation* 105 (14), 1708-12.
14. Chapman D, Thomlinson W, Johnston RE, Washburn D, Pisano E, Gmür N, Zhong Z, Menk R, Arfelli F, Sayers D. (1997). "Diffraction enhanced X-ray imaging". *Phys Med Biol* 42 (11), 2015-25.
15. Kunisada T, Shimao D, Sugiyama H, Takeda K, Ozaki T, and Ando M. (2008). "X-ray dark field imaging of human articular cartilage: possible clinical application to orthopedic surgery". *Eur J Radiol.,* 68, (3S), S18-21.
16. Pfeiffer, F., Weitkamp, T., Bunk, O., and David, C. (2006). "Phase retrieval and differential phase-contrast imaging with low brilliance X-ray sources". *Nat Phys.* 2, 258 - 261.
17. Izadifar Z, Chapman D, and Chen D. (2014). "Computed tomography diffraction enhanced imaging for *in situ* visualization of tissue scaffolds implanted in cartilage". *Tissue Eng Part C* Methods 20 (2), 140-8
18. Zhu N, Chapman D, Cooper D, Schreyer DJ, and Chen X. (2011). "X-ray diffraction enhanced imaging as a novel method to visualize low-density scaffolds in soft tissue engineering". *Tissue Eng Part C Methods.* 17 (11), 1071-80.
19. Gao D, Pogany A, Stevenson AW, and Wilkins SW. (1998). "Phase-contrast radiography". *Radiographics.* 18 (5), 1257-6.
20. Greaves AN. (2010). "Phase Contrast in X-rays Imaging [Doctoral thesis]". *Swinburne University of Technology, Melbourne, Australia*.
21. Zernike F. (1955). "Nobel lecture: how I discovered phase contrast". *Science, New Series*. 121 (3141), 345-349.
22. Appel, A, Anastasio MA, and Brey EM. (2011). "Potential for imaging engineered tissues with X-ray phase contrast". *Tissue Eng Part B Rev.* 17 (5), 321-30.
23. Gabor D. (1948). A new microscopic principle. *Nature* 1 161, 777-778.
24. Wilkins SW, Gureyev TE, Gao D, Pogany A, and Stevenson AW. (1996). "Phase-contrast imaging using polychromatic hard X-rays". *Nature*. 384, 335 - 338.
25. Spanne P, Raven C, Snigireva I, and Snigirev A. (1999). "In-line holography and phase-contrast

microtomography with high energy x-rays". *Phys Med Biol.* 44 (3), 741-9.

26. Krol, A. (2011). "In-line hard X-ray holography for biomedical imaging". In: Rosen, J., ed. Holography, Research and Technologies. Rijeka, Croatia: Intech.
27. Kieffer JC, Krol A, Jiang Z, Chamberlain CC, Scalzetti E, and Ichalalene Z. (2002). "Future of laser-based X-ray sources for medical imaging". *J Appl Phys. B* 74, S s75–s81.
28. Zhou SA and Brahme A. (2008). "Development of phase-contrast x-ray imaging techniques and potential medical applications". *Phys Med.* 24 (3), 129-48.
29. Bonse U and Hart M. (1966). "An X-ray interferometer with Bragg case beam splitting and beam recombination". *Z Phys* 194, 1–17.
30. Yoneyama A, Yamada S and Takeda T. (2011). "Fine bio-medical imaging using X-ray phase-sensitive technique". In: Gargiulo, G.D., and McEwan, A. (Eds). Advanced Bio-medical Engineering. Rijeka, Croatia: Intech.
31. Grubel G, Stephenson G.B, Gutt C, Sinn H and Tschentsche, T. (2007). "XPCS at the European X-ray free electron laser facility". *Nucl Instrum Methods Phys Res.* B262, 357–367.
32. Momose A. (2002). "Phase-contrast X-ray imaging based on interferometry". *J Synchrotron Radiat.* 9, 136-142.
33. Ingal VN and Beliaevskaya EA. (1995). "X-ray plane-wave topography observation of the phase contrast from a non-crystalline object". *J Phys D Appl Phys.* 28 (11), 2314-2317.
34. Davi, TJ, Gao D, Gureyev TE, Stevenson AW, and Wilkins SW. (1995). "Phase-contrast imaging of weakly absorbing materials using hard X-rays". *Nature.* 373, 595 – 598.
35. Zhong Z, Thomlinson W, Chapman D, and Sayers D. (2000). "Implementation of diffraction-enhanced imaging experiments at the NSLS and APS". *Nucl Instrum Methods Phys Res.* 450 (2-3), 556–567.
36. Hasnah MO, Zhong Z, Oltulu, O, Pisano E., Johanston RE, Sayers D, et al. Diffraction enhanced imaging contrast mechanisms in breast cancer specimens. *Med Phys.* 29 (10), 2216-21.
37. Rigon L, Arfelli F and Menk RH. (2007). "Three-image diffraction enhanced imaging algorithm to extract absorption, refraction, and ultrasmall-angle scattering". *Appl Phys Lett.* 90, 14102.
38. Chou CY, Anastasio MA, Brankov JG, Wernick, MN, Brey EM, Connor DM, and Zhong Z. (2007). "An extended diffraction-enhanced imaging method for implementing multiple-image radiography". *Phys Med Biol.* 52 (7), 1923-45.
39. Khelashvili G, Brankov JG, Chapman D, Anastasio MA, Yang Y, Zhong Z and Wernick MN.

(2006). “A physical model of multiple-image radiography”. *Phys Med Biol.* 51(2):221-36.

40. Li J, Zhong Z, Connor D, Mollenhauer J and Muehleman C. (2009). “Phase-sensitive X-ray imaging of synovial joints”. *Osteoarthritis Cartilage*. 17 (9), 1193-6.
41. Sunaguchi N, Yuasa T, Huo Q, Ichihara S and Ando M. (2010). “X-ray refraction-contrast computed tomography images using dark-field imaging optics”. *Appl Phys Lett.* 97, 153701.
42. Revol V, Plank B, Kaufmann R, Kastner J, Kottler C, and Neels A. (2013). “Laminate fibre structure characterisation of carbon fibre-reinforced polymers by X-ray scatter dark-field imaging with a grating interferometer”. *NDT&E Int.* 58, 64–71.
43. Pfeiffer F, Bech M, Bunk O, Kraft P, Eikenberry EF., Bro¨nnimann C, Gru¨nzweig C, and David C. (2008). “Hard X-ray dark-field imaging using a grating interferometer”. *Nat Mater.* 7, 134 – 137.
44. Li K, Zambelli J, Bevins N, Ge Y, and Chen G.H. (2013). “Spatial resolution characterization of differential phase contrast CT systems via modulation transfer function (MTF) measurements”. *Phys Med Biol.* 58 (12), 4119-35. Stutman D, Beck TJ, Carrino JA, and Bingham CO. (2011). “Talbot phase-contrast x-ray imaging for the small joints of the hand”. *Phys Med Biol.* 56(17):5697-720.
45. Chen GH, Bevins N, Zambelli J, and Qi Z. (2010). “Small-angle scattering computed tomography (SAS-CT) using a Talbot-Lau interferometer and a rotating anode x-ray tube: theory and experiments”. *Opt Express.* 18 (12), 12960-70.
46. Hauser N, Wang Z, Kubik-Huch RA, Trippel M, Singer G, Hohl MK, Roessl E, Köhler T, van Stevendaal U, Wieberneit N, Stampanoni M. “A study on mastectomy samples to evaluate breast imaging quality and potential clinical relevance of differential phase contrast mammography”. *Invest Radiol.* 49 (3), 131-7.
47. Olivo A, and Speller RA. (2007). “Coded-aperture technique allowing x-ray phase contrast imaging with conventional sources”. *Appl Phys Lett.* 91, 074.
48. Munro PRT, Ignatyev K, Speller RD and Olivo A. (2010). “Source size and temporal coherence requirements of coded aperture type x-ray phase contrast imaging systems”. *Opt Express.* 18 (19), 19681–19692.
49. Krejci F, Jakubek J and Kroupa M. (2011). “X-ray phase contrast imaging using single absorption coded aperture”. *Nucl Instrum Methods Phys Res.* A633, S181–S184.
50. Kavanagh A and Vojnovic B. (2011). Phase contrast x-ray imaging. Retrieved on 25 June, 2013

from http://users.ox.ac.uk/ *atdgroup/technicalnotes/Phase%20Constrast%20X-ray %20imaging.pdf.

51. Bewer B, Zhang H, Zhu Y, Zhang L, George GN. Pickering IJ and Chapman D. (2008). "Development of a combined K-edge subtraction and fluorescence subtraction imaging system for small animals". *Rev Sci Instrum.* 79 (8), 085102
52. Jacobson B. (1953). "Dichromatic absorption radiography; dichromography". *Acta Radiol.* 39(6):437-52.
53. Sarnelli A, Taibi A, Tuffanelli A, Baldazzi, G, Bollini D, Cabal Rodriguez AE, Gombia M, Prino F, Ramello L, Tomassi E and Gambaccini M. (2004). "K-edge digital subtraction imaging based on a dichromatic and compact x-ray source". *Phys Med Biol.* 49 (14), 3291-305.
54. Zhong Z, Chapman D, Menk R, Richardson J, Theophanis S and Thomlinson W. (1997). "Monochromatic energy subtraction radiography using a rotating anode source and a bent Laue monochromator". *Phys Med Biol.* 42 (9), 1751-62.
55. Zhu Y. (2012). "Bent Laue Crystals in Biomedical X-ray Imaging Applications [Doctoral dissertation]". *University of Saskatchewan, Saskatoon, Canada.* Retrieved on June 26, 2013, from http:// ecommons.usask.ca/handle/10388/ETD-2012-11-768.
56. Bayat S, Le Duc G, Porra L, Berruyer G, Nemoz C, Monfraix S, Fiedler S, Thomlinson W, Suortti P, Standertskjöld-Nordenstam CG, Sovijärvi AR. (2001). "Quantitative functional lung imaging with synchrotron radiation using inhaled xenon as contrast agent". *Phys Med Biol.* 46 (12), 3287-99.
57. Riederer SJ, Kruger RA and Mistretta CA. (1981). "Three-beam K-edge imaging of iodine using differences between fluoroscopic video images: theoretical considerations". *Med Phys* 8 (4), 471-9. Lewin JM, Isaacs, PK, Vance V and Larke FJ. (2003). "Dual-energy contrast enhanced digital subtraction mammography: feasibility". *Radiology.* 229(1), 261-8.
58. Cooper DM, Chapman LD, Carter Y, Wu Y, Panahifar A, Britz HM, Bewer B, Zhouping W, Duke MJ, Doschak M. (2012). "Three-dimensional mapping of strontium in bone by dual energy K-edge subtraction imaging". *Phys Med Biol.* 57(18), 5777-86.
59. Feldkamp LA, Goldstein SA, Parfitt AM, Jesion G and Kleerekoper M. (1989). "The direct examination of three-dimensional bone architecture *in vitro* by computed tomography". *J Bone Miner Res.* 4 (1), 3-11.
60. Cooper DM, Turinsky A, Sensen C and Hallgrimsson B. (2007). "Effect of voxel size on 3D micro-

CT analysis of cortical bone porosity". *Calcif Tissue Int.* 80 (3), 211-9.

61. Peter ZA and Peyrin F. (2011). "Synchrotron radiation micro-CT imaging of bone tissue". In: Homma, N. (Ed.) Theory and Applications of CT Imaging and Analysis. Rijeka, Croatia: Intech.
62. Stock SR. (2008). "Recent advances in X-ray microtomography applied to materials". *Int Mat Rev*. 53, 129-181.
63. Cooper DML, Erickson, B, Peele AG, Hannah K, Thomas CDL and Clement, J.G. (2011). "Visualization of 3D osteon morphology by synchrotron radiation micro-CT". *J Anat.,* 219 (4), 481-9 Yue S, Lee PD, Poologasundarampillai G, Yao Z, Rockett P, Devlin AH, Mitchell CA, Konerding MA, Jones JR. "Synchrotron X-ray microtomography for assessment of bone tissue scaffolds". *J Mater Sci Mater Med*. 21 (3), 847-53.
64. Peyrin F, Mastrogiacomo M, Cancedda R, and Martinetti, R. (2007). "SEM and 3D Synchrotron radiation microtomography in the study of bioceramic scaffolds for tissue-engineering applications". *Biotechnol Bioeng.* 97 (3), 638-48.
65. Albertini G, Giuliani A, Komlev V, Moroncini F, Pugnaloni A, Pennesi G, Belicchi M, Rubini C, Rustichelli F, Tasso R, Torrente Y. (2009). "Organization of extracellular matrix fibers within polyglycolic acid-polylactic acid scaffolds analyzed using X-ray synchrotron-radiation phase-contrast microcomputed tomography". *Tissue Eng Part C Methods.* 15 (3), 403-11.
66. Zehbe R, Haibel A, Schmidt F, Riesemeier H, Kirkpatrick CJ, Schubert H and Brochhausen C. (2011). "High-resolution x-ray tomography—3D imaging for tissue engineering applications". In: Eberli, D., (ed). Tissue Engineering. Rijeka, Croatia: Intech.
67. Mastrogiacomo M1, Komlev VS, Hausard M, Peyrin F, Turquier F, Casari S, Cedola A, Rustichelli F, Cancedda R. (2004). "Synchrotron radiation microtomography of bone engineered from bone marrow stromal cells". *Tissue Eng.* 10 (11-12), 1767-74.
68. Papadimitropoulos A, Mastrogiacomo M, Peyrin F, Molinari E, Komlev VS, Rustichelli F, and Cancedda R. (2007). "Kinetics of *in vivo* bone deposition by bone marrow stromal cells within a resorbable porous calcium phosphate scaffolds: a X-ray computed microtomography study". *Biotechnol Bioeng.* 98 (1), 271-81.
69. Komlev VS, Peyrin F, Mastrogiacomo M, Cedola A, Papadimitropoulos A, Rustichelli, F and Cancedda R. (2006). "Kinetics of *in vivo* bone deposition by bone marrow stromal cells into porous calcium phosphate scaffolds: an X-ray computed microtomography study". *Tissue Eng.* 98 (1), 271-81.

70. Astolfo A, Arfelli F, Schultke E, James S, Mancinie L, and Menke RH. (2013). "A detailed study of gold-nanoparticle loaded cells using X-ray based techniques for cell-tracking applications with single-cell sensitivity". *Nanoscale.* 5 (8), 3337-45.
71. Astolfo A, Schültke E, Menk RH, Kirch RD, Juurlink BH, Hall C, Harsan LA, Stebel M, Barbetta D, Tromba G, Arfelli F. (2013). "*In vivo* visualization of gold-loaded cells in mice using x-ray computed tomography". *Nanomedicine.* 9 (2), 284-92.
72. Weiss P1, Obadia L, Magne D, Bourges X, Rau C, Weitkamp T, Khairoun I, Bouler JM, Chappard D, Gauthier O, Daculsi G. (2003). "Synchrotron X-ray microtomography (on a micron scale) provides three-dimensional imaging representation of bone ingrowth in calcium phosphate biomaterials". *Biomaterials.* 24 (25), 4591-601
73. Komlev VS, Mastrogiacomo M, Peyrin F, Cancedda R, and Rustichelli F. (2009). "X-ray synchrotron radiation pseudo-holotomography as a new imaging technique to investigate angio- and microvasculogenesis with no usage of contrast agents". *Tissue Eng Part C Methods.* 15 (3), 425-30.
74. Issever AS, Diederichs G, Majumdar S, Rogalla P, Hamm BK, Lange A, Harwardt M, Hentschel MP, Mueller BR. (2008). "Analyser-based tomography images of cartilage". *J Synchrotron Radiat.* 15(5), 525-7
75. Muehleman C, Majumdar S, Issever AS, Arfelli F, Menk RH, Rigon L, Heitner G, Reime B, Metge J, Wagner A, Kuettner KE, Mollenhauer J. (2004). "X-ray detection of structural orientation in human articular cartilage". *Osteoarthritis Cartilage.* 12(2):97-105.
76. Wagner A, Aurich M, Sieber N, Stoessel M, Wetzel WD, Schmuck K, et al. (2005). "Options and limitations of joint cartilage imaging: DEI in comparison to MRI and sonography". *Nucl Inst Methods Phys Res. A* 548 (1-2), 47–53.
77. Muehleman C, Fogarty D, Reinhart B, Tzvetkov T, Li J and Nesch I. (2010). "In-laboratory diffraction-enhanced X-ray imaging for articular cartilage". *Clin Anat.* 23 (5), 530-8.
78. Mollenhauer J, Aurich ME, Zhong Z, Muehleman C, Cole AA, Hasnah M, Oltulu O, Kuettner KE, Margulis A and Chapman LD. (2002) "Diffraction-enhanced X-ray imaging of articular cartilage". *Osteoarthritis Cartilage.* 10 (3), 163-71.
79. Ando M, Hashimoto E, Hashizume H, Hyodo K, Inoue H, Kunisada T, et al. (2005). "Clinical step onward with X-ray dark-field imaging and perspective view of medical applications of synchrotron radiation in Japan". *Nucl Instrum Methods Phys Res. A* 548C (1-2), 1–16.

80. Bech M, Jensen TH, Bunk O, Donath T, David C, Weitkamp T, Le Duc G, Bravin A, Cloetens P, Pfeiffer F. (2010). "Advanced contrast modalities for X-ray radiology: phase-contrast and dark-field imaging using a grating interferometer". *Z Med Phys.* 20 (1), 7-16. Sun W, Li ZR, Yang, YR, Shi ZC, Wang B, Liu B and Shi S. (2011). "Experimental study on phase-contrast imaging with synchrotron hard X-ray for repairing osteonecrosis of the femoral head". *Orthopedics.* 34 (9), e530-4.
81. Zehbe R, Haibel A, Riesemeier H., Gross U, Kirkpatrick CJ, Schubert H and Brochhausen C. (2010). "Going beyond histology: synchrotron μCT as a complementary methodology for biological tissue characterization". *J R Soc Interface.* 7(42): 49–59.
82. Thurner P, Karamuk E and Muller B. (2001). "3D characterization of fibroblast cultures on PET-textiles". *Eur Cell Mater.* 2, 57-58.
83. Muller B., Riedel M and Thurner PJ. (2006). "Three-dimensional characterization of cell clusters using synchrotron-radiation-based micro-computed tomography". *Microsc Microanal,* 12 (2), 97-105.
84. Zehbe R, Geobbels Y, Ibold Y, Gross U, and Schubert H. (2010). "Three-dimensional visualization of *in vitro* cultivated chondrocytes inside porous gelatine scaffolds: a tomographic approach". *Acta Biomater.* 6 (6), 2097–2107.
85. Choi CH, Kim HT, Choe JY, Kim SK, Choi GW, Jheon S, and Kim J.K. (2010). "*In vivo* high-resolution synchrotron radiation imaging of collagen-induced arthritis in a rodent model". *J Synchrotron Radiat.* 17 (3), 393-9.
86. Muehleman C, Li J and Zhong Z. (2006). "Preliminary study on diffraction enhanced radiographic imaging for a canine model of cartilage damage". *Osteoarthritis Cartilage.* 14 (9), 882–888.
87. Coan P, Bamberg F, Diemoz PC, Bravin A, Timpert K, Mützel E, Raya JG, Adam-Neumair S, Reiser MF, Glaser C. (2010). "Characterization of osteoarthritic and normal human patella cartilage by computed tomography X-ray phase-contrast imaging: a feasibility study". *Invest Radiol.* 45 (7), 437-44.
88. Coan P, Wagner A, Bravin A, Diemoz PC, Keyrilainen J and Mollenhauer J. (2010). "*In vivo* x-ray phase contrast analyzer-based imaging for longitudinal osteoarthritis studies in guinea pigs". *Phys Med Biol.* 55 (24), 7649-62.
89. Cooper DM, Bewer B, Wiebe S, Wysokinski TW, and Chapman D. (2011). "Diffraction enhanced X-ray imaging of the distal radius: a novel approach for visualization of trabecular bone

architecture". *Can Assoc Radiol. J* 62 (4), 251–255.

90. Muehleman C, Chapman LD, Kuettner KE, Rieff J, Mollenhauer JA, Massuda K, and Zhong Z. (2003). "Radiography of rabbit articular cartilage with diffraction enhanced imaging". *Anat Rec.* 272 (1), 392-7.
91. Connor DM, Sayers D, Sumner DR and Zhong Z. (2006). "Diffraction enhanced imaging of controlled defects within bone, including bone-metal gaps". *Phys Med Biol.* 51 (12), 3283-300.
92. Connor DM, Hallen HD, Lalush DS, Sumner DR, and Zhong Z. (2009). "Comparison of diffraction-enhanced computed tomography and monochromatic synchrotron radiation computed tomography of human trabecular bone". *Phys Med Biol.* 54 (20), 6123-33.
93. Thurner P, Müller R, Raeber G, Sennhauser U and Hubbel JA. (2005). "3D morphology of cell cultures: a quantitative approach using micrometer synchrotron light tomography". *Microsc Res Tech.* 66 (6), 289-98.
94. Zehbe R, Haibel A, Brochhausen C, Gross U, Kirk-patrick CJ and Schubert H (2007). "Characterization of oriented protein-ceramic and protein-polymer-composites for cartilage tissue engineering using synchrotron μCT". *Int J Mater Res.* 98, 562.
95. Li J, Zhong Z, Lidtke R, Kuettner KE, Peterfy C, Aliyeva E and Muehleman C. (2004). "Radiography of soft tis-sue of the foot and ankle with diffraction enhanced imaging". *J Am Podiatr Med Assoc.* 202 (5), 463–470.
96. Bolland BJRF, Kanczler JM, Ginty PJ, Howdle SM, Shakesheff, KM, Dunlop DG, and Oreffo ROC. (2008). "The application of human bone marrow stromal cells and poly (DL-lactic acid) as a biological bone graft extender in impaction bone grafting". *Biomaterials.* 29 (22), 3221-7
97. Lao J, Nedelec JM and Jallot E. (2009). "New strontium based bioactive glasses: physicochemical reactivity and delivering capability of biologically active dissolution products". *J Mater Chem.* 19, 2940-2949.
98. Kaur G, Sharma P, Kumar V and Singh K. (2012). "Assessment of in-vitro bioactivity of SiO2-BaOZnO-B2O3-Al2O3 glasses: an optico-analytical approach". *Mat Sci Eng. Part C* 32 (7), 1941–1947.
99. Jung D1, Minami I, Patel S, Lee J, Jiang B, Yuan Q, Li L, Kobayashi S, Chen Y, Lee KB, Nakatsuji N. (2012). "Incorporation of functionalized gold nanoparticles into nanofibers for enhanced attachment and differentiation of mammalian cells". J *Nanobiotechnol.* 10, 23
100. Kashyap YS, Yadav PS, Roy T, Sarkar PS, Shukla M and Sinha A. (2008). "Laboratory-

based X-ray phase-contrast imaging technique for material and medical science applications". *Appl Radiat Isot*. 66 (8), 1083-90.

101. Kelly KL and Tanner BK. (2006). "Factors affecting in-line phase contrast imaging with a laboratory microfocus x-ray source". *JCPDS-International Centre for Diffraction Data.* Retrived on July 10, 2013 from www.icdd.com/resources/axa/ vol49/V49_04.pdf .

102. Stampanoni M1, Wang Z, Thüring T, David C, Roessl E, Trippel M, Kubik-Huch RA, Singer G, Hohl MK, Hauser N. (2011). "The first analysis and clinical evaluation of native breast tissue using differential phase-contrast mammography". *Invest Radiol.* 46 (12), 801-6.

103. Bravin A, Coan P and Suortti P. (2013). "X-ray phase-contrast imaging: from pre-clinical applications towards clinics". *Phys Med Biol.* 58(1), R1-35.

104. Tanaka J, Nagashima M, Kido K, Hoshino Y, Kiyohara J, Makifuchi C, Nishino, S, Nagatsuka S and Momose, A. (2013). "Cadaveric and *in vivo* human joint imaging based on differential phase contrast by X-ray Talbot-Lau interferometry". *Z Med Phys.* 23 (3), 222-7.

105. Argonne National Laboratory. The advanced photon source (APS) overview: Insertion devices and brilliance. Retrieved on July 10, 2013, from www.aps.anl.gov/About/APS_Overview/ insertion_devices.html.

Chapter 3: Using Synchrotron Radiation Inline-Phase-Contrast Imaging Computed Tomography to Visualize Three-Dimensional Printed Hybrid Constructs for Cartilage Tissue Engineering

This chapter was adopted from the publication of “Olubamiji AD, Izadifar Z, Zhu N, Chang T, Chen X, Eames BF. Using synchrotron radiation inline phase-contrast imaging computed tomography to visualize three-dimensional printed hybrid constructs for cartilage tissue engineering. Journal of Synchrotron Radiation 23.3 (2016):802-12”. Per the Copyright Agreement, "the authors retain the right to include the journal article, in full or in part, in a thesis or dissertation".

3.1. Abstract

SR-inline-PCI-CT offers great potential for non-invasive characterization and three-dimensional visualization of fine features in weakly absorbing materials and tissues. For cartilage tissue engineering, the biomaterials and any associated cartilage extracellular matrix (ECM) that is secreted over time are difficult to image using conventional absorption-based imaging techniques. For example, three-dimensional printed PCL/alginate/cell hybrid constructs have low, but different, refractive indices and thicknesses. This paper presents a study on the optimization and utilization of inline-PCI-CT for visualizing the components of three-dimensional printed PCL/alginate/cell hybrid constructs for cartilage tissue engineering. First, histological analysis using alcian blue staining and immunofluorescent staining assessed the secretion of sulfated GAGs and Col2 in the cell-laden hybrid constructs over time. Second, optimization of inline-PCI-CT was performed by investigating three SDD: 0.25 m, 1 m and 3 m. Then, the optimal SDD was utilized to visualize structural changes in the constructs over a 42-day culture period. The results showed that there was progressive secretion of cartilage-specific ECM by ATDC5 cells in the hybrid constructs over time. An SDD of 3 m provided edge- enhancement fringes that enabled simultaneous visualization of all components of hybrid constructs in aqueous solution. Structural changes that might reflect formation of ECM also were evident in SR-inline-PCI-CT images. Summarily, SR-inline-PCI-CT images captured at the optimized SDD enables visualization of the different components in hybrid cartilage constructs over a 42-day culture period.

3.2. Introduction

Three-dimensional (3D)-printed hybrid constructs fabricated from PCL, alginate hydrogel and living cells can mimic the multi-composite and biphasic nature of articular cartilage. Therefore, they have attracted attention for CTE applications [1-3]. However, PCL, alginate hydrogel and embedded cells found in these hybrid constructs have low but different refractive indices and thicknesses. Alginate hydrogel is a hydrophilic, anionic polysaccharide comprised of 97.5 % water, while the PCL component is a hydrophobic, polyester-based solid. Furthermore, newly forming cartilage tissues are often not as thick as native articular cartilage. These features make it challenging to non-invasively characterize architecture of the different components of these constructs, let alone progression of associated tissue growth within the constructs in a fluid-filled environment, without the use of contrast agent [4-6]. Histological examinations complemented by 2D imaging techniques are used typically for standard quantitative and qualitative assessments of tissue-engineered constructs [7-9]. Unfortunately, histological examinations are invasive and destructive, involving chemical fixation, paraffin- or resin-embedding and sample staining, all of which might introduce artifacts. Therefore, these methods are not suitable for 3D, non-invasive and longitudinal monitoring of material degradation or cartilage growth of engineered constructs in live animals.

Three-dimensional optical imaging techniques, such as confocal microscopy, optical coherence tomography and Raman spectroscopy, have been explored as alternatives to two-dimensional analysis for tissue engineering applications [10-13]. However, penetration depth and the need for contrast agents to enhance sensitivity have placed limitations on these methods for CTE applications [6]. Currently, MRI is the prevalent non-invasive imaging technique to characterize cartilage, scaffolds and associated tissue growth [14-18]. Nevertheless, MRI cannot provide three-dimensional microstructure [16], owing to limited spatial and temporal resolution, and cannot resolve well multi-density samples, such as partly hydrophobic and partly hydrophilic samples. For example, even a 17.6 T MRI scanner could not visualize microstructural features of an alginate-based, highly anisotropic capillary hydrogel in the injured spinal cord [16]. Other non-invasive techniques, such as X-ray μCT enable high-resolution imaging of scaffolds with high refractive indices [19], but μCT provides poor imaging contrast of samples with low refractive indices and high water content, such as alginate hydrogel [20].

SR-inline-PCI-CT enables three-dimensional, non-invasive characterization of tissues and constructs with weak X-ray absorption and low refractive indices, making it very useful for CTE applications [5, 17, 21, 28]. Compared with conventional X-ray absorption imaging techniques, inline-PCI provides an imaging signal due to refraction (i.e. a phase shift in the transmitted X-rays) that is up to 1000 times greater [22]. Taking advantage of high lateral (spatial) coherence, the advanced refraction-based X-ray imaging technique uses an edge-enhancement property to characterize interfaces between different materials (e.g. PCL, alginate hydrogel, cartilage tissue and surroundings) [23]. Critical for CTE research, inline-PCI can characterize low-density scaffolds and soft tissues [17, 25, 29]. However, its capability for delineation of fine details was declared inferior to other phase-contrast based methods, such as diffraction-enhanced imaging [5, 17, 25]. Contrast agents, which may affect the functionality of cells in CTE, were used in some cases to enhance imaging contrast of inline-PCI for characterization of samples with low refractive indices [4]. Mainly, inline-PCI-CT has been used to visualize samples with a high refractive index, such as bone [5-6]. Inspired by these previous studies, we hypothesize that inline-PCI can be optimized for characterization of samples with a low refractive index, a critical issue for monitoring the successful application of soft-tissue engineering.

In principle, the X-ray source and the SDD play important roles in achieving high spatial coherence of the incident X-rays [26-28, 30]. With focus on the effect of SDD, the SDD should fall in the Fresnel zone, a region between near-field and Fraunhofer zones, to achieve excellent spatial coherence and diffraction fringes [23]. Fresnel diffraction fringes become visible as you progress from the near field to the Fresnel zone, causing edge enhancement at interfaces of different sample components and increasing image contrast. Moreover, penumbral blurring and degradation of image quality occur on progression from the Fresnel to the Fraunhofer zone [23, 26-28]. Refractive indices and thickness of the sample, pixel size of the detector, and the imaging energy used for acquiring SR-inline-PCI images also determine the optimum SDD, and may contribute to the shift in SDD at which blurriness starts to occur [24].

A few studies have explored the SDD as a key parameter for optimization of inline-PCI for imaging of samples with varying densities and refractive indices. The SDD used for image acquisition determines whether the image contrast obtainable will be absorption or phase contrast [25]. For example, for a PLLA/chitosan scaffold imaged in air at 20 keV, an SDD of 2

cm was identified as the absorption- based imaging region and an SDD of 72 cm was identified as the phase-based imaging region [25]. Sets of nylon threads imaged at 12 keV, 11 mm pixel size and SDDs ranging from 0 m to 1.63 m demonstrated that edge contrast at 0.4 m could delineate fine structural details, which became vague at a 1.155 m or higher SDD [24]. Similarly, imaging of mouse lung 'speckles', a low-density tissue, at 30 keV, 6.5 mm pixel size and four different SDDs in the range 0.25 m – 5.98 m demonstrated that SDDs in the range 1–4 m was effective [27]. The confirmation of effects of SDD on the phase contrast and spatial coherence of X-rays, on edge enhancement at interfaces of materials within samples, and consequently on image quality by these studies were explicit and convincing. However, most of these samples were imaged in air, which resulted in excellent phase contrast and, thereby, making it easier to delineate material interfaces. Imaging low- density materials surrounded by fluid or tissues of similar density or X-ray attenuation is challenging. Specifically, for hybrid cartilage constructs, immersion in fluid makes the generation of huge phase contrast within the biomaterials difficult, because the attenuation coefficients of PCL, alginate hydrogel (with 97.5 % water content) and growing cartilage- specific ECM are all low and close to that of water. Coupled with that, optimization of the SDD for inline-PCI-CT characterization of material degradation or tissue growth during engineering of cartilage tissues has not been carried out.

In the present study, we printed multi-density hybrid constructs, comprising PCL and chondrocyte-impregnated alginate hydrogel, and cultured them up to 42 days *in vitro*. Cell viability as well as secretion of sulfated GAGs and Col2, which are produced by chondrocytes during the formation of hyaline cartilage [37], were analyzed over time of culture. Then, we optimized inline-PCI-CT for visualization of multi-density hybrid constructs in fluid (to better mimic non-invasive assessment in a physiological condition) by varying the SDD from 0.25 to 3 m. The most suitable SDD was utilized for characterization of the overall architecture and structural changes, which might be due to secretion of cartilage-specific ECM, in the hybrid constructs over 42 days of culture. Our findings demonstrate the utility of SR-inline-PCI-CT for non-invasive monitoring of soft tissues, especially for CTE applications.

3.3. Materials and Methods

3.3.1. Design and Biofabrication of PCL/alginate/ATDC5 Cells Constructs

Using the Magics Envisiontec (v13, Materialize, Belgium) software, we designed two computer-aided-design (CAD) models to be made from PCL and alginate hydrogel–cell

mixture, respectively, and combined them together to create one for the hybrid construct with an oversize of 10 mm x 10 mm x 0.96 mm. The combined model was then imported into Bioplotter RP (v2.9, Envisiontec GmbH, Germany) for slicing the bulk structure into four layers, each featured by cylindrical strands with 1 mm inter-strand spacing and $0 - 90^0$ perpendicular pattern. The sliced model was eventually imported into VisualMachine (BP, v2.2, Envisiontec GmbH, Germany) for fabricating the hybrid constructs on a three-dimensional bioplotter (Envisiontec GmbH, Germany).

PCL (average M_W~5000), alginic acid sodium salt [medium viscosity alginate (MVA)], calcium chloride dehydrate ($CaCl_2$), 4-(2-hydroxyethyl)-1-piperazineethanesulfonic acid (HEPES) buffer, mouse chondrogenic cell line ATDC-5 and Stemline1 Keratinocyte Medium II calcium free (SKM) were all purchased from Sigma-Aldrich (St Louis, MO, USA) and the hybrid constructs were fabricated in a sterile environment as previously described in [3]. Briefly, PCL was fed into the syringe of a high-temperature dispensing head, heated up to 358 K and dispensed through a cylindrical metal needle with an inner diameter of 300 mm by using a pneumatic pressure of 0.8 MPa and a deposition speed of 1 mms^{-1}. An alginate hydrogel (3.3 % w/v) was prepared by dissolving alginic acid sodium salt in the SKM. Then, ATDC-5 cells were suspended in the alginate solution at a density of 8 x 10^6 cells per ml to make a final concentration of 2.5 % w/v of the alginate–cells solution. The cells–alginate solution was fed into a low-temperature dispensing head and maintained at 283 K. In each layer, PCL strands were first printed using the assigned parameters and then cell-impregnated alginate was dispensed in the spaces between the PCL strands through a conical needle with inner diameter of 200 mm using a pneumatic pressure of 0.03 MPa and a deposition speed of 25 mms^{-1}.

After fabrication of each layer, alginate strands were partially cross-linked using 170 mM $CaCl_2$ in 4.2 mM HEPES (in 0.35 M sucrose) fume released in the direction of the fabrication procedure through an ultrasonic nebulizer (MY-520). After the desired number of layers was reached, the constructs were dipped in 100mM $CaCl_2$ [in 4.2 mM HEPES, 0.35 M sucrose solution (pH 7.4)] for 20 min to complete cross-linking of the cells–alginate hydrogel network within the PCL framework. After cross-linking, constructs were washed for 5 min in DMEM twice, placed in culture medium in 12-well culture plates, transferred to the incubator and maintained at 310 K and under 5 % CO_2. The culture medium was changed every two days: it consisted of DMEM/F-12 HAMs (1:1) supplemented with 5 % fetal bovine serum (FBS),

penicillin (100 unit/ml), streptomycin (100 mg/ml), 10 mg/ml glutamine, 10 mg/ml insulin–transferrin–selenium plus (ITS+) liquid media supplement and 0.05 mg/ml ascorbate-2-phosphate (all purchased from Life Technologies). At day 0, 14, 28 and 42 days of culture, cultured constructs were collected as described for each assay below.

3.3.2. Cell Viability in Hybrid Constructs by Live/Dead Assay

The viability of the ATDC-5 cells in the hybrid constructs was examined using a two-color fluorescence LIVE/DEAD1 Kit (Molecular Probes, OR, USA) and fluorescence microscopy at days 0, 14, 28 and 42 of culture as previously described in [3]. Briefly, the constructs were removed from culture, washed with DMEM for 30 minutes and submerged in staining solution containing 2 mM calcein-AM and 0.5 mM ethidium homodimer (EthD-1) in DMEM. This procedure was conducted in the dark and constructs were then wrapped in tin foil to prevent any light exposure, then transferred to a 310 K, 5 % CO_2 incubator for about 60 minutes to allow the staining solution to penetrate the layers of the constructs. After 60 minutes, photomicrographs of stained constructs were taken for live cells (fluoresced green) and dead cells (fluoresced red) using a DP70 camera attached to a Nikon fluorescent inverted microscope (Nikon, ECLIPSE E600, SPOT Insight2 Camera, USA). Then, green and red fluoresced images were merged in ImageJ software [31] to localize the distribution of live and dead cells in the constructs. To quantify cell viability, the cells were released from the constructs by dipping constructs in 1 ml of 50 mM EDTA solution to depolymerize alginate hydrogel strands. While protected from light, gentle pipetting was used to pick up 10 ml of the cells suspension onto glass slides and then covered with coverslip. Then, five to six photomicrographs of live and dead cells at different locations on the glass slide were taken using a fluorescent inverted microscope (Nikon, ECLIPSE E600, SPOT Insight2 Camera, USA). The procedure was repeated three times per construct, and live and dead cells from these images were counted for each construct using ImageJ software [31].

3.3.3. Estimation of Secretion of Sulfated GAGs in Constructs by Alcian Blue Staining

ATDC-5 cells spatially distributed in the hybrid constructs were examined for secretion of sulfated GAGs at days 0, 14, 28 and 42 days of culture using alcian blue staining assay as previously described in [3]. Hybrid constructs ($n = 4$ for each time-point) were removed from culture, washed in DMEM for 30 minutes and fixed in methanol: acetone (1:1) on ice for

another 30 min. The fixed constructs were stained with 0.5 mg/ml alcian blue in 3 % acetic acid (pH = 1) and kept overnight at room temperature on a rocker for the stain to penetrate the constructs. The stained constructs were de-stained in 25 % ethanol in 3 % acetic acid for one hour and stored in 50 % ethanol in 3 % acetic acid before photomicrographs were obtained using light microscopy. Using ImageJ software [31], the regions covered by acian blue stains were segmented out of the collected images for further quantitative analysis. Four regions of interest were taken for each construct, and the appropriate threshold was applied to segment the alcian blue-stained areas of the alginate hydrogel, which were then measured. For each time-point, such segmentation was carried out to estimate the area covered by alcian blue stains compared to the total area of the alginate hydrogel in the regions of interest. These measurements were obtained at the four time-points used and compared.

3.3.4. Estimation of Secretion of Col2 in the Hybrid constructs by Immunostaining

Secretion of Col2 in the hybrid constructs was examined at days 0, 14, 28 and 42 ($n = 4$ for each time-point) using immunofluorescent staining assay. The hybrid constructs were removed from culture at each time-point, fixed in cacodylate buffer [that consists of 200mM sodium cacodylate, 2 % paraformaldehyde, 2 % glutaraldehyde, and 0.7 % ruthenium (III) hexamine trichloride] and incubated for 2 hour in 1:100 purified anti-Col2 antibody (purchased from Developmental Studies Hybridoma Bank, Iowa City, USA) in blocking buffer [4 % normal goat serum and 2 % normal sheep serum in phosphate buffer saline Tween-20 (PBST)]. These constructs were washed 6-8 times in the blocking buffer over a 2 hours' period after first incubation and then in 1:1000 goat anti-mouse IgG-488 conjugate (purchased from EMD Millipore, Temecula, California, USA) in blocking buffer. After incubation in the secondary antibody, these constructs were washed in PBST over another period of two hours to reduce the background stains and photomicrographs were taken at different positions; horizontally and vertical sections through the constructs, using a DP70 camera attached to fluorescent inverted microscope (Nikon, ECLIPSE E600, SPOT Insight2 Camera, USA). In addition, 0.1 ml ml-1 of 40, 6-diamidino-2-phenylindole (DAPI) was added to the immunofluorescent staining assay for DNA labelling of cells to confirm that the cells secreted the Col2 matrix. Like the alcian blue staining, four regions of interest were taken for each construct, and the appropriate threshold was applied to segment the images collected from Col2-stained hybrid

constructs at the different time-points in ImageJ software [31] and used for quantitative measurements.

3.3.5. SR-inline-PCI-CT of Hybrid Constructs

Hybrid constructs were fixed at days 0, 14, 28 and 42 of culture in methanol: acetone (1:1) on ice for 20 minutes and kept in 3 % acetic acid for the inline-PCI-CT imaging, performed at the Biomedical Imaging and Therapy-Insertion Device (BMIT-ID) 05ID-2 of the Canadian Light Source using a double-crystal bent Laue monochromator tuned to 30 keV imaging energy [32]. The hybrid constructs were placed in a sample holder and positioned on the rotating scanning stage for CT imaging. Because calculation of optimum SDD for characterization of multi-density and different low-refractive-indices hybrid constructs have not been previously reported, this study took cues from [27-28, 33-34] who reported that an SDD between 1 and 3 m was good for imaging whole mouse lungs and that a SDD greater than 3 m may have negative impact of in-air photon scattering. Thus, tomographic data sets were collected at SDDs of 0.25 m, 1 m and 3 m using a beam monitor AA-60 (Hamamatsu) coupled to a camera C9300 (Hamamatsu) with effective pixel sizes of 8.9, 8.77 and 8.47 µm, respectively. Three thousand projections were collected over a 180^{o} rotation and a set of ten flat-field and ten dark-field images were acquired at the beginning and at the end of each scan to correct the acquired projections. Images of the multi-density hybrid constructs obtained at 0.25 m, 1 m and 3 m SDD were reconstructed and analysed for identification of the optimum SDD. The identified optimum SDD was then used for CT imaging of the hybrid constructs collected from culture at day 0, 14 and 28 ($n = 4$ for each time-point). Phase-retrieved and non-phase-retrieved CT reconstructions of the tomographic data were then performed. NRecon (v1.6.10.1; Skyscan) [38] was used for the non-phase- retrieved CT reconstruction, whereas phase-retrieved CT reconstruction was performed in PITRE (v3.1) (Phase-sensitive X-ray Image processing and Tomography Reconstruction). For the non-phase-retrieved reconstruction, flat- and dark-field corrections and image normalization were carried out on the data sets with an ImageJ macro plugin before the reconstruction. Then, a modified Feldkamp algorithm was used to obtain image slices. For the phase-retrieved reconstruction, flat- and dark-field corrections, sinogram generation, phase retrieval and slice reconstruction were all included and carried out in PITRE (v3.1) with a phase-attenuation duality Born algorithm (PAD-BA) and " = 8/ {3 = 900. Then, three-dimensional volume rendering was performed after the reconstruction in visualization

and analysis software Avizo (v9; FEI Visualization Sciences Group, Dusseldorf, Germany), without decomposing the images into geometric primitives, to support the two-dimensional greyscale information of the reconstructed slices.

3.3.6. Statistical Analysis

All statistical tests were performed with SPSS (released 2013 IBM SPSS Statistics for Windows, v21.0. Armonk, NY: IBM Corp.). For the alcian blue staining and the Col2 staining, measurements from the analysis were performed in ImageJ software [31].to quantify secretion of GAGs and Col2, respectively. Five different images of each construct ($n = 4$ for each time-point) were captured and used for each analysis. Repeated measures analysis of variance (ANOVA) was used to determine the change in area stained over time. Post hoc tests using the Bonferroni correction were conducted to estimate the statistical significance between these areas over time. The value of $p < 0.05$ was considered statistically significant.

3.4. Results

3.4.1 Cell Viability of Hybrid Constructs Remained High at All Time-points

Viability of the ATDC-5 cells impregnated in the hybrid constructs ($n = 4$ for each time-point) was estimated over time of culture using a two-color fluorescence LIVE/DEAD1 Kit (Molecular Probes, OR, USA). Cells were distributed uniformly throughout the hybrid constructs and their viability was 84.4 ± 2.2 % at day 0. At day 14, cell viability reduced to 77.2 ± 2.1 % and increased to 84.3 ± 2.8 % at day 28 and 85.0 ± 5.4 % at day 42 (Fig. 3.1). Cells in the alginate hydrogels strands of the hybrid constructs formed clusters or aggregates, which increased in size, from day 14 onwards (Figs. 3.1 B-D). Moreover, cross-section images obtained by cutting transversely the center of the constructs at day 14 and 28 showed that cells in the middle of constructs had comparable spatial distribution and viability to the cells in the periphery (Figs. 3.1E-1F).

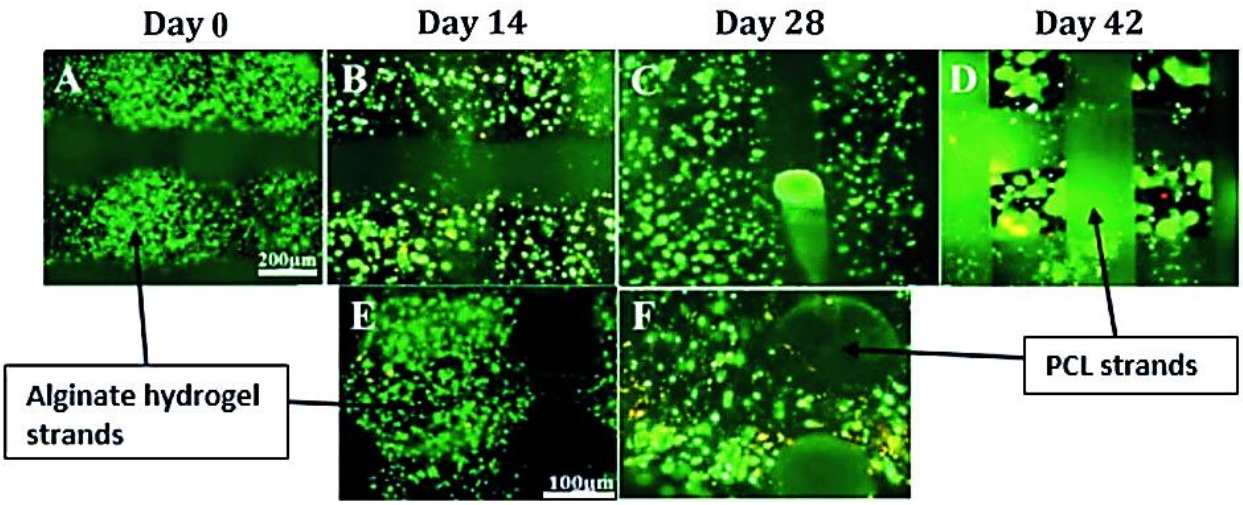

Fig. 3.1: Fluorescent microscopy images of merged live (green) and dead (red) ATDC-5 cells spatially distributed in hybrid constructs at day 0-42: panels A-D are images looking down on the intact constructs over the entire culture period, whereas panels E and F are cross-section images through the center of the hybrid constructs at day 14 and 28.

3.4.2 Secretion of Sulfated GAGs in Hybrid Constructs Increased Over Time

Secretion of sulfated GAGs in the three-dimensional printed cell-impregnated hybrid constructs was examined by alcian blue staining at the four time-points (Fig. 3.2). The blue- stained area was well dispersed and darkened over time, reflecting a progressive increase in the production of sulfated GAGs in the ECM (Figs. 3.2 A - 3.2 H). Cross-section views of the constructs also indicated that secretion of sulfated GAGs was distributed in the inner layers of the constructs (Figs. 3.2 I – 3.2 L). Using one-way repeated measures ANOVA with sphericity assumed, the mean area covered by the alcian blue stains in the hybrid constructs differed with statistical significance between time-points [$F(3, 9) = 113.194$, $P < 0.001$]. Post hoc tests using the Bonferroni correction (graphically presented in Fig. 3.2) showed a statistically significant difference between day 0 and day 14 (p-value = 0.011), day 0 and day 28 (p-value = 0.005), day 0 and day 42 (p-value = 0.001), and day 14 and day 42 (p-value = 0.030).

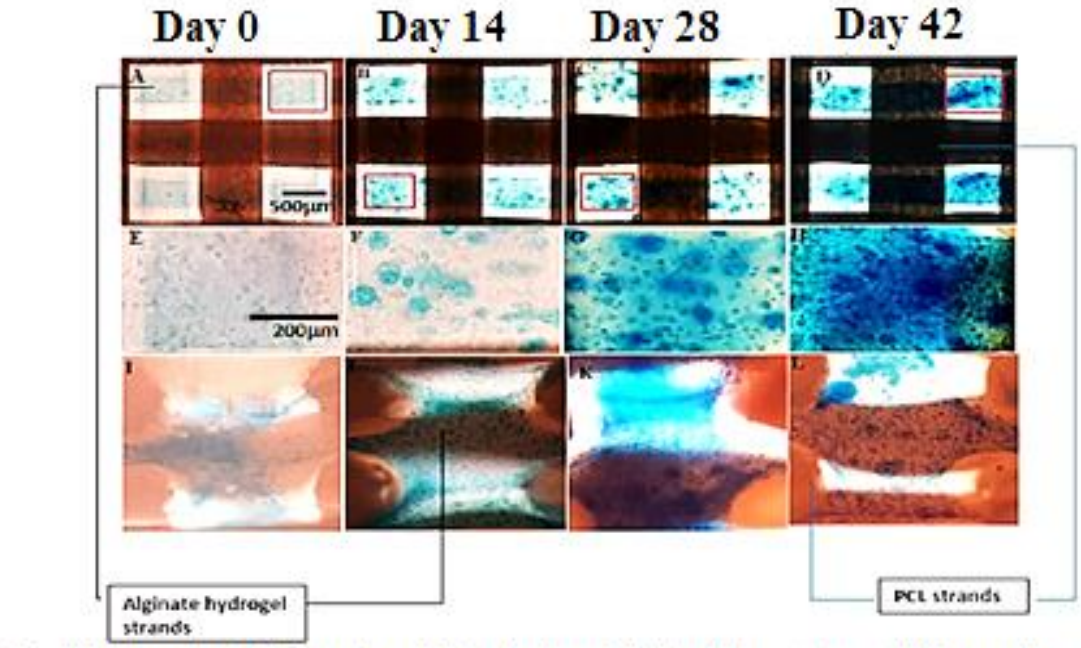

Panel M: Graphical illustration of distribution of Alcian blue stains at different time points

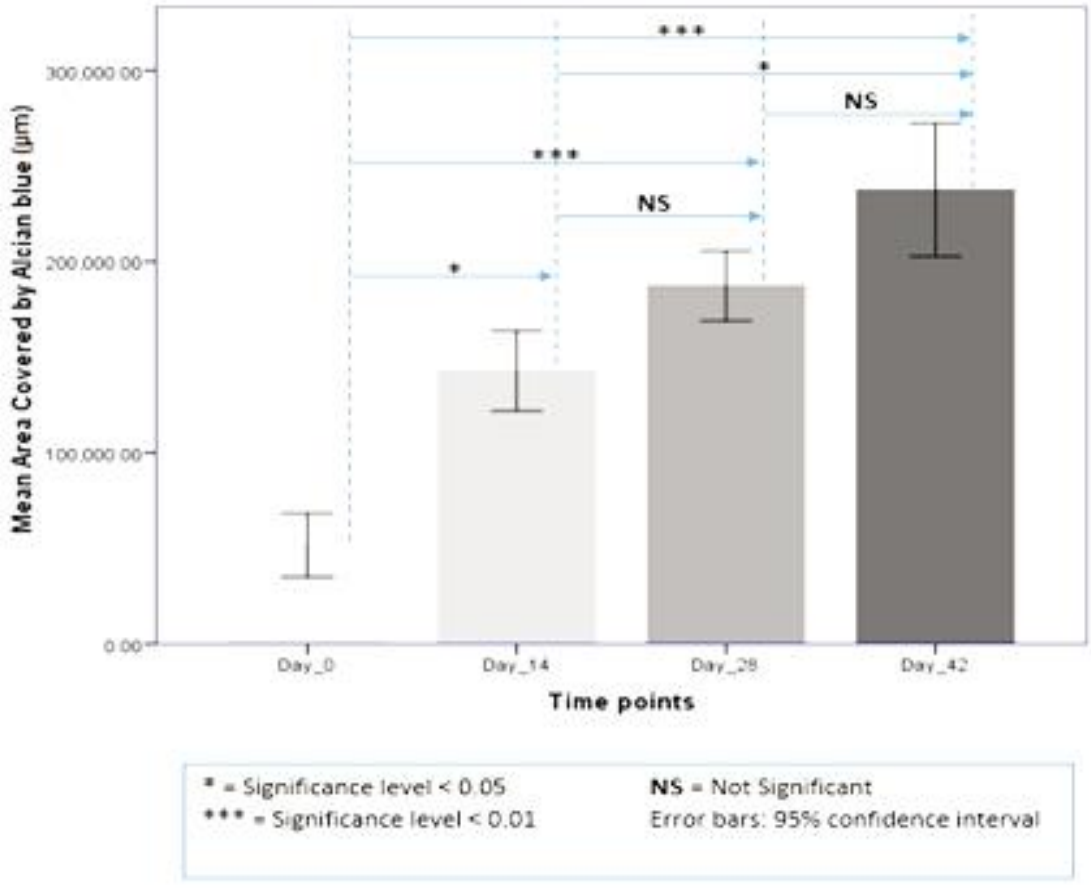

Fig. 3.2: Comparison of alcian blue staining in three-dimensional printed cell-impregnated constructs, showing secretion of sulfated

GAGs at different time-points. Panels A – D demonstrate progressive secretion of sulfated GAGs, and E-H are high-magnification views of the regions of interest highlighted in the red boxes of panels A-D. Panels I-L are cross-section images through the center of the hybrid constructs. Panel M represents the quantitative analysis of alcian blue stained area in the hybrid constructs at days 0, 14, 28 and 42 showing statistically significant difference in secretion of GAGs at the different time points.

3.4.3 Estimation of Secretion of Col2 in the Hybrid Constructs

Secretion of Col2 in the hybrid constructs was examined at days 0, 14, 28 and 42 ($n = 4$ for each time-point) using immunofluorescence. Like the alcian blue staining results, secretion of Col2 increased progressively from day 0 to day 42 (Figs. 3.3 A - 3.3 D). DAPI staining reflected the locations of cells in the Col2-positive areas (Figs. 3.3 E - 3.3 H). Cross-section views of the transected constructs indicated that secretion of Col2 also occurred in the inner layers of the constructs (Figs. 3.3 I - 3.3 L). In addition, high-magnification views of constructs cultured for 42 days showed that clusters of cells secreting matrix were present in alginate hydrogel strands and around the PCL strands (Figs. 3.3 M - 3.3 P), suggesting that some cells in the alginate migrated to the PCL strands and secreted Col2 matrix.

One-way repeated measures ANOVA with sphericity assumed demonstrated that the mean area covered by Col2 staining were significantly different between time-points [$F(3, 9) = 207.021$, $P < 0.001$]. In fact, post hoc tests using Bonferroni correction (graphically presented in Fig. 3.3) revealed that secretion of Col2 over time showed a statistically significant difference between day 0 and day 14 (p-value = 0.048), day 0 and day 28 (p-value = 0.002), day 0 and day 42 (p-value = 0.002), day 14 and day 42 (p-value = 0.005) and between day 28 and day 42 (p-value = 0.003).

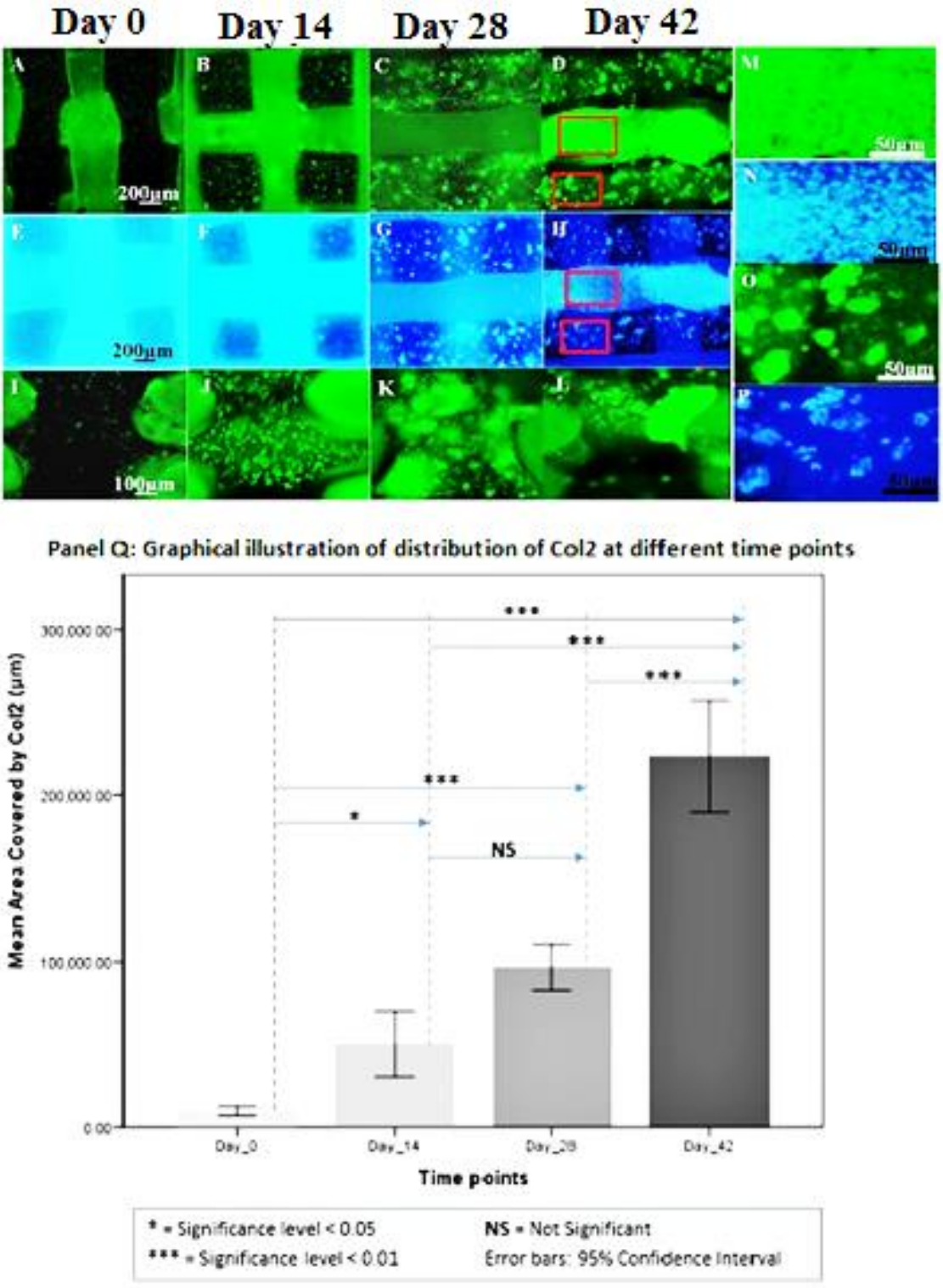

Fig. 3.3: Comparison of Col2 immunostaining and DNA labelling in three-dimensional printed cell- impregnated constructs at different time-points. Panels A-D and E-H show progressive secretion of Col2 and corresponding DAPI staining, respectively. Panels I-L are cross-section images through the center of the hybrid constructs. Panels M and N are high-magnification views of the upper region of interest outlined in red boxes of panels D and H, whereas panels O and P are high-magnification views of the

lower region of interest outlined in red boxes of panels D and H. Panel Q represents quantitation of Col2 immunostained area in the hybrid constructs, showing statistically significant differences in Col2 secretion at different time-points.

3.4.4 Effect of SDD on Visualizing the Different Components of the Hybrid Constructs

Non-phase-retrieved and phase-retrieved CT reconstruction applications were investigated to determine the reconstruction method that provides better details of the individual components of the multi-density constructs in fluid. CT reconstructions were used to obtain image slices from the imaging data of day 14 hybrid constructs obtained at 3 m. The edge contrast obtained from phase-retrieved images after reconstruction revealed the PCL strands, but could not discriminate the lower-refractive-index alginate hydrogel strands in between the PCL from the surrounding fluid (Figs. 3.4 A and 3.4 C). On the other hand, the edge contrast obtained from the non-phase-retrieved CT reconstruction clearly delineated the interfaces of all components of the hybrid construct: PCL-fluid, PCL-alginate and alginate-fluid (Figs. 3.4 B and 3.4 D). Therefore, the edge-enhancement attribute of the non-phase- retrieved CT reconstruction better characterized features of the multi-density, multi-refractive-index hybrid constructs compared with the phase- retrieved CT reconstruction.

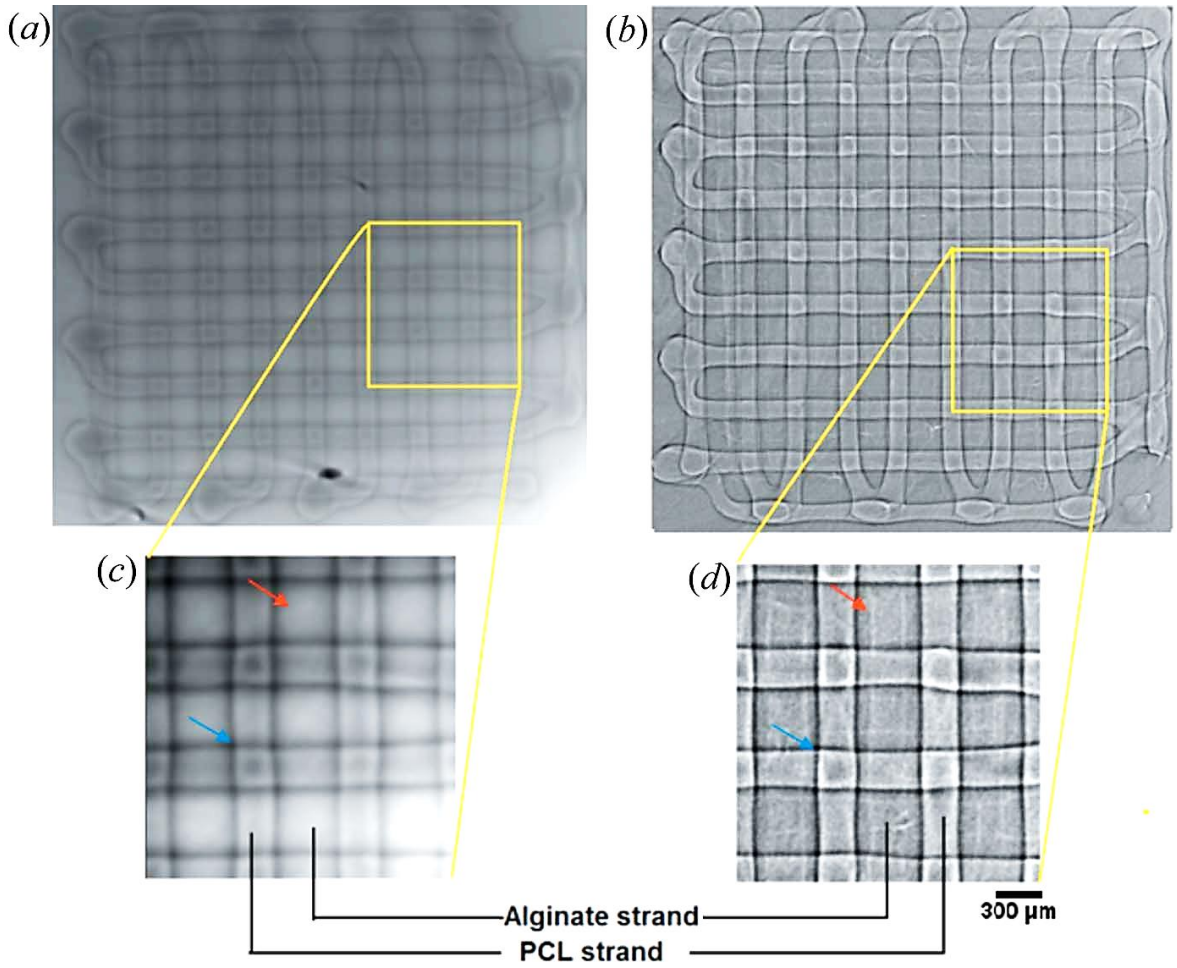

Fig. 3.4: Comparison of output slices of the same image dataset reconstructed using (a) phase-retrieved CT reconstruction; (b) non-phase-retrieved CT reconstruction; (c) magnified region of interest cropped from (a); and (d) magnified region of interest cropped from (b). The PCL strands of the hybrid constructs were visible in both cases. However, alginate hydrogel strands in between the PCL strands were more visible in the non-phase- retrieved image slice than the phase-retrieved image slice. Edge effects show the boundaries of PCL and alginate hydrogel strands in the same location of the hybrid construct (arrow heads).

As the non-phase-retrieved reconstruction technique of NRecon (v1.6.10) provided the details required for characterizing each component of our hybrid constructs, it was used to establish the optimum imaging SDD among those tested: 0.25 m, 1 m and 3 m. After identifying that the non-phase-retrieved reconstruction technique provided details required for characterization of our multi-component constructs, hybrid construct images obtained from SDDs of 0.25 m, 1 m and 3 m were reconstructed using a non-phase-retrieved reconstruction technique and compared (Fig. 3.5). Images from the exact same location in a hybrid construct cultured for 42 days were compared [yellow box in Fig. 3.5 A]. The edge contrast provided at an SDD of 0.25 m identified edges of the PCL strands, but the alginate hydrogel strands were not readily apparent (Figs. 3.5 B and 3.5

E). At an SDD of 1 m, edges of the PCL strands had higher contrast compared with that obtained at 0.25 m SDD (Figs. 3.5 C and 3.5 F). In addition, the lower-density alginate strands were faintly visible, due to minimal edge contrast. At an SDD of 3 m, there was an increase in visibility of individual and the interfaces between the PCL and alginate hydrogel strands and surrounding fluid (Figs. 3.5 D and 3.5 G). The lower-refractive-index and high-water-content alginate hydrogel strands benefited more as the phase contrast more clearly highlighted the edges of these strands.

The distributions of grey values along a line drawn across two PCL strands in the exact same location of the imaged construct were used to quantitate the imaging capabilities of various SDDs [yellow lines in Figs. 3.5 B – 3.5 G]. Prominent peaks are expected because edge contrast or enhancement associated with the difference in refractive indices at material–material or material–fluid interfaces. No high peak was observed from data obtained at 0.25 m SDD (Fig. 3.5 H), but two prominent peaks corresponding to the edges of PCL strands were apparent in data obtained at 1 m SDD (Fig. 3.5 I). Smaller peaks were also seen between these two prominent peaks that may correspond to the edges of the alginate hydrogel strand. Similar analyses of data obtained at 3 m demonstrated two prominent peaks that corresponded with the edges of PCL strands and other smaller peaks that correspond to the edges of the highly porous alginate hydrogel strand (Fig. 3.5 J). The smaller peaks in this case are larger compared with those obtained at 1 m SDD [compare Figs. 3.5 I and 3.5 J]. These data demonstrate that the phase contrast at 3 m SDD provides the most adequate interference fringes among these three SDDs for characterization of each component of the hybrid constructs in aqueous medium.

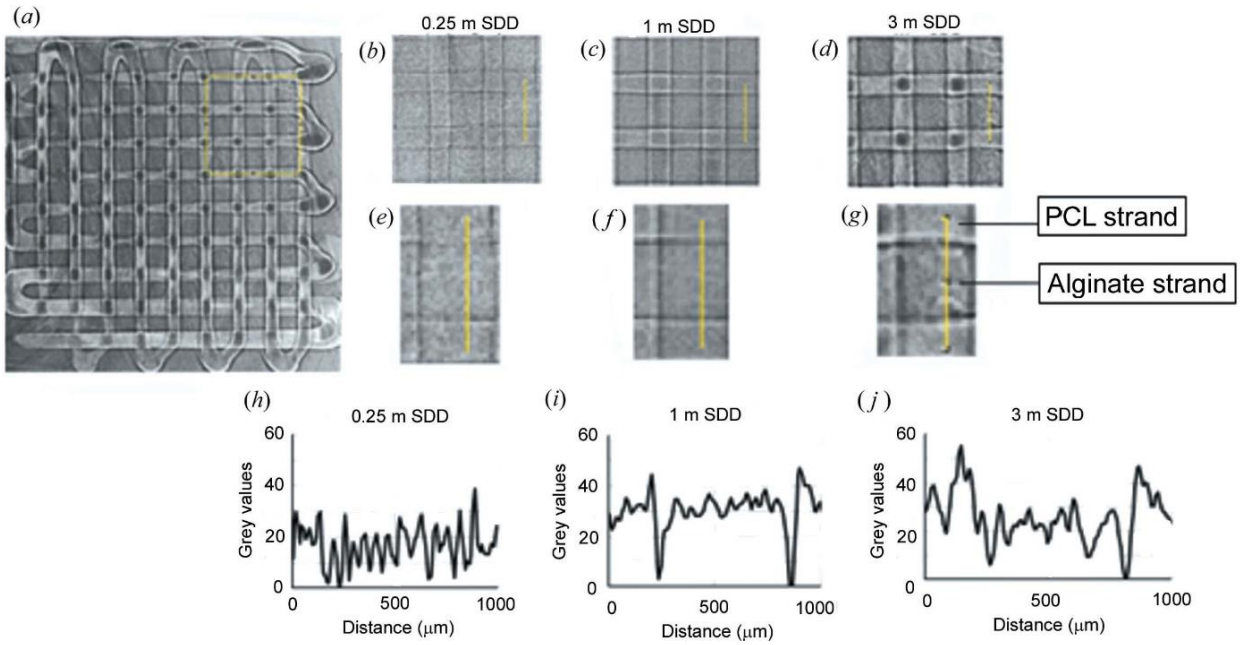

Fig. 3.5: Comparison of inline-PCI-CT images of three-dimensional printed hybrid construct imaged in aqueous medium at three different SDDs. (a) Image slice of inline-PCI showing the whole construct imaged at three different SDDs and the region of interest (in yellow box) cropped for analysis of the components of the construct. Inline-PCI-CT image slice obtained at (b) 0.25 m SDD, (c) 1 m SDD and (d) 3 m SDD; (e) region of interest cropped out of (b) showing the line drawn across two PCL strands; (f) region of interest cropped out of (c) showing the line drawn across two PCL strands; (g) region of interest cropped out of (d) showing the line drawn across two PCL strands; (h)-(j) distribution of grey values near the line shown in (e)-(g) respectively.

3.4.1 SR-inline-PCI-CT Reveals Structural Changes over time in Hybrid Constructs

Based on the previous data, an SDD of 3 m was used for SR-inline-PCI-CT characterization of structural changes in hybrid constructs at days 0, 14, 28 and 42 ($n = 4$) in culture. Images representing equivalent regions of a limited series of reconstructed slices showed visible structural changes in the constructs during this culture period, especially in the alginate strands (Fig. 3.6). At days 0 and 14, edges of both the PCL and alginate strands appeared uniform from reconstructed images (Figs. 3.6 A and 3.6 B). By day 28, changes in the uniformity of the alginate strands in the constructs were apparent (Fig. 3.6 C, arrow head). By day 42, the alginate strands were more visible compared with other time-points and non-uniform structural changes in the alginate strands were more prominent (Fig. 3.6D, arrow head). Three-dimensional volume rendering was performed in Avizo 3D software (v9) to support the results of the two-dimensional greyscale images and to provide a three-dimensional image that further showed the different components of the hybrid constructs (day 14 at 3 m SDD). Rendering clearly indicated

the interfaces between PCL strands, alginate strands and surrounding fluid (Fig. 3.7). Therefore, even though alginate strands contain 97.5 % water and other components of the constructs are submerged in fluid, SR-inline-PCI can provide details of the different low-density and low-refractive-index biomaterial constructs present in the hybrid constructs.

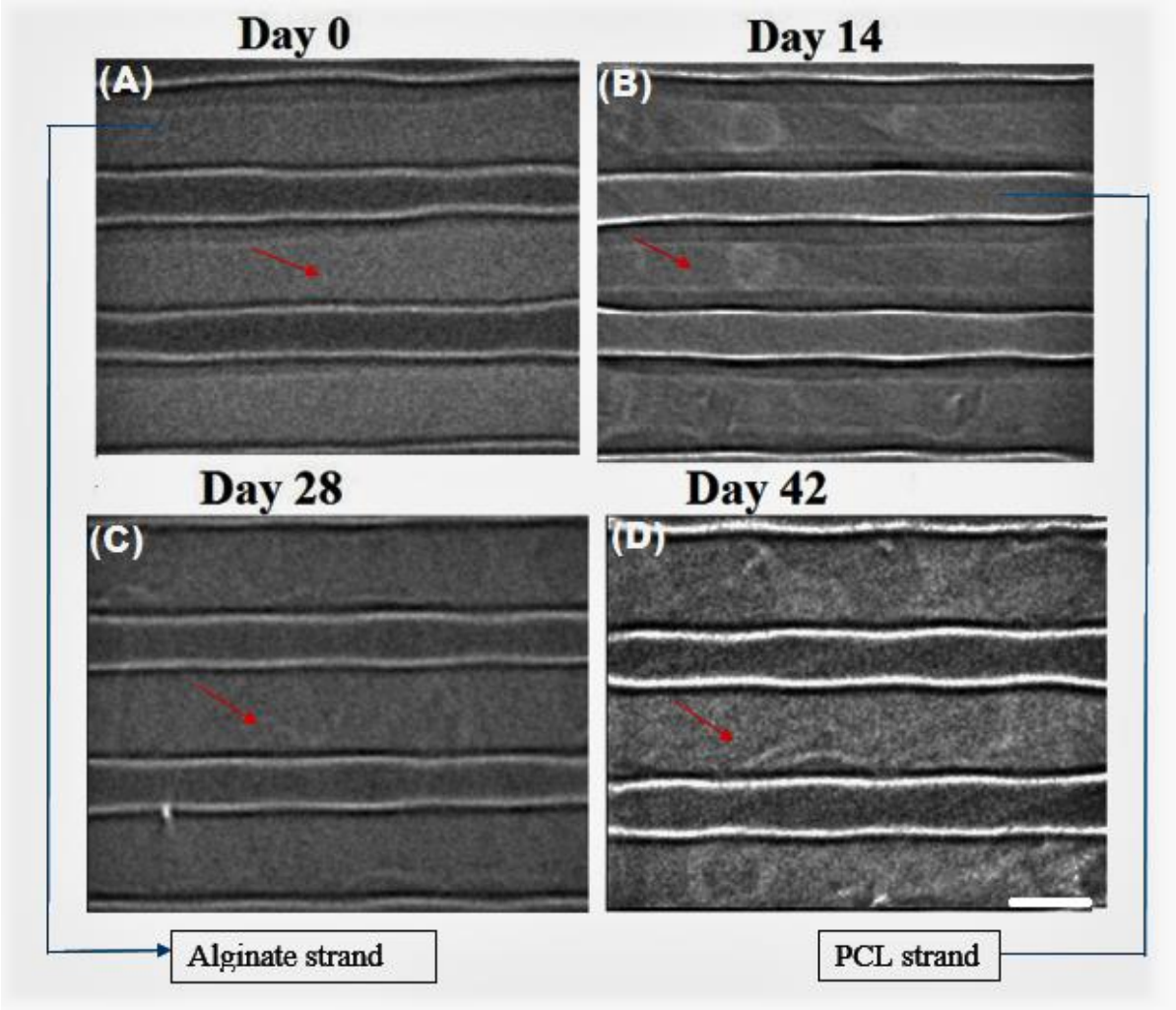

Fig. 3.6: Comparison of SR-inline-PCI-CT images of multi-density hybrid constructs in aqueous medium at the different time-points. Images were obtained at 30 keV using 3 m SDD, pixel size of 8.47 µm. Scale bar: 300 mm. Arrowheads show how cell-impregnated alginate strands changed over time.

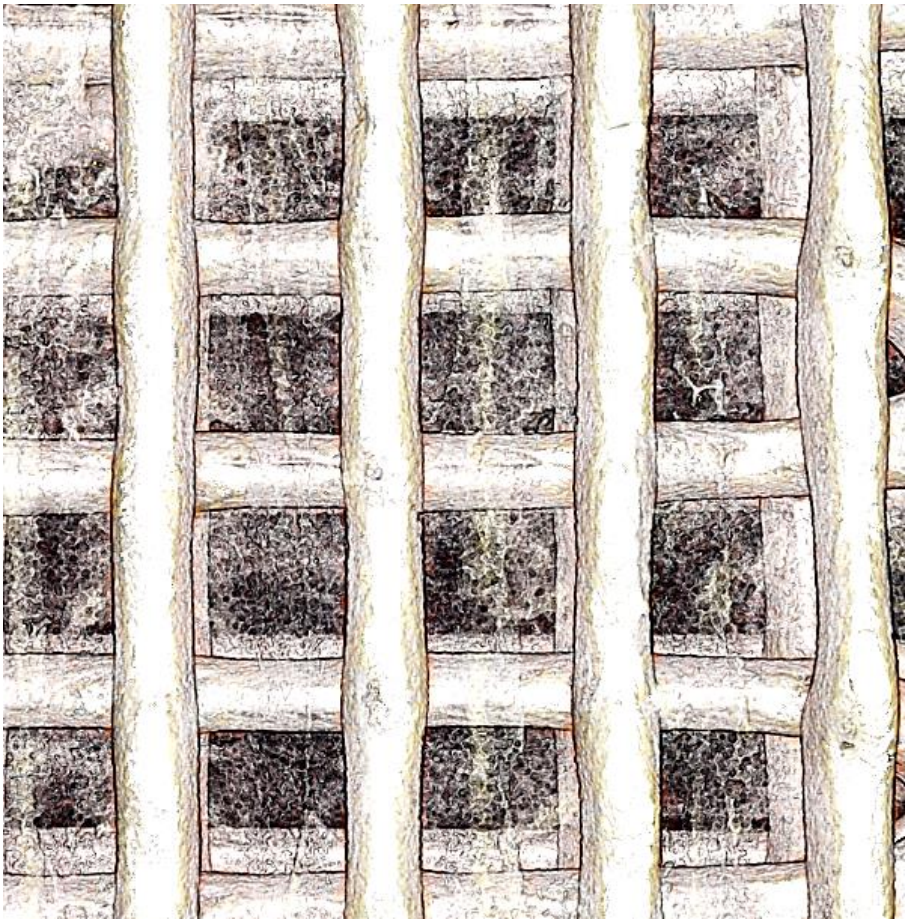

Fig. 3.7: Three-dimensional rendered image of hybrid constructs submerged in fluid showing the interface between PCL strands, alginate hydrogel strands and surrounding fluid.

3.5. Discussion

Non-invasive three-dimensional visualization of the architecture and progression of tissue repair is essential to track the success of various tissue engineering strategies, including those based on three-dimensional printed hybrid construct CTE applications. This is particularly true when the applications are advanced from *in vitro* to *in vivo* and eventually to human studies. The novel technique of SR-inline-PCI-CT enables the characterization of a variety of biomaterials *in vitro* and *in vivo* for tissue engineering applications [4-5, 17, 25, 36]. However, most SR-inline-PCI studies have criticized its capability for delineation of fine details, instead preferring other phase-contrast-based methods, such as diffraction-enhanced imaging [5, 17, 25]. Imaging contrast of inline PCI can be enhanced by contrast agent [4], but this may affect (either inhibit or enhance) the functionality of embedded cells [39]. Other studies mainly focused on characterization of materials with high refractive index, such as bone [5-6].

To optimize SR-inline-PCI-CT for soft tissue engineering applications, this study explored three SDDs, deducing an optimum SDD with excellent edge-enhancement fringes for characterization of each component of multiple low-refractive-index hybrid constructs consisting of PCL, cell- impregnated alginate and surrounding fluid. Increasing the SDD from 0.25 m to 3 m resulted in incremental increases in edge contrast and thus increased the ability of SR-inline-PCI-CT to delineate the different components [especially the low-refractive-index cell-impregnated alginate of the multi-density constructs submerged in fluid (Fig. 3.5)]. However, there was very little phase contrast and thus faint visibility of the alginate strands at SDDs of 0.25 m and 1 m. At an SDD of 3 m, the edge-enhancement fringes were optimal among these SDDs, enabling effective characterization of both PCL and alginate components of the constructs submerged in fluid. Though a 4 m SDD was not examined, the edges of PCL strands at a 3 m SDD were already very bright and slightly prone to blurriness, so using an SDD greater than 3 m may not be beneficial for imaging PCL with these imaging parameters. Increasing the SDD did provide increasing edge contrast for the lower-refractive-index alginate hydrogel strands, however, so perhaps an SDD greater than 3 m would permit better visualization of alginate. Despite this possibility, previous studies suggest that an SDD larger than 3 m might experience too much photon scattering, producing a negative effect on image contrast [33-34]. In fact, an SDD of 1 m worked better for characterization of airway interfaces of a rat at 30keV and 12.9 mm when compared with SDDs of 2 m or 3 m [27]. In addition, the edge contrast of sets of nylon threads imaged at an SDD of 0.4 m using a pixel size of 11mm provided adequate structural details, which became vague at an SDD of 1.155 m or higher [24]. That said, all these studies used samples that had a different refractive index. Also, they were not multi-density hybrid samples and were not imaged submerged in fluid. For example, the edge contrast at the interface between alveoli tissues and air will be larger than the interface between alginate strands (containing 97.5 % water) and submerged fluid. Also, the optimal SDD depends on the refractive indices found in the sample, the imaging energy and the detector pixel size; therefore, it should be tailored to obtain effective edge-enhancement fringes for each application.

Critically, SR-inline-PCI-CT at a 3 m SDD generated edge enhancement that allowed unparalleled characterization of the overall architecture and structural features of multi- density hybrid constructs in medium. Strands of PCL and alginate were clearly delineated from surrounding fluid in three dimensions, which should greatly increase visualization of *in vivo*

integration of tissue constructs [4-6]. The observed micro-structural features in the alginate may reflect changes in density due to either degradation of the alginate [29, 35] or ECM deposition by the impregnated cells (tissue growth) [4-6]. Regarding the former possibility, X-ray PCI-CT of PGA microfiber scaffolds implanted for 28 days in rats showed that mass density loss caused by degradation resulted in a reduction of the refractive index and density of the implanted scaffold and this consequently caused a reduction in the phase contrast [29]. In contrast, the alginate strands in our hybrid constructs did not appear to have lower phase contrast over time and visible mass loss was not evident, even at day 42. Regarding the possibility that the observed microstructural features in the alginate reflected ECM deposition by impregnated cells, increased phase contrast during culture time of hybrid constructs paralleled increased ECM secretion by impregnated ATDC5 cells (Figs. 3.2 and 3.3). Indeed, increases in phase contrast were also associated with deposits of mineralized ECM by mesenchymal stem cells in alginate beads during *in vitro* culture [6]. Future work to resolve this issue should examine exact spatial correlation between observed patterns of ECM secretion and phase contrast.

Furthermore, our data demonstrate that the CT reconstruction method (i.e. phase retrieval or non-phase retrieval) might affect subsequent data analyses. Phase retrieval can provide quantitative information [25], but it did not produce better qualitative images in this paper. Importantly, the non-phase-retrieved CT reconstruction provided edge contrasts that enabled clear delineation of interfaces between all components of the hybrid construct: PCL–fluid, PCL–alginate and alginate–fluid. Non-phase-retrieval CT reconstruction is also achievable using PITRE (v3.1) and this study also obtained details like the non-phase-retrieved CT reconstruction carried out in NRecon (v1.6.10.1; data not shown). Overall, the progressive secretion of sulfated GAGs and Col2 while maintaining high cell viability (Fig. 3.1) verified that three-dimensional printed hybrid constructs have the capability to develop into articular cartilage [3]. These features were present throughout the full thick- ness of the constructs, suggesting that the process can be scaled up to the approximate thickness of native articular cartilage, which would make it even easier to characterize using inline-PCI, especially if cultured for longer times [1-2]. Even though the alginate strands contain 97.5 % water and the constructs are immersed in fluid, our study demonstrates that inline-PCI can provide details of the different low-density and low-refractive-index biomaterial constructs and their surroundings. Thus, the promising capability of inline- PCI-CT in visualizing subtle structural changes in these constructs suggests further application of this technique to

assessment of larger tissue constructs at much longer culture times *in vitro* and *in vivo.*

3.6. Conclusions

This study illustrates that SR-inline-PCI-CT offers an unparalleled technique for non-invasive, non-destructive and three- dimensional characterization of overall architecture of the different components of hybrid constructs in aqueous solution, which would be impossible by using absorption-based imaging techniques. For three-dimensional printed samples of PCL and cell-impregnated alginate submerged in fluid, an SDD of 3 m provided the edge-enhancement fringes that enabled effective characterization of each component. Despite the similar refractive indices between alginate hydrogel (contains 97.5 % water content) and surrounding fluid, SR-inline-PCI-CT allowed assessment of subtle changes within the cell-impregnated alginate over time. Furthermore, histological analyses demonstrated a progressive increase in secretion of sulfated GAGs and Col2 in the cell-impregnated hybrid constructs over time, confirming the utility of three- dimensional printed hybrid constructs for CTE application. We argue that subtle changes in the inline-PCI-CT images of cell-impregnated alginate strands at later time-points reflected ECM secreted in the constructs over time. Therefore, this study reveals the promising potential of SR-inline-PCI-CT for non-invasive, nondestructive, three-dimensional and longitudinal characterization of soft tissues in hybrid constructs.

3.7. Acknowledgements

The authors acknowledge the funding for the present research from the Saskatchewan Health Research Fund (SHRF), Canadian Institutes of Health Research (CIHR) and Natural Sciences and Engineering Council of Canada (NSERC). We also acknowledge that images presented in this paper were captured at the Canadian Light Source (CLS), which was supported by the Canadian Foundation for Innovation (CFI), NSERC, the University of Saskatchewan, the Government of Saskatchewan, Western Economic Diversification (WED) Canada and CIHR.

3.8. References

1. Schuurman W, Khristov V, Pot MW, van Weeren PR, Dhert WJ, Malda J. (2011). "Bioprinting of hybrid tissue constructs with tailorable mechanical properties." *Biofabrication* 3 (2), 021001-021008.

2. Kundu J, Shim JH, Jang J, Kim SW, Cho DW. (2015). "An additive manufacturing-based PCL-alginate-chondrocyte bioprinted scaffold for cartilage tissue engineering." *J Tissue Eng Regen Med.* 9 (11),1286-97.

3. Izadifar Z, Chang T, Kulyk W, Chen DXB., Eames BF. (2016). "Analyzing biological performance of 3D-printed, cell-impregnated hybrid constructs for cartilage tissue engineering." *Tissue Engineering, Part C: Methods.* 22 (3), 173-88.

4. Zehbe R, Schmitt VH, Kirkpatrick CJ, Brochhausen C. (2015). "High resolution X-ray tomography – three-dimensional characterisation of cell-scaffold constructs for cartilage tissue-engineering." *Materials Science and Technology* 31 (2), 167-173.

5. Sun W, Li ZR, Yang YR, Shi ZC, Wang B, Liu. (2011). "Experimental study on phase-contrast imaging with synchrotron hard X-ray for repairing osteonecrosis of the femoral head." *Orthopedics.* 34 (9), e530-e534.

6. Appel AA, Larson JC, Garson AB 3rd, Guan H, Zhong Z, Nguyen BN, Fisher JP, Anastasio MA, Brey EM. (2014). "X-ray phase contrast imaging of calcified tissue and biomaterial structure in bioreactor engineered tissues." *Biotechnol Bioeng* 112 (3), 612-620.

7. Boskey A, Pleshko Camacho N. (2007). "FT-IR imaging of native and tissue-engineered bone and cartilage." *Biomaterials* 28 (15), 2465–2478.

8. Huebsch N.D., Mooney D.J. (2007). "Fluorescent resonance energy transfer: a tool for probing molecular cell–biomaterial interactions in three dimensions." *Biomaterials* 28 (15), 2424–2437.

9. Matsumoto B. (2002). *Cell Biology Applications of Confocal Microscopy*. San Diego, Carlifornia: Academic Press.

10. Hofmann MC, Whited BM, Criswell T, Rylander MN, Rylander CG, Soker S, Wang G, Xu Y. (2012). "A fiber-optic-based imaging system for nondestructive assessment of cell-seeded tissue-engineered scaffolds." *Tissue Eng Part C Methods.* 18 (9), 677-687.

11. Ahearne M, Bagnaninchi PO, Yang Y, El Haj A. (2008). "Online monitoring of collagen fibre alignment in tissue-engineered tendon by PSOCT." *J Tissue Eng Regen Med* 2 (8), 521–52.

12. Huzaira M., Rius F., Rajadhyaksha M., Anderson R.R., Gonzalez S. (2001). "Topographic variations in normal skin, as viewed by *in vivo* reflectance confocal microscopy." *J Invest Dermato* 116 (6), 846-852.

13. Muller M., Zumbusch A. (2007). "Coherent anti-Stokes Raman scattering microscopy." *Chemphyschem* 8 (15), 2156–217.

14. Potter K, Butler JJ, Horton WE, Spencer RG. (2000). "Response of engineered cartilage tissue to biochemical agents as studied by proton magnetic resonance microscopy." *Arthritis Rheum* 43 (7), 580-90.

15. Wagner A, Aurich M, Sieber N, Stoessel M, Wetzel WD et al. (2005). "Options and limitations of joint cartilage imaging: DEI in comparison to MRI and sonography." *Nuclear Instruments and Methods in Physics Research Section A: Accelerators, Spectrometers, Detectors and Associated Equipment* 548 (1-2), 47–53.

16. Prang P, Müller R, Eljaouhari A, Heckmann K, Kunz W, Weber T, Faber C, Vroemen M, Bogdahn U, Weidner N. (2006). "The promotion of oriented axonal regrowth in the injured spinal cord by alginate-based anisotropic capillary hydrogels." *Biomaterials* 27 (19), 3560-9.

17. Izadifar Z, Chapman LD, Chen X. (2014). "Computed tomographydiffractionenhanced imaging for *in situ* visualization of tissue scaffolds implanted in cartilage." *Tissue Eng Part C Methods* 20 (2), 140–148.

18. Othman SF, Curtis ET, Plautz SA, Pannier AK, Butler SD, Xu H. (2012). "MR elastography monitoring of tissue-engineered constructs." *NMR Biomed* 25 (3), 452–463.

19. Cartmell S, Huynh K, Lin A, Nagaraja S, Guldberg R. (2004). "Quantitative microcomputed tomography analysis of mineralization within threedimensional scaffolds *in vitro*." . *J Biomed Mater Res A* 69 (1), 97–104.

20. van Lenthe GH, Hagenmüller H, Bohner M, Hollister SJ, Meinel L, Müller R. (2007). "Nondestructive micro-computed tomography for biological imaging and quantification of scaffold-bone interaction *in vivo*." *Biomaterials* 28 (15), 2479-90.

21. Zhu N, Rajaram A, Olubamiji AD, Schreyer DJ, Wysokinski TW, Belev G, Chen XB. (2015). "Optimization of in-line phase contrast imaging setup for *in vivo* visualization of hydrogel scaffolds in nerve tissue engineering applications." *4th TERMIS 2015 World Congress.* Boston, MA.

22. Davis TJ, Gao D, Gureyev TE, Stevenson AW, and Wilkins AW. (1995). "Phase-contrast imaging of weakly absorbing materials using hard X-rays." *Nature* 373, 595 – 598.

23. Zhou S, Brahme A. (2008). "Development of phase-contrast X-ray imaging techniques and potential medical applications." *Physica Medica* 24 (3), 129-148.

24. Jia QJ, Chen Y, Li G, and Jiang XM. (2012). "Optimization of the in-line X-ray phase-contrast imaging setup considering edge-contrast enhancement and spatial resolution." *2012 Chinese Physical Society and the Institute of High Energy Physics of the Chinese Academy of Sciences and the Institute of Modern Physics of the Chinese Academy of Sciences and IOP Publishing Ltd* 36 (3), 267-274.

25. Zhu N, Chapman D, Cooper D, Schreyer DJ, Chen X. (2011). "X-ray diffraction enhanced imaging as a novel method to visualize low-density scaffolds in soft tissue engineering." *Tissue Eng Part C Methods.* 17 (11), 1071-1080.

26. Wilkins SW, Gureyev TE, Gao D, Pogany A & Stevenson AW. (1996). "Phase-contrast imaging using polychromatic hard X-rays." *Nature* 384, 335 - 338.

27. Murrie RP, Stevenson AW, Morgan KS, Fouras A, Paganin DM, Siu KK. (2014). "Feasibility study of propagation-based-contrast X-ray lung imaging on the imaging and Medical Beamline at the Australian Synchrotron." *J Synchrotron Radiat.* 21 (2), 430-445.

28. Murrie RP, Morgan KS, Maksimenko A, Fouras A, Paganin DM, Hall C, Siu KK, Parsons DW, Donnelley M. (2015). "Live small-animal X-ray lung velocimetry and lung micro-tomography at the Australian Synchrotron Imaging and Medical Beamline." *J Synchrotron Radiat* 22 (4), 1049-1055.

29. Takashima K, Hoshino M, Uesugi K, Yagi N, Matsuda S, Nakahira A, Osumi N, Kohzuki M, Onodera H. (2015). "X-ray phase-contrast computed tomography visualizes the microstructure and degradation profile of implanted biodegradable scaffolds after spinal cord injury." *J Synchrotron Radiat* 22 (1), 136-42.

30. Spanne P, Raven C, Snigireva I, Snigirev A. (1999). "In-line holography and phase-contrast microtomography with high energy x-rays." *Phys Med Biol.* 44 (3), 741-749.

31. Schneider CA, Rasband WS, Eliceiri KW. (2012). "NIH Image to ImageJ: 25 years of image analysis." *Nature Methods* 9, 671-675.

32. Wysokinski T, Chapman D, Adams G, Renier M, Suortti P, Thomlinson W. (2015). "Beamlines of the biomedical imaging and therapy facility at the Canadian Light Source-Part 3." *Nuclear Instruments and Methods in Physics Research A* 77 (1), 1-4.

33. Lewis RA, Yagi N, Kitchen MJ, Morgan MJ, Paganin D, Siu KK, Pavlov K, Williams I, Uesugi K, Wallace MJ, Hall CJ, Whitley J, Hooper SB. (2005). "Dynamic imaging of the lungs using x-ray phase contrast." *Phys Med Biol.* 50 (21), 5031-5040.

34. Kitchen MJ, Lewis RA, Morgan MJ, Wallace MJ, Siew ML, Siu KK, Habib A, Fouras A, Yagi N, Uesugi K, Hooper SB. (2008). "Dynamic measures of regional lung air volume using phase contrast x-ray imaging." *Phys Med Biol* 53 (21), 6065-6077.

35. Moya ML, Morley M, Khanna O, Opara EC, Brey EM. (2012). " Stability of alginate microbead properties *in vitro*. ." *J Material Sci: Mater Med* 23 (4), 903–912.

36. Olubamiji AD, Izadifar Z, Chen DX. (2014). "Synchrotron imaging techniques for bone and cartilage tissue engineering: potential, current trends, and future directions." *Tissue Eng Part B Rev* 20 (5), 503-22.

37. Eames BF, de la Fuente L, Helms JA. (2003). "Molecular ontogeny of the skeleton." *Birth Defects Res C Embryo Today* 69 (2), 93-101.

38. Skyscan. (2011) "NRecon User Manual." Retrieved from <http://www.skyscan.be/next/NReconUserGuide.pdf>.

39. Henning TD, Sutton EJ, Kim A, Golovko D, Horvai A, Ackerman L, Sennino B, McDonald D, Lotz J, Daldrup-Link HE. (2009). "The influence of ferucarbotran on the chondrogenesis of human mesenchymal stem cells." *Contrast Media Mol Imaging.* 4 (4), 65-73.

Chapter 4: Traditional Invasive and Synchrotron-Based Non-Invasive Assessments of 3D-printed Hybrid Cartilage Constructs

This chapter was adopted from the publication of "Adeola D Olubamiji, Ning Zhu, Tuanjie Chang, Chijioke Nwankwo, Zohreh Izadifar, Ali Honaramooz, Xiongbiao Chen and B Frank Eames. Traditional Invasive and Synchrotron-Based Non-Invasive Assessments of 3D-printed Hybrid Cartilage Constructs. Submitted to "Tissue Engineering Part C" in October 2016. Per the Copyright Agreement, "the authors retain the right to include the journal article, in full or in part, in a thesis or dissertation".

4.1. Abstract

Three-dimensional (3D)-printed constructs made of polycaprolactone (PCL) and chondrocyte-impregnated alginate hydrogel (hybrid cartilage constructs) mimic the biphasic nature of articular cartilage, offering promise for cartilage tissue engineering (CTE) applications. However, the regulatory pathway for medical device development requires validation of such constructs through *in vitro* bench tests and *in vivo* preclinical examinations premarket approval. Furthermore, non-invasive imaging techniques are required for effective evaluation of the progress of these cartilage constructs, especially when implanted in animal models or human subjects. However, characterization of the individual components of the hybrid cartilage constructs and their associated time-dependent structural changes by currently available non-invasive techniques is challenging as these constructs contain a combination of hydrophobic and hydrophilic biomaterials with different refractive indices.

Here, we report the use of a novel synchrotron-radiation inline phase contrast imaging computed tomography (SR-inline-PCI-CT) approach for non-invasive (*in situ*) characterization of 3D-printed hybrid cartilage constructs that has been implanted subcutaneously in mice over a 21-day period. In parallel, traditional invasive assays was used to evaluate the *in vivo* performance of the implanted hybrid cartilage constructs with respect to their cell viability and secretion of cartilage-specific extracellular matrix (ECM) over the 21-day period post-implantation in mice. SR-inline-PCI-CT allowed striking visualization of the individual components within the 3D-printed hybrid cartilage constructs as well as characterization of the time-dependent structural changes after implantation. In addition, the relationship between the implanted constructs and the surrounding tissues was delineated. Furthermore, traditional assays showed that cell viability

within the cartilage constructs was at least 70 % at all three time-points, and secretion of alcian blue- and collagen type 2-positive matrices increased progressively over the 21-days period post-implantation. Overall, these results demonstrate the 3D-printed hybrid cartilage constructs have good *in vivo* performance and validate their potential for regeneration of articular cartilage *in vivo*. In addition, SR-inline-PCI-CT has demonstrated potential for longitudinal and non-invasive monitoring of the functionality of 3D-printed hybrid cartilage constructs in a way that is translatable to other soft tissue engineering applications.

4.2. Introduction

Cartilage tissue engineering (CTE) offers great potential for regeneration of articular cartilage damaged by osteoarthritis or trauma. However, cartilage is hard to mimic because its functionality relies on the biphasic nature of cartilage extracellular matrix (ECM). Its solid phase is a framework of collagen fibrils and proteoglycan aggregates, while its liquid phase contains cells and nutritive fluid [1-3]. 3D-printed hybrid cartilage constructs fabricated from hydrophobic polycaprolactone (PCL) (for structural support) and highly hydrophilic cell-impregnated alginate hydrogel (for hydration and biological function) mimic the biphasic nature of the articular cartilage ECM and provide structural integrity, load-bearing capabilities, a cell-friendly environment, and 100 % pore interconnectivity (for easy fluid transfer) required for secretion of cartilage ECM [4–7]. To regenerate structural and functional features of articular cartilage, the hybrid constructs must function such that the cells within the cell-impregnated alginate strands gradually secrete cartilage-specific ECM (including collagen type 2 (Col2) and sulfated glycosaminoglycans (GAGs)) as the PCL strands gradually degrade. A few *in vitro* studies showed that cells within these 3D-printed hybrid cartilage constructs remained highly viable and progressively secreted cartilaginous matrix over time [4-7]. Moreover, limited data suggest suitable performance of these 3D-printed hybrid cartilage constructs *in vivo,* with the secretion of Col2 over a 4-week period after implantation in athymic mice [5]. Thus, more comprehensive *in vivo* studies are needed to examine the functionality of the 3D-printed hybrid cartilage constructs and their potentials for clinical applications. Furthermore, a major limitation to examining the *in vivo* performance of cartilage constructs is current non-invasive visualizationtechniques that preclude longitudinal monitoring and assessment of the 3D-printed hybrid cartilage constructs in the same animal over time. Histological analyses, complemented by two-dimensional (2D) imaging techniques, is known to provide standard assessments of cell viability and secretion of ECM in engineered constructs [5,

7-10]. However, these traditional techniques are invasive and samples can only be assayed at one time-point as they ought to be excised prior to the analyses.

Confocal microscopy, optical coherence tomography, and Raman spectroscopy have been studied as alternatives to 2D imaging techniques for TE applications [11-14]. Unfortunately, these techniques have inadequate penetration depth and often require the use of contrast agents to enhance their sensitivity [15-18]. Positron emission tomography and single-photon emission computed tomography have high penetration depth and have been praised for enabling successful tracking of cells *in vivo* [19-21]. However, these techniques require the use of contrast agents that might have a negative effect on cell performance. In addition, these techniques often experience poor temporal and spatial resolution that consequently limit visualization of microstructural details, which is critical to the tracking time-dependent biomaterial degradation and tissue growth [19-21]. Furthermore, radiography (such as micro-CT and CT) can assess structural details within tissue constructs [22-23], but poor contrast from highly hydrophilic materials with low attenuation coefficients, such as cartilage and hydrogels, is their major drawback for CTE applications [24]. Magnetic resonance imaging (MRI) is an established preclinical and clinical technique, well known for its ability to delineate soft tissue contrast; therefore, it is often used for visualizing cartilage damage, tissue remodeling, soft tissue constructs, and, recently, with contrast agents to track cells in constructs [25-30]. However, MRI has poor spatial resolution, provides poor imaging contrast for hydrophobic materials and tissues, and may require contrast agents to boost sensitivity. These drawbacks are the bottlenecks that makes it challenging to use MRI for non-invasive characterization of thin growing neo-tissues and our multi-material cartilage constructs [26, 31]. Overall, the trade-offs of currently available imaging techniques made their utilization challenging with respect to non-invasive characterization of the biphasic cartilage constructs investigated in this study and their time-dependent structural changes.

An effective non-invasive 3D imaging technique intending to monitor the functionality of the hybrid cartilage constructs should have the capability to (1) visualize the hydrophobic and the hydrophilic components of the hybrid cartilage constructs; (2) enable visualization of the progression of the newly forming neo-tissues within the constructs and the biodegradation profiles of all the components of the cartilage constructs; (3) delineate the relationship between the cartilage constructs and their surrounding host tissues without destroying or posing any risk to the host animal model or human subject [16, 18, 30, 32]. Owing to the presence of multiple attenuation

coefficients, densities and other material properties (i.e. the combination of hydrophobic PCL and hydrophilic cell-impregnated alginate hydrogel) within the hybrid cartilage constructs, their non-invasive characterization is challenging [10, 16, 18, 33]. The novel method of synchrotron-radiation inline phase contrast imaging computed tomography (SR-inline-PCI-CT) circumvents most of the limitations of the other imaging techniques discussed above, and therefore have potentials for non-invasive monitoring of the 3D-printed hybrid cartilage constructs and their performance over time either *in situ*, *ex vivo* or *in vivo.* Although at least six specific PCI techniques are being explored, SR-inline-PCI-CT has the simplest experimental setup, uses no optical element (e.g., gratings or diffracting crystals) and was the first phase-contrast technique to be pioneered [18, 34-37]. SR-inline-PCI-CT uses variations in phase shifts of X-rays passing through the samples to visualize materials with different refractive indices, electron densities, and atomic numbers present within the samples without requiring the use of exogenous contrast agents [18, 34-36]. At diagnostic X-ray energies, SR-inline-PCI-CT produces its image signal from refraction generated from the real part of the material refractive index, which is up to 1000 times greater than the absorption signal used by conventional absorption-based imaging techniques [34-36, 38]. Due to the high lateral (spatial) coherence of synchrotron X-rays, SR-inline-PCI-CT translates variations in densities and refractive indices of different materials into edge enhancement at their interfaces in the images. Thus, SR-inline-PCI-CT offers a robust capability to simultaneously characterize newly growing or native hard and soft tissues. SR-inline-PCI-CT can also visualize time-dependent structural changes in multiple biomaterials over time post-implantation [7, 10, 30, 39-41]. In relation to this present study, we have recently reported that SR-inline-PCI enabled unparalleled and non-invasive visualization of the 3D-printed hybrid cartilage constructs submerged in fluid (to mimic physiological conditions) and their associated time-dependent subtle structural changes over a-42-day period of *in vitro* culture [7].

In the present study, we used *in vivo* evaluation of the 3D-printed hybrid cartilage constructs as therapeutics for damaged articular cartilage and assessment of their performance using both traditional invasive and synchrotron-based non-invasive techniques. 3D-printed hybrid cartilage constructs (PCL/alginate/cells construct) were implanted subcutaneously in the backs of nude mice and tracked over a 21-day period. Invasive assessments of the functionality of these constructs demonstrated high cell viability and secretion of cartilage-specific ECM over the 21-day post-implantation in mice. Importantly, SR-inline-PCI-CT enabled *in situ* non-invasive characterization

of the individual components of the 3D-printed hybrid cartilage constructs, their surrounding tissues, and associated structural variations over 21 days post-implantation in mice. Summarily, these data further validate the potentials of the 3D-printed hybrid cartilage constructs for CTE applications (this time *in vivo*), and proved that non-invasive longitudinal monitoring of the functionality and degradation of the multi-components tissue constructs might be possible using SR-inline-PCI-CT.

4.3. Materials and Methods

4.3.1. Materials

Polycaprolactone (average Mw~45,000), alginic acid sodium salt; medium viscosity alginate (MVA), mouse chondrogenic cell line ATDC5, calcium chloride dehydrate ($CaCl_2$), Stemline® Keratinocyte Medium II-Calcium free (SKM), 4-(2-hydroxyethyl)-1-piperazineethanesulfonic acid (HEPES) buffer, phosphate buffer saline Tween-20 (PBST) and ethylenediaminetetraacetic acid (EDTA) were purchased from Sigma-Aldrich, St. Louis, MO, USA. Dulbecco's modified Eagle's medium (DMEM)/Ham's F-12 (1:1), foetal bovine serum (FBS), penicillin, streptomycin, buprenorphine, glutamine and ascorbate-2-phosphate and insulin-transferrin-selenium plus (ITS+) liquid media supplement were purchased from Life Technologies, Carlsbad, CA, USA. Purified anti-Col2 antibody [CIIC1] was purchased from Developmental Studies Hybridoma Bank, Iowa City, IA, USA and goat anti-mouse IgG (H+L) secondary antibody, Alexa Fluor® 488 conjugate was purchased from EMD Millipore, Temecula, CA, USA. Twenty adult male athymic immunodeficient nude (Crl: *NU(NCr)-Foxn1^{nu}*) mice were purchased from Charles River Laboratories, NY, USA.

4.3.2. Cell Culture / Expansion

Frozen ATDC5 cells were thawed and 2D cultured in tissue culture dishes for one week in a humidified incubator with 5 % CO_2 at 37°C. Culture media were changed every 2 - 3 days to enable cell expansion. The culture medium consisted of DMEM/Ham's F-12 (1:1) supplemented with 5 % FBS, 100 unit/mL penicillin, 100 µg/mL streptomycin, 10 mg/mL glutamine, and 0.05 mg/mL ascorbate-2-phosphate. After one week, expanded cells were collected from tissue culture plates, counted, and re-suspended in culture medium for fabrication of the hybrid constructs.

4.3.3. Design and Fabrication of Hybrid Cartilage Constructs

Design and fabrication of the 3D-printed hybrid cartilage constructs were conducted as previously described [6-7]. The geometry of the designed model of the constructs was 10 mm × 10 mm × 0.96 mm, and consisted of four layers of cylindrical strands with 1 mm inter-strand spacing and an alternating 0-90° perpendicular pattern from one layer to the other. For the fabrication, PCL pellets were loaded into the high-temperature dispensing head of a 3D Bioplotter system (Envisiontec, Germany), heated up to 150°C for 20 min to destroy potential microbial contamination and cooling to the dispensing temperature of 85°C. MVA was dissolved in SKM medium to obtain 3.3 % w/v alginate hydrogel. Then, alginate-cells solution was prepared by suspending 8×10^6 cells per ml of alginate hydrogel solution for the preparation of a final concentration of 2.5 % w/v. The prepared alginate-cell solution was loaded into the low-temperature dispensing head and maintained at 10°C. During the printing, melted PCL strands were dispensed from a 300 μm inner diameter cylindrical metal needle at deposition speed (the same as the needle's horizontal speed) of 1 mm/s and a pneumatic pressure of 0.08 MPa and cell-laden alginate strands were printed within two adjacent PCL strands from a 200 μm inner diameter conical needle at deposition speed of 25 mm/s and pneumatic pressure of 0.03 MPa. The side-by-side and layer-by-layer alternating deposition of PCL and alginate strands continued for each construct until four hybrid layers were printed. Strand thicknesses were 0.3 mm for the PCL strands and 0.2 mm for the alginate strands respectively. After printing each layer, alginate strands were partially crosslinked using fumes released from a nebulizer, which contained 170 mM $CaCl_2$ in 4.2 mM HEPES (in 0.35 M sucrose). Once a construct was completely printed, it was immediately transferred into 100 mM $CaCl_2$ (in 4.2 mM HEPES and0.35 M sucrose solution (pH 7.4)) for 20 min to further crosslink the alginate-cells strands within the constructs. After crosslinking, the constructs were washed in DMEM solution for 5 min twice and placed in 12-well culture plates with culture medium and subsequently transferred into an incubator operating at 37ºC and 5 % CO_2. The culture medium was changed every 2 d to enhance cell differentiation and consisted of DMEM/ Ham's F-12 (1:1) supplemented with 5 % FBS, 100 unit/mL penicillin, 100 μg/mL streptomycin, 10 mg/mL glutamine, 10 mg/mL ITS+ liquid media and 0.05 mg/mL ascorbate-2-phosphate. The constructs were cultured *in vitro* for 2 weeks in the incubator to initiate cell differentiation before implantation into the mice. Hybrid scaffolds with no impregnated cells were also fabricated, as described above, to serve as controls.

4.3.4. Surgical Implantation of Hybrid Cartilage Constructs

The Animal Research Ethics Board of the University of Saskatchewan, SK, Canada, approved the protocol for implantation of the 3D-printed hybrid constructs in mice in compliance with guidelines for humane animal care set by the Canadian Council on Animal Care. Upon their arrival, the 20 adult male nude mice (Crl: *NU(NCr)-Foxn1^{nu}*) were acclimatized for 2 weeks prior to scheduled surgical implantation. The mice were housed in groups of three in individual Plexiglass cages, lined with sterile sawdust in a room with a controlled photoperiod (lights on from 06:00 through 18:00), at a constant 21ºC and 60 % humidity. The mice were handled aseptically, provided *ad libitum* with sterile water and standard mouse chow, and were randomly divided into control and treatment groups. Hybrid construct-implanted mice were prepared for (i) histological assessments and (ii) *in situ* SR-inline-PCI-CT. For the surgery, the mice were anaesthetized in a biosafety cabinet and kept warm using a heated pad. Small incisions were created along the backs of the mice for four constructs to be implanted in their dorsal subcutaneous pockets: two on the left and two on the right sides (Fig.1). All four constructs implanted into the mice for histological analysis were cell-laden and the mice prepared for SR-inline-PCI-CT imaging were each implanted with two cell-laden constructs on the right and two cell-free hybrid constructs on the left sides. The animals were injected with 0.1 mg/kg subcutaneous (sc) of buprenorphine as an analgesic once immediately after the surgery, again 12 h post-operatively, and followed by its addition into their drinking water for a period of one week.

Fig. 4.1: Image of a nude mouse undergoing surgical implantation of 3D-printed hybrid cartilage constructs. Subcutaneous pockets were created lateral to a midline incision, through which the constructs for the left and right sides were inserted.

4.3.5. Invasive Assessments of Hybrid Cartilage Constructs

At each of the three time-points (7, 14 and 21 days) post-implantation, three mice were sacrificed by decapitation for histological analysis of the 3D-printed cartilage constructs. All four cell-laden constructs were excised from the mice and, each construct was cut into four square sections and each of them was used for the different histological and biological analyses, as described below (each assay had *n=12* per time-point).

4.3.6. Cell Viability of Cells within the Hybrid Cartilage Constructs

For the cell viability assay, two-colour florescence LIVE/DEAD® Kit (Molecular Probes, OR) was used. At each time-point, the samples were stained as previously described [6-7]. Briefly, samples were washed with DMEM and submerged in staining solution containing 2 μM calcein-AM and 0.5 μM ethidium homodimer (EthD-1) in DMEM and kept in the dark for about 1 h in an incubator running at 37ºC and 5 % CO_2. After staining, photomicrographs of the horizontal and cross-section views of the stained constructs were acquired to visualize live cells (fluorescing green) and dead cells (fluorescing red) using a DP70 camera attached to a Nikon fluorescent inverted microscope (Nikon, ECLIPSE E600, SPOT Insight™ Camera, USA). For quantification of cell viability, constructs were submerged in 50 mM EDTA solution to dissolve the alginate strands and release the cells. Then, 10 μl of the cell suspension was gently pipetted onto a glass slide and covered with a coverslip to acquire photomicrographs of live and dead cells at different locations on the glass slide. Live and dead cells numbers were counted in randomly selected regions of interest cropped from photomicrographs in ImageJ software [42].

4.3.7. *In vivo* Secretion of Sulfated GAGs within Hybrid Cartilage Constructs

To estimate secretion of sulfated GAGs in the excised hybrid constructs, samples were stained with alcian blue and analysed as previously described [6-7]. Briefly, the samples were washed in DMEM, fixed in acetone: methanol (1:1), submerged in 0.5 mg/mL alcian blue in 3 % acetic acid (pH=1) and kept on rocking tray overnight at room temperature. The stained constructs were then de-stained in 25 % ethanol in 3 % acetic acid for 1 h and stored in 50 % ethanol in 3 % acetic acid prior to acquisition of photomicrographs of the constructs. For quantitative analysis, randomly selected regions of interest within the alginate hydrogel strands were cropped for each of the three time-points using ImageJ software [42]. An appropriate threshold was applied to

segment the alcian-blue-stained region from the background for each image. The measured values of the stained region in relation to the entire region of interest were used to calculate the area covered by alcian blue staining in the constructs at 7, 14 and 21 days post-implantation and used to quantify the secretion of sulfated GAGs at each time-point.

4.3.8. *In vivo* Secretion of Col2 within the Hybrid Cartilage Constructs

Immunofluorescent staining was used for analysis of the progression of secretion of Col2 within the hybrid constructs at 7, 14 and 21 days post-implantation as previously described [6 - 7]. The specimens were fixed, washed three times in PBST for 15 min each time, washed in 0.05 % EDTA in PBS and digested in trypsin solution (0.1 % trypsin, 1 mM EDTA and 1x PBS). After the trypsin step, constructs were incubated for 2 h in 1:100 purified anti-Col2 [CIIC1] antibody in blocking buffer (4 % normal goat serum and 2 % normal sheep serum in PBST). The constructs were then washed 6 to 8 times in blocking buffer over a 2 h period. For the second incubation, 1:1000 goat anti-mouse IgG-488 conjugate in blocking buffer was used. The constructs were washed again in PBST over another 2 h period to minimize background stains. Subsequently, photomicrographs of the horizontal and cross-sectional views of stained constructs at different time-points were taken using a DP70 camera, as described above. For quantitative analysis, randomly selected regions of interest within the alginate hydrogel strands were cropped from photomicrographs per time–point in ImageJ [42]. An appropriate threshold was applied to segment the Col2-stained region within the alginate strands from the background for each image in ImageJ as previously described [7]. The measured values of stained region in relation to the region of interest were used to quantify the area covered by Col2 stain in the constructs at 7, 14 and 21 days post-implantation.

4.3.9. Non-Invasive Visualization of Hybrid Cartilage Constructs in Mice using SR-Inline-PCI-CT

Non-invasive SR-inline-PCI-CT imaging of the 3D-printed hybrid constructs at 7 and 21 days post-implantation in mice was performed at the Biomedical Imaging and Therapy facility 05ID-2 beamline at the Canadian Light Source (CLS), Saskatoon, Canada. Sacrificed animals in intact condition were transported to the CLS on ice for non-invasive *in situ* imaging. The imaging set-up consisted of a double crystal bent Laue monochromator tuned to 30 keV imaging energy, and a superconducting wiggler X-rays source with a beam of 220 mm horizontal size and 11 mm

vertical size at a distance of 55 m from the source [43]. The mice were placed in sample holders and positioned on a rotating scanning stage for CT scanning. Based on our previous data [7], tomographic data sets were collected at a 3-m sample-to-detector-distance (SDD) using a beam monitor AA-60 (Hamamatsu) coupled to a Hamamatsu camera C9300-124 with effective pixel size of 8.47 µm and exposure time between 0.03 to 0.06 s. For each data set, 3000 projections were collected over a 360° rotation, and a set of 10 flat-field and 10 dark-field images were acquired before and after each scan to correct the acquired projections. Two to three scans were required to capture the entire mouse in each case.

Prior to the image reconstruction, the flat- and the dark-field images were used for projection corrections with an ImageJ macro plugin (written by Dr. Cooper, College of Medicine, University of Saskatchewan, SK., Canada). Then, Modified Feldkamp Algorithm in NRecon V 1.6.10.1 (Bunker, Kontich, Belgium) was used for the non-retrieved image reconstruction to obtain image slices based on recommendations made in [7]. The images were cropped and exported into FEI Amira 6.0.1 (Oregon, USA) 3D visualization and analysis software for rotation and 3D volume rendering to further visualize the microarchitecture of the different components and minute details in the hybrid constructs within the mice. In addition, 3D visualization of the 3D-printed constructs in the mice was subsequently performed in ImageJ [42].

4.3.10. Statistical Analysis

To evaluate changes in Col2-stained area, alcian blue-stained area, and cell viability within the 3D-printed cartilage constructs at 7, 14 and 21 days post-implantation in mice, a one-way repeated measures analysis of variance (RM-ANOVA) was carried out in SPSS (Released 2013 IBM SPSS Statistics for Windows, Version 21.0. Armonk, NY: IBM Corp.). Due to violation of sphericity by the alcian blue staining data, a Greenhouse–Geisser correction was applied. *Post hoc* tests using the Bonferroni's correction were conducted to estimate the statistical significance between cell viability, areas covered by alcian blue stain and areas covered by Col2 stain at the different time-points. Statistical significant was set at $P < 0.05$ for all analyses conducted.

4.4. Results

4.4.1. Cells Embedded in Hybrid Cartilage Constructs Remained Viable Post-Implantation in Mice

To evaluate cell distribution and viability, 3D-printed hybrid cartilage constructs were harvested from the backs of mice at various time-points and subjected to LIVE/DEAD stains. The

results showed that uniform cell viability and cell distribution were maintained in both the periphery and the centre of the alginate strands within the hybrid cartilage constructs over the 21 day post-implantation period (Fig. 2). Quantification confirmed that the cell viabilities was 83 ± 5.4% at 7 days post-implantation, 70 ± 6.6% at 14 days post-implantation, and 73 ± 7.9% at 21 days post-implantation (Fig 2I). A one-way repeated measures ANOVA (assuming sphericity) demonstrated that cell viability was significantly different among time-points *(F (2, 18) = 505.719, P = 0.002)*. Specifically, *post hoc* tests showed that cell viability significantly differed between 7 and 14 days post-implantation *(P>0.001;* Fig. 2I). Overall, cell viability in the 3D-printed hybrid constructs in nude mice remained at a minimum of 70% throughout the entire 21-day implantation period.

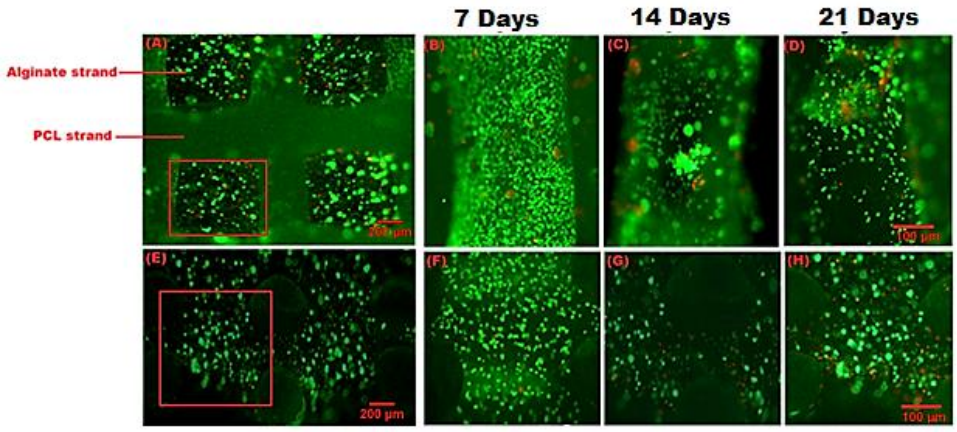

(I): Graphical illustration of cell viability within the constructs at different timepoints

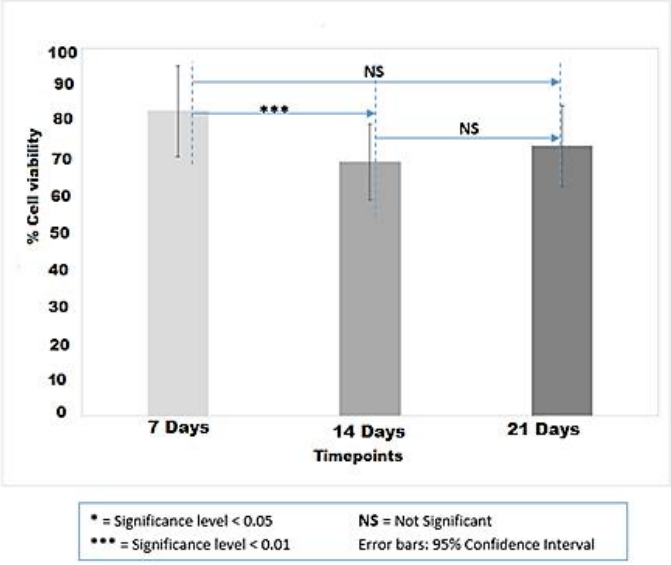

Fig. 4.2: High cell viability in 3D-printed hybrid cartilage constructs over 21 days subcutaneous implantation in nude mice. (A)

Fluorescence imaging showed that live (green) and dead (red) cells were distributed uniformly in 3D-printed constructs at 21 days post-implantation. (B-D) Higher magnification images of similar regions as indicated by the red box in panel A showed high levels of cell viability at 7, 14 and 21 days post-implantation. (E) Image taken after cutting the construct transversely showed good cell distribution and viability throughout the alginate strand at 21 days post-implantation. (F-H) Higher magnification images of regions of interest similar to the red box in panel E demonstrated high viability at 7, 14 and 21 days post-implantation. (I) Statistical quantitation confirmed high cell viability in 3D-printed hybrid cartilage constructs excised from nude mice at 7, 14, and 21 days post-implantation (see footnote 1).

4.4.2. Progressive Secretion of Cartilage Matrix in Constructs Post-Implantation in Mice

To examine cartilage matrix secretion, harvested 3D-printed hybrid cartilage constructs were subjected to alcian blue and Col2 staining. Alcian blue staining demonstrated that secretion of sulfated GAGs increased progressively over the 21 days post-implantation (Fig. 3). Specifically, the area covered by alcian blue staining in the excised hybrid constructs seemed to increase and staining intensity appeared to darken progressively when the data obtained at 7 days and 21 days post-implantation were compared (Fig. 3A - D). This progressive increase in alcian blue-positive matrix occurred around cells at both the centre and periphery of the alginate strands (Fig. 3E-H). Quantitative analyses (Fig 3I) in the form of a one-way repeated measures ANOVA demonstrated that the mean area covered by alcian blue-positive matrix in the 3D-printed hybrid constructs differed significantly among time-points ($F\ (1.091, 7.636) = 10.879$, $P = 0.011$). *Post hoc* tests revealed that the area covered by the alcian blue-positive matrix increased significantly between 7 and 14 days ($P < 0.006$) and between 7 and 21 days ($P < 0.020$) post-implantation.

Col2 immunostaining suggested that Col2 matrix was progressively secreted in the 3D-printed hybrid cartilage constructs over the 21-day period post-implantation in mice (Fig. 4A-D). This apparent increase in Col2-positive matrix occurred around cells at both the centre and periphery of the alginate strands (Fig. 4F-H). Quantitative analyses of the area covered by Col2-stained matrix confirmed progressive secretion of collagen matrix in the excised hybrid constructs (Fig. 4I). Specifically, the mean area covered by Col2 staining in the alginate strands was significantly different among time-points ($F(2, 14) = 57.624$, $P<0.001$; Fig. 7). *Post hoc* tests revealed that Col2 secretion increased significantly between 7 and 21 days ($P<0.001$) and between 14 and 21 days ($P<0.001$).

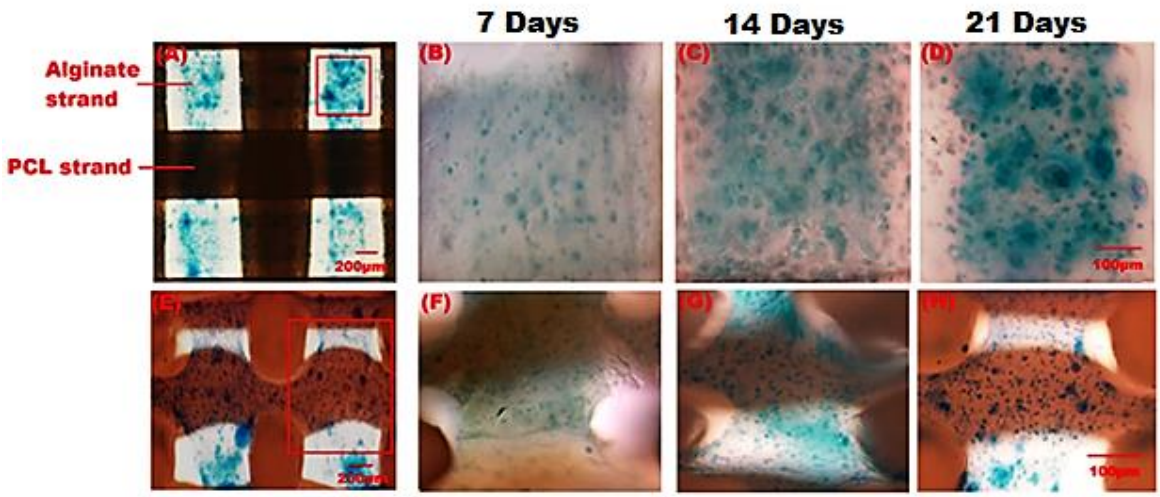

I: Graphical illustration of distribution of Alcian blue stains at different timepoints

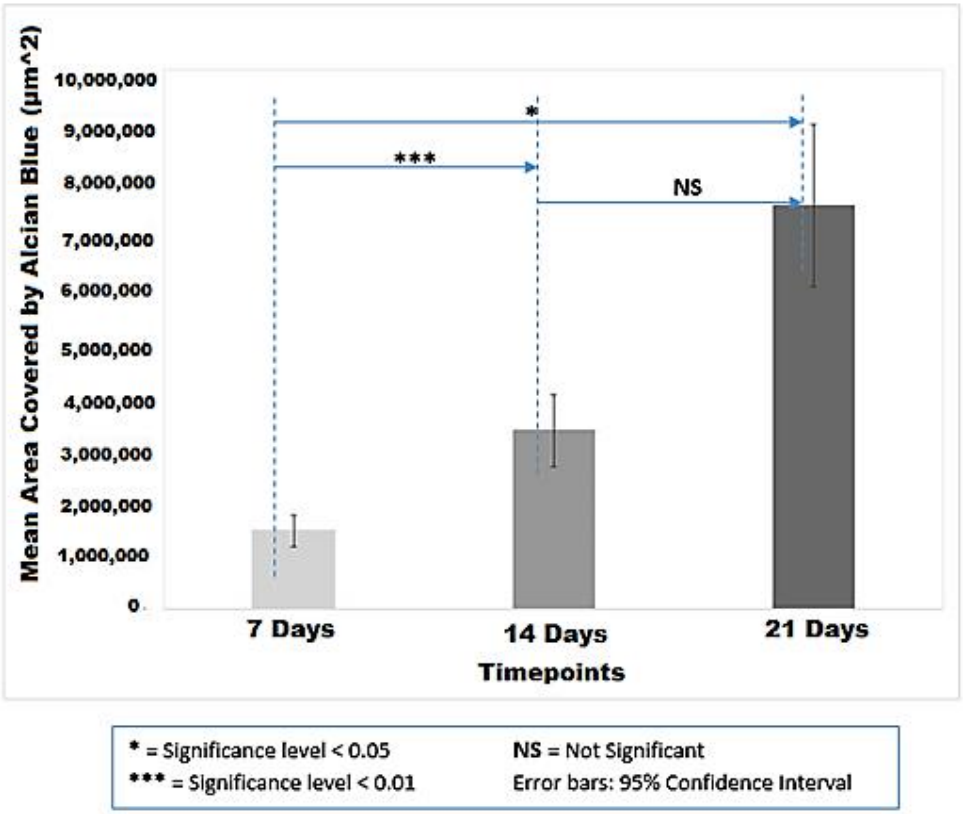

Fig. 4.3: Alcian blue-positive matrix increased over time in 3D-printed hybrid cartilage constructs implanted subcutaneously into the backs of nude mice. (A) Alcian blue staining in alginate strands of the hybrid construct was detected at 21 days post-implantation. (B-D) Higher magnification images of similar regions as indicated by the red box in panel A showed increased Alcian blue staining at 7, 14 and 21 days post-implantation. (E) Image taken after cutting the construct transversely demonstrated Alcian

blue staining throughout the alginate strands at 21 days post-implantation. (F-H) Higher magnification images of regions of interest similar to the red box in panel E showed increased Alcian blue staining at 7, 14 and 21 days post-implantation. (I) Quantitation confirmed that Alcian blue staining increased in 3D-printed hybrid cartilage constructs excised from nude mice at 7, 14, and 21 days post-implantation [(see footnote 1)].

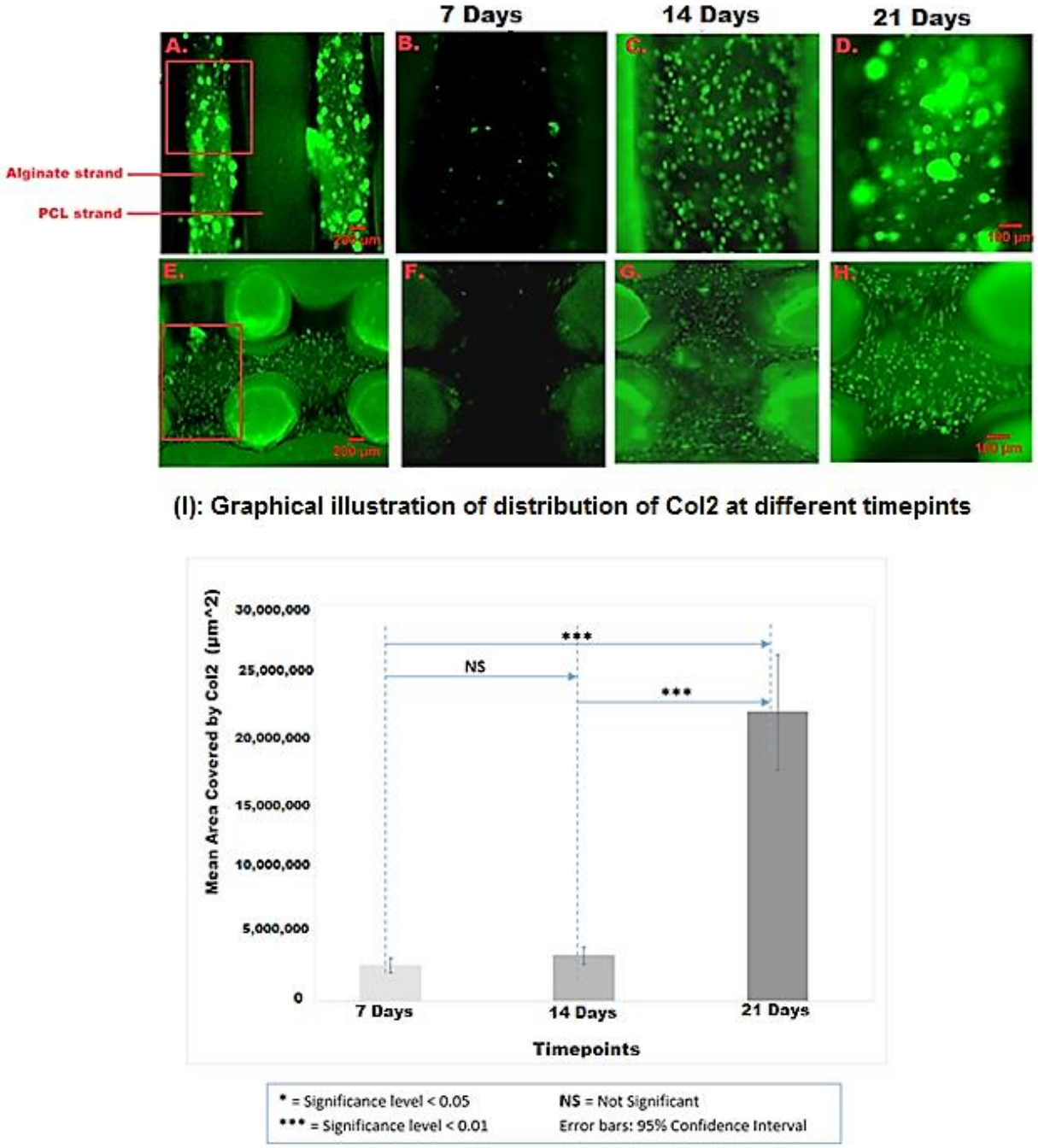

Fig. 4.4: Col2 staining increased over time in 3D-printed hybrid cartilage constructs implanted subcutaneously into the backs of nude mice. (A) Col2 staining in alginate strands of the hybrid construct was detected at 21 days post-implantation. (B-D) Higher

magnification images of similar regions as indicated by the red box in panel A showed increased Col2 staining at 7, 14 and 21 days post-implantation. (E) Image taken after cutting the construct transversely demonstrated Col2 staining throughout the alginate strand at 21 days post-implantation. (F-H) Higher magnification images of regions of interest similar to the red box in panel E showed increased Col2 staining at 7, 14 and 21 days post-implantation. (I) Quantitation confirmed that Col2 staining increased in 3D-printed hybrid cartilage constructs excised from nude mice at 7, 14, and 21 days post-implantation (see footnote 1).

4.4.3. SR-Inline-PCI-CT Enabled Non-Invasive Visualization of the Individual Components within Constructs and Surrounding Host Tissues

To visualize intact 3D-printed hybrid cartilage constructs non-invasively, SR-inline-PCI-CT was conducted using parameters established in our previous *in vitro* study of the 3D-printed hybrid cartilage constructs [7]. Mice were sacrificed at 7 and 21 days post-implantation and the SR-inline-PCI-C images were acquired. Reconstructed images of SR-inline-PCI-CT projection data clearly showed various soft and hard tissues such as skin, bone, lung, intestine, and internal soft tissues, of the host mouse (Fig. 5A). Importantly, the reconstructed slices appeared to show the individual alginate and PCL strands within the hybrid cartilage constructs in intact conditions within the mice at the earlier time-point (Fig. 5B). In addition, 3D rendering of the reconstructed slices from SR-inline-PCI-CT data further enhanced the delineation of interfaces between the PCL and alginate strands within the hybrid cartilage constructs (Fig. 5C).

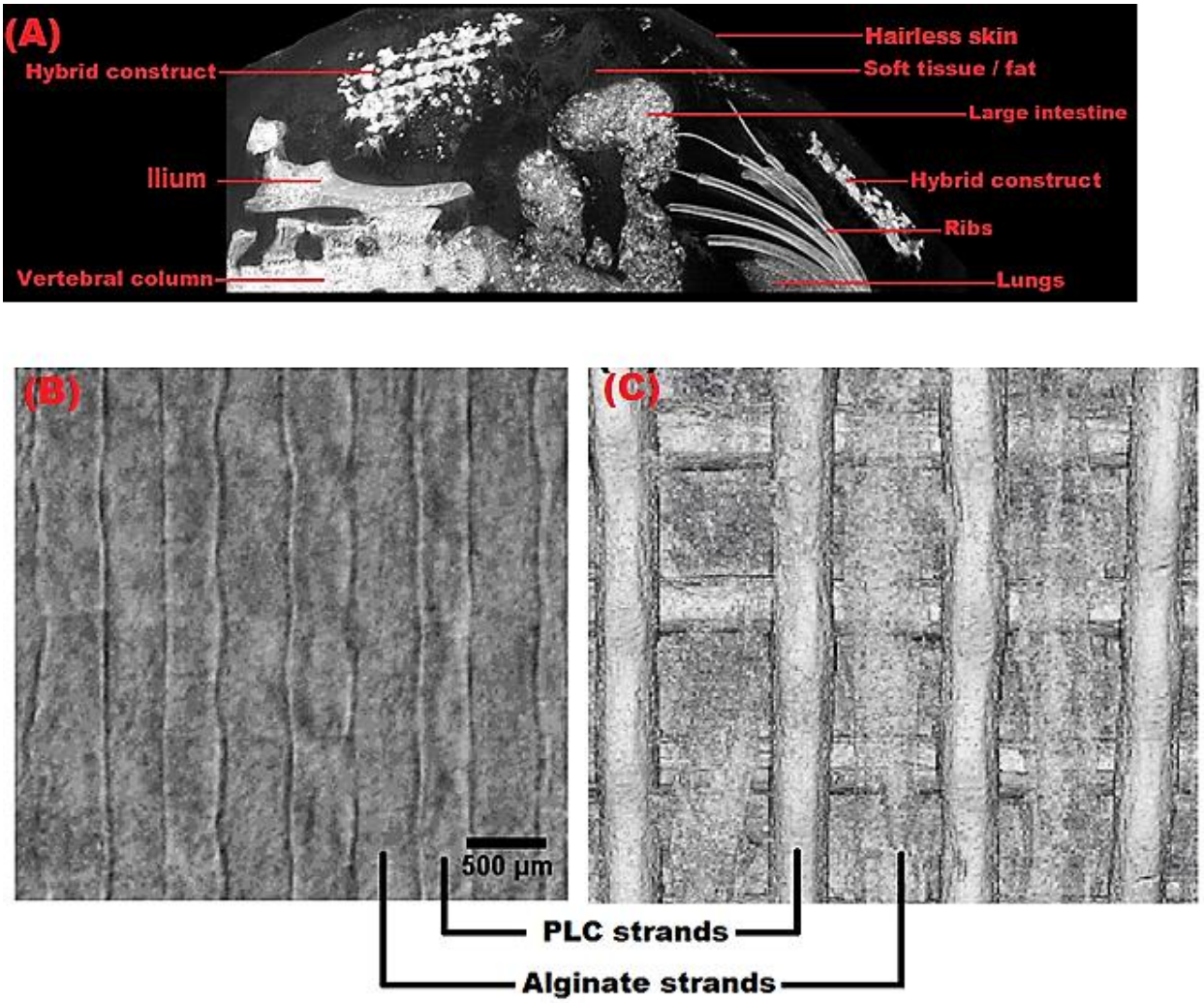

Fig. 4.5: SR-inline-PCI-CT visualized 3D-printed hybrid cartilage constructs in vivo. (A) SR-inline-PCI-CT image showed two of the hybrid cartilage constructs 7days after being implanted subcutaneously into the back of a nude mouse. Their relationship to surrounding host tissues was also evident. Higher magnification images (B, grey-scale image of reconstructed slices; C, 3D-rendered image) of a hybrid cartilage construct distinguished both PCL and alginate strands 7 days after in vivo implantation.

4.4.4. SR-Inline-PCI-CT Enabled Non-Invasive Visualization of Time-Dependent Structural Changes within Cartilage Constructs post-implantation in Mice

Furthermore, structural changes within the 3D-printed hybrid cartilage constructs over the 21 days post-implantation were explored non-invasively using SR-inline-PCI-CT. Images representing equivalent regions of a stack of reconstructed slices showed visible structural changes within the cell-impregnated hybrid constructs between 7 and 21 days post-implantation (Fig. 6). At 7 and 21 days post-implantation, representative alginate and PCL strands were apparent (Fig. 6B, C). Careful analyses of image pixel intensities more clearly demonstrated the capabilities of SR-inline-PCI-CT to distinguish components of the hybrid cartilage constructs. Very large grey-

value peaks reflecting high phase contrast correlated with the edges of the PCL strands and the interfaces between the alginate and PCL strands (Fig. 6 E-G, H-J; see regions 1 and 3). Much lower grey-value peaks correlated with changes apparent within the alginate strands (Fig. 6 E - G, H - J; see region 2). Comparison of the cell-laden alginate strands at 7 and 21 days post-implantation showed time-dependent structural changes. Recorded grey values tend to decrease overall at 21 days post-implantation, but visible structural changes in the alginate strands between 7 and 21 days post-implantation were associated with increased peak correlating to grey values (Fig. 6 E - G, H - J; see region 2). These time-dependent changes within alginate strands revealed by SR-inline-PCI-CT may be in part dependent on the presence of cells within the alginate strands. This is because cell-free alginate strands looked very different from these cell-impregnated alginate strands at 21 days post-implantation (Fig. 6C, D). In some regions, the cell-free alginate strands have varying phase contrast and edge enhancement characteristics (Fig. 6D, upper left region). This characteristic was apparent after harvesting the constructs from the mice, as regions similar to those analysed in the SR-inline-PCI-CT for the cell-free constructs showed clear and opaque alginate strands in-between the PCL strands (data not shown). In regions showing differences between the PCL and alginate strands, there was much less phase contrast information over the width of the alginate strand (Fig. 6J, region 2). In summary, non-invasive SR-inline-PCI-CT revealed time-dependent structural changes with the 3D-printed hybrid cartilage constructs.

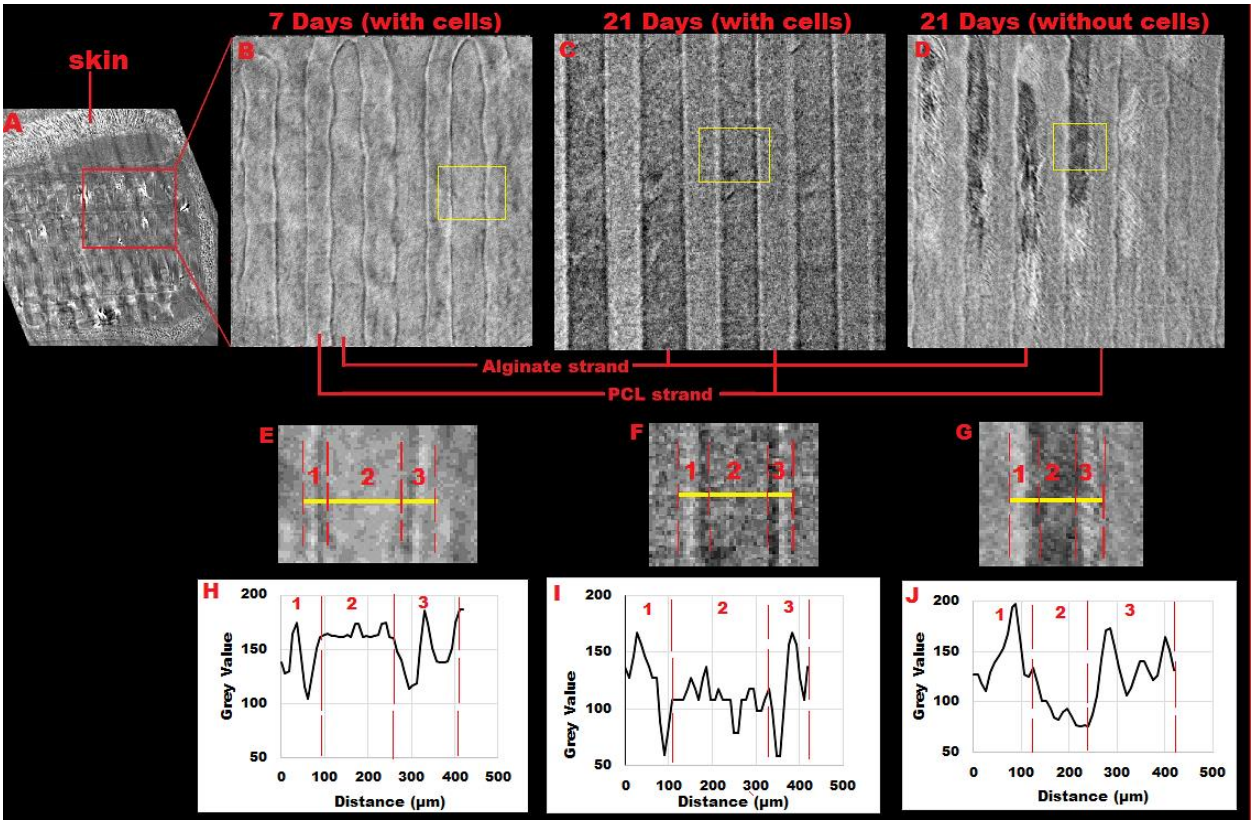

Fig. 4.6: SR-inline-PCI-CT reflected time-dependent structural changes to 3D-printed hybrid cartilage constructs in nude mice. (A) Reconstructed slices of a hybrid construct demonstrated its association with overlying skin. (B-D): Higher magnification images of regions of interest similar to the red box in panel (A) showed clear interfaces between alginate and PCL strands at days 7 and 21 post-implantation. Structural changes were apparent within alginate strands of cell-impregnated hybrid constructs between days 7 (B) and 21 (C) post-implantation. Similar changes were not seen in cell-free alginate strands at 21 days post-implantation (D). (E-G) Even higher magnification images of regions outlined by the yellow box in panels B-D emphasized further these imaging results. (H-J) Grey-value distributions along specific regions of the images (yellow lines in panels E-G) demonstrated large peaks for PCL strand edges (regions 1 and 3). Changes in the amplitude of grey-value peaks within alginate strands (region 2) relative to peaks for PCL strand edges were apparent in cell-impregnated hybrid cartilage constructs between days 7 and 21 post-implantation.

Footnote 1: "*Statistical significance was determined using p-values. When any two of the error bars do not overlap, we have a higher degree of certainty that both means may differ significantly. However, when an overlap exists, we cannot confidently say if both means significantly differ or not [52]. Thus, while we have the bar charts with error bars to allow for a quick visual estimation of the differences that may exist, statistical testing with p-values is more precise and recommended to identify differences.*"

4.5. Discussion

Two of the main problems facing CTE today are: 1) fabrication of constructs that mimic the native human articular cartilage; and 2) non-invasive imaging of the progression of functionality of these cartilage constructs post-implantation in either animal models or human subjects. In recent years, rapid-prototyping-based additive manufacturing (i.e., 3D-printing) techniques are being investigated for fabrication of hybrid cartilage constructs. Specifically, 3D-printed cartilage constructs fabricated from PCL and cell-impregnated alginate mimic the biphasic nature of native articular cartilage and are attracting attention from researchers around the globe. A few *in vitro* studies have shown that cells impregnated within these 3D-printed hybrid cartilage constructs stayed viable and progressively secreted cartilage-specific ECM over time [4-7]. Furthermore, secretion of Col2 by cells within the hybrid cartilage constructs has been demonstrated *in vivo* [5]. However, the *in vivo* performance of these constructs needs further investigation and extensive study to transition this approach to commercialization or clinical application. Regarding non-invasive assessments of construct performance, it is currently a challenge for clinically available techniques (e.g., MRI, radiography, or ultrasound) to simultaneously delineate samples with a combination of hydrophilic and hydrophobic properties such as found in these cartilage constructs [24-27, 31]. To address this knowledge gap, 3D-printed hybrid cartilage constructs were implanted subcutaneously in the backs of nude mice, and their performance was evaluated over a 21-day period using both traditional invasive histological and synchrotron-based non-invasive assessments.

The suitable *in vivo* performance of the 3D-printed hybrid cartilage constructs demonstrated here supports their continued development for clinical CTE applications. Cell viability within the hybrid cartilage constructs remained at least as high as 70 % over the 21-day implantation period in nude mice (Fig. 2). Although, a cell viability of 70 % is still sufficient for ECM secretion, the *in vivo* results indicated a 10 % drop in cell viability in the constructs at 14 days post–implantation in mice. The change from *in vitro* to *in vivo* conditions, along with other unknown physiological conditions, is speculated to have caused the drop in cell viability within these constructs. Interestingly, a slight increase in cell viability wasobserve at 21 days post-implantation in mice i.e., the cell viability increased from 70 ± 6.6 % to 73 ± 7.9 %. This trend is similar to what we reported in our previously reported *in vitro* study, where cell viability also decreased at 14 days but increased at 28 and 42 days [7].

Meanwhile, cells in these 3D-printed cartilage constructs progressively secreted cartilage-specific ECM (Col2 and sulfated GAGs) that are essential to maintain both structural and biological functionality of the hyaline cartilage [44-46] (Figs. 3.4). Tthe secretion of these cartilage-specific ECM is speculated to have the potential to continue and eventually generate articular cartilage neotissue at more distant time-points. However, questions such as length of time required for generation of articular cartilage, how to increase the amount of cartilage-specific ECM secreted over time to hasten articular cartilage formation, whether secretion of articular cartilage-specific ECM will be influenced by mechanical stimulation when these cartilage constructs are implanted in the stifle joint of animal models, and so on, require answers. While cartilage-specific ECM is secreted within these hybrid cartilage constructs, the PCL framework ensured their structural integrity in a manner not possible in hydrogel-only constructs. Because complete degradation of PCL is expected within approximately 2 years [51], the PCL strands did not exhibit any apparent degradation over the 21-day implantation period. In the future, long-term *in vivo* studies are needed to examine the rate of degradation of the PCL strands and determine how the degradation of PCL affects the structural integrity of the neo-tissues formed within hybrid cartilage constructs is suggested.

In summary, the favorable biological performance of the 3D-printed hybrid cartilage constructs presented here supports the conclusions of with previous *in vitro* studies [4-7], adds to the considerably limited *in vivo* data published [5] and indeed demonstrates the potential of the 3D-printed hybrid cartilage constructs for generation of articular cartilage. Looking forward, hybrid cartilage constructs might solve a few major challenges currently facing clinical CTE applications. First, the mechanical and biological roles of native articular cartilage can be mimicked by the 3D-printed cell-impregnated hybrid constructs in this hybrid biofabrication approach. Second, articular cartilage has four basic zones with different mechanical and biological properties. This zonal structure can be mimicked during the layer-by-layer deposition of the 3D-printing technique by adjusting materials and printing parameters [47]. Finally, patient-specific parameters that correspond to the shape and size of the defect to be repaired can be incorporated directly into the 3D CAD model used for fabrication of the hybrid cartilage constructs in the future.

Non-invasive imaging techniques to examine the performcance of soft-tissue-engineered constructs (from multiple biomaterials with different material properties) and their time-dependent structural changes at high spatial resolution are hard to come by. We previously investigated how

changing the sample-to-detector distance of SR-inline-PCI-CT affected phase contrast, edge enhancement, and consequent image quality of the 3D-printed hybrid cartilage constructs *in vitro* [7]. To build of the findings of the *in vitro* study, here wepresented the first attempt to use SR-inline-PCI-CT to non-invasively characterize (*in situ*) the different components of 3D-printed hybrid cartilage constructs. Importantly, the phase contrast and edge-enhancement fringes of SR-inline-PCI-CT enabled characterization of both the hydrophobic (i.e., PCL) and the hydrophilic (i.e., cell-laden or cell-free alginate) components of the hybrid cartilage constructs with different densities and refractive indices (Figs. 5, 6). In addition, hard and soft tissues around hybrid constructs were clearly apparent in the SR-inline-PCI-CT images (Fig. 5), allowing evaluation of a critical clinical parameter: integration of the construct with surrounding host tissues. Not only could SR-inline-PCI-CT visualize the multiple components of the hybrid cartilage constructs and their surrounding host tissues, but it does this with a relatively high spatial resolution compared to conventional clinical imaging techniques. The spatial resolution of PCI is hard to specifically calculate because it depends upon many factors, including the exact hardware and samples used, but the images presented here clearly appear to exceed the resolution achievable by MRI or absorption-based radiography. Although these findings are phenomenon, imaging parameters such as detector pixel size, imaging energy, and number of projections, need to be optimized to lower the absorbed radiation dose without affecting the image quality for prospective future live animal studies, [30].

Apart from characterization of the overall macrostructural details of the implanted construct, SR-inline-PCI-CT also enabled evaluation of time-dependent structural changes to the biomaterials within the constructs. Structural changes were evident in the alginate strands at 21 days compared to 7 days post-implantation (Fig. 6). Whether the time-dependent changes observed in images of alginate strands reflect new ECM secretion by the impregnated cells is unclear. On the one hand, the timing of these changes correlated with the timing of ECM secretion in parallel invasive experiments (Figs. 2 - 4). An increase in phase contrast was associated with secretion of ECM by cells within constructs in reported *in vitro* and *in vivo* studies [7, 10, 39, 48]. On the other hand, the cell-free hybrid scaffolds also showed structural changes, especially within the alginate strands (Fig. 6). Loss of phase contrast might be due to gradual degradation of the alginate hydrogel strands as previously concluded [49-50]. In fact, phase contrast decreased in alginate strands in some regions of the cell-free scaffolds, while it increased in other regions of the alginate strands.

This might be due to dryness experienced within the cell-free alginate strands, because similar regions were observed to be opaque (white) upon harvesting, and these changes were not seen in cell-impregnated alginate strands. More distant time-points are required to resolve what the change in phase contrast within the hybrid cartilage constructs represents, because thicker cartilage should be easily visualized by SR-inline-PCI-CT. In summary, this study supports the conclusion that phase contrast information provided by optimized SR-inline-PCI-CT has potentials for non-invasive characterization of soft tissues, hybrid tissue-engineered constructs and their associated time-dependent structural changes [7, 40-41].

4.6. Conclusions

In summary, these results not only detail the *in vivo* functionality of 3D-printed hybrid cartilage constructs for CTE applications, but also demonstrate the potentials of SR-inline-PCI-CT for non-invasive assessments of these multi-material cartilage constructs and their associated time-dependent structural changes *in situ.* Over a 21-day period, hybrid cartilage constructs (consisting of strands of PCL and cell-impregnated alginate hydrogel) subcutaneously implanted in the backs of nude mice demonstrated good biological performance. Cell viability was always above 70 %, and cartilage-specific ECM secretion significantly increased over time. As such, this study presents a breakthrough in the implementation of 3D-printed hybrid cartilage constructs for CTE applications. Furthermore, SR-inline-PCI-CT enabled characterization of the individual components of the hybrid cartilage constructs, their time-dependent structural changes, interfaces and the surrounding host tissues (all with different refractive indices) *in situ*. Therefore, SR-inline-PCI-CT offers great potential for non-invasive 3D visualization of fine features in weakly absorbing materials and tissues commonly encountered in soft-tissue engineering applications.

4.7. Acknowledgements

The authors acknowledge funding from the Saskatchewan Health Research Fund (SHRF), Canadian Institutes of Health Research (CIHR), and the Natural Sciences and Engineering Research Council of Canada (NSERC). Images presented in this paper were produced from data captured at the Canadian Light Source (CLS), which is supported by the Canada Foundation for Innovation (CFI), NSERC, the University of Saskatchewan, the Government of Saskatchewan, Western Economic Diversification (WED) Canada, and CIHR.

4.8. References

1. Ateshian GA, Warden WH, Kim JJ, Grelsamer RP, Mow VC. (1997). "Finite deformation biphasic material properties of bovine articular cartilage from confined compression experiments." *J Biomech.* 30 (11-12), 1157-64.

2. Mow VC, Guo XE. (2002). "Mechano-electrochemical properties of articular cartilage: their inhomogeneities and anisotropies." *Annu Rev Biomed Eng* 4, 175-209.

3. Flik KR, Verma N, Cole BJ, Bach BR. (2007). "Articular Cartilage: Structure, Biology and Function." In Williams R. (Ed.) *Cartilage Repair Strategies* (pp 1-12). *Humana Press Inc.*, Totowa, New Jersey, USA.

4. Schuurman W, Khristov V, Pot MW, van Weeren PR, Dhert WJ, Malda J. (2011). "Bioprinting of hybrid tissue constructs with tailorable mechanical properties." Biofabrication 3 (2), 021001-021008.
5. Kundu J, Shim JH, Jang J, Kim SW, Cho DW. (2015). "An additive manufacturing-based PCL-alginate-chondrocyte bioprinted scaffold for cartilage tissue engineering." *J Tissue Eng Regen Med.* 9 (11), 1286-97

6. Izadifar Z, Chang T, Kulyk W, Chen DXB., Eames BF. (2016). "Analyzing biological performance of 3D-printed, cell-impregnated hybrid constructs for cartilage tissue engineering." *Tissue Engineering, Part C: Methods.* 22 (3), 173-88

7. Olubamiji AD, Izadifar Z, Zhu N, Chang T, Chen X, Eames BF. (2016). "Using synchrotron radiation inline phase-contrast imaging computed tomography to visualize three-dimensional printed hybrid constructs for cartilage tissue engineering. 23 (3), 802-12.

8. Boskey A, Pleshko Camacho N. (2007). "FT-IR imaging of native and tissue-engineered bone and cartilage." *Biomaterials* 28 (15), 2465–2478.

9. Huebsch ND, Mooney DJ. (2007). "Fluorescent resonance energy transfer: a tool for probing molecular cell–biomaterial interactions in three dimensions." *Biomaterials* 28 (15), 2424–2437.

10. Appel AA, Larson JC, Garson AB 3rd, Guan H, Zhong Z, Nguyen BN, Fisher JP, Anastasio MA, Brey EM. (2014). "X-ray phase contrast imaging of calcified tissue and biomaterial structure in bioreactor engineered tissues." *Biotechnol Bioeng* 112 (3), 612-620.

11. Huzaira M., Rius F., Rajadhyaksha M., Anderson R.R., Gonzalez S. (2001). "Topographic variations in normal skin, as viewed by *in vivo* reflectance confocal microscopy." *J Invest Dermato* 116 (6), 846-852.

12. Muller M., Zumbusch A. (2007). "Coherent anti-Stokes Raman scattering microscopy." *Chemphyschem* 8 (15), 2156–217.

13. Ahearne M, Bagnaninchi PO, Yang Y, El Haj A. (2008). "Online monitoring of collagen fibre alignment in tissue-engineered tendon by PSOCT." *J Tissue Eng Regen Med* 2 (8), 521–52.

14. Hofmann MC, Whited BM, Criswell T, Rylander MN, Rylander CG, Soker S, Wang G, Xu Y. (2012). "A fiber-optic-based imaging system for nondestructive assessment of cell-seeded tissue-engineered scaffolds." *Tissue Eng Part C Methods.* 18 (9), 677-687.

15. Heinrich L, Freyria AM, Melin M, Tourneur Y, Maksoud R, Bernengo JC, Hartmann DJ. (2007). “Confocal laser scanning microscopy using dialkylcarbocyanine dyes for cell tracing in hard and soft biomaterials.” *J Biomed Mater Res B Appl Biomater* 81 (1), 153-61.
16. Zehbe R., Haibel A., Riesemeier H, Gross U, Kirkpatrick CJ, Schubert H, Brochhausen C. (2011). "Going beyond histology. Synchrotron micro-computed tomography as a methodology for biological tissue characterization: from tissue morphology to individual cells." J R Soc Interface 7 (42), 49-59.
17. Appel AA, Anastasio MA, Larson JC, Brey EM. (2013).“Imaging challenges in biomaterials and tissue engineering.” *Biomaterials* 34 (28), 6615–6630.
18. Olubamiji AD, Izadifar Z, Chen DX. (2014). “Synchrotron imaging techniques for bone and cartilage tissue engineering: potential, current trends, and future directions.” *Tissue Eng Part B Rev*. 20 (5), 503-22.
19. Nam SY, Ricles LM, Suggs LJ, Emelianov SY. (2015). “Imaging strategies for tissue engineering applications.” *Tissue Eng Part B Rev.* 21 (1), 88-102.

20. Mertsching H., Walles T., Hofmann M., Schanz J., and Knapp W.H. (2005). “Engineering of a vascularized scaffold for artificial tissue and organ generation.” *Biomaterials* 26 (33), 6610-7

21. Zhou S, Brahme A. (2008). "Development of phase-contrast X-ray imaging techniques and potential medical applications." *Physica Medica* 24 (3), 129-148.

22. Olubamiji AD, Izadifar Z, Si JL,Cooper DML, Eames BF and Chen XB. (2016). “Modulating mechanical behaviour of 3D-printed cartilage-mimetic PCL scaffolds: influence of molecular weight & pore geometry.” *Biofabrication*. 8 (2), 025020

23. Cartmell S, Huynh K, Lin A, Nagaraja S, Guldberg R. (2004). "Quantitative microcomputed tomography analysis of mineralization within threedimensional scaffolds *in vitro*." . *J Biomed Mater Res A* 69 (1), 97–104.

24. van Lenthe GH, Hagenmüller H, Bohner M, Hollister SJ, Meinel L, Müller R. (2007). "Non-destructive micro-computed tomography for biological imaging and quantification of scaffold-bone interaction *in vivo*." *Biomaterials* 28 (15), 2479-90.

25. Potter K, Butler JJ, Horton WE, Spencer RG. (2000). "Response of engineered cartilage tissue to biochemical agents as studied by proton magnetic resonance microscopy." *Arthritis Rheum* 43 (7), 580-90.

26. Prang P, Müller R, Eljaouhari A, Heckmann K, Kunz W, Weber T, Faber C, Vroemen M, Bogdahn U, Weidner N. (2006). "The promotion of oriented axonal regrowth in the injured spinal cord by alginate-based anisotropic capillary hydrogels." *Biomaterials* 27 (19), 3560-9.

27. Nitzsche H, Metz H, Lochmann A, Bernstein A, Hause G, Groth T, Mäder K. (2009). “Characterization of scaffolds for tissue engineering by benchtop-magnetic resonance imaging.” *Tissue Eng Part C Methods.* 15 (3), 513-21.

28. Poirier-Quinot M, Frasca G, Wilhelm C, Luciani N, Ginefri JC, Darrasse L, Letourneur D, Le Visage C, Gazeau F. (2010). “High-resolution 1.5-Tesla magnetic resonance imaging for tissue-engineered constructs: a noninvasive tool to assess three-dimensional scaffold architecture and cell seeding.” *Tissue Eng Part C Methods.* 16 (2), 185-200.

29. Guermazi A, Eckstein F, Hayashi D, Roemer FW, Wirth W, Yang T, Niu J, Sharma L, Nevitt MC, Lewis CE, Torner J, Felson DT. (2015). “Baseline radiographic osteoarthritis and semi-quantitatively assessed meniscal damage and extrusion and cartilage damage on MRI is related to quantitatively defined cartilage thickness loss in knee osteoarthritis: the Multicenter Osteoarthritis Study.” *Osteoarthritis Cartilage* 23 (12), 2191-2198.
30. Izadifar Z, Chang T, Kulyk W, Chen DXB., Eames BF. (2016). "Analyzing biological performance of 3D-printed, cell-impregnated hybrid constructs for cartilage tissue engineering." *Tissue Engineering, Part C: Methods.* 22 (3), 173-88.
31. Izadifar Z, Chapman LD, Chen X. (2014). "Computed tomography diffraction enhanced imaging for *in situ* visualization of tissue scaffolds implanted in cartilage." *Tissue Eng Part C Methods* 20 (2), 140–148.
32. Zhu N, Chapman D, Cooper D, Schreyer DJ, Chen X. (2011). "X-ray diffraction enhanced imaging as a novel method to visualize low-density scaffolds in soft tissue engineering." *Tissue Eng Part C Methods.* 17 (11), 1071-1080.
33. Zhu N, Rajaram A, Olubamiji AD, Schreyer DJ, Wysokinski TW, Belev G, Chen XB. (2015). "Optimization of in-line phase contrast imaging setup for *in vivo* visualization of hydrogel scaffolds in nerve tissue engineering applications." *4th TERMIS 2015 World Congress.* Boston, MA.
34. Gabor D. (1948). A new microscopic principle. *Nature* 1 (161), 777-778.
35. Wilkins SW, Gureyev TE, Gao D, Pogany A & Stevenson AW. (1996). "Phase-contrast imaging using polychromatic hard X-rays." *Nature* 384, 335-338.
36. Spanne P, Raven C, Snigireva I, Snigirev A. (1999). "In-line holography and phase-contrast microtomography with high energy x-rays." *Phys Med Biol.* 44 (3), 741-749.
37. Krol, A. (2011). “In-line hard X-ray holography for biomedical imaging”. In: Rosen, J., ed. Holography, Research and Technologies. Rijeka, Croatia: Intech.
38. Davis TJ, Gao D, Gureyev TE, Stevenson AW, and Wilkins SW. (1995). “Phase-contrast imaging of weakly absorbing materials using hard X-rays”. *Nature* 373, 595-598.

39. Sun W, Li ZR, Yang YR, Shi ZC, Wang B, Liu. (2011). "Experimental study on phase-contrast imaging with synchrotron hard X-ray for repairing osteonecrosis of the femoral head." *Orthopedics.* 34 (9), e530-e534.

40. Murrie RP, Morgan KS, Maksimenko A, Fouras A, Paganin DM, Hall C, Siu KK, Parsons DW, Donnelley M. (2015). "Live small-animal X-ray lung velocimetry and lung micro-tomography at the Australian Synchrotron Imaging and Medical Beamline." *J Synchrotron Radiat* 22 (4), 1049-1055.

41. Murrie, R.P., Stevenson, A.W., Morgan, K.S., Fouras, A., Paganin, D.M. & Siu K.K.W. (2016). "Phase contrast x-ray velocimetry of small animal lungs: optimising imaging rates." *Biomed Opt Express* 7(1), 79–92**.**

42. Schneider CA, Rasband WS, Eliceiri KW. (2012). "NIH Image to ImageJ: 25 years of image analysis." *Nature Methods* 9, 671-6752.

43. Wysokinski T, Chapman D, Adams G, Renier M, Suortti P &Thomlinson W. (2015). Nucl. Beamlines of the biomedical imaging and therapy facility at the Canadian light source—Part 1. *Instrum. Methods Phys. Res. A,* 775, 1–4.

44. Buckwalter JA, Hunzinker E, Rosenberg L, et al. (1988). "Articular cartilage: composition and structure." In Woo SLY, Buckwalter JA (Eds). *Injury and Repair of the Musculoskeletal Soft Tissues (*pp 405-425). Park Ridge, *American Academy of Orthopaedic Surgeons*.

45. Buckwalter JA, Mankin HJ. (1998): "Articular cartilage, part 1: tissue design and chondrocyte-matrix interaction." *Instr Course Lect.* 47, 477-86.

46. Buckwalter JA, Mankin HJ. (1997). "Articular cartilage, part 1: tissue design and chondrocyte-matrix interaction." *J Bone Joint Surg Am.* 79, 600-611.

47. Kim TK, Sharma B, Williams CG, Ruffner MA, Malik A, McFarland EG, Elisseeff JH. (2003). Experimental model for cartilage tissue engineering to regenerate the zonal organization of articular cartilage. *Osteoarthritis Cartilage*. 11(9), 653-64.

48. Zehbe R, Schmitt VH, Kirkpatrick CJ, Brochhausen C. (2015). "High resolution X-ray tomography – three-dimensional characterisation of cell-scaffold constructs for cartilage tissue-engineering." Materials Science and Technology 31 (2), 167-173.

49. Moya ML, Morley M, Khanna O, Opara EC, Brey EM. (2012). " Stability of alginate microbead properties *in vitro*. ." *J Material Sci: Mater Med* 23 (4), 903–912.

50. Takashima K, Hoshino M, Uesugi K, Yagi N, Matsuda S, Nakahira A, Osumi N, Kohzuki M, Onodera H. (2015). "X-ray phase-contrast computed tomography visualizes the microstructure and degradation profile of implanted biodegradable scaffolds after spinal cord injury." *J Synchrotron Radiat* 22 (1), 136-42.

51. He H, Karpa V, Yen C, LaPerle K, Zhang X, Jones NB, Liang MI, Lesinski GB, Ho WS, Carson WE 3rd, Lee LJ. (2011). Use of a nanoporous biodegradable miniature device to regulate cytokine release for cancer treatment. *J Control Release.* 151(3), 239-45.

52. Payton ME, Greenstone MH, Schenker N. (2003). Overlapping confidence intervals or standard error intervals: What do they mean in terms of statistical significance? *Journal of Insect Science* 3, 34.

Chapter 5: Modulating Mechanical Behaviour of 3D-Printed Cartilage-Mimetic PCL Scaffolds: Influence of Molecular Weight and Pore Geometry

The chapter was adopted from the publication of "Olubamiji AD, Izadifar Z, Si JL, Cooper DM, Eames BF, Chen DX. Modulating mechanical behavior of 3D-printed cartilage-mimetic PCL scaffolds: influence of molecular weight and pore geometry. Biofabrication. 28.2 (2016):025020". According to the Copyright Agreement, "the authors retain the right to include the journal article, in full or in part, in a thesis or dissertation".

5.1. Abstract

Three-dimensional (3D)-printed poly(ε)-caprolactone (PCL)-based scaffolds are increasingly being investigated for cartilage tissue engineering (CTE) applications. However, ensuring that the mechanical properties of these PCL-based constructs are comparable to that of articular cartilage that they are meant to regenerate is an area that has been under-explored. This paper presents the effects of PCL's molecular weight (M_W) and scaffold's pore geometric configurations; strand size (SZ), strand spacing (SS), and strand orientation (SO), on mechanical properties of the 3D-printed PCL scaffolds. The results illustrate that M_W has significant effect on compressive moduli and yield strength of 3D-printed PCL scaffolds. Specifically, PCL with M_W of 45 K was a more feasible choice for fabrication of viscoelastic, flexible and load-bearing PCL scaffolds. Furthermore, pore geometric configurations; SZ, SS, and SO, all significantly affect tensile moduli of scaffolds. However, only SZ and SS have statistically significant effects on compressive moduli and porosity of these scaffolds. Furthermore, an inverse linear relationship was observed between porosity and mechanical properties of 3D-printed PCL scaffolds in Pearson's correlation tests. Altogether, this study illustrates that modulating M_W of PCL and pore geometrical configurations of the scaffolds enabled design and fabrication of PCL scaffolds with mechanical and biomimetic properties that better mimic mechanical behaviour of human articular cartilage. Thus, the modulated PCL scaffold proposed in this study is a framework that offers great potentials for CTE applications.

5.2. Introduction

One major strategy in CTE is fabricating three-dimensional (3D) constructs that mimic biological and mechanical properties of human articular cartilage [1-5]. Naturally occurring biomaterials, such as collagen [23], fibroin [6], chitosan [7] and hyaluronic acid [8] have shown great potential for CTE, especially in terms of promoting chondrogenesis and mimicking biochemical properties of articular cartilage. However, these natural biomaterials are expensive, exhibit poor mechanical properties and relatively quick degradation rates, especially when not crosslinked [9-10]. Thus, researchers are motivated to explore cheap and easily sourced synthetic polymers with better mechanical and degradation properties. Synthetic polymers, such as polyglycolide (PGA) [11], poly(L-lactide) (PLLA) [12] and poly(d,l-lactic-co-glycolic acid) (PLGA) [63] are commonly used for scaffold-based TE applications. Then again, the high rigidity of scaffolds fabricated using these biomaterials makes their exploration for CTE applications challenging [12]. With this is mind, composite of these biomaterials has been investigated for reduction of rigidity of these scaffolds. Interestingly, composite of PLLA and poly-ε-caprolactone (PCL) investigated for CTE applications concluded that addition of PCL enabled reduction of rigidity, thereby causing increased viscoelasticity and flexibility of these scaffolds [12]. In addition, PCL has good bioresorbability, slower degradation rate (ranging from months to years), low cost, excellent viscoelastic properties, cellular biocompatibility and is non-immunogenicity [13-14]. Based on the potentials of PCL, this study focuses on optimization of 3D-printed PCL scaffolds for CTE applications.

Both compressive and tensile behaviors of human articular cartilage are important for its functionality and integrity, so any scaffold for CTE application should mimic these properties. Compressive integrity of articular cartilage primarily depends on its glycosaminoglycans (GAGs) content, while its tensile integrity relies largely on its collagen type II content [15-16]. Furthermore, biosynthesis activities of cells near the articular cartilage or in CTE constructs are sensitive to mechanical stimuli [17]. In fact, dynamic compression as little as 0.5 MPa – 1.0 MPa at physiological frequencies of 0.01 MPa – 1.0 Hz have been reported to stimulate secretion of extracellular matrix (ECM) [18-19]. Despite the popularity of PCL-based scaffolds for CTE applications in recent times, these studies neither focused nor considered how tailoring mechanical properties of their PCL framework, to match that of articular cartilage, can indirectly change the game when it comes to secretion of cartilage-specific ECM in these scaffolds [14, 20]. In fact,

Table 5.1 comparing compressive and tensile moduli of PCL scaffolds fabricated using different methods and human articular cartilage of femoral heads showed the existence of a wide gap. Based on the previous explanations, the use of PCL scaffolds listed in Table 5.1 as a framework for CTE applications will result in stress-shielding of mechano-transduction and hinder transmission of mechanical stimuli directed at cells in these scaffolds, and consequently affect ECM secretion [18-19]. In general, researchers are majorly focusing on ensuring that their PCL-based hybrid constructs for CTE applications secrete cartilage-specific ECM [14, 20-21] and paid little to no attention to the mechanical properties of these scaffolds. Another issue is the use of fabrication techniques that encourage uncontrollable porosity within scaffolds, do not allow fabrication of hybrid scaffolds from multiple materials and may involve use of toxic solvents [1, 4, 22, 26]. Examples of these fabrication techniques include electrospinning, selective laser sintering (SLS), injection molding, precision extruding deposition (PED), fused deposition modelling (FDM), drop on demand printing (DDP) etc. [22-25]. Forthwith, it is difficult to modulate their mechanical behavior to mimic articular cartilage. Furthermore, most investigations on optimization of mechanical behavior of PCL scaffolds for TE applications mostly focused on bone TE applications [22, 24, 25, 27]. Considering these limitations, fabrication techniques that will enable easy modulation of mechanical properties, 100 % pore interconnectivity and requires no solvent must be considered and explored for fabrication and optimization of mechanical properties of PCL scaffolds for CTE applications.

Rapid-prototyping (RP)-based 3D plotting technology developed at the Freiburg Materials Research Center circumvents most of the limitations of conventional fabrication techniques. It enables easy control of fabrication parameters, such as SZ, SS and SO, offers versatile pore geometry, 100 % pore-interconnectivity, reproducibility without the use of solvents and fabrication of hybrid constructs from multiple materials [14, 21, 28]. Thereby, it enables users to tailor mechanical properties and load-bearing attributes of their scaffolds to mimic articular cartilage in a manner not possible with conventional fabrication techniques [22-26]. These hybrid constructs with alternating strands of PCL and cell-impregnated hydrogel are promising for CTE as they biologically mimic native articular cartilage and enable secretion of cartilage-specific ECM [14, 21, 29]. The PCL component of these hybrid constructs offers tensile strength, compressive strength, and resilience [22]. On the other hand, the hydrogel component helps with transmission or redistribution of nutrients through pores of the PCL scaffold. While both components play roles

in the overall mechanical behavior of the constructs, the compressive modulus of alginate is negligible compared to PCL [24, 30-31]. Therefore, modulation of mechanical properties of PCL-based hybrid constructs to better mimic articular cartilage should focus on optimizing the PCL component of these PCL-based hybrid constructs.

Table 5.1: Compressive and tensile moduli of human articular cartilage and PCL scaffolds reported in literature

	Compressive moduli (MPa)	**Tensile moduli (MPa)**
Articular cartilage (human femoral head)	1.16 ± 0.20 – 7.75 ± 1.45 [32]; 4.3 ± 1.4 – 13.0 ± 4.2 [33]; 3.2 ± 1.6 [34]; 2.22 ± 0.65 – 3.10 ± 0.84 [35]; 1 – 19.5 [36]; 0.079 ± 0.039 – 2.10 ± 2.69 [37]; 0.679 ± 0.162 – 1.816 ± 0.868 [38]	54.6 ± 37.6 [34]; 0.76 ± 0.13 [39]; 10.1 [40]; 24 [41]
PCL scaffolds fabricated by SLS, Injection molding, electrospinning, PED, FDM, DDP	215.4 ± 6.6 [24]; 52 ± 2 – 67 ± 4 [30]; 14.9 ± 0.6 [42]; 59 [63]; 150 – 200 [43]; 44.0 ± 3.2 [44]; 41.9 [45].	105 ± 15 [24]; 53 ± 36 [27]; 277.06 ± 27.66 [46]; 2.9 - 5.2 [47]; 35.5 ± 5.8 [42]

The influence of porosity on mechanical properties of tissue scaffolds has been well studied. A scaffold's porosity is associated directly with its pore geometrical con- figurations; SZ, SS, and SO [1, 4, 22, 48-49]. That said, a direct relationship is reported to exist between porosity and mechanical properties of scaffolds. Therefore, understanding this relationship may enable better design of porous structures for different TE applications [2, 4, 22, 48]. A few studies that used RP-based techniques have explored modulation of SZ, SS, and SO as a metric to control scaffold's porosity and consequently tailor mechanical properties of scaffolds for TE applications [2-5]. Moreover, none of these studies focused on CTE applications of PCL scaffolds. Thus, the first objectives of this study are to investigate the effect of modulating pore geometrical configurations (SS, SO and SZ) on porosity and mechanical behaviour of 3D-printed PCL scaffolds, and then compare these values with those of human articular cartilage. Furthermore, several investigators have studied the effect of molecular weight (M_W) on biomaterials' and scaffolds' mechanical parameters such as elastic modulus, yield stress, fracture toughness, and

impact strength [50-53]. For example, mechanical properties of scaffolds increased with an increase in M_W of PCL blended with Poly (ethylene terephthalate) (PET) [54]. Unfortunately, no systematic study has considered modulation of PCL's M_W as a parameter to tailor mechanical properties of PCL scaffolds or PCL-based constructs for CTE applications. Thus, the second objective of this study is to evaluate the influence of modulating M_W on mechanical behaviour of PCL scaffolds, and to determine the most suitable M_W for 3D printing of PCL scaffolds for CTE applications.

5.3. Materials and Methods

5.3.1. Design and Fabrication of PCL Scaffolds

In experiment I, scaffolds for investigation of the influence of M_W of PCL on mechanical behaviour were fabricated. PCL with M_W characteristics-number average Mw (Average Mn) of approximately 80 000 $gmol^{-1}$ (PCL80), 45 000 $gmol^{-1}$ (PCL45) and 10 000 $gmol^{-1}$ (PCL10) were purchased from Sigma Aldrich (St. Louis, MO, USA). For scaffold design, a computer-aided design (CAD) model of the bulk/block PCL scaffold was designed in Magics Envisiontec (V13, Materialise, Belgium). The bulk model was exported into Bioplotter RP (V2.9, Envisiontec GmbH, Germany) and sliced into 10 horizontal layers. After slicing, model was exported into Visual Machine (BP, V2.2, Envisiontec GmbH, Germany) and assigned fabrication parameters. The final 3D model had a cuboid geometry with dimensions 15 mm x 15 mm x 2.4 mm, 10 layers, 0.26 mm strand thickness, 1 mm inter-SS, and 0° – 90° patterns. For scaffold fabrication, the different M_Ws of PCL were fed into the syringe of high temperature dispensing head at different times and dispensed through cylindrical metal needle with inner diameter of 300 μm using pneumatic pressure, crosshead speed and temperature presented in Table 5.2. Once the scaffolds were fabricated, structural features were compared with the original dimensions assigned during design. Then, the design parameters were adjusted and scaffolds were re-fabricated where necessary to ensure that the fabricated features were like the assigned designed dimensions. To investigate the effect of pore geometry on porosity and mechanical properties in experiment II, PCL scaffolds with SZ of 200 μm, 300 μm, or 400 μm; SS of 1 m, 1.5 m or 2 mm; and SO of 0°–90°, 0°–45°, or 0°–45°–90°–135° were fabricated using the M_W recommended in experiment I. Design of experiment called Box–Behnken design (BBD); a response-surface-methodology based experimental design [55-56], was used to reduce the number of experimental groups required to 13 from 27 that could have been required for this experiment if a full-factorial design of

experiment was considered.

Table 5.2: Processing parameters for fabrication of 3D-printed PCL scaffolds with varying molecular weight

Scaffold Average Mn	Cross head speed (mm/s)	Pressure (MPa)	Temperature (ºC)
PCL10	2.5	0.4	65
PCL45	1.5	0.8	90
PCL80	1	0.8	110

5.3.2. Qualitative Analysis of Pore Morphology of 3D-printed PCL Scaffolds

Scanning electron microscopy (SEM) images of uncoated PCL scaffolds were acquired using JEOL JSM 6010 SEM version 1.02 (JEOL, Tokyo, Japan). Prior to imaging, uncoated scaffolds were mounted on aluminum stubs using double-sided tape and positioned on the stage in the imaging compartment of the device. Then, SEM images of all the scaffolds in experiments I and II were collected using a secondary electron image (SEI) detector at an acceleration voltage of 2.1 kV. Subsequently, 2D assessments of scaffolds morphology, pore-interconnectivity and pore geometry were conducted. Comparatively, 3D assessments of scaffold morphology, pore-interconnectivity and pore geometry were performed on the 3D volume rendered images of scaffolds obtained from the μCT data using FEI Amira 6.0.1 (Oregon, USA) visualization and analysis software.

5.3.3. Mechanical Testing

Uniaxial unconfined compression and tensile tests were performed using Instron 3366 Material testing System (Norwood, MA, USA). Compression tests were performed on the PCL10, PCL45 and PCL80 scaffolds ($k = 4$ for each M_W) in experiment I while both compression and tensile tests were conducted on PCL scaffolds of the 13 experimental groups in experiment II ($n = 3$ for compression tests, and $m = 3$ for tensile tests). Prior to each mechanical test, the gauge length, width and thickness of each scaffold were measured by a digital Vernier calipers. For the compression tests, each scaffold was placed in between the two smooth and rigid platens of the Instron system, and load cell of 1 kN (Norwood, MA, USA) was used to subject each scaffold to a step force at a crosshead speed of 1 mm/min until a 1 mm displacement was reached in the scaffold. We ensured that homogenous compression with mean load intensity on the loaded side was applied throughout the compression. The force F (kN) and deformation d (mm) were recorded throughout the tests, and apparent stress and strain values were calculated to plot the stress–strain

curve for each scaffold. Elastic compressive moduli were estimated using the initial linear region of the plotted stress–strain curve. For the tensile tests, custom-made aluminum clamps were used to hold the scaffold in place. The surfaces of the aluminum clamps were layered with epoxy glue and each scaffold was carefully placed in between the aluminum clamps. Attachment of the two ends of scaffold to the clamps was done carefully to ensure that glue was only holding the scaffold in place and not migrating into the pores within the scaffold. These assemblies were allowed to set overnight before performing the mechanical test. Furthermore, the dimensions of the scaffolds in the test setup were adjusted carefully to obtain a set-up similar to those used in the compression tests. The initial gauge lengths were set to 0 and the scaffolds were subjected to displacements using the same load cell and displacement rate used in the compression test. The force and displacement values were collected as in the compression test, and the stress–strain curves were calculated and plotted accordingly to obtain elastic tensile moduli from the initial linear region of the curves.

5.3.4. Quantitative Analysis of Porosity of 3D-printed PCL Scaffolds

Porosity distribution was analyzed non-destructively and quantitatively from the micro-CT images of the scaffolds. First, micro-CT imaging of 3D-printed PCL scaffolds was conducted using a Bruker micro-CT SkyScan 1172 (Kontich, Belgium) scanner. PCL scaffolds ($n = 3$) representing the 13 experimental groups were scanned with acquisition protocol that consisted of pixel size of 6.92 μm, X-ray tube settings of 40 kV and 250 μA, rotation step of 0.2°, 1 mm aluminum filter, 4-frame averaging, 500 ms exposure time, and 1 hour 6 minutes' scan time per sample. Isotropic 2D slices of the scaffolds were acquired from the projection datasets in a reconstruction procedure using NRECON V 1.6.10.1 (Skyscan 2011). Datasets were rotated in Dataviewer v.1.5.2 (Bunker) to achieve a standardized reorientation prior to analysis and exported into CT Analyser 1.3.2.2 (Bunker) for 3D morphometric analysis of scaffolds. A region of interest that consists of 4.0 × 4.0 mm^2 of 80 image slices selected from each dataset were thresholded to distinguish scaffolds from background noise and pore voids as previously described in [1, 57]. Then, morphological information was extracted or calculated from the thresholded images. The quantitative morphological information included total volume, object volume, percentage object volume, and percentage porosity of scaffolds.

5.3.5. Statistical Analysis

A one-way ANOVA F-test for independent samples was carried out using SPSS (Released 2013 IBM SPSS Statistics for Windows, Version 21.0. Armonk, NY: IBM Corp.) to determine the effect of PCL's M_W on compressive moduli of produced scaffolds in experiment I. Furthermore, post-hoc tests using Tukey's test for difference of means was conducted to identify any significant difference present amongst compressive moduli of PCL10, PCL45 and PCL80 scaffolds. Statistical significance was set at 0.05. For experiment II, Design-Expert Software Version 9 (Stat-Ease Inc., 2021E, Hennepin Ave., Minneapolis, MN, USA) was used for the RSM-based BBD experimental design. Then, model fitting was accomplished by linear regression analysis of the experimental data in SPSS (Released 2013 IBM SPSS Statistics for Windows, Version 21.0. Armonk, NY: IBM Corp.). The predictive models presented in equations (1) – (3) were used to evaluate the effect of each independent variable: SS, SO and SZ, on compressive modulus, tensile modulus and porosity of scaffolds respectively.

Predictive model equation for compressive modulus (CM):

$$Y_{CM} = \beta_0 + \beta_{SS}X_{SS} + \beta_{SO}X_{SO} + \beta_{SZ}X_{SZ} + \varepsilon \quad (5.1)$$

Because of violation of the homoscedasticity assumption, equation (1) was log-transformed to yield equation (1.1)

Log-transformed predictive model for compressive modulus (CM):

$$\text{Ln } Y_{CM} = \beta_0 + \beta_{SS}X_{SS} + \beta_{SO}X_{SO} + \beta_{SZ}X_{SZ} + \varepsilon \quad (5.1.1)$$

Predictive model equation for tensile modulus (TM):

$$Y_{TM} = \beta_0 + \beta_{SS}X_{SS} + \beta_{SO}X_{SO} + \beta_{SZ}X_{SZ} + \varepsilon \quad (5.2)$$

Log-transformed predictive model for tensile modulus (TM):

$$\text{Ln } Y_{TM} = \beta_0 + \beta_{SS}X_{SS} + \beta_{SO}X_{SO} + \beta_{SZ}X_{SZ} + \varepsilon \quad (5.2.1)$$

Predictive model equation for porosity (P):

$$Y_{P} = \beta_0 + \beta_{SS}X_{SS} + \beta_{SO}X_{SO} + \beta_{SZ}X_{SZ} + \varepsilon \quad (5.3)$$

Lastly, Pearson's correlation was used to assess the relationship between compressive moduli and porosity and tensile moduli and porosity for the data points collected. Then, the results of these correlations were graphically presented. Statistical significance was set at $p < 0.001$.

5.4. Results

5.4.1. Modulating M_W Influenced Mechanical Behaviour of 3D-printed PCL Scaffolds

Uniaxial unconfined compression test results showing the effect of varying M_W on compressive moduli of 3D-printed PCL scaffolds are presented in Fig 5.1. The results of the one-way ANOVA F-test for independent samples showed a significant difference among compressive moduli of PCL10, PCL45 and PCL80 scaffolds. More specifically, post-hoc tests using Tukey's test for difference of means revealed that significant differences existed between compressive moduli of PCL10 and PCL45 scaffolds ($p < 0.001$), and PCL45 and PCL80 scaffolds ($p < 0.001$). In addition, yield strengths of 0.56 ± 0.2 MPa, 1.4 ± 0.7 MPa, and 9.8 ± 0.8 MPa were measured for PCL10, PCL45 and PCL80 scaffolds respectively. Although PCL10 scaffolds have the lowest compressive moduli and compressive strengths (Fig. 5.1 B), these scaffolds were found to be highly brittle, have lower toughness, and reached failure the quickest, compared to PCL45 and PCL80 scaffolds (Fig. 5.1 A).

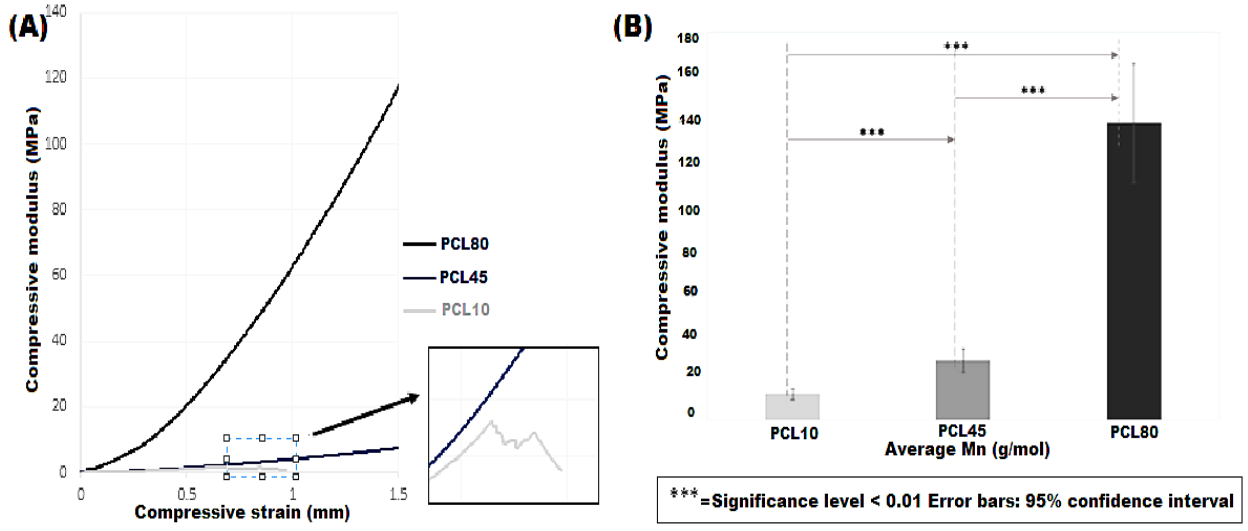

Fig. 5.1: (A) Example stress–strain curves obtained from PCL scaffolds fabricated using average Mn of 10 K, 45 K and 80 K g mol^{-1}, (B) graphical illustration depicting significant difference in the compressive moduli of PCL scaffolds fabricated using average Mn of 10 K, 45 K and 80 K $gmol^{-1}$

5.4.2. Qualitative Analysis of Pore Morphology of PCL Scaffolds

The images from SEM revealed interconnected pores and homogenous structure. In addition, the SEM images of scaffolds depicted that morphology of the scaffolds had close resemblance to the CAD models used fabrication of scaffolds. Representative SEM images from

three of the experimental groups are presented in Fig. 5.2. From Fig. 5.2 A, the green line drawn across two strands clearly showed that the spacing between the two strands was approximately 1800 µm (as expected from the CAD design). The cross-section of pore morphology shown in Figs. 5.2 D – F also provided evidence that strands in all cases maintained cylindrical shape except in the contact area. Similarly, 3D volume rendering performed on the micro-CT datasets of PCL scaffolds revealed 100 % interconnected pores and homogenous structure. In addition, 3D-rendering images confirmed that designed CAD models and 3D-printed PCL scaffolds were well correlated. Similar to Fig. 5.2 (A), the green line drawn across two strands in Fig. 5.3 A clearly showed that the spacing between the two strands was approximately 1800 µm (as expected from the CAD design). The cross-sections of pore morphology shown in Figs. 5.3 D – F demonstrated that strands in all cases maintained uniform cylindrical shape except in the contact areas where strands are fused to the stands from top and bottom layers.

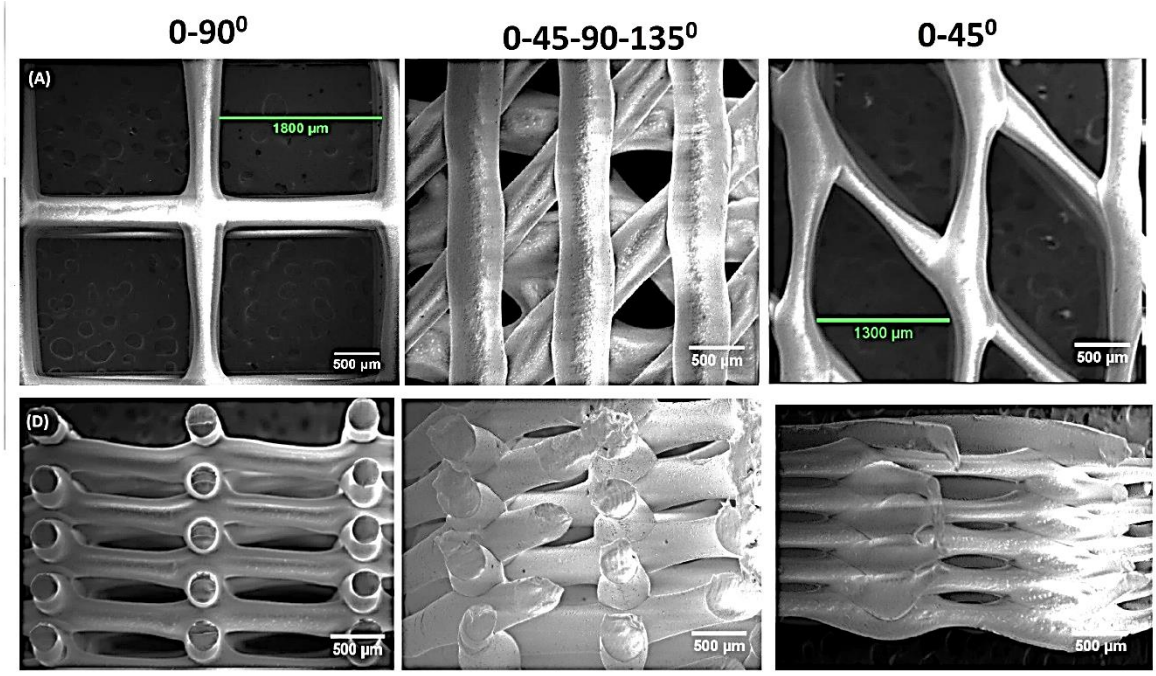

Fig. 5.2: SEM images of 3D-printed PCL scaffolds with pore geometric configurations: (A) SZ: 200 µm, SS: 2 mm and SO: 0°–90°;(B) SZ: 400 µm, SS: 1 mm and SO: 0°–45°–90°–135°;(C) SS: 1.5 mm, SZ: 200 µm and SO: 0°–45°;(D) – (F) are cross-sections through (A), (B) and (C) respectively.

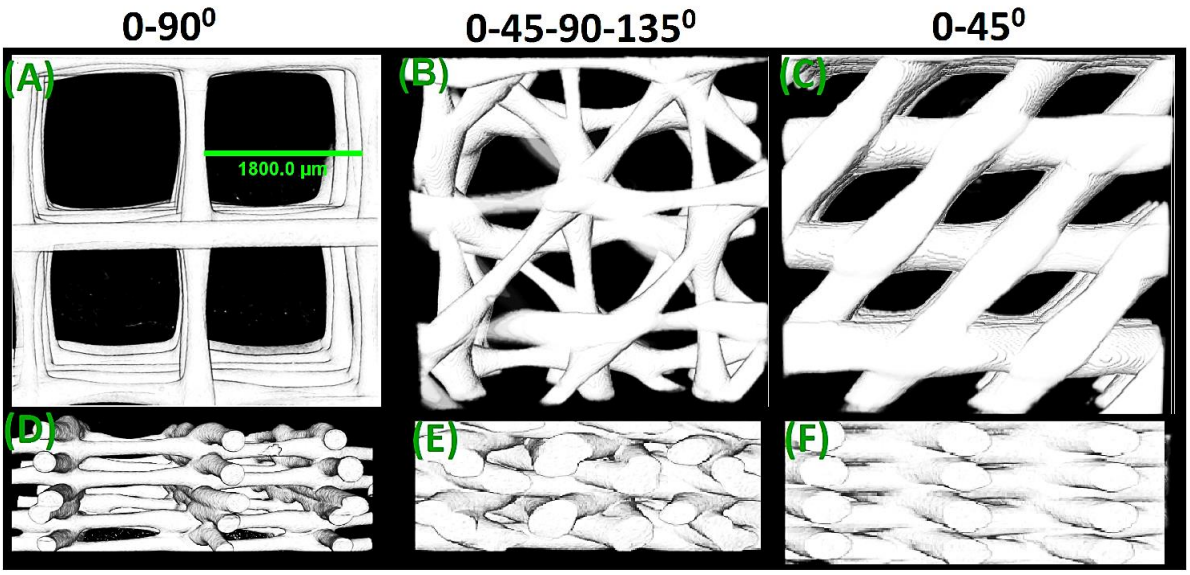

Fig. 5.3: 3D rendering of 3D-printed PCL scaffolds with pore geometric configurations: (A) SZ: 200 µm, SS: 2 mm and SO: 0–90°; (B) SZ: 200 µm, SS: 1.5 mm and SO: 0°–45°–90°–135°; (C) SZ: 400 µm, SS: 1 mm and SO: 0°–45°; (D) – (E) are cross-sections through (A), (B) and (C) respectively.

5.4.3. Modulating Pore Geometrical Configurations Influenced Mechanical Behaviour of PCL Scaffolds

5.4.1.1 Effect of modulating pore geometrical configurations on compressive moduli of 3D-printed PCL scaffolds

As shown in Table 5.3, the compressive moduli of 3D-printed PCL scaffolds obtained by modulating SZ, SS and, SO varied from 56.46 ± 3.267 MPa to 6.63 ± 0.50 MPa. The stress–strain curves for the 13 experimental groups, whose initial regions were used for calculation of compressive moduli, are presented in Fig. 5.4 (A). The figure labeled 13 at the top left corner of Fig. 5.4 A is an example of the complete stress–strain curve (for experimental group 13) and showed the important regions in each of the individual compressive stress–strain curves. Under compression, the PCL scaffolds were non-brittle and exhibited a linear elastic deformation at small strain followed by a yielding deformation high strain and then, strain hardening region at higher strain. Furthermore, regression equation (5.4) obtained from (1.1) clearly showed that pore geometric parameters SZ and SS significantly influenced CM of scaffolds (equation (5.1.1) is a log-transformed model of equation (5.1)). Every 100 µm increase in SZ caused CM to increase by approximately 1.39 times ($p < 0.001$) when all other factors were held constant. For example, compressive moduli of scaffolds fabricated with SS of 1.5 mm and SO of 0°– 45°, but with SZ of 400 µm or 200 µm, had compressive moduli of 17.16 ± 1.44 MPa or 8.68 ± 0.52 MPa, respectively (i.e. approximately 2 times decrease).

$$\hat{Y}_{CM} = 29.67 + 0.53X_{SS} + 1.39X_{SZ} \quad (5.4)$$

Similarly, every 0.5mm increase in SS caused CM to decrease by approximately 2 times when all other factors were held constant ($p < 0.001$). For instance, scaffolds fabricated with SZ of 200 μm and SO of 0°– 90°, but with SS of 1 mm or 2 mm, had compressive moduli of 28.79 ± 2.66 MPa or 6.63 ± 0.50 MPa, respectively (i.e. approximately 4 times decrease). Moreover, change in SO did not have a 'statistically significant' effect on compressive moduli of scaffolds ($p > 0.05$) and so was removed from the regression equation (4).

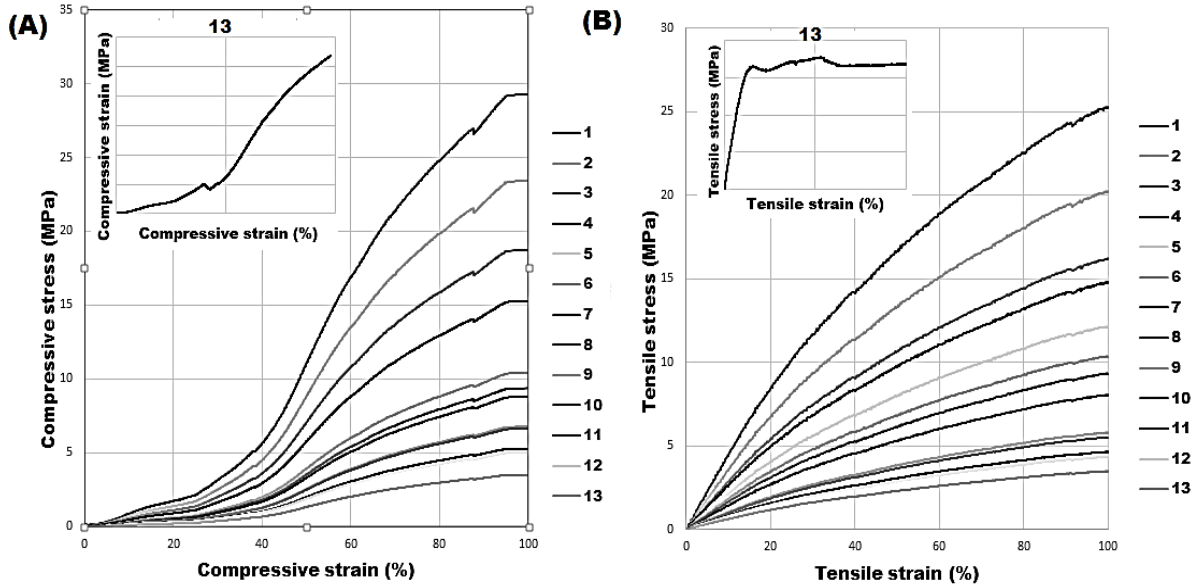

Fig. 5.4: (A) Compressive stress–strain curves showing the initial regions of each curve for the 13 experimental groups of the 3Dprinted PCL scaffolds; (B) tensile stress–strain curves showing the initial region of each curve for the 13 experimental groups of the 3D-printed PCL scaffolds; (13) on the top left corner of (A) and (B) are examples of the complete stress–strain curves.

5.4.1.2 Effect of Modulating Pore Geometrical Configurations on Tensile Moduli of PCL Scaffolds

Modulating SZ, SS and SO caused tensile moduli of 3D-printed PCL scaffolds to vary from 46.04 ± 3.67 MPa to 6.03 ± 1.01 MPa (Table 5.3). The stress–strain curves for the 13 experimental groups, whose initial regions were used for calculation of tensile moduli, are presented in Fig. 5.4 B. The figure labeled 13 (for experimental group 13) on the top of Fig. 4 B is an example of the complete stress–strain curve and showed the important regions in the individual tensile stress–strain curves. Under tension, the PCL scaffolds were non-brittle and exhibited a linear elastic deformation at small strain, followed by yielding deformation at high strain, strain hardening, necking at higher strain before getting to their breaking points. The regression equation (5.5) obtained from (5.2.1) showed that pore geometric configurations; SS, SO and SZ, all have notable influence on tensile moduli of the fabricated PCL scaffolds (equation (2) was log-transformed to

yield (5.2.1): appendix provides explicit details of regression modeling of compressive moduli). In general, tensile modulus increases as SZ increases, decreases as SS increases, and increases with change in SO from 0°– 45° to 0°–90°; 0°–45° to 0°–45°–90°–135°; or from 0°–90° to 0°–45°–90°–135°. Precisely, every 0.5 mm increase in SS caused tensile modulus to decrease by approximately 1.5 times when all other factors were held constant ($p < 0.001$). For example, scaffolds fabricated with SZ of 200 μm and SO of 0°–90°, but with SS of 1 or 2 mm, had tensile moduli of 18.15 ± 1.36 MPa or 6.03 ± 1.01 MPa, respectively (i.e. 3 times decrease). Similarly, every 100μm increase in SZ caused tensile modulus to increase by approximately 1.6 times ($p < 0.001$) when all other factors were held constant. For example, tensile moduli of scaffolds fabricated with SS of 1.5 mm and SO of 0°–45°, but with SZ of 400 μm or 200 μm had 24.75 ± 4.76 MPa or 9.66 ± 1.61 MPa, respectively (i.e. approximately 2.56 times decrease). Furthermore, as SO changes from 0°–45°to 0°–90° or from 0°–90° to 0°–45°–90°–135°, the tensile modulus increased by 1.2 times when all other factors were held constant ($p < 0.001$).

$$\hat{Y}_{TM} = 11.02 + 0.67X_{SS} + 1.19X_{SO} + 1.58X_{SZ} \quad (5.5)$$

Table 5.3: Summary showing results of porosity and corresponding compressive and tensile modulus of 3D-printed PCL scaffolds

RUNS	SZ (μm)	SO (degrees)	SS (mm)	Porosity (%)	Compressive Modulus (MPa)	Tensile Modulus (MPa)
1	400	0-90	1	36.91 ± 0.16	56.46 ± 3.267	46.04 ± 3.67
2	300	0-45	1	42.65 ± 0.51	39.23 ± 3.58	20.83 ± 2.50
3	300	0-45-90-135	1	44.53 ± 0.80	33.62 ± 2.71	25.36 ± 1.46
4	200	0-90	1	56.84 ± 2.66	28.79 ± 2.66	18.15 ± 1.36
5	400	0-45	1.5	51.98 ± 0.56	17.16 ± 1.44	24.75 ± 4.76
6	400	0-45-90-135	1.5	53.53 ± 0.31	15.59 ± 0.98	34.44 ± 4.73
7	400	0-90	2	63.72 ± 0.04	13.31 ± 1.86	15.86 ± 1.27
8	300	0-90	1.5	67.39 ± 0.95	14.81 ± 1.08	9.74 ± 0.74
9	300	0-45-90-135	2	68.73 ± 0.55	11.43 ± 2.47	16.41 ± 1.00
10	300	0-45	2	70.65 ± 0.96	11.47 ± 1.47	11.68 ± 2.94
11	200	0-45	1.5	72.13 ± 0.80	8.68 ± 0.52	9.66 ± 1.61
12	200	0-45-90-135	1.5	75.98 ± 0.45	8.69 ± 0.52	14.59 ± 0.51
13	200	0-90	2	80.28 ± 2.94	6.63 ± 0.50	6.03 ± 1.01

5.4.4. Effect of Modulating Pore Geometry on Porosity and Relationship Between Porosity and Mechanical Behaviour of PCL Scaffolds

As shown in Table 5.3, porosity of 3D-printed PCL scaffolds varied from 36.91 ± 0.16 % to 80.28 ± 2.94 %. As expected, variations in porosity of these scaffolds were influenced significantly by modulation of pore geometrical parameters; SS and SZ (see regression equation

(5.6) obtained from (5.3) and appendix for detailed explanation). Specifically, every 0.5 mm increase in SS caused porosity to increase by 12.81 % ($p < 0.001$), while a 100 μm increase in SZ caused a decrease of 9.84 % in porosity ($p < 0.001$), when all other factors were held constant. For instance, porosity of scaffolds fabricated by increasing SS from 1 to 2 mm, while keeping SZ at 300 μm and SO at 0°–45°, resulted in a porosity change from 42.65 ± 0.51 % to 70.65 ± 0.96 % (approximately twice of 12.81 %). Similarly, increasing SZ from 200 μm to 400 μm, while keeping SO at 0°–90° and SS at 1 mm, resulted in porosity of 56.84 ± 2.66 % and 36.91 ± 0.16 %, respectively (approximately twice of 9.84 %).

$$\hat{Y}_P = 54.62 - 9.84X_{SZ} + 12.81X_{SS} \quad (5.6)$$

Similarly, modulating SZ significantly influenced porosity of scaffolds, where every 100 μm increase in SZ caused porosity to decrease by 9.84 % ($p < 0.001$) when all other factors were held constant. For example, increasing SZ from 200 μm to 400 μm, while keeping SO at 0°–90° and SS at 1 mm resulted in porosity of 56.84 ± 2.66 % and 36.91 ± 0.16 %, respectively (approximately twice of 9.84 %). Similar to regression equation (4), change in SO did not have a significant effect on porosity of scaffolds ($p > 0.05$) and so was removed (6). Correspondingly, an inverse linear relationship was found between porosity and compressive moduli, and porosity and tensile moduli of these 3D-printed PCL scaffolds (Figs. 5 A and B respectively). In a Pearson's correlation test at 5 % level of significance, there was no evidence to reject the assumption that a linear inverse relationship exists between the compressive moduli and porosity of PCL scaffolds obtained ($r = -0.868$, $p < 0.001$). In the same manner, there is no evidence to reject the assumption that an inverse linear relationship exists between the tensile modulus and porosity measurements obtained ($r = -0.826$, $p < 0.001$) in a Pearson's correlation test at 5 % level of significance. In sum, these data support a strong inverse relationship between the mechanical behaviour (i.e. compressive moduli and tensile moduli) and porosity of 3D-printed PCL scaffolds. All things considered, modulation of SS, SZ and SO resulted in fabrication of 3D-printed PCL scaffolds with compressive and tensile modulus values similar to reported values for human articular cartilage. These PCL scaffolds were tagged 'modulated PCL scaffolds' and have CM of 6.63 ± 4.2 MPa and tensile modulus of 6.03 ± 1.01MPa. CM of modulated PCL scaffolds (6.63 ± 4.2 MPa) can be concluded to be in the acceptable range when compared to compressive moduli of human articular cartilage already reported i.e. 0.079 ± 0.039 MPa – 13.0 ± 4.2 MPa [33, 34, 37] (see Table 5.1 for complete list). Similarly, the modulated PCL scaffolds' tensile moduli of 6.03 ± 1.01 MPa is in

the acceptable range when compared with 0.76 MPa – 54.6 MPa reported as tensile moduli of human articular cartilage [34, 39, 40, 41] (see Table 5.1).

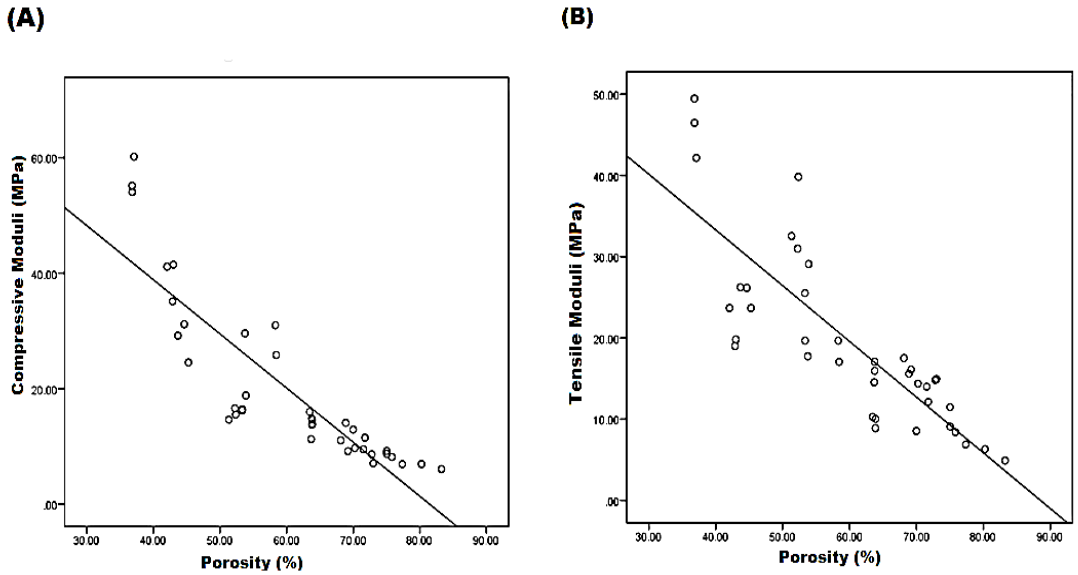

Fig. 5.5: Plot of data points showing inverse linear relationships between (A) compressive moduli and porosity (B) tensile moduli and porosity, of 3D-printed PCL scaffolds.

5.5. Discussion

This study examined the effect of modulating molecular weight of PCL and pore geometry parameters: SS, SZ and SO on mechanical properties of scaffolds, motivated by a need to establish design parameters to enable fabrication of 3D-printed PCL-based constructs with framework that mechanically mimic native human articular cartilage. PCL is popularly used in musculoskeletal tissue engineering applications because of its biocompatibility, degradability, elasticity and it is FDA-approved. In addition, PCL-based 3D-printed hybrid constructs with living cells biologically mimic the multi-composite and biphasic nature of the articular cartilage and have therefore attracted attention for CTE applications [14, 21, 28-29]. However, these PCL-based cartilage regeneration constructs primarily aimed at biologically mimicking native human articular cartilage but pay little or no attention to ensuring that the TE constructs biomechanically mimic the tissues [14, 21, 28-29]. In fact, to the best of our knowledge, this study is the first to examine the effect of molecular weight of PCL and these pore geometry parameters in a direct head-to-head comparison to establish design parameters to enable fabrication of 3D-printed mimetic PCL-based constructs with framework that mechanically mimic native human articular cartilage.

The results from this study demonstrated that reducing molecular weight of PCL biomaterials (80 K, 45 K and 10 K) used for fabrication caused drastic and significant reduction in the compressive moduli of scaffolds from 138.01 ± 3.78 MPa - 12.26 ± 1.44 MPa and compressive strength of scaffolds from 20.93 ± 1.07 MPa - 1.31 ± 0.06 MPa (Fig. 5.1). Although PCL10 scaffolds have significantly lower compressive moduli (12.26 ± 1.44 MPa), PCL10 scaffolds experienced drastic and high brittleness, very low compressive strength, less toughness and reached failure quickly. Thereby making PCL10 scaffolds less feasible for fabrication of scaffolds for repair of tissues in high load-bearing regions such as joints where articular cartilage are often present. This phenomenon correlated with study of [54] where reducing molecular weight of PCL deteriorated the mechanical properties of the resultants when effect of adding various molecular weight of PCL to PET/PCL blends was examined. In fact, they recommended using blends containing PCL with molecular weight higher than 10000 g/mol for industrial applications and that PCL with 10K or less molecular weight would not be feasible [54]. Furthermore, increasing molecular weight has been previously reported to increase number of tie molecules and consequently affect mechanical properties such as elastic modulus, yield stress, fracture toughness or impact strength of different materials [50-52, 58]. Since PCL45 was non-brittle and possesses higher toughness than PCL10, PCL45 was further explored for fabrication of mimetic 3D-printed scaffolds for CTE applications in experiment II. Summarily, modulation of molecular weight enable tailoring mechanical properties of PCL scaffolds explored for CTE applications.

The results from this study also showed that modulation of pore geometry parameters: SS, SZ and SO have direct effect on porosity distribution of scaffolds. Furthermore, multiple regression (5.6) showed that varying SZ and SS independently resulted in significant difference ($p < 0.001$) in porosity of scaffolds. This change is such that an increase of 0.5 mm in SS caused porosity to increase by an additional 12.81 % while an increase of 100 μm in SZ caused porosity to increase by an additional 9.81% ($p < 0.001$) when all other factors are held constant. Although modulation of SO affected porosity of scaffolds, the influence was not significant in the presence of SS and SZ ($p > 0.05$). For example, the porosity of scaffolds fabricated with same SZ of 300 μm and SS of 1 mm but different SO were 42.65 ± 0.51 % and 44.53 ± 0.80 % respectively. Similarly, scaffolds fabricated with SZ of 200 μm and SS of 1.5 mm but different SO: 0-45^o and 0-45-90-135^o were 72.43 ± 0.80 % and 75.28 ± 0.45 % respectively.

This difference (see Table 5.2) has been previously described in a simulation experiment of these 3D-printed scaffolds to be because of contact angle made by the strands during strand fusion and the "spreading process" [59]. Although porosity of scaffolds increased while modulating pore geometry from 36.91 ± 0.16 % to 80.28 ± 2.94 %, this increment did not cause the scaffolds to collapse. In fact, 3D-printed PCL scaffolds with higher porosity tend to possess better elasticity and flexibility that can enable them better mimic native articular cartilage. Furthermore, 2D characterization of the morphology of the scaffolds by SEM and 3D rendering showed that the architecture of scaffolds has optimal resemblance when compared to the CAD models used for 3D-printing of scaffolds. The results also demonstrated that based on the concept of RP-based 3D-printing, scaffolds were reproducible with the same properties always during fabrication. These images also showed that the scaffolds possess 100 % pore-interconnectivity. Cross-section of pore morphology shown in Fig. 5.2 and 5.3 (D) – (E) provided us with evidence that strands in all cases maintained cylindrical shape except in the contact area where strand fusion caused a "spreading process" previously described in a simulation experiment of these 3D-printed scaffolds in [59].

3D-printed mimetic PCL scaffolds were mechanically characterized through unconfined compressive and tensile tents for different pore geometrical configurations (SO, SS and SZ). From a mechanical point of view, the deduced that change in organization and volume caused by modulation of SO, SS and SZ played a determinant role in both porosity, tensile and compressive properties of the whole scaffold. That said, it was indeed clear that an inverse but linear relationship existed between compressive or tensile moduli and porosity of scaffolds (Fig. 5.4 and 5.5). In addition, increasing SS and reducing SZ increased porosity and reduced both compressive and tensile moduli (Equation 5.4 and 5.5), while changing SO notably affected tensile moduli of scaffolds (Equation 5.5). These modulations consequently caused the elasticity and flexibility of scaffolds to increase and better mimic native articular cartilage. Although modulation of SO affected compressive moduli of scaffolds, these effects were not notable in the presence of SS and SZ ($p > 0.05$). For example, the compressive moduli of scaffolds fabricated using the same SZ of 300 μm and SS of 1 mm but different SO: 0-45^o and 0-45-90-135^o were 39.23 ± 3.58 MPa and 31.62 ± 2.71 MPa respectively. Similarly, the compressive moduli of scaffolds fabricated using SZ of 200μm and SS of 1.5 mm but different SO: 0-450 and 0-45-90-1350 were 8.68 ± 0.52 MPa and 8.40 ± 1.23 MPa respectively.

Interestingly, change in SO notably affected tensile moduli of scaffolds in the presence of SS and SZ. These results correspond to the findings of [4, 22, 48, 61] who reported change in mechanical properties of their scaffolds as a results of varying pore geometry parameters. Our results also supported other studies that claimed that a relationship exists between porosity and mechanical properties of scaffolds [4, 48-49, 60].

Furthermore, fabricated using SZ of 200 μm, SO of 0-90^{o} and SS of 2mm reported the lowest compressive moduli of 6.63 ± 0.50 MPa and tensile moduli of 6.03 ± 1.01 MPa and was tagged "modulated PCL scaffolds". In the context of this study, the published data on compressive moduli and tensile moduli of human articular cartilage obtained from heads / femoral condyles are in the range 1.16 MPa – 13 MPa [32-33, 40, 61-62] and 5 MPa - 25 MPa [40, 62] respectively. In comparison, tensile moduli of PCL scaffolds of different sizes fabricated using different methods are in the range 25.7 MPa – 277.06 MPa [24, 27, 30, 46] and reported compressive moduli varied from 20 MPa - 67 MPa [23, 24, 26, 45]. Based on these results, the modulated PCL scaffolds fall in the range of compressive and tensile moduli of native human articular cartilage reported in literature. Therefore, this study suggests that the specifications for fabrication of the modulated PCL scaffolds may be adopted for 3D-printing of PCL-based scaffolds with framework that will not only biologically mimic but also mechanically mimic the microenvironment of native human articular cartilage.

5.6. Conclusions

In this study, we successfully modulate the mechanical properties of 3D-printed PCL scaffolds to mimic human articular cartilage by varying M_W of PCL biomaterials and pore geometrical configurations of SS, SZ and SZ. Based on compression tests, we showed that PCL biomaterial with a M_W value of 45 K was a more appropriate choice for fabrication of viscoelastic, flexible and load-bearing scaffolds. We also found that the pore geometric configurations of SS, SZ and SZ could be modulated to influence porosity, tensile and compressive moduli of scaffolds. In addition, we reported that an inverse linear relationship existed between porosity and mechanical properties (i.e. increasing porosity caused reduction in the compressive and tensile moduli) of these scaffolds. Ultimately, these modulations resulted in 'modulated PCL scaffolds' with compressive and tensile moduli of 6.63 ± 0.50 MPa and 6.03 ± 1.01 MPa, respectively, which are in the reported range of human femoral articular cartilage. In sum, this study illustrates that modulating M_W and pore geometrical configurations

offer great potential for manipulation of mechanical behavior of 3D-printed PCL-based mimetic scaffolds for CTE applications.

5.7. Acknowledgments

Funding for this research was supported by grants from Saskatchewan Health Research Fund (SHRF) and Natural Sciences and Engineering Council of Canada (NSERC). The authors also acknowledge Dr. Chijioke Nwankwo and Dr. Kingsley Lawrence Iroba for their statistical analyses contributions, Louis Roth and Ken Jodrey for the help received during the mechanical testing.

5.8. References

1. Lin AS, Barrows TH, Cartmell SH, Guldberg RE. (2003). "Microarchitectural and mechanical characterization of oriented porous polymer scaffolds." *Biomaterials* 24 (3), 481-489.

2. Woodfield TB, Malda J, deWijn J, Péters F, Riesle J, van Blitterswijk CA. (2004). "Design of porous scaffolds for cartilage tissue engineering using a three-dimensional fiber-deposition technique." *Biomaterials* 25(18), 4149-61

3. Malda J, Woodfield TB, van der Vloodt F, Wilson C, Martens DE, Tramper J, van Blitterswijk CA, Riesle J. (2005)"The effect of PEGT/PBT scaffold architecture on the composition of tissue engineered cartilage.The effect of PEGT/PBT scaffold architecture on the composition of tissue engineered cartilage." *Biomaterials* 26 (1), 63-72.

4. Moroni L, de Wijn JR, van Blitterswijk CA. (2006). "3D fiber-deposited scaffolds for tissue engineering: influence of pores geometry and architecture on dynamic mechanical properties." *Biomaterials* 27 (7), 974-985.

5. Woodfield TB, Moroni L, Malda J. (2009). "Combinatorial approaches to controlling cell behaviour and tissue formation in 3D via rapid-prototyping and smart scaffold design." *Comb Chem High Throughput Screen.* 12 (6), 562-579.

6. Talukdar S, Nguyen QT, Chen AC, Sah RL, Kundu SC. (2011). "Effect of initial cell seeding density on 3D-engineered silk fibroin scaffolds for articular cartilage tissue engineering." *Biomaterials.* 32 (34), 8927-37.

7. Bhardwaj N, Nguyen QT, Chen AC, Kaplan DL, Sah RL, Kundu SC. (2011). "Potential of 3-D tissue constructs engineered from bovine chondrocytes/silk fibroin-chitosan for *in vitro* cartilage tissue engineering." *Biomaterials* 32 (25), 5773-81.

8. Correia CR, Moreira-Teixeira LS, Moroni L, Reis RL, van Blitterswijk CA, Karperien M, Mano JF. (2011). "Chitosan scaffolds containing hyaluronic acid for cartilage tissue engineering." *Tissue Eng Part C Methods.* 17 (7), 717-30.

9. Sell SA, Francis MP, Garg K, McClure MJ, Simpson DG, Bowlin GL. (2008). "Cross-linking methods of electrospun fibrinogen scaffolds for tissue engineering applications." *Biomed Mater*. 3 (4), 045001.

10. Zeugolis DI, Khew ST, Yew ES, Ekaputra AK, Tong YW, Yung LY, Hutmacher DW, Sheppard C, Raghunath M. (2008). "Electro-spinning of pure collagen nano-fibres - just an expensive way to make gelatin?" *Biomaterials.* 29 (15), 2293-305.

11. Kuo YC, Leou SN. (2006). "Effects of Composition, Solvent, and Salt Particles on the Physicochemical Properties of Polyglycolide/Poly(lactide-co-glycolide) Scaffolds." *Biotechnol Prog.* 22 (6), 1664-70.

12. Zhao J, Yuan X, Cui Y, Ge Q, Yao K. (2004). "Preparation and characterization of poly(L -lactide)/ poly(ϵ-caprolactone) fibrous scaffolds for cartilage tissue engineering." *Journal of Applied Polymer Science,* 91 (3), 1676-168.

13. Woodruff MA, Hutmacher DW. "The return of a forgotten polymer—Polycaprolactone in the 21st century." *Progress in Polymer Science* 35.10 (2010): 1217-1256.

14. Olubamiji AD, Izadifar Z, Zhu N, Chang T, Chen XB, Eames FB. (2016). "Characterization of architecture and tissue growth in 3D-printed hybrid constructs using SR-inline-phase-contrast CT ." *Journal of Synchrotron Radiation*. 23 (3), 802-12.

15. Maroudas A. (1979). "Physiochemical properties of articular cartilage." In: Freeman MAR. (Ed.) *Adult Articular Cartilage*. Kent : Cambridge University Press, 215-290.

16. Sophia Fox AJ, Bedi A, Rodeo SA. (2009). "The basic science of articular cartilage: structure, composition, and function." *Sports Health.* 1 (16), 461-468.

17. Hendrikson W J, Rouwkema J, van Blitterswijkac C A and L Moroni L. (2015). Influence of PCL molecular weight on mesenchymal stromal cell differentiation *RSC Adv*. 5, 54510.

18. Sah RL, Kim YJ, Doong JY, Grodzinsky AJ, Plaas AH, Sandy JD. (1989)/ "Biosynthetic response of cartilage explants to dynamic compression." *J Orthop Res.* 7 (5), 619-636.

19. Wong M, Siegrist M, Cao X. (1999). "Cyclic compression of articular cartilage explants is associated with progressive consolidation and altered expression pattern of extracellular matrix proteins." *Matrix Biol.* 18 (4), 391-399.

20. Pati F, Jang J, Ha DH, Won Kim S, Rhie JW, Shim JH, Kim DH, Cho DW. (2014). "Printing three-dimensional tissue analogues with decellularized extracellular matrix bioink." *Nature Communicature* 2 (5), 3935.

21. Izadifar Z, Chang T, Kulyk W, Chen X, Eames BF. (2016). "Analyzing Biological Performance of 3D-Printed, Cell-Impregnated Hybrid Constructs for Cartilage Tissue Engineering." *Tissue Eng Part C Methods.* 22 (3), 173-88.

22. Lebourg M, Sabater Serra R, Más Estellés J, Hernández Sánchez F, Gómez Ribelles JL, Suay Antón J. (2008). "Biodegradable polycaprolactone scaffold with controlled porosity obtained by modified particle-leaching technique." *J Mater Sci Mater Med* 19 (5), 2047-53.

23. Lu L, Zhang Q, Wootton D, Lelkes P I, Zhou, J. (2010). "A novel sucrose porogen-based solid freeform fabrication system for bone scaffold manufacturing." *Rapid Prototyping Journal* 16 (5), 365-376.

24. Lu L, Zhang Q, Wootton DM, Chiou R, Li D, Lu B, Lelkes PI, Zhou J. (2014). "Mechanical study of polycaprolactone-hydroxyapatite porous scaffolds created by porogen-based solid freeform fabrication method." *J Appl Biomater Funct Mater.* 12 (3), 145-154.

25. Minton J, Janney C, Akbarzadeh R, Focke C, Subramanian A, Smith T, McKinney J, Liu J, Schmitz J, James PF, Yousefi AM. (2014). "Solvent-free polymer/bioceramic scaffolds for bone tissue engineering: fabrication, analysis, and cell growth." *J Biomater Sci Polym Ed.* 25 (16) 1856-74.

26. Correlo VM, Boesel LF, Pinho E, Costa-Pinto AR, Alves da Silva ML, Bhattacharya M, Mano JF, Neves NM, Reis RL. (2009). "Melt-based compression-molded scaffolds from chitosan-polyester blends and composites: Morphology and mechanical properties." *J Biomed Mater Res A* 91 (2), 489-504.

27. Baker SR, Banerjee S, Bonin K, Guthold M. (2016). "Determining the mechanical properties of electrospun poly-ε-caprolactone (PCL) nanofibers using AFM and a novel fiber anchoring technique." *Mater Sci Eng C Mater Biol Appl.* 59, 203-12.

28. Kundu J, Shim JH, Jang J, Kim SW, Cho DW. (2015). "An additive manufacturing-based PCL-alginate-chondrocyte bioprinted scaffold for cartilage tissue engineering." *J Tissue Eng Regen Med.* 9 (11), 1286-97.

29. Schuurman W, Khristov V, Pot MW, van Weeren PR, Dhert WJ, Malda J. (2011), "Bioprinting of hybrid tissue constructs with tailorable mechanical properties." *Biofabrication* 3 (2), 021001-021008.

30. Williams JM, Adewunmi A, Schek RM, Flanagan CL, Krebsbach PH, Feinberg SE, Hollister SJ, Das S. (2005). "Bone tissue engineering using polycaprolactone scaffolds fabricated via selective laser sintering." *Biomaterials.* 26 (23), 4817-27.

31. Jang J, Seol YJ, Kim HJ, Kundu J, Kim SW, Cho DW. (2014)."Effects of alginate hydrogel cross-linking density on mechanical and biological behaviors for tissue engineering." *J Mech Behav Biomed Mater* 37, 69-77.

32. Chen SS, Falcovitz YH, Schneiderman R, Maroudas A, Sah RL. (2001). "Depth-dependent compressive properties of normal aged human femoral head articular cartilage: relationship to fixed charge density." *Osteoarthritis Cartilage.* 9 (6) 561-569.

33. Shepherd DE, Seedhom BB. (1999). "The 'instantaneous' compressive modulus of human articular cartilage in joints of the lower limb." *Rheumatology (Oxford).* 38 (2), 124-32.

34. Magnussen RA, Guilak F, Vail TP. (2005). "Cartilage degeneration in post-collapse cases of osteonecrosis of the human femoral head: altered mechanical properties in tension, compression, and shea." *J Orthop Res.* 23 (3), 576-583.

35. Démarteau O, Pillet L, Inaebnit A, Borens O, Quinn TM. (2006). "Biomechanical characterization and *in vitro* mechanical injury of elderly human femoral head cartilage: comparison to adult bovine humeral head cartilage." *Osteoarthritis Cartilage.* 14 (6), 589-96.

36. Barker MK, Seedhom BB. (2001). "The relationship of the compressive modulus of articular cartilage with its deformation response to cyclic loading: does cartilage optimize its modulus so as to minimize the strains arising in it due to the prevalent loading regime?" *Rheumatology (Oxford).* 40 (3), 274-84.

37. Schinagl RM, Gurskis D, Chen AC, Sah RL. (1997). "Depth-dependent confined compression modulus of full-thickness bovine articular cartilage." *J Orthop Res.* 15 (4), 499-506.

38. Athanasiou KA, Agarwal A, Dzida FJ. (1994). "Comparative study of the intrinsic mechanical properties of the human acetabular and femoral head cartilage." *J Orthop Res.* 12 (3), 340-9.

39. Wong BL, Sah RL. (2010). "Mechanical asymmetry during articulation of tibial and femoral cartilages: local and overall compressive and shear deformation and properties." *J Biomech* 43 (9), 1689-95.

40. Akizuki S, Mow VC, Müller F, Pita JC, Howell DS, Manicourt DH. (1986). "Tensile properties of human knee joint cartilage: I. Influence of ionic conditions, weight bearing, and fibrillation on the tensile modulus." *J Orthop Res.* 4 (4), 379-92.

41. Temple MM, Bae WC, Chen MQ, Lotz M, Amiel D, Coutts RD, Sah RL. (2007):. "Age- and site-associated biomechanical weakening of human articular cartilage of the femoral condyle." *Osteoarthritis Cartilage.* 15 (9), 1042-52.

42. Eshraghi S, Das S. (2010). "Mechanical and microstructural properties of polycaprolactone scaffolds with one-dimensional, two-dimensional, and three-dimensional orthogonally oriented porous architectures produced by selective laser sintering." *Acta Biomater.* 6 (7), 2467-76.

43. Wang F, Shor L, Darling A, Khalil, S. (2004). "Precision extruding deposition and characterization of cellular poly-epsilon-caprolactone tissue scaffold." *Rapid Prototyping Journal* 10 (1), 42-49.

44. Mondrinos MJ, Dembzynski R, Lu L, Byrapogu VK, Wootton DM, Lelkes PI, Zhou J. (2006). "Porogen-based solid freeform fabrication of polycaprolactone-calcium phosphate scaffolds for tissue engineering." *Biomaterials.* 27 (25), 4399-4408.

45. Hutmacher DW, Schantz T, Zein I, Ng KW, Teoh SH, Tan KC. (2001). "Mechanical properties and cell cultural response of polycaprolactone scaffolds designed and fabricated via fused deposition modeling." *J Biomed Mater Res.* 55 (2), 203-16.

46. Doyle H, Lohfeld S, McHugh P. (2014). "Predicting the elastic properties of selective laser sintered PCL/β-TCP bone scaffold materials using computational modelling." *Ann Biomed Eng.* 42 (3), 661-77.

47. Croisier F, Duwez AS, Jérôme C, Léonard AF, van der Werf KO, Dijkstra PJ, Bennink ML. (2012). "Mechanical testing of electrospun PCL fibers." *Acta Biomater* 8 (1), 218-24.

48. Zein I, Hutmacher DW, Tan KC, Teoh SH. (2002). "Fused deposition modeling of novel scaffold architectures for tissue engineering applications." *Biomaterials* 23 (4), 1169-85.

49. Kovacik J. (1999). "Correlation between Young's modulus and porosity in porous materials." *Journal of Material Science Letters* 18, 1007-1010.

50. Nunes RW, Martin JR, Johnson J.F. (1982). "Influence of molecular weight and molecular weight distribution on mechanical properties of polyme." *Polymer Engineering & Science* 22 (4), 205–228.

51. Walsh DJ and Termonia Y. (1988). "Mechanical Properties of Low Molecular Weight Polymers as a Function of Temperature." *Polymer Communications* 29, 90-92.

52. Tuba F, Oláh L, Nagy P. (2014). "Towards the understanding of the molecular weight dependence of essential work of fracture in semicrystalline polymers: A study on polycaprolactone)." *eXPRESS Polymer Letters* 8 (11), 869–879.

53. Tiptipakorn S, Punuch W, Okhawilai M, Rimdusi S. (2015). "Effects of polycaprolactone molecular weights on thermal and mechanical properties of polybenzoxazine." *Journal of Polymer Researc* 22 (7), 41915 (pp 11).

54. Lim K.Y., Kim B.C., and Yoon K.J. (2002). "The Effect of Molecular Weight of Polycaprolactone on the Ester Interchange Reactions during Melt Blending with Poly(ethylene terephthalate)." *Polymer Journal* 34 (5), 313—319.

55. Ferreira SL, Bruns RE, Ferreira HS, Matos GD, David JM, Brandão GC, da Silva EG, Portugal LA, dos Reis PS, Souza AS, dos Santos WN. (2007). "Box-Behnken design: an alternative for the optimization of analytical methods." *Anal Chim Acta.* 6 (597), 179-86.

56. Ma H, Liu WW, Chen X, Wu YJ, Yu ZL. (2009). "Enhanced enzymatic saccharification of rice straw by microwave pretreatment." *Bioresour Technol* 100 (3), 1279-84.

57. Cooper D, Turinsky A., Sensen C., Hallgrimsson B. (2007). "Effect of Voxel Size on 3D Micro-CT Analysis of Cortical Bone Porosity." *Calcif Tissue Int* 80, 211-219.

58. Karger-Kocsis, József. (1999). "Dependence of the fracture and fatigue performance of polyolefins and related blends and composites on microstructural and molecular characteristics." *Macromolecular Symposia* 143, 185–205.

59. Li MG, Tian XY, Chen XB. (2009). "A brief review of dispensing-based rapid prototyping techniques in tissue scaffold fabrication: role of modeling on scaffold properties prediction." *Biofabrication* 1 (3), 032001- 032011.

60. Asmania M, Kermela C, Lerichea A, Ourakb M. (2001). "Influence of porosity on Young's modulus and Poisson's ratio in alumina ceramics." *Journal of the European Ceramic Society* 21 (8), 1081–1086.

61. Kempson GE, Spivey CJ, Swanson SAV, Freeman MAR. (1971)."Patterns of cartilage stiffness on normal and degenerate human femoral heads." *Jounal of Biomechanics* 4 (6), 609-608.

62. Kempson GE, Muir H, Pollard C, Tuke M. (1973). "The tensile properties of the cartilage of human femoral condyles related to the content of collagen and glycosaminoglycans." *Biochim Biophys Acta* 297 (2), 456-72.

63. Yoo HS, Lee EA, Yoon JJ, Park TG. (2008). "Hyaluronic acid modified biodegradable scaffolds for cartilage tissue engineering." *Biomaterials.* 26.14 (2005): 1925-33.Yue ZB,

Yu HQ, Hu ZH, Harada H, Li YY. "Surfactant-enhanced anaerobic acidogenesis of Canna indica L. by rumen cultures." *Bioresour Technol* 99 (9), 3418-23.

64. Shor L, Güçeri S, Chang R, Gordon J, Kang Q, Hartsock L, An Y, Sun W. (2009). "Precision extruding deposition (PED) fabrication of polycaprolactone (PCL) scaffolds for bone tissue engineering." *Biofabrication.* 1 (1), 015003 (pp 10).

Chapter 6: Conclusions and Future Work

6.1. Conclusions

Three-dimensional (3D)-printed cartilage constructs fabricated from polycaprolactone and chondrocyte-impregnated alginate hydrogel mimic the biphasic nature of articular cartilage and offer promise for CTE applications. However, ascertaining that these constructs provide both biologically conducive environment and mechanical support for cellular activities and cartilage regeneration is still a challenge. Having said that, the regulatory pathway for medical device development requires validation of implants, such as these cartilage constructs, through *in vitro* bench test and *in vivo* preclinical examination prior to their premarket approval. Since mechano-transduction and secretion of cartilage-specific ECM are influenced by mechanical stimuli directed at cells within these constructs, ensuring that these cartilage constructs have mechanical properties similar to those of human articular cartilage is also critical to their success. Furthermore, an effective non-invasive imaging technique is required for evaluation of progression of these hybrid cartilage constructs. However, current non-invasive techniques cannot decipher components of the hybrid cartilage constructs, nor their time-dependent structural changes, because they contain hydrophobic and hydrophilic biomaterials with different X-ray refractive indices.

The aims of this thesis were to develop 3D-printed cartilage constructs that biologically and mechanically mimic human articular cartilage and to investigate SR-inline-PCI-CT as a non-invasive imaging technique to characterize components of these constructs and associated time-dependent structural changes. Specifically, the research was carried out along the following three directions:

a. Investigation of SR-inline-PCI-CT by modulation of SDDs to obtain the optimal SDD with effective edge enhancement fringes with capability to decipher the individual components of the 3D-printed PCL/alginate/cells constructs and associated structural changes. Complementarily, *in vitro* biological functionality of the cartilage constructs over a 42-day period *in vitro* was investigated by traditional invasive histological assays.
b. Analysis of the *in vivo* biological functionality of the 3D-printed hybrid cartilage constructs over a 21-day period post-implantation in nude mice by invasive histological assays. Then, characterization of individual components and associated structural changes within 3D-printed cartilage constructs over a 21-day period post-implantation in nude mice by the optimal SR-inline-PCI-CT parameters previously reported.

c. Modulation of the M_W of the PCL and pore geometrical configurations of PCL scaffolds enabled design and fabrication of PCL scaffolds with mechanical and biomimetic properties that better mimic mechanical behaviour of human articular cartilage.

The main conclusions drawn from this research are summarized as follows:

- This thesis illustrated that SR-inline-PCI-CT offers an unparalleled technique for non-invasive, non-destructive and three-dimensional characterization of samples with multiple low X-rays attenuation coefficient in a manner that would be impossible by conventional non-invasive imaging techniques. Specifically, an SDD of 3 m provided the edge enhancement fringes with capability for effective visualization of all components of the cell-impregnated biphasic cartilage constructs in aqueous solution and *in situ* in mice. In addition, the optimal SDD of 3 m allowed assessment of subtle structural changes within the 3D-printed PCL/alginate/cells constructs and surrounding fluid over a 42-day period *in vitro* and *in situ* over a 21-day period post-implantation in mice.
- Cell-impregnated 3D-printed cartilage constructs showed successful biological performance *in vitro* over a 42-day period and *in vivo* in mice over a 21-day period. In detail, cell viability was above 70 % at all time-points, and there was progressive secretion of sulfated GAGs and Col2 over time both *in vitro* and *in vivo*. Thus, the 3D-printed cell-impregnated cartilage constructs can be scaled-up for regeneration of articular cartilage *in vivo* and as such have great potential for articular cartilage regeneration.
- Experimental results showed that modulating molecular weight (M_W) and pore geometrical configurations have statistically significant effect on the mechanical behavior of the PCL scaffolds. “Modulated PCL scaffolds” identified have compressive and tensile moduli of 6.63 ± 0.50 MPa and 6.03 ± 1.01 MPa respectively and these values are in the reported range of human femoral articular cartilage. The PCL framework of the “modulated PCL scaffolds” was recommended as framework for subsequent studies focused on fabrication of PCL-based constructs for CTE applications.

6.2. Future Work

Based on the research presented in this thesis, the following are the recommendations and suggested projects that can be conducted to extend or build upon these results:

1. Although the mechanical properties of the PCL framework were modulated to mimic those of human articular cartilage, this thesis did not study the difference between the mechanical properties of individual zones of the articular cartilage and how the PCL scaffolds could be modulated to represent the individual zones of the articular cartilage. Therefore, a study focused on modulation of the framework of the PCL scaffolds to mimic each zone of the articular cartilage is recommended.
2. Mechanical stimuli exerted on chondrocytes in articular cartilage has been reported to affect secretion of cartilage-specific ECM. Therefore, a study considering the effect of mechanical stimuli on secretion of ECM within the 3D-printed hybrid constructs implanted in the stifle joint of larger animal such as pigs or goats is suggested.
3. Both *in vitro* and *in vivo* studies ended within a 42-day period and the period were too short for growth of thick cartilage neo-tissues that might be easier to delineate by SR-inline-PCI-CT. As such, a clinically-relevant longer period than explored in this thesis (e.g. 6 - 12 months) is recommended for investigation of the secretion of ECM within these constructs. Furthermore, long-term non-invasive assessment of the progression of tissue growth in animal models over a long period (e.g. 6 - 12 months) by SR-inline-PCI-CT. Lastly, measurement of the absorbed radiation dose during imaging of these cartilage constructs and possibly optimization of this technique to ensure radiation safety without diminishing the image quality provided is recommended.
4. The progression towards the use of non-immunodeficient large animals such as pigs or rabbits will require investigation of autologous viable chondrocytes or mesenchymal stem cells extracted from these animals. Since the biphasic 3D-printed cartilage constructs have proven to be successful with different cell types, a large *in vitro* study may not be necessary. Thus, this thesis recommends conducting a pilot *in vitro* study to examine the functionality of autologous cells (from an animal of interest) within the biphasic 3D-printed cartilage constructs. Then, a subsequent *in vivo* examination of the functionality of the cartilage constructs in an animal model of interest after the successful completion and troubleshooting of the *in vitro* feasibility study.

5. Because an increase in secretion of cartilage-specific ECM is highly desirable for effective regeneration of hyaline cartilage, this thesis also recommends:
    a. Examination of the effect of inclusion of bioactive molecules or growth factors to enhance cell proliferation and amount of cartilage-specific ECM secreted within the biphasic 3D-printed PCL/alginate/cells constructs over time.
    b. Investigation of decellularized extracellular matrix (which contains the components of the extracellular matrix without cells) as an alternative to alginate hydrogel for promotion of biomimetic cell differentiation and cell viability within the biphasic 3D-printed PCL/alginate/cells constructs.

Appendix for Chapter 3: Regression Modelling of Compressive Moduli, Tensile Moduli and Porosity

Modelling Compressive Modulus

Predictive Model:

$Y = \beta_0 + \beta_{\text{strand spacing}} X_{\text{strand spacing}} + \beta_{\text{strand orientation}} X_{\text{strand orientation}} + \beta_{\text{strand size}} X_{\text{strand size}} + \varepsilon$

Test of assumptions for model

Dependent variable is continuous – Implicit by design

Two or more independent variables – Implicit by design

Homoscedasticity – The scatter plot of the standardized residuals and the standardized predicted values shows some divergence of the points. The variance is noted to be increasing across residuals suggesting a violation of the homoscedasticity assumption. *Analysis to be re-run with the outcome variable transformed.*

Test of Assumptions with Y Log-Transformed

Predictive model:

$\text{Ln } Y = \beta_0 + \beta_{\text{strand spacing}} X_{\text{strand spacing}} + \beta_{\text{strand orientation}} X_{\text{strand orientation}} + \beta_{\text{strand size}} X_{\text{strand size}} + \varepsilon$

Dependent variable is continuous – Implicit by design

Two or more independent variables – Implicit by design

Independence of residuals (Durbin Watson test for autocorrelation of residuals) – Durbin Watson test statistic of 2.148 is greater than the upper bound (1.392) from the Savin and White tables (N=39, k=2). Thus, we cannot reject the null hypothesis of zero autocorrelation.

Model Summary[b]

Model	R	R Square	Adjusted R Square	Std. Error of the Estimate	Durbin-Watson
1	.904[a]	.818	.808	.27636	2.148

a. Predictors: (Constant), Strand_ Spacing, Strand_Size

b. Dependent Variable: Ln_Compressive_Modulus

Linear relationship between the dependent variable and each independent variable – Independent variables are categorical

Homoscedasticity – The scatter plot of the standardized residuals and the standardized predicted values do not fan out. There is no distinct pattern. Using the Breusch-Pagan test for homoscedasticity, the p-value = 0.955 > α = 0.05. Thus, we cannot reject the hypothesis that the variances of the residuals are constant.

ANOVA[a]

Model		Sum of Squares	df	Mean Square	F	Sig.
1	Regression	.069	2	.035	.046	.955[b]
	Residual	27.032	36	.751		
	Total	27.101	38			

a. Dependent Variable: Residuals_Sq

b. Predictors: (Constant), Strand_ Spacing, Strand_Size

Similarly, using the abridged White test, the p-value = 0.575 > α = 0.05. Thus we cannot reject the hypothesis that the variances of the residuals are constant.

ANOVA[a]

Model		Sum of Squares	df	Mean Square	F	Sig.
1	Regression	.820	2	.410	.562	.575[b]
	Residual	26.281	36	.730		
	Total	27.101	38			

a. Dependent Variable: Residuals_Sq

b. Predictors: (Constant), Pred_Values_Sq, Standardized Predicted Value

Multicollinearity – All predictor variables are independent of each other, with the correlation matrix showing non-significant Pearson correlations. Also, neither the VIF and condition number for each variable is greater than 10 or 30 respectively.

Outliers or influential points – The standardized residuals are not less than -3 or greater than 3. Mean values for Cook's distance was less than 4/n and no Cook's value was greater than 1; thus influential points are unlikely.

Residuals Statistics[a]

	Minimum	Maximum	Mean	Std. Deviation	N
Predicted Value	1.8215	3.7585	2.7900	.56985	39
Std. Predicted Value	-1.699	1.699	.000	1.000	39
Standard Error of Predicted Value	.044	.091	.076	.013	39
Adjusted Predicted Value	1.8076	3.7302	2.7870	.56855	39

Residual	-.50039	.48888	.00000	.26899	39
Std. Residual	-1.811	1.769	.000	.973	39
Stud. Residual	-1.875	1.832	.005	1.012	39
Deleted Residual	-.53650	.52416	.00304	.29099	39
Stud. Deleted Residual	-1.946	1.897	.004	1.024	39
Mahal. Distance	.000	3.167	1.949	.923	39
Cook's Distance	.000	.085	.027	.024	39
Centered Leverage Value	.000	.083	.051	.024	39

a. Dependent Variable: Ln_Compressive_Modulus

Normality of residuals – At the 5 % level of significance, there is insufficient evidence to reject the assumption that the standardized residuals of the compressive modulus are normally distributed (p-value = 0.129).

Tests of Normality

	Kolmogorov-Smirnov[a]			Shapiro-Wilk		
	Statistic	df	Sig.	Statistic	df	Sig.
Standardized Residual	.122	39	.147	.956	39	.129

a. Lilliefors Significance Correction

Hypothesis testing

	Beta Coefficient	t	Sig	95 % Confidence Interval for Beta	
				Lower bound	Upper bound
Constant	3.508	17.528	.000	3.102	3.915
Strand_Size	0.334	5.925	.000	0.220	0.448
Strand_Spacing	-0.635	-11.621	.000	-0.749	-0.520
Strand_Orientation	-0.058	-1.037	.307	-0.173	0.056

a. Dependent Variable: Ln_Compressive_Modulus

	Beta Coefficient	t	Sig	95 % Confidence Interval for Beta	
				Lower bound	Upper bound
Constant	3.391	20.482	.000	3.056	3.727

Strand_Size	0.334	5.919	.000	0.219	0.448
Strand_Spacing	-0.635	-11.249	.000	-0.749	-0.520

a. Dependent Variable: Ln_Compressive_Modulus

b. Strand_Orientation was not a statistically significant predictor of compressive modulus and thus eliminated from the model.

Conclusion

Final regression equation modelling the transformed compressive modulus:

$\text{Ln } \hat{y} = 3.39 - 0.64X_{\text{strand spacing}} + 0.33X_{\text{strand size}}$

For every unit increase in strand spacing, the log of the compressive modulus will decrease by 0.64 units (when all other factors are held constant). For every unit increase in strand size, the log of the compressive modulus will increase by 0.33 units (when all other factors are held constant). Thus, the compressive modulus increases with increasing strand size and decreases with increasing strand spacing.

Exponentiated Interpretation

Final regression equation modelling the compressive modulus:

$\text{Ln } \hat{Y} = 3.39 - 0.64X_{\text{strand spacing}} + 0.33X_{\text{strand size}}$

Exponentiate to reverse transformation

$\hat{Y} = 29.67 + 0.53X_{\text{strand spacing}} + 1.39X_{\text{strand size}}$

For every unit increase in strand spacing, the compressive modulus will increase by 0.5 times (or decrease by 2) when all other factors are held constant. For every unit increase in strand size, the compressive modulus will increase by 1.3 times (when all other factors are held constant). Thus, the compressive modulus increases with increasing strand size and decreases with increasing strand spacing.

NB: Unit increments as referred to in this interpretation correspond to the following:

- *Strand spacing: 1 unit increase = 0.5 mm increase in strand spacing*
- *Strand size: 1 unit increase = 100 µm increase in strand size*

Modelling the Tensile Modulus

Predictive Model:

$Y = \beta_0 + \beta_{\text{strand spacing}} X_{\text{strand spacing}} + \beta_{\text{strand orientation}} X_{\text{strand orientation}} + \beta_{\text{strand size}} X_{\text{strand size}} + \varepsilon$

Test of assumptions for model

Dependent variable is continuous – Implicit by design

Two or more independent variables – Implicit by design

Homoscedasticity – The scatter plot of the standardized residuals and the standardized predicted values shows some divergence of the points. The variance is noted to be increasing across residuals suggesting a violation of the homoscedasticity assumption. *Analysis to be re-run with the outcome variable transformed.*

Test of Assumptions with Y log-Transformed

Predictive model (n=39):

$\text{Ln } Y = \beta_0 + \beta_{\text{strand spacing}} X_{\text{strand spacing}} + \beta_{\text{strand orientation}} X_{\text{strand orientation}} + \beta_{\text{strand size}} X_{\text{strand size}} + \varepsilon$

Normality of residuals – At the 5 % level of significance, there is evidence to reject the assumption that the standardized residuals of the tensile modulus are normally distributed (p-value =0.023). The normality assumption has been violated.

Tests of Normality

	Kolmogorov-Smirnov[a]			Shapiro-Wilk		
	Statistic	df	Sig.	Statistic	df	Sig.
Standardized Residual	.116	39	.200*	.933	39	.023

*. This is a lower bound of the true significance.

a. Lilliefors Significance Correction

Outliers or influential points – More than 5 % of the data points lie outside the standardized score range of -2 to 2.

Casewise Diagnostics[a]

Case Number	Std. Residual	Ln_Tensile_Modulus	Predicted Value	Residual
15	-2.045	2.33	2.8240	-.49375
17	-2.644	2.19	2.8240	-.63846
18	-2.147	2.31	2.8240	-.51837

a. Dependent Variable: Ln_Tensile_Modulus

Given the above finding and the violation of the normality assumption, the model would need to be refit eliminating the data points that were significant outliers (starting with case number 17 and 18).

Refit Log-Transformed Model

Refit predictive log transformed model (n = 37):

$\text{Ln } Y = \beta_0 + \beta_{\text{strand spacing}} X_{\text{strand spacing}} + \beta_{\text{strand orientation}} X_{\text{strand orientation}} + \beta_{\text{strand size}} X_{\text{strand size}} + \varepsilon$

Dependent variable is continuous – Implicit by design

Two or more independent variables – Implicit by design

Independence of residuals (Durbin Watson test for autocorrelation of residuals) – Durbin Watson test statistic of 2.418 is greater than the upper bound (1.446) from the Savin and White tables (N=37, k=3). Thus, we cannot reject the null hypothesis of zero autocorrelation.

Model Summary[b]

Model	R	R Square	Adjusted R Square	Std. Error of the Estimate	Durbin-Watson
1	.937[a]	.879	.868	.20058	2.418

a. Predictors: (Constant), Strand_Orientation, Strand_Thickness, Strand_Size

b. Dependent Variable: Ln_Tensile_Modulus

Linear relationship between the dependent variable and each independent variable – Independent variables are categorical

Homoscedasticity – The scatter plot of the standardized residuals and the standardized predicted values do not fan out. There is no distinct pattern. Using the Breusch-Pagan test for homoscedasticity, the p-value = 0.630 > α = 0.05. Thus, we cannot reject the hypothesis that the variances of the residuals are constant.

ANOVA[a]

Model		Sum of Squares	df	Mean Square	F	Sig.
1	Regression	3.163	3	1.054	.583	.630[b]
	Residual	59.689	33	1.809		
	Total	62.851	36			

a. Dependent Variable: Std_Resid_Sq

b. Predictors: (Constant), Strand_Orientation, Strand_Thickness, Strand_Size

Similarly, using the abridged White test, the p-value = 0.564 > α = 0.05. Thus, we cannot reject the hypothesis that the variances of the residuals are constant.

ANOVA[a]

Model		Sum of Squares	df	Mean Square	F	Sig.
1	Regression	2.083	2	1.042	.583	.564[b]

	Residual	60.768	34	1.787		
	Total	62.851	36			

a. Dependent Variable: Std_Resid_Sq

b. Predictors: (Constant), Standardized Predicted Value, Std_Pred_Values_Sq

Multicollinearity – All predictor variables are independent of each other, with the correlation matrix showing non-significant Pearson correlations. Also, neither the VIF and condition number for each variable is greater than 10 or 30 respectively.

Outliers or influential points – The standardized residuals are not less than -3 or greater than 3. Mean values for Cook's distance was less than 4/n and no Cook's value was greater than 1; thus, influential points are unlikely.

Residuals Statistics[a]

	Minimum	Maximum	Mean	Std. Deviation	N
Predicted Value	1.9925	3.7180	2.8552	.51719	37
Std. Predicted Value	-1.668	1.668	.000	1.000	37
Standard Error of Predicted Value	.033	.067	.066	.006	37
Adjusted Predicted Value	2.0004	3.7150	2.8539	.51763	37
Residual	-.52502	.37644	.00000	.19204	37
Std. Residual	-2.617	1.877	.000	.957	37
Stud. Residual	-2.654	1.990	.003	1.006	37
Deleted Residual	-.53960	.42314	.00137	.21215	37
Stud. Deleted Residual	-2.946	2.089	-.005	1.041	37
Mahal. Distance	.000	3.000	2.919	.493	37
Cook's Distance	.000	.139	.026	.030	37
Centered Leverage Value	.000	.083	.081	.014	37

a. Dependent Variable: Ln_Tensile_Modulus

Normality of residuals – At the 5 % level of significance, there is insufficient evidence to reject the assumption that the standardized residuals of the tensile moduli are normally distributed (p-value = 0.258)

Tests of Normality

	Kolmogorov-Smirnov[a]			Shapiro-Wilk		
	Statistic	df	Sig.	Statistic	df	Sig.
Standardized Residual	.108	37	.200*	.963	37	.258

*. This is a lower bound of the true significance.

a. Lilliefors Significance Correction

Hypothesis Testing

	Beta Coefficient	t	Sig	95 % Confidence Interval for Beta	
				Lower bound	Upper bound
Constant	2.403	16.504	.000	2.107	2.700
Strand_Spacing	-0.401	-9.791	.000	-0.484	-0.318
Strand_Orientation	0.165	4.029	.000	0.082	0.248
Strand_Size	0.462	11.281	.000	0.379	0.545

b. Dependent Variable: Ln_Tensile_Modulus

Conclusion

Final regression equation modelling the transformed tensile modulus:

$\text{Ln } \hat{Y} = 2.40 - 0.40X_{\text{strand spacing}} + 0.17X_{\text{strand orientation}} + 0.46X_{\text{strand size}}$

For every unit increase in strand spacing, the log of tensile modulus will decrease by 0.40 units (when all other factors are held constant) and as strand orientation changes from 0-45 to 0-90 or from 0-90 to 0-45-90-135, the log of the tensile modulus will increase by 0.17 units (when all other factors are held constant). For every unit increase in strand size, the log of the tensile modulus will increase by 0.46 units (when all other factors are held constant). Thus, the tensile modulus increases with increasing strand size and decreases with increasing strand spacing. It also increases with change in strand orientation from 0-45 to 0-90; 0-45 to 0-45-90-135 or from 0-90 to 0-45-90-135.

Exponentiated Interpretation

Final regression equation modelling the tensile modulus:

$\text{Ln } \hat{y} = 2.40 - 0.40X_{\text{strand spacing}} + 0.17X_{\text{strand orientation}} + 0.46X_{\text{strand size}}$

Exponentiate to reverse transformation

$\hat{Y} = 11.02 + 0.67X_{\text{strand spacing}} + 1.19X_{\text{strand orientation}} + 1.58X_{\text{strand size}}$

For every unit increase in strand spacing, the tensile modulus will increase by 0.67 times (or decrease by 1.5 times) when all other factors are held constant. As strand orientation changes from 0-45 to 0-90 or from 0-90 to 0-45-90-135, the tensile modulus will increase by 1.2 times (when all other factors are held constant). Furthermore, for every unit increase in strand size, the tensile modulus will increase by 1.6 times (when all other factors are held constant). Thus, tensile modulus increases with increasing strand size and decreases with increasing strand spacing. It also increases with change in strand orientation from 0-45 to 0-90; 0-45 to 0-45-90-135 or from 0-90 to 0-45-90-135.

NB: Unit increments as referred to in this interpretation correspond to the following:

- *Strand spacing: 1 unit increase = 0.5mm increase in strand spacing*
- *Strand size: 1 unit increase = 100 µm increase in strand size*
- *Strand orientation is a nominal variable and was represented with ordinal values (1, 2, 3) for the regression analysis. Thus, the interpretation is made to reflect the actual nominal nature of the orientation.*

Modelling Object Porosity

Predictive Model:

$Y = \beta_0 + \beta_{\text{strand spacing}} X_{\text{strand spacing}} + \beta_{\text{strand orientation}} X_{\text{strand orientation}} + \beta_{\text{strand size}} X_{\text{strand size}} + \varepsilon$

Test of Assumptions for Model

Dependent variable is continuous – Implicit by design

Two or more independent variables – Implicit by design

Independence of residuals (Durbin Watson test for autocorrelation of residuals) – Durbin Watson test statistic of 2.361 is greater than the upper bound (1.392) from the Savin and White tables (N=39, k=2). Thus, we cannot reject the null hypothesis of zero autocorrelation.

Model Summary[b]

Model	R	R Square	Adjusted R Square	Std. Error of the Estimate	Durbin-Watson
1	.952[a]	.906	.901	4.24939	2.361

a. Predictors: (Constant), Strand_ Spacings, Strand_Size

b. Dependent Variable: Object_Porosity

Linear relationship between the dependent variable and each independent variable – Independent variables are categorical.

Homoscedasticity – The scatter plot of the standardized residuals and the standardized predicted values do not fan out. There is no distinct pattern. Using the Breusch-Pagan test for homoscedasticity, the p-value = 0.730 > α = 0.05. Thus, we cannot reject the hypothesis that the variances of the residuals are constant.

ANOVA[a]

Model		Sum of Squares	df	Mean Square	F	Sig.
1	Regression	1.606	2	.803	.318	.730[b]
	Residual	91.054	36	2.529		
	Total	92.661	38			

a. Dependent Variable: Residuals_Sq

b. Predictors: (Constant), Strand_ Spacing, Strand_Size

Similarly, using the abridged White test, the p-value = 0.391 > α = 0.05. Thus, we cannot reject the hypothesis that the variances of the residuals are constant.

ANOVA[a]

Model		Sum of Squares	df	Mean Square	F	Sig.
1	Regression	4.715	2	2.357	.965	.391[b]
	Residual	87.946	36	2.443		
	Total	92.661	38			

a. Dependent Variable: Residuals_Sq

b. Predictors: (Constant), Pred_Values_Sq, Standardized Predicted Value

Multicollinearity – All predictor variables are independent of each other, with the correlation matrix showing non-significant Pearson correlations. Also, neither the VIF and condition number for each variable is greater than 10 or 30 respectively.

Outliers or influential points – The standardized residuals are not less than -3, but one data point has a residual greater than 3 suggestive of an outlier. However, closer inspection of the data point revealed no cause for concern. Mean values for Cook's distance was less than 4/n and no Cook's value was greater than 1; thus, influential points are unlikely.

Residuals Statistics[a]

	Minimum	Maximum	Mean	Std. Deviation	N
Predicted Value	37.9159	83.2032	60.5596	12.83372	39

Std. Predicted Value	-1.764	1.764	.000	1.000	39
Standard Error of Predicted Value	.680	1.403	1.162	.197	39
Adjusted Predicted Value	38.0172	83.9175	60.6092	12.84894	39
Residual	-5.84036	12.87175	.00000	4.13605	39
Std. Residual	-1.374	3.029	.000	.973	39
Stud. Residual	-1.456	3.069	-.006	1.001	39
Deleted Residual	-6.55465	13.21048	-.04963	4.37612	39
Stud. Deleted Residual	-1.480	3.521	.007	1.046	39
Mahal. Distance	.000	3.167	1.949	.923	39
Cook's Distance	.000	.086	.019	.021	39
Centered Leverage Value	.000	.083	.051	.024	39

a. Dependent Variable: Object_Porosity

Normality of residuals – At the 5 % level of significance, there is insufficient evidence to reject the assumption that the standardized residuals of the compressive modulus are normally distributed (p-value = 0.051)

Tests of Normality

	Kolmogorov-Smirnov[a]			Shapiro-Wilk		
	Statistic	df	Sig.	Statistic	df	Sig.
Standardized Residual	.096	39	.200*	.944	39	.051

*. This is a lower bound of the true significance.

a. Lilliefors Significance Correction

Hypothesis Testing

	Beta Coefficient	t	Sig	95 % Confidence Interval for Beta	
				Lower bound	Upper bound

Constant	55.725	17.937	.000	49.418	62.033
Strand_Size	-9.836	-11.245	.000	-11.612	-8.060
Strand_ Spacing	12.808	14.642	.000	11.032	14.583
Strand_Orientation	-0.554	-0.634	.530	-2.330	1.221

a. Dependent Variable: Object_Porosity

	Beta Coefficient	t	Sig	95 % Confidence Interval for Beta	
				Lower bound	Upper bound
Constant	54.617	21.452	.000	49.453	59.780
Strand_Size	-9.836	-11.340	.000	-11.595	-8.077
Strand_ Spacing	12.808	14.765	.000	11.048	14.567

a. Dependent Variable: Object_Porosity

Strand_Orientation was not a statistically significant predictor of object porosity and was thus eliminated from the model.

Conclusion

Final regression equation modelling object porosity:

$\hat{Y} = 54.62 - 9.84X_{\text{strand size}} + 12.81X_{\text{strand spacing}}$

For every unit increase in strand size, the object porosity will decrease by 9.84 % (when all other factors are held constant). Then, for every unit increase in strand spacing, the object porosity will increase by 12.81 % (when all other factors are held constant). Thus, object porosity decreases with increasing strand size and increases with increasing strand spacing.

NB: Unit increments as referred to in this interpretation correspond to the following:

- *Strand spacing: 1 unit increase = 0.5mm increase in strand spacing*
- *Strand size: 1 unit increase = 100 µm increase in strand size*

Relationship between Tensile Modulus and Object Porosity

Pearson's Correlation

Correlations

		Object_Porosity	Tensile_Modulus
Object_Porosity	Pearson Correlation	1	-.826**
	Sig. (2-tailed)		.000

	N	39	39
	Pearson Correlation	-.826**	1
Tensile_Modulus	Sig. (2-tailed)	.000	
	N	39	39

**. Correlation is significant at the 0.01 level (2-tailed).

At the 5 % level of significance, there is no evidence to reject the assumption that a linear relationship exists between the tensile modulus and object porosity measurements obtained (r= -0.826, p-value < 0.001). The correlation coefficient of -0.826 is suggestive of a strong inverse relationship between the tensile modulus and object porosity measurements.

Relationship between Compressive Modulus and Object Porosity

Pearson's Correlation

Correlations

		Object_Porosity	Compressive_Modulus
Object_Porosity	Pearson Correlation	1	-.868**
	Sig. (2-tailed)		.000
	N	39	39
Compressive_Modulus	Pearson Correlation	-.868**	1
	Sig. (2-tailed)	.000	
	N	39	39

**. Correlation is significant at the 0.01 level (2-tailed).

At the 5 % level of significance, there is no evidence to reject the assumption that a linear relationship exists between the compressive modulus and object porosity measurements obtained (r= -0.868, p-value < 0.001). The correlation coefficient of -0.868 is suggestive of a strong inverse relationship between the compressive modulus and object porosity measurements.